



NEAR INFRARED TUNABLE DIODE LASER  
SPECTROSCOPY FOR AERO ENGINE  
RELATED APPLICATIONS

James R.P. Bain

Centre for Microsystems and Photonics  
Department of Electronic and Electrical Engineering

A thesis presented in fulfilment of the requirements for the degree of

Doctor of Engineering

August 2012

This thesis is the result of the author's original research. It has been composed by the author and has not been previously submitted for examination which has lead to the award of a degree.

The copyright of this thesis belongs to the author under the terms of the United Kingdom Copyright Acts as qualified by University of Strathclyde Regulation 3.50. Due acknowledgment must always be made of the use of any material contained in, or derived from, this thesis.

Signed:

Date:

# Acknowledgements

There are many people who have contributed directly and indirectly towards my EngD over the last four years. I owe a lot to Walter Johnstone for agreeing to take me on for this project and for his supervision throughout. Even when he became Head of Department, not long after I started, he still found time to help me out when it was needed and placed a lot of faith in my ability to go away and get things done. The fact that he kept me on for a while beyond the end of the project is a promising sign but I cannot emphasise enough how much that extension has helped me since I became ill at the start of the year. There is a rarely a dull moment in the gas sensing team and I have really appreciated the opportunity to travel to several conferences with the guys.

John Black at Rolls-Royce was the driving force of the project from the company end and without him this particular project would have never come about. His guidance and insight into the applications of the work was invaluable and he instigated several of the most interesting and enjoyable areas of the project, in particular the three engine test campaigns. These were definitely some of the most stressful and yet ultimately satisfying and exciting aspects of the project. His assistance on the tests and his work behind the scenes at Rolls-Royce are greatly appreciated.

As the details of the project became clear in the early stages, I began to realise how much I would owe to the impressive insight and gracious assistance of George Stewart. His grasp of the tougher theoretical elements of our work and his creativity in problem solving played a huge role in the successful outcomes of this project. There were many times, after days and months of running around in circles in the lab and in my head, that a chat with George would lead to progress for which I am very thankful.

I am not entirely sure that working in close proximity to Mick Lengden for as long as I have is a great idea but without him the last four years would have been entirely different. Mick had some involvement in the majority of the work and play over the course of the project and he has seen me at my best and worst.

I am very thankful for his contributions throughout but in particular: for passing on his MATLAB skills, for allowing me to overcome several logistical obstacles and attend his wedding, for encouraging me to use L<sup>A</sup>T<sub>E</sub>X to create this fine thesis and for all the evenings, weekends, travels and fire alarms that we spent in the pub. I would like to state categorically that I believe Yorkshire is the superior county.

Kev Duffin did a lot to help me get up to speed in the early stages and his early work with Andy provided a foundation for a lot of the research that I ended up doing. The trans-Pennine football tour tradition was a great distraction from the office routine and we need to make sure it lives on despite Mick's current lack of enthusiasm. Ian Armstrong deserves a medal for fielding countless tricky practical questions from me and also for creating Übercontrol which came in very handy. Keith Ruxton and Arup Lal Chakraborty deserve a special mention although I would like to point out that, despite his protestations, Arup was in fact horrendously hungover at the Hofbräuhaus. I am grateful to Gordon Flockhart who has been generous with his time and insight on many occasions and also to Carol, Sadie, Rachel and Jo who have all been helpful with the administrative tasks. I apologise to the other members of the Centre for Microsystems and Photonics that I have omitted to mention but thank everybody for providing a stimulating and friendly working environment. My sister Ailsa deserves a mention for letting me move in with her at the very start and my current flatmate Alan Cameron, who has kept me fed for the duration, is due some credit for providing some quality distractions outside the office.

I would like to acknowledge the Industrial Doctorate Centre in Optics and Photonics at Heriot-Watt University for their oversight and for allowing me to sit on the IDC Management Committee and also the Engineering and Physical Sciences Research Council and Rolls-Royce for their funding.

# Abstract

Tunable diode laser spectroscopy is a widely used technique for recovering quantitative gas information in a range of industrial applications. Established methods often use readily available, robust and low cost optoelectronic hardware in the near-infrared, with output wavelengths that coincide with the absorption spectra of several important gas species of interest, providing a versatile platform for gas analysis instrumentation.

In this work the challenges associated with the recovery of gas information from harsh detection environments, particularly for aero engine diagnostics, are considered. For stand-alone instrumentation, calibration-free direct absorption measurements are highly advantageous yet calibrated techniques employing wavelength modulation spectroscopy are often favoured due to their significantly higher sensitivities. Recent developments have enabled calibration-free line shape recovery using lock-in amplifier detection of the residual amplitude modulation in wavelength modulated signals. These techniques have significant potential in harsh environments, but the overall sensitivity is limited by distortions to the recovered line shapes at high modulation amplitudes and by large background signals that saturate the detection electronics.

In this thesis, solutions to these two problems are proposed, investigated and validated. A correction function is derived that is able to account for line shape distortions at arbitrarily high modulation indices. Application of the function depends upon knowledge of the experimental modulation index and two methods for extracting this information directly from the experimental signals are described. The full correction procedure has been experimentally validated. An investigation was made into the use of autobalanced photoreceivers, typically used for common mode noise cancellation, for direct absorption measurements and in a different configuration for nulling of the residual amplitude modulation (RAM) in wavelength modulation spectroscopy. Initial measurements suggest that removal of the background RAM can increase the lock-in detection sensitivity by over an order of magnitude. In addition an external amplitude modulator has been

shown to be an effective method for producing sensitive absorption signals that are free of distortions, recoverable at frequencies that are outside the bandwidth of most environmental noise sources.

A temperature sensor based on ratio thermometry of ambient water vapour absorption was designed and evaluated. The sensor is intended to provide accurate intake gas temperature information during aero engine ground testing when misting conditions prevent standard thermocouples from providing reliable data. Direct detection and second harmonic wavelength modulation spectroscopy experiments were undertaken in an environmental chamber, over the range 273-313 K, to test the potential accuracy of the proposed system. Using a second harmonic peak height method, temperature information based on a calibration was able to recover temperature measurements with precision of  $\pm 0.4$  K however the overall accuracy suffered from a problematic calibration drift.

Three engine test campaigns are described in which a range of recovery methods and potential optical system layouts are evaluated for the purposes of intake and exhaust mounted test bed sensor systems. The effects of extreme noise conditions were observed on a variety of measurements and favourable detection and modulation options were identified for the purpose of planning proposed future engine tests. Exhaust plume measurements of high temperature water vapour on the Rolls-Royce Environmentally Friendly Engine demonstrator established the viability of temperature and concentration measurements up to 850 K.

# Contents

<b>1</b>	<b>Introduction</b>	<b>1</b>
1.1	Gas Sensor Applications . . . . .	1
1.2	Traditional Gas Sensing Techniques . . . . .	3
1.3	Principles of Tunable Diode Laser Spectroscopy . . . . .	5
1.4	Gas Sensing in Aero Engine Diagnostics . . . . .	8
1.5	Thesis Objectives . . . . .	11
1.6	Thesis Overview . . . . .	11
<b>2</b>	<b>Review of Tunable Diode Laser Spectroscopy</b>	<b>13</b>
2.1	Introduction . . . . .	13
2.2	TDLS with Direct Detection . . . . .	14
2.2.1	Balanced Ratiometric Detection . . . . .	19
2.3	TDLS with Modulation Spectroscopy . . . . .	19
2.3.1	Overview of Modulation Spectroscopy . . . . .	19
2.3.2	Wavelength Modulation Spectroscopy . . . . .	22
2.3.3	Mathematical Descriptions of WMS . . . . .	27
2.3.4	Taylor Series Approach to Absolute Line shape Recovery . . . . .	29
2.4	RAM-based Calibration-free TDLS Techniques . . . . .	30
2.4.1	RAM Method . . . . .	30
2.4.2	Phasor Decomposition Method . . . . .	32
2.4.3	Operation at High Modulation Indices . . . . .	34
2.4.4	RAM-nulling . . . . .	35
2.5	TDLS in Aero Engine Diagnostics . . . . .	37
2.5.1	Monitoring Combustion Products . . . . .	37

2.5.2	Mass Flux Measurements . . . . .	39
2.5.3	TDLs in Misty Environments . . . . .	41
2.6	Summary & Objectives . . . . .	42
<b>3</b>	<b>Analytical Methods in Tunable Diode Laser Spectroscopy</b>	<b>44</b>
3.1	Introduction to Molecular Spectroscopy . . . . .	44
3.1.1	Spectral Absorption Lines . . . . .	44
3.1.2	Vibrational and Rotational Energy Levels . . . . .	45
3.2	Absorption Spectra Characteristics . . . . .	49
3.2.1	Spectral Broadening . . . . .	49
3.2.2	Spectral Line Intensity . . . . .	50
3.3	Modelling Spectral Line Shapes . . . . .	51
3.3.1	The Lorentzian Profile . . . . .	52
3.3.2	The Gaussian Profile . . . . .	53
3.3.3	The Voigt Profile . . . . .	53
3.3.4	HITRAN . . . . .	54
3.4	Extracting Gas Parameters . . . . .	56
3.4.1	Concentration and Pressure . . . . .	57
3.4.2	Temperature . . . . .	60
3.5	Summary . . . . .	62
<b>4</b>	<b>Experimental Methodology</b>	<b>63</b>
4.1	Introduction to Experimental Techniques . . . . .	63
4.2	In-Line Gas Cell . . . . .	64
4.3	Free-Space Layout . . . . .	66
4.3.1	Environmental Chamber . . . . .	68
4.4	Data Acquisition . . . . .	69
4.5	Wavelength Referencing . . . . .	70
4.6	Baseline Methods . . . . .	76
4.7	Characterisation Techniques . . . . .	78
4.7.1	AM/WM Phase Shift . . . . .	78
4.7.2	Tuning Coefficient . . . . .	82

4.8	TDLS in Harsh Environments . . . . .	85
<b>5</b>	<b>Absolute Line Shape Recovery at High Modulation Indices</b>	<b>86</b>
5.1	Introduction . . . . .	86
5.2	Mathematical Description of Correction Function . . . . .	88
5.2.1	Nonlinear Absorption Measurements . . . . .	94
5.2.2	Practical Considerations Related to High Modulation Index Operation . . . . .	95
5.3	Modulation Index Determination . . . . .	97
5.3.1	Ratio Method . . . . .	98
5.3.2	Fit Method . . . . .	100
5.4	Experimental Validation of Correction Function . . . . .	101
5.4.1	Experimental Procedure and Settings . . . . .	101
5.4.2	Modulation Index Determination . . . . .	106
5.4.3	Absolute Line Shape Recovery . . . . .	108
5.5	Summary . . . . .	112
<b>6</b>	<b>Autobalanced Photoreceivers for Direct Detection and Electronic RAM-nulling</b>	<b>114</b>
6.1	Introduction to Autobalanced Photoreceivers . . . . .	114
6.2	Derivation of Normalisation Technique for Autobalanced Detectors	117
6.3	Experimental Validation of Normalisation Technique . . . . .	119
6.4	Autobalanced Photoreceivers for Electronic RAM-nulling . . . . .	121
6.5	Electronic Background Nulling for RAM-based Signals . . . . .	126
6.5.1	Principles of Electronic RAM Nulling . . . . .	126
6.5.2	Preliminary Investigations into External Pure Amplitude Modulation with RAM-Nulling . . . . .	131
6.6	Summary . . . . .	133
<b>7</b>	<b>Aero Engine Intake Temperature Sensor Development</b>	<b>136</b>
7.1	Introduction . . . . .	136
7.2	Selection of Absorption Lines for Ratio Thermometry . . . . .	137

7.3	Temperature Determination with Direct Detection . . . . .	142
7.4	Temperature Determination with 2f WMS . . . . .	148
7.5	Summary . . . . .	155
<b>8</b>	<b>Aero Engine Ground Testing</b>	<b>157</b>
8.1	Ansty Tests . . . . .	157
8.1.1	Experimental Setup . . . . .	157
8.1.2	Direct Detection . . . . .	159
8.1.3	Wavelength Modulation Spectroscopy . . . . .	160
8.2	East Rogerton Tests . . . . .	162
8.2.1	Experimental Setup . . . . .	162
8.2.2	Signal Recovery . . . . .	166
8.2.3	Beam Steering in Turbulent Exhaust Gases . . . . .	169
8.3	Bristol Tests . . . . .	170
8.3.1	Experimental Setup . . . . .	171
8.3.2	Experimental Data . . . . .	173
8.4	Summary . . . . .	179
<b>9</b>	<b>Conclusions and Further Work</b>	<b>182</b>
9.1	Discussion and Conclusions . . . . .	182
9.1.1	Introduction: Aims & Objectives . . . . .	182
9.1.2	Extending RAM-based Line Shape Recovery Techniques to High Modulation Indices . . . . .	183
9.1.3	Autobalanced Photoreceivers for Noise Cancellation and RAM-nulling . . . . .	184
9.1.4	Sensor Design for Ambient Aero Engine Intake Water Vapour Temperature . . . . .	185
9.1.5	Aero Engine Exhaust Plume Measurement Systems . . . . .	187
9.1.6	Summary . . . . .	188
9.2	Further Work . . . . .	190
9.2.1	High Sensitivity Absolute Line Shape Recovery . . . . .	190
9.2.2	RAM-Nulling and Pure Amplitude Modulation . . . . .	190

9.2.3	Ambient Ratio Thermometry Measurements . . . . .	191
9.2.4	Future Aero Engine Test Bed Systems . . . . .	192
	<b>References</b>	<b>195</b>
	<b>Publications</b>	<b>213</b>
	<b>List of Abbreviations and Symbols</b>	<b>215</b>
A	<b>MATLAB Voigt Simulation Code</b>	<b>219</b>
B	<b>MATLAB Wavelength Reference Code</b>	<b>224</b>
C	<b>MATLAB Phasor Decomposition Method and Correction Function Code</b>	<b>227</b>

# List of Figures

1.1	Gas sensing in aero engine diagnostics . . . . .	9
1.2	Aero Engine ground test intake misting . . . . .	10
2.1	Direct detection output simulation . . . . .	15
2.2	Generic direct detection system . . . . .	16
2.3	Simulated absorption line shape . . . . .	17
2.4	Generic modulation spectroscopy system . . . . .	20
2.5	WMS signal simulation . . . . .	23
2.6	Gas line interaction with modulation . . . . .	23
2.7	Harmonic line shapes . . . . .	25
2.8	1f lock-in amplifier output . . . . .	26
2.9	RAM method phasor diagram . . . . .	31
2.10	PD method phasor diagram . . . . .	33
2.11	Generic optical RAM-nulling system . . . . .	36
2.12	Mass flux measurement system . . . . .	41
3.1	Two-level energy system . . . . .	45
3.2	Generic absorption line from two-level system . . . . .	45
3.3	Potential energy levels in anharmonic oscillator . . . . .	46
3.4	H <sub>2</sub> O Symmetric stretch, $\nu_1$ . . . . .	48
3.5	H <sub>2</sub> O Bending mode, $\nu_2$ . . . . .	48
3.6	H <sub>2</sub> O Asymmetric stretch, $\nu_3$ . . . . .	48
3.7	CH <sub>4</sub> Symmetric stretch, $\nu_1$ . . . . .	48
3.8	CH <sub>4</sub> Symmetric bend, $\nu_2$ . . . . .	48
3.9	CH <sub>4</sub> Asymmetric stretch, $\nu_3$ . . . . .	48

3.10	CH <sub>4</sub> Asymmetric bend, $\nu_4$	48
4.1	TDLS system schematic	64
4.2	In-line gas cell	65
4.3	Detection optics: normal beam	67
4.4	Detection optics: focused beam	67
4.5	Detection optics: diffuse beam	67
4.6	Detection optics: expanded beam	67
4.7	Breadboard-mounted free space optical layout	68
4.8	Fibre ring resonator diagram	71
4.9	Resonator output with absorption signal	72
4.10	FSR determination using known absorption wavelengths	73
4.11	Effect of FSR error	74
4.12	Example baseline fit	77
4.13	Change in AM/WM phase angle with modulation frequency	79
4.14	$\psi$ determination using resonator output	80
4.15	$\psi$ determination comparing FM and AM signals	81
4.16	$\psi$ determination phasor diagram	82
4.17	Calculating tuning coefficient using resonator output	83
4.18	Change in tuning coefficient with modulation frequency	84
5.1	Change in RAM magnitude with modulation index	87
5.2	Distortion of Lorentzian line shape with modulation index	92
5.3	Distorted and undistorted line shapes with correction function	93
5.4	Simulation of ratio method for $m$ determination	98
5.5	Experimental PD method outputs	104
5.6	Line shapes with error in $\psi'$	105
5.7	Line shapes with correct $\psi'$	105
5.8	Line shape of 1% CH <sub>4</sub> at m=1 with reference	109
5.9	Line shape of 10% CH <sub>4</sub> at m=2 with reference	109
5.10	Line shape of 1% CH <sub>4</sub> at m=2 with theory	110
5.11	Line shape of 10% CH <sub>4</sub> at m=2 with theory	110

6.1	Original Hobbs autobalanced photoreceiver . . . . .	115
6.2	10% CH <sub>4</sub> from Hobbs circuit with theory . . . . .	120
6.3	0.1% CH <sub>4</sub> from Hobbs circuit with theory . . . . .	120
6.4	2f H <sub>2</sub> O absorption with increasing $m$ (transimpedance) . . . . .	123
6.5	2f H <sub>2</sub> O absorption with increasing $m$ (autobalanced) . . . . .	123
6.6	Electrical spectrum analysis of background signals . . . . .	124
6.7	RAM-nulled 10% CH <sub>4</sub> output with theory . . . . .	130
6.8	External modulation system schematic . . . . .	131
6.9	RAM-nulling with AM modulation . . . . .	132
6.10	RAM-nulled 10% CH <sub>4</sub> output with equivalent direct signal . . . . .	132
7.1	H <sub>2</sub> O lines between 1-2 $\mu$ m from HITRAN . . . . .	138
7.2	Schematic of environmental chamber measurement system . . . . .	143
7.3	1430 nm H <sub>2</sub> O spectra at different temperatures . . . . .	144
7.4	1350 nm H <sub>2</sub> O spectra at different temperatures . . . . .	144
7.5	Change in H <sub>2</sub> O concentration with temperature and humidity . . . . .	145
7.6	Direct detection H <sub>2</sub> O absorption with theoretical fit . . . . .	147
7.7	Temperature fit results compared to actual temperatures . . . . .	148
7.8	Modified Hobbs circuit for 2f ratio thermometry . . . . .	149
7.9	Signal outputs from LabVIEW acquisition program . . . . .	150
7.10	Temperature output over 1 day chamber cycle (1430 nm) . . . . .	152
7.11	Temperature output over 1 week chamber cycle (1350 nm) . . . . .	154
7.12	Recorded ratios with temperature over 1 week chamber cycle . . . . .	154
8.1	Ansty test cell photo . . . . .	158
8.2	Direct detection signals at different engine speeds . . . . .	159
8.3	1f RAM signals at different engine speeds . . . . .	161
8.4	2f WMS signals at different engine speeds . . . . .	161
8.5	East Rogerton test cell photo . . . . .	163
8.6	East Rogerton detuner mount schematic . . . . .	164
8.7	Diagram showing exhaust plume measurement layout . . . . .	164
8.8	Simulated hot and cold H <sub>2</sub> O spectra at 1430 nm . . . . .	165

8.9	Direct detection signals with averaging (8 Hz)	167
8.10	Direct detection signals with averaging (1 kHz)	167
8.11	Direct detection signals at different engine speeds	168
8.12	Micro-corner cube retroreflective tape	170
8.13	Glass bead retroreflective tape	170
8.14	Bristol test cell photo	172
8.15	Direct detection signal with theoretical fit (62% NH)	175
8.16	Direct detection signal with theoretical fit (80% NH)	175
8.17	2f line shapes at different engine speeds	177
8.18	2f line shapes indicating position of hot lines	177
8.19	Comparison of 2f signals at different modulation frequencies	178

# Chapter 1

## Introduction

### 1.1 Gas Sensor Applications

The ability to measure gaseous properties, particularly composition, has become a vital tool in several sectors of the modern economy. There are many gases of interest and a wide range of scenarios in which quantitative determination of gas parameters can provide critical information. The global gas detection market totals £2.5bn per year and continued progress in enabling technologies, such as semiconductor technology and software, is providing new opportunities for gas sensor application [1]. Knowledge of species concentration, pressure, temperature and velocity allow users to optimise physical and chemical processes and monitor environments. Some applications require identification of the components of unknown gas mixtures which may have constituents down to trace levels. Others may look at specific gases used or produced in chemical, biological or combustion processes, for instance, to determine accurate quantitative gas parameters for control, safety or evaluation purposes.

The key applications of gas sensing can be broken down into: industrial, environmental, medical, security/ military and domestic fire/ gas detection. An important driver for innovation in gas sensing and the focus of this work is in industrial systems. Industrial applications generally require reliable, economical

and real-time gas diagnostics for safety, feedback in process control or for optimization in system design. Combustion processes in internal combustion engines [2,3], aero engines [4–6] and advanced propulsion systems [7] have been widely investigated over the last two decades. The automotive and aerospace industries are increasingly dependent on such diagnostic tools for pushing the limits of efficiency and environmentally-friendly technology. The petrochemical industry has a strong interest in hydrocarbon detection where species specific detection provides a significant challenge due the difficulty of differentiating between similar molecules. The petrochemical industry is one of many that use gas sensing technology as an industrial safety tool for both preventing and indicating hazardous situations [8,9]. There are several industrial environments where gas detection provides feedback for process control, for instance in semiconductor manufacture or in fuel cells [10,11]. This can involve regulating reactions to improve performance, reduce costs or to keep system constituents to within safe limits if hazardous species are involved.

Gas sensing has a significant role to play in environmental monitoring where measurement of atmospheric gases, particularly greenhouse gases, is increasingly important to the climate change debate [12,13]. The improvement in capability for in-situ and airborne measurements of atmospheric constituents has enabled detailed analysis of pollutants such as carbon dioxide, oxides of nitrogen, ozone and sulphur dioxide, assisting the creation and enforcement of pollution regulations [14,15]. There are other pollutants that are important on slightly smaller scales, where emissions from commercial activities need to be measured to protect the environment and local population. Common examples of this are emissions from automotive sources, manufacturing facilities and landfill sites.

In recent years there has been significant progress in applying gas sensor technology in the field of healthcare. Breath analysis is a highly desirable method of diagnosis due to its simplicity and non-invasive nature [16]. Capnography is the study of the components of exhaled breath and gives an indication of the partial pressures of gases in the blood stream. An established clinical technique is the detection of *H. pylori* in the stomach using isotopes of carbon

that can highlight the onset of stomach ulcers. A technique currently of major interest is diagnosing illness from the measurement of chemical markers associated with specific ailments such as cancers. This remains a significant challenge for clinicians and engineers as individual body chemistry can vary wildly between subjects and the target volatile organic compounds (VOC's) are difficult to isolate and identify at trace levels. Initial work in this field made use of gas chromatography but recent advances have been enabled by the availability of room temperature quantum cascade laser sources for absorption spectroscopy.

Among the other major applications, the security and defence applications provide some of the most significant challenges. Homeland security spending and research has increased massively in the past decade but the constraints on detection systems for explosives and other high-risk substances still need to be overcome. The domestic fire and gas detection market is the most widespread application of gas sensing technology. Many residential and commercial buildings in developed nations require some kind of fire detection system, which is often coupled with a carbon monoxide monitor.

## 1.2 Traditional Gas Sensing Techniques

The conventional techniques for gas sensing are dominated by gas chromatography, catalysis, electrochemistry, chemiluminescence and optical absorption. There are a variety of other available technologies that are not widely used. Some of the newer methods, such as nanoscale devices, may go on to be commercially successful in the future but the majority serve a small niche and do not merit individual mention in a broad overview of gas sensing alternatives. It is important that the techniques used to interrogate gases need to be chosen carefully to cope with potentially harsh environments and hazardous gas mixtures.

Catalytic sensors such as pellistors have been widely used to detect hydrocarbons since the 1960s. The detectors use two filament coils, one of which is able to heat a catalyst to promote oxidation of the target gas [17]. The

detector element is heated by this reaction and changes resistance in proportion to the gas concentration which can be recovered by comparison to a calibration. Electrochemistry is a standard technique for measuring oxygen and toxic gases by oxidising or reducing the target at an electrode and measuring the resultant change in current. The gas of interest can be selected using a membrane, so that it is the only active species present at a sensing electrode, designed to pass current linearly proportional to gas concentration.

Gas chromatography can be used to identify the components of a gas mixture [18]. The mixture, normally diluted by a carrier gas, flows through a column packed with an adsorbing medium. Different components of the mixture experience various degrees of adsorption and thus pass through the column at varying speeds, emerging at a detector at different times. Components can be identified by their characteristic transit time in a given column, or by sensors after the column, e.g. a mass spectrometer or an optical absorption spectrometer. Whilst gas chromatographs are capable of making measurements down to the parts-per-billion level, they have several limitations. In most cases gas samples are collected and processed afterwards using a method that is slow and is not real-time. The equipment required is usually somewhat large and expensive, especially if a mass spectrometer is included, making it a poor choice for field applications. The nature of the gas discrimination process does not lend itself well to dealing with harsh environments as the gas mixture, temperature and pressure are all subject to limitations.

A number of techniques based on optical absorption are commonly used to measure gas species and parameters. Optical absorption sensors work by quantifying how much light is absorbed over a given path at characteristic wavelengths of the absorbing species. There are a number of molecules that exhibit favourable absorption between the ultra-violet (UV) and mid-infrared (IR). The mid-IR wavelengths typically correspond to strong fundamental molecular rotational and vibrational transitions. The weaker overtones of these transitions can be interrogated in the near-IR and at UV wavelengths several molecules exhibit absorption due to electronic transitions in the molecule.

Spectrophotometry is capable of wide-band multicomponent sensing by using a dispersed broadband source in conjunction with a Fourier transform infrared (FTIR) or a grating spectrometer [19]. Alternatively, non-dispersive infrared (NDIR) techniques use a broadband source with optical filters to probe absorbing and non-absorbing spectral regions to quantify the relative absorption [8]. Although the components are generally low-cost, there is a requirement that the target gas is spectrally isolated, over a wide range, from any other species that may be present in the sample.

Whilst many applications will continue to be well served by the methods mentioned here, their general limitations prevent them from being used to solve some of the major gas sensing challenges currently being tackled. These disadvantages can include: regular calibration requirements, high maintenance costs, slow response, low sensitivity, low gas specificity, low portability and incompatibility with harsh, high temperature environments. Tunable diode laser spectroscopy (TDLS) and related techniques can provide a highly sensitive and accurate method for fast recovery of absorption spectra and hence gas parameters, yet can remain compact or be operated remotely. Relying only on the interaction of the laser beam with the target gas, TDLS is compatible with high temperature, hazardous and corrosive environments. There are a growing number of high-value gas sensing applications that have adopted TDLS, making use of the high resolution and accuracy, and the increasing availability of standard components. This work has focussed on several aspects of TDLS and its application to aero engine diagnostics.

## **1.3 Principles of Tunable Diode Laser Spectroscopy**

Tunable diode laser spectroscopy uses a technique that sweeps the centre wavelength of narrow emission line width diode lasers across the absorption feature of a target gas, recovering spectra with high resolution and accuracy. Early implementation of the technique used IV-VI lead-salt diode lasers in the

mid-IR [20–22]. Since then several types of diode laser have been used for TDLS, including distributed Bragg reflector (DBR), distributed feedback (DFB) and vertical cavity surface emitting lasers (VCSELs) in the near-IR and more recently quantum cascade lasers (QCLs) in the mid-IR [23,24]. Despite the strength of the fundamental rotational-vibrational absorption features in the mid-IR, TDLS has been most widely used to interrogate the overtone transitions in the near-IR where low-cost room temperature diode lasers can be used with uncooled detectors whilst benefitting from the low cost and robust optoelectronic hardware originally developed for the telecommunications industry. This body of work has focused on the use of InGaAsP DFB lasers in the near-IR.

In its simplest form TDLS is performed using a method known as direct detection, where the laser is thermally tuned so that the centre wavelength coincides with a target absorption feature [14,24]. A low-frequency sawtooth or triangle waveform is then applied to the drive current of the laser which induces a corresponding shift in the laser centre frequency and output power. Typically the laser line width is of the order of 1 MHz which is small in comparison to absorption line widths which could be 3 GHz or more, enabling absorption spectra to be recovered with high resolution. The spectrum of interest is recovered by simply normalising the detected signal to a non-absorbing reference which will provide an absolute absorption line shape, without any requirement for calibration, with an output signal given by the Beer-Lambert law for optical transmission. The Beer-Lambert law states the measured absorption in terms of the local values for gas concentration, absorbing path length and absorption cross-section. This cross-section is a function of gas temperature and pressure as well as characteristic absorption parameters, for example line strength, which have been extensively catalogued in spectral databases such as HITRAN for many common molecules. [25,26]. Quantitative gas parameters can be extracted by fitting theoretical line shape profiles, based on known gas parameters and spectral data, to the recovered experimental signals.

A widely used extension of this method sees the addition of a high frequency sinusoidal dither signal to the low frequency current ramp. In the same way that

the ramp induced a change in the laser operating frequency and output power, the dither creates both a frequency modulation and an intensity modulation at the drive frequency [14,23,24,27–29]. This process, known as wavelength modulation spectroscopy (WMS), enables phase sensitive detection to be performed with a lock-in amplifier (LIA) which can greatly increase sensitivity and signal-to-noise ratio (SNR) by limiting the detection bandwidth and reducing  $1/f$  noise. The absorption signals are generally recovered at  $f$ , the fundamental of the modulation frequency, or at  $2f$ , the second harmonic. For certain regimes of modulation, the LIA output signals at each harmonic, which represent the amplitude envelope of the signals, approximate to the equivalent derivative of the absolute absorption line shape, i.e. detection at the  $n^{\text{th}}$  harmonic will yield the  $n^{\text{th}}$  derivative.

The most common implementations of TDLS with WMS use  $2f$  detection where the line centre peak height of the recovered line shape is proportional to concentration and the pressure can be determined from the separation of the zero crossings. These line shapes generally sit on a small background signal, as opposed to line shapes recovered at  $1f$ , which have a large DC background arising from the intensity modulation signal. The recovered  $2f$  peak height is not only a function of concentration, but also of pressure and instrumental factors such as gain and laser line width. This means that in general calibration is needed so that the measured signals can be compared to a known signal, assuming constant experimental conditions. The harmonic signals exhibit a maximum at a particular value of current modulation amplitude which is also the point where sensitivity is maximised. The optimum modulation depth is a function of absorption line width and hence pressure, which in harsh environments cannot always be assumed to be constant. For gas information recovery in harsh environments the ideal setup is a system that can utilise the high frequency benefits of lock-in detection, whilst allowing maximum signal amplitude through suitable modulation amplitude selection and being free from calibration requirements.

Recent efforts towards this ideal situation have adopted two approaches. The first uses the  $1f$  signals to normalise the recovered  $2f$  signals, in conjunction with a full characterisation of the laser operating settings and a theoretical fit

to known gas parameters [30, 31]. This avoids the need for calibration and can be used at the optimum modulation amplitudes but it utilises complex analytical techniques, requires elaborate characterisation of system parameters from which the experimental settings cannot drift and requires good knowledge or assumptions about the pressure. An alternative method uses the interaction of the absorption with the inherent intensity modulation or residual amplitude modulation (RAM). The absolute absorption line shape can be recovered from the RAM signal and gas parameters can be extracted in the same way as in direct detection [32–35].

## 1.4 Gas Sensing in Aero Engine Diagnostics

Ground testing of aero engines is an important process during the development, evaluation and refurbishment phases of a given engine’s lifetime. The more information that can be recovered about an engine’s performance the easier it is to optimise the many processes that occur. The characteristics of the gases present in the various parts of an engine are fundamental to its operation. In Fig. 1.1 a schematic of a typical aero engine is shown which highlights some key areas where gas data is of interest. The analysis of the exhaust plume is of particular importance as this gives direct information about the combustion processes without the need for engine-mounted sensors capable of operating at extreme temperatures and pressures. Aero engine design emphasis is shifting heavily towards more fuel economy and cleaner burning engines. Legislation requires measurement of carbon monoxide, oxides of nitrogen, unburnt hydrocarbons and smoke for certification. The measurements used for engine certification are currently performed using gas sampling which is difficult and expensive. [36–41].

The amount of unburnt hydrocarbons and carbon monoxide provide a quantitative measure of the combustion efficiency, which is close to 100%. Carbon dioxide and water are always the main combustion products yet minor pollutants including carbon monoxide and the oxides of nitrogen need to be measured and if possible minimized, whilst the water vapour contained in the exhaust plume

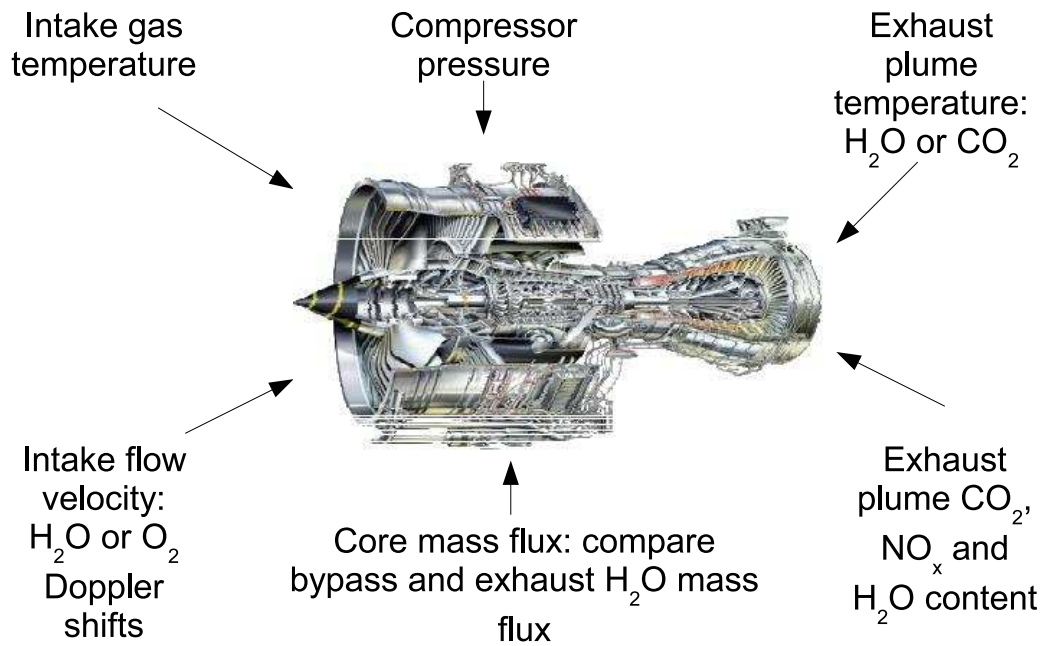


Figure 1.1: Potential areas for gas sensing in generic aero engine diagnostics [42]

can also provide information, such as exhaust temperature. It is possible to use measurements of these to build up a 2D tomographic map of the temperature or pollutant distribution of the plume, given suitable flexibility in measurement geometry.

The ambient temperature of the intake gases is always recorded and compared to a standard temperature. Normally thermocouples are used for this purpose but under misting conditions, as shown in Fig. 1.2, water condenses on the thermocouples, which then do not give a true measure of air temperature. When atmospheric water condenses, it gives up its latent heat to the air, increasing the temperature and reducing the density of air entering the engine. In Fig. 1.2, condensation is taking place in the lower half of the engine intake, making it very difficult to make true measurements of engine performance and efficiency. There are many occasions when test beds are unable to run because of high atmospheric humidity at significant cost to the test bed operator, when test bed occupancy for large engines costs  $>£10\text{K}$  per day. Other factors such as atmospheric pollen may initiate condensation even when humidity levels are within the normal running limits. A method of ambient temperature

determination that could maintain accuracy under conditions of high humidity and misting could increase test bed throughput with major savings for engine manufacturers.

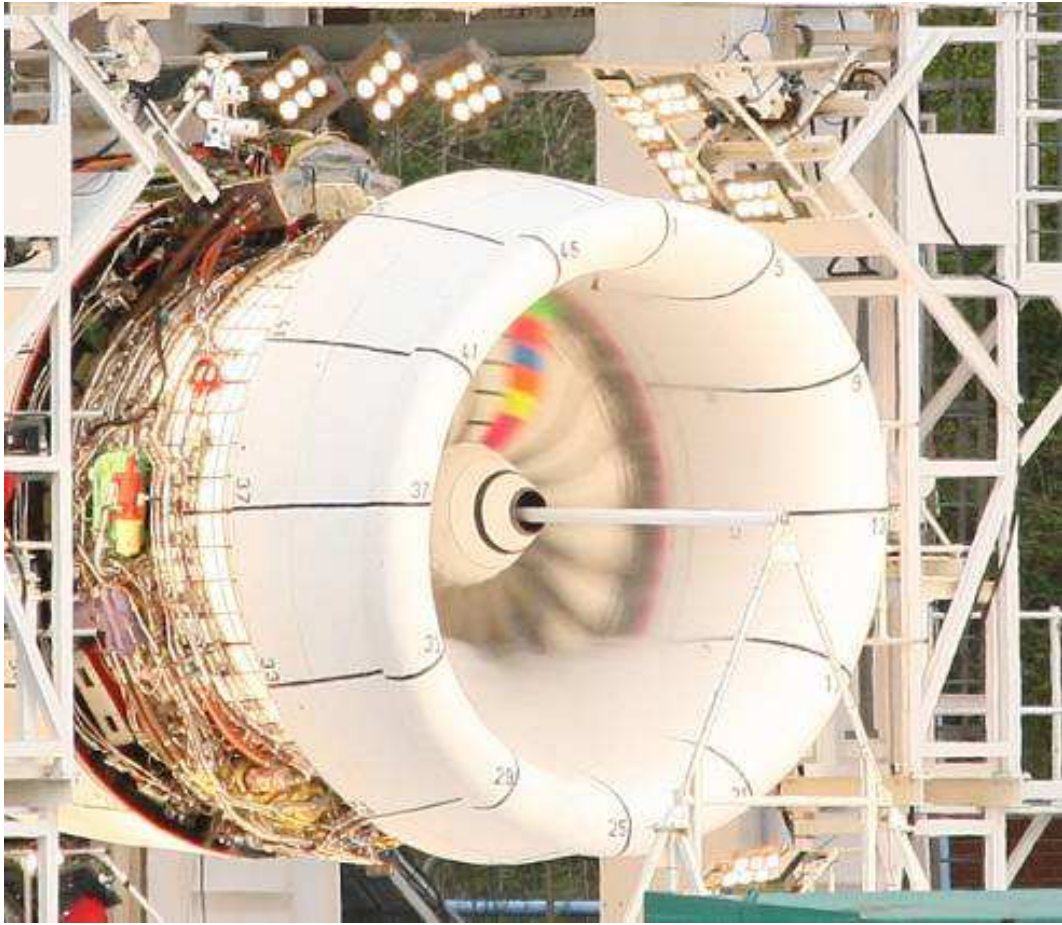


Figure 1.2: Aero engine intake misting during ground testing. [42]

Mass flux measurements of air entering an engine can be made using TDLS [5]. When TDLS measurements are made across an engine intake in two different directions relative to the engine axis, the Doppler shift of the absorption peak of a target molecule, such as water vapour or oxygen is a measure of axial velocity. Absorbance is a measure of the concentration of the target gas, i.e. the static pressure in the intake, which when multiplied by the velocity gives the total mass per unit time. A measure of total thrust could in principle be achieved by measuring mass flux at the intake and then at the exhaust. Similarly a measure of the mass flux through the core could be made by simultaneously measuring the mass flux through the intake and the bypass, the difference of which would

give the mass flux through the core. An alternative approach to this, could be to measure the ambient water vapour in the intake and compare with the exhaust water vapour content. This would provide an indirect measure of core mass flux as the additional hydrogen has come from combusted fuel, the rate of which is measured.

## **1.5 Thesis Objectives**

The aims of the project at the broadest level were twofold: to further the state of the art techniques in TDLS-based gas parameter determination in harsh environments and to apply TDLS techniques to solving specific problems in aero engine diagnostics. The specific objectives for the first aim were: to extend calibration-free RAM-based absolute line shape recovery methods to modulation regimes where the signal amplitude is optimised, to demonstrate an electrical analogue of the RAM-nulling techniques used previously and to experimentally evaluate recovery methods based on dual detector photoreceivers. The objectives for the second aim were: to implement a temperature sensor based on TDLS ratio thermometry for measuring intake gas under misting conditions and to test experimental setups and optical hardware for use in the harsh environments experienced in aero engine test beds, for future TDLS-based sensing applications.

## **1.6 Thesis Overview**

This introduction has served to give an overview of the subject of the thesis in the context of general gas sensing methods. Although a diverse field in terms of applications and methods it is easy to see how the characteristics of certain techniques lend themselves to solving some gas sensing problems but not others. A brief introduction has been given to tunable diode laser spectroscopy, which is the focus of this thesis, and the limitations of conventional TDLS techniques are identified. The application of gas sensing in aero engine ground testing is introduced with an emphasis on those areas that could benefit from TDLS

technology.

Chapter 2 provides a review of TDLS techniques, examining the evolution of theoretical and experimental techniques by the main protagonists in the field. This also pays particular interest to the application of TDLS to aero engine ground testing and related applications. Chapter 3 covers the analytical methodologies involved in molecular spectroscopy whilst Chapter 4 describes in detail the experimental systems employed in the various laboratory experiments and discusses a number of important experimental techniques used throughout the project. Chapter 5 describes and validates the use of the phasor decomposition (PD) method for recovery of absolute absorption line shapes at high modulation indices. Chapter 6 introduces the use of dual-beam dual-detector photoreceivers in TDLS. An autobalanced photoreceiver was modified to null the background RAM in  $1f$  detection of the RAM absorption. Chapter 7 investigates the feasibility of an ambient temperature sensor based on TDLS ratio thermometry from design to laboratory testing and Chapter 8 illustrates the use of TDLS sensors on aero engine test beds, over three test campaigns. Chapter 9 summarises the conclusions of the work presented and suggests some further work.

# Chapter 2

## Review of Tunable Diode Laser Spectroscopy

### 2.1 Introduction

In Chapter 1, the principles of tunable diode laser spectroscopy were introduced. This chapter is intended to provide a more detailed overview of the field by identifying and describing the important advances in theoretical and experimental practices that have been made in the extensive body of literature already generated. The developments and previous work that have been of particular significance in aero engine diagnostics will also be examined.

Since the first use of tunable diode lasers for absorption spectroscopy by Hinkley [20], the field has enjoyed constant progress and steadily increasing application. The driving force for progress has generally been the continuous improvement in enabling technologies which is still fuelling the advancement of TDLS today. In particular, the rapid maturity of the electro-optical hardware designed for use in the telecommunications industry brought the cost and practicality of TLDS systems within the reach of many market sectors. The capabilities of each system depend on the strength of the target molecule's absorption spectrum at a particular wavelength and the quality and availability

of laser sources and detection electronics. Early research into measuring the stronger absorption features in the mid-IR was largely replaced by near-IR measurement of molecular overtones, when the low-cost telecommunications lasers, fibre components and detectors could clearly provide more sensitive, flexible and rugged detection systems. The lasers and detectors could be operated effectively with Peltier cooling and no longer required cryogenic systems. The miniaturisation of components and the potential for remote deployment with fibre networks and components made industrial deployment practical and feasible. These advances in technology were soon followed by advances in the theoretical and mathematical descriptions of the techniques employed. The capability of the hardware and software used for data acquisition and signal processing has continued to grow, allowing increasingly complex detection methods to be implemented efficiently.

## 2.2 TDLS with Direct Detection

Direct detection is regarded as the simplest form of TDLS due to the straightforward modulation, detection and signal processing that is required to obtain gas information. The simplicity comes at the expense of the sensitivity that can be achieved in gas parameter measurements. Direct detection recovers the change in transmitted intensity of a laser beam as it is tuned in frequency over an absorption feature of interest. The laser tuning is most frequently created by varying the drive current of a laser diode, such as a DFB. Thermal tuning of the diode can be used to increase the tuning range for slightly greater spectral coverage or, in the case of external cavity diode lasers (ECDLs), some intracavity element can give tuning over a wide range [43]. A sawtooth ramp or triangle wave function, applied to the laser drive current, will produce a corresponding change in the laser centre frequency and output power which is close to but not truly linear. The ramp waveform frequencies used for the tuning range from a few hertz [23, 32, 33] to a few kilohertz [7, 40].

At higher ramp frequencies the tuning efficiency begins to drop off so

that for a given change in drive current, a smaller change in frequency will be achieved. Fig. 2.1 shows the ramp current signal applied to the laser driver and the corresponding transmitted intensity recovered by a photodiode in the presence of gas absorption and in the absence of gas.

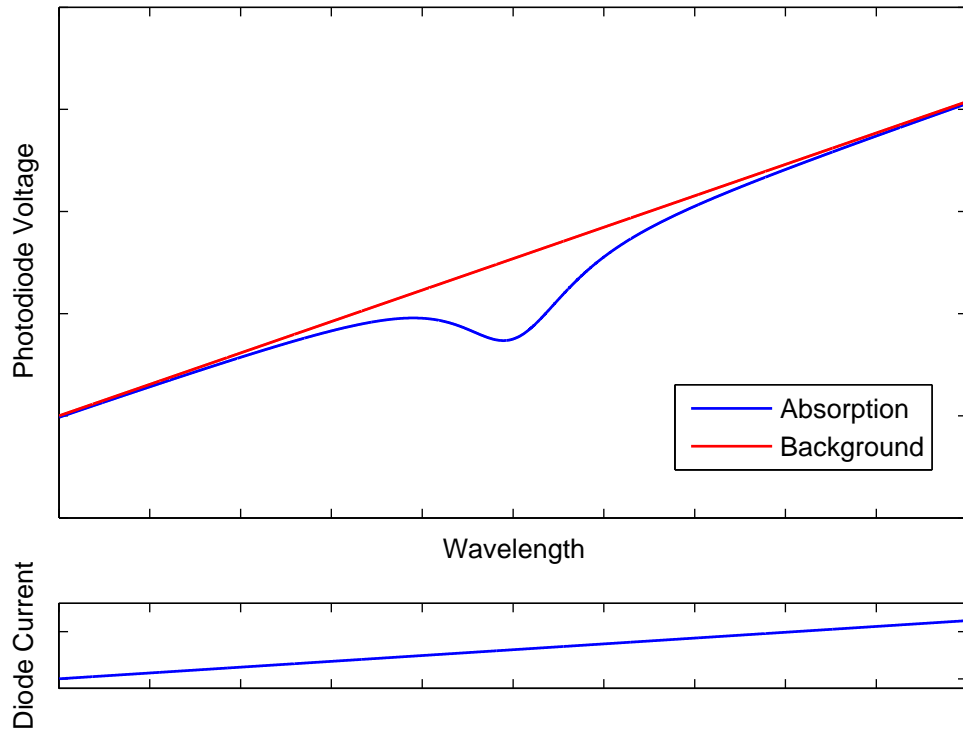


Figure 2.1: Simulated photodiode output for a direct detection scheme with gas absorption (blue) and with no absorption or baseline fit (red), shown with the corresponding laser diode drive current

Fig. 2.2 shows a schematic of a typical direct detection system. The DFB laser source is controlled by appropriate drive electronics and the fibre-coupled laser output is split between an open gas absorption path and a fibre resonator path, the outputs of which are both recorded by suitable photodiodes connected to data acquisition hardware. The gas path yields the target absorption signal whilst the fibre resonator output can be used to create a wavelength reference scale on the time base of the absorption signals, which will be discussed further in Chapter 4.

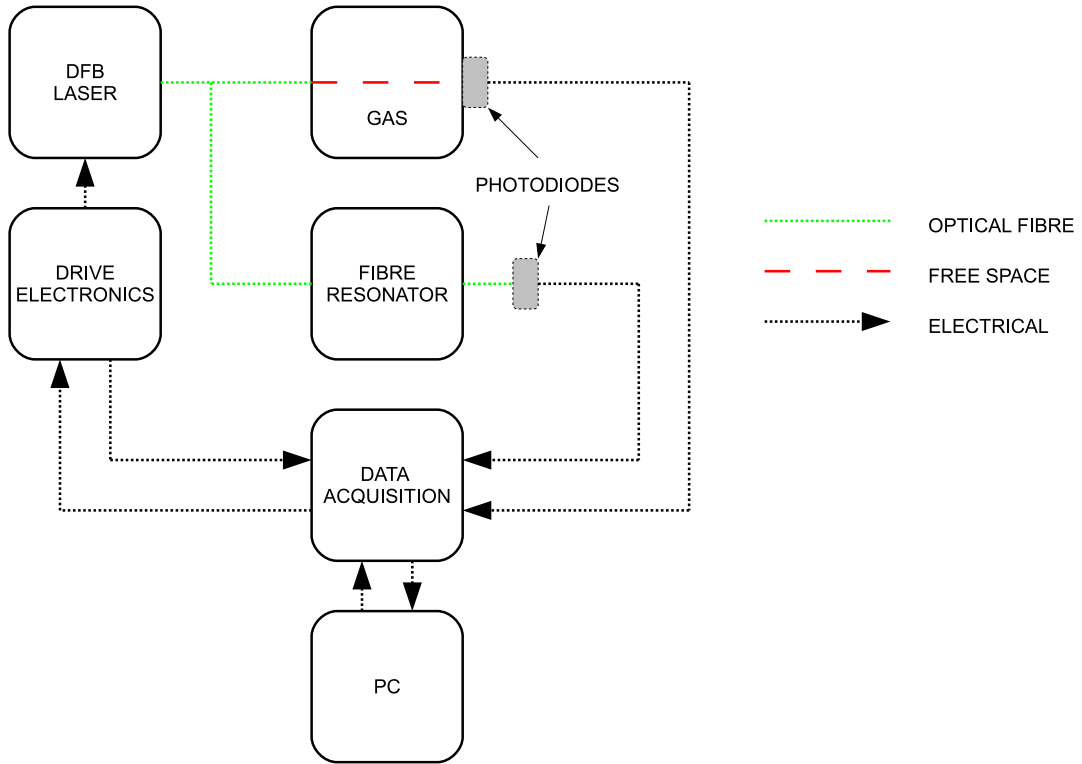


Figure 2.2: A schematic of a generic direct detection system

In basic direct detection the gas absorption signal alone is not sufficient to infer any gas parameter information. It is also necessary to have some measure or assumption of the transmission signal in the absence of absorption, which along with a zero-point reference provides the information necessary for normalisation. The non-absorbing reference is simply divided by the absorption signal to yield the absolute transmission function. In laboratory systems this is often achieved by flushing the gas path with a non-absorbing gas such as nitrogen and then taking a further measurement. This method has the advantage of providing a reliable non-absorbing reference whilst accounting for optical noise caused by etalons in the bulk and fibre optics. In practical systems this method is not always possible and a non-absorbing baseline needs to be assumed in order to perform the normalisation necessary to recover the absolute transmission function. Prudent selection of spectral regions can provide an isolated absorption feature that has enough non-absorbing regions throughout the frequency scan to perform a baseline fit to extrapolate across the regions of absorption [44].

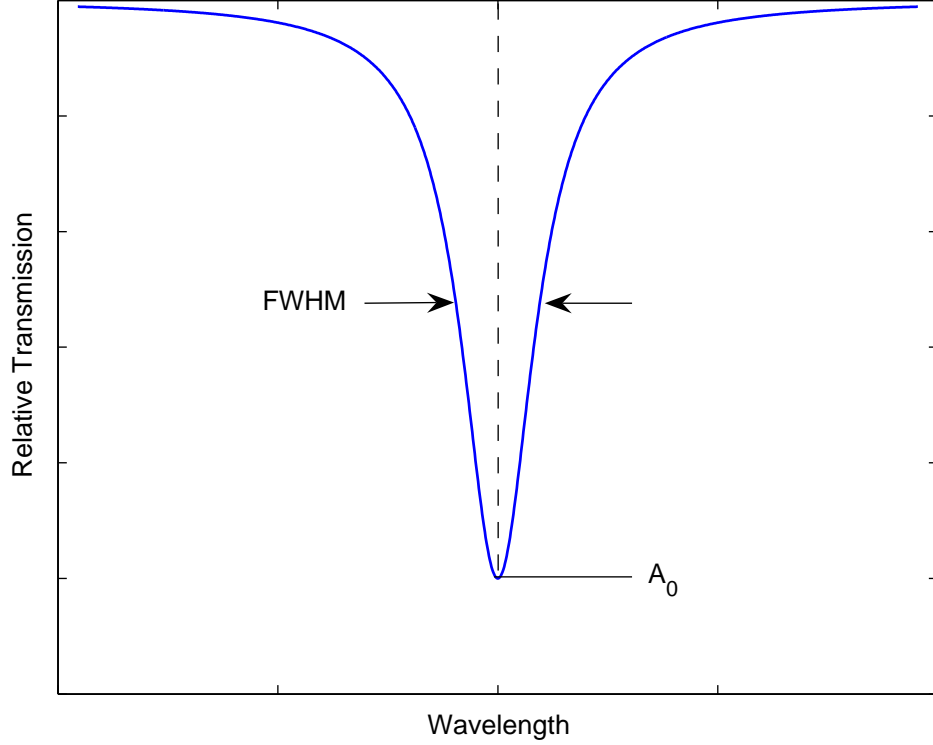


Figure 2.3: A normalised absorption profile modelled by a Lorentzian line shape. The measured full-width half-maxima (FWHM),  $2\gamma$  and the integrated absorbance,  $A$ , can be used to extract values for gas pressure and concentration.

In order to calculate gas parameters the absolute transmission function is recovered, given mathematically by the Beer-Lambert law for optical transmission through an absorbing medium:

$$I_{out} = I_{in}e^{-\alpha(\nu)Cl} \quad (2.1)$$

where  $I_{in}$  is the incident laser intensity,  $\alpha(\nu)$  is the absorption cross section with laser frequency  $\nu$ ,  $C$  is the species mole fraction and  $l$  is the absorption path length. The absorption cross section depends upon path-averaged local values for pressure and temperature but also on characteristic absorption parameters which have been extensively catalogued in spectral databases such as HITRAN, HITEMP and GEISA for many common molecules [25, 26, 45, 46]. Theoretical

simulations of the transmission function require an assumption of a line shape function, often chosen to be Lorentzian, Gaussian or Voigt depending on the experimental conditions. The absorbance part of the exponent in (2.1) is shown in Fig. 2.3 and given by:

$$A = \alpha(\nu)Cl = PCIS(T)\Phi(\nu - \nu_0) \quad (2.2)$$

where  $S(T)$  is the temperature dependent line strength and  $\Phi(\nu - \nu_0)$  is the line shape profile,  $\nu_0$  is the line centre frequency and  $P$  is the pressure. To extract gas information, the integrated absorbance and half-width half-maxima can be measured directly or simulation spectra based on known spectral data can be fitted to the experimental signals with gas parameters such as concentration, pressure and temperature as variables. The various methods for extracting gas parameters from recovered spectra and theoretical fits will be discussed in more detail in Chapter 3.

In general, the performance of direct detection is limited by the poor signal-to-noise ratio achievable with relatively small signals on large backgrounds. There will be many applications where path lengths or species concentrations are high enough to allow large absorbances, where poor SNR is not a major issue. In these cases direct detection is highly desirable as recovering absolute absorption profiles directly greatly simplifies the gas information recovery process. The overall system complexity and, as a result, cost are reduced as the high speed detection electronics required for wavelength modulation spectroscopy are not required. The simple normalisation procedure and ability to recover absolute transmission functions without any calibration are the main advantages of direct detection. A significant proportion of TDLS applications to date have dealt with gas detection at trace concentration levels, at which point SNR does become a major concern. An extension of direct detection that is capable of highly sensitive measurements uses dual-beam autobalanced detection to cancel common-mode noise and greatly improve the SNR.

### 2.2.1 Balanced Ratiometric Detection

Highly sensitive autobalanced dual-beam dual-detector systems were first demonstrated by Hobbs [47–49] and have been developed and modified by several other groups since. This direct detection technique has already been used for aero engine diagnostic applications by Physical Sciences Inc. [4,5] and Lyle [50], where the improved sensitivity aids Doppler shift measurement of an oxygen absorption peak between counter-propagating beams in an intake air flow. Others have used variations of the autobalanced circuit for more general detection applications or with non-DFB laser sources such as VCSELs or QCLs [51,52]. Balanced ratiometric detectors designed for oxygen sensing near 760 nm ( $13150\text{ cm}^{-1}$ ) use Si photodiodes whilst applications between 1-2  $\mu\text{m}$  ( $5000\text{--}10000\text{ cm}^{-1}$ ) use InGaAs and mid-IR detection has been demonstrated using InSb diodes.

The dual beam approach is intended to cancel the common-mode laser noise that is incident on both the signal beam and a non-absorbing reference beam. Initially this was achieved by balancing the optical intensity of the two beams onto their respective photoreceivers with great precision. This method was limited by the difficulty in maintaining balance and the poor temporal coherence bandwidth of normal transimpedance amplifiers. The Hobbs-type circuit, described in detail in Chapter 6, achieves balancing by matching the photocurrents electronically rather than optically and commercially available versions of this circuit are made by New Focus [53].

## 2.3 TDLS with Modulation Spectroscopy

### 2.3.1 Overview of Modulation Spectroscopy

The limits of achievable SNR in direct detection have already been highlighted and the main approach to improving the sensitivity of TDLS has been the technique of modulation spectroscopy introduced in Chapter 1. AC detection at high frequencies, often tens or hundreds of kilohertz, reduces the effective laser  $1/f$  noise compared to direct detection signals, whilst the use of lock-in

amplifiers greatly reduces the detection bandwidth to further improve SNR. The AC modulation is most commonly created by summing the slow ramp sweep modulation with a high frequency sinusoidal component. This can be done using two function generators and a bias-tee circuit or alternatively by generating modulation signals using control software and addressing the laser driver with analogue output hardware. The relative merits of both of these methods are discussed in Chapter 4. It is technically possible to modulate the laser signal externally, with a phase modulator, to create pure frequency modulation [54] but for reasons of practicality this method is not discussed further in this work. In general, the use of modulated absorption signals significantly increases the complexity of signal recovery and analysis. A typical modulation spectroscopy layout is shown in Fig. 2.4. This shows essentially the same layout as Fig. 2.2 except in this system the photodiode signal from the gas absorption path is demodulated by a LIA that uses a reference signal created by the drive electronics used to modulate the laser diode.

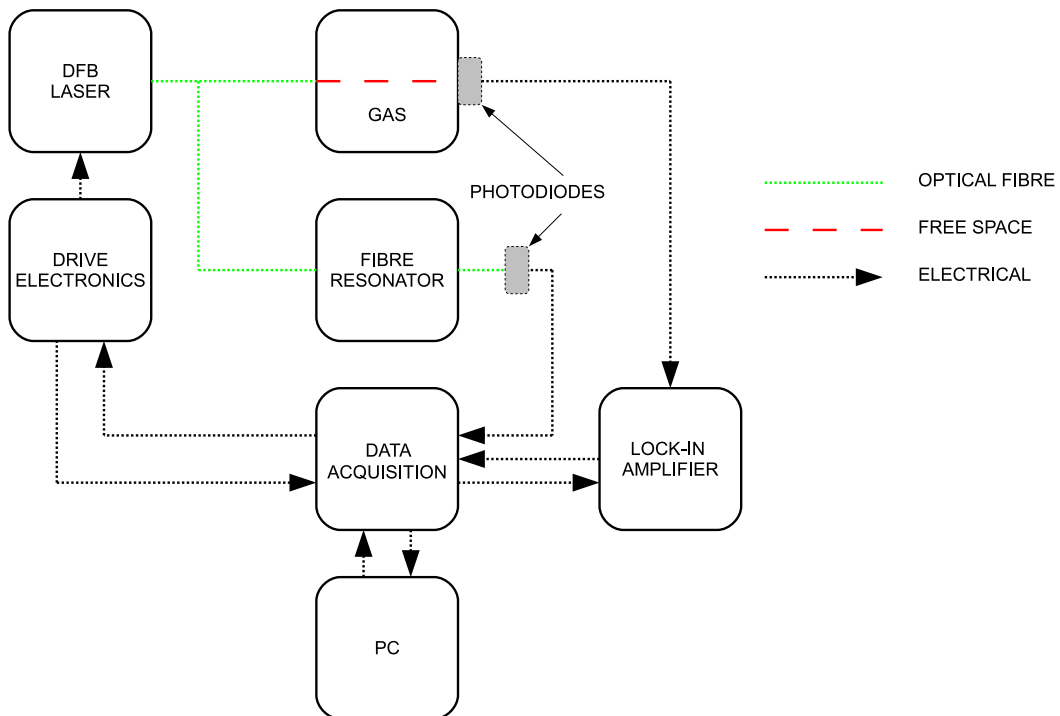


Figure 2.4: A schematic of a generic modulation spectroscopy system

The slowly varying ramp applied to the laser drive current in direct detection

was primarily used to sweep the laser output frequency yet it also exhibited a change in laser output intensity, as can be seen from the sloping background in Fig. 2.1. The application of a high frequency sinusoidal current modulation makes the laser emit with a similar synchronous frequency and intensity modulation, with some additional complications due to the high frequency operation of the laser diode. The laser output is modulated using an input current modulation,  $\delta i$ , which creates a frequency modulation,  $\delta\nu$ , along with an intensity modulation,  $\delta I$ . It is convenient to consider the modulation of laser output power as an intensity modulation (IM) although in the literature it is conventional to use the terms amplitude modulation (AM) and residual amplitude modulation (RAM) to describe the detected photocurrents that are recovered and demodulated.

Modulation spectroscopy can be split into two regimes of operation: frequency modulation spectroscopy (FMS) and wavelength modulation spectroscopy (WMS). The two techniques evolved in parallel with initial work in FMS [23, 28, 29, 55–60] being performed around the same time as WMS [23, 28, 29, 59–61]. The process used to create both is similar but the distinction between FMS and WMS relates to the sinusoidal modulation frequency,  $f_m$ , which is comparable to the half-width at half-maxima (HWHM) of the target absorption feature in the case of FMS, so that  $f_m \approx \gamma$ . In WMS the modulation frequency is much smaller than the absorption HWHM,  $f_m \ll \gamma$ . In both cases the current dither amplitude,  $\delta i$ , gives rise to a frequency change,  $\delta\nu$ . A useful parameter is the frequency modulation index,  $\beta = \delta\nu/f_m$ , which for FMS is small and for WMS is much greater than unity. Further understanding of the relation between FMS and WMS can be gained when the temporal and spectral characteristics of the two methods are compared, as in [62]. The temporal viewpoint shows the instantaneous frequency varying sinusoidally between two frequencies separated by  $\pm\delta\nu$  from the laser centre frequency at that point in the ramp cycle. The spectral viewpoint however shows a broadening of the spectrum with sidebands at the carrier frequency  $\pm n f_m$ , where  $n$ , the number of sidebands is a function of  $\beta$ . As  $f_m$  approaches  $\gamma$  and therefore the FMS regime, the distribution of sidebands tends towards a single pair of sidebands at  $\pm f_m$ , where the presence

of absorption will create a differential signal between the sidebands. In WMS, where the number of sidebands is large, a simpler consideration is the net intensity summing over all sidebands. The high speed nature of FMS requires expensive modulation and detection electronics in most cases and as a result the rest of this work considers only WMS.

### 2.3.2 Wavelength Modulation Spectroscopy

In this work the frequency of the sinusoidal modulation used for WMS is between 10 kHz and 2 MHz, satisfying the condition,  $f_m \ll \gamma$  for pressure-broadened absorption lines. Fig. 2.5a shows a simulation of the laser drive current during WMS operation with the simulated sinusoidal modulation frequency chosen here to show the modulation effects visually, although in an actual WMS system, the sinusoidal modulation frequency is typically much higher relative to the ramp sweep. The sinusoidal current dither induces, in the laser output, both an intensity modulation and a frequency modulation. The intensity modulation is in phase with the current modulation whilst the frequency modulation exhibits a phase lag,  $\psi$ , the magnitude of which is dependent upon the contributions from slow thermal and fast carrier effects in the DFB diode [63].

If the frequency modulation is considered in isolation, it is clear that in the absence of absorption any change in transmission of the instantaneous frequency of the laser output will not result in any change in the recovered signal. In the presence of gas however the rapid change in frequency due to the current dither will interact with the gas absorption signal and a change in the recovered intensity will be observed, as illustrated in Fig. 2.6. The red line represents the observed frequency dither that has a phase lag,  $\psi$ , relative to the current modulation. The purely frequency modulated laser signal will interact with the absorption line shape to produce an intensity modulation arising solely from the frequency modulation (the green line in Fig. 2.6) which can be detected by a photodiode before undergoing phase sensitive detection with a lock-in amplifier.

Phase sensitive detection of the modulated detector output using a lock-in amplifier allows narrow-band detection of signals, rejecting all noise components

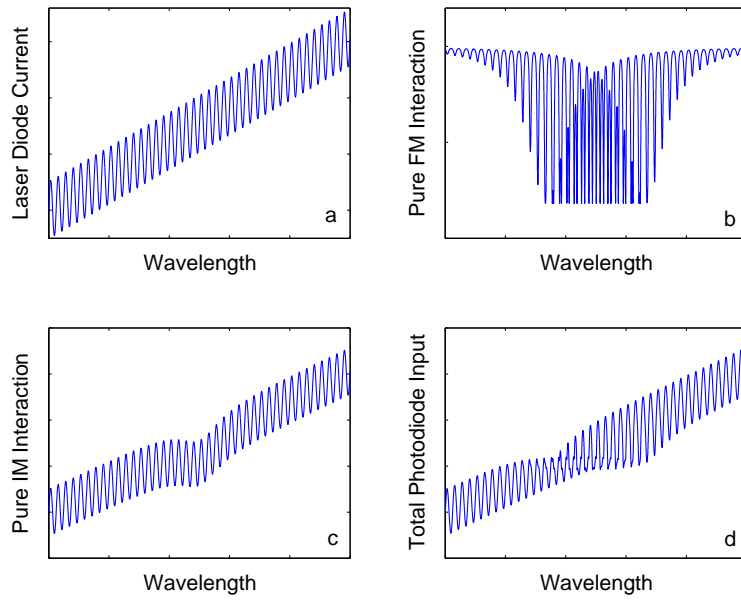


Figure 2.5: A simplified simulation of signals in modulation spectroscopy illustrating the laser diode drive current (a), the interaction of the pure FM (b), pure IM (c) and total laser modulation (d).

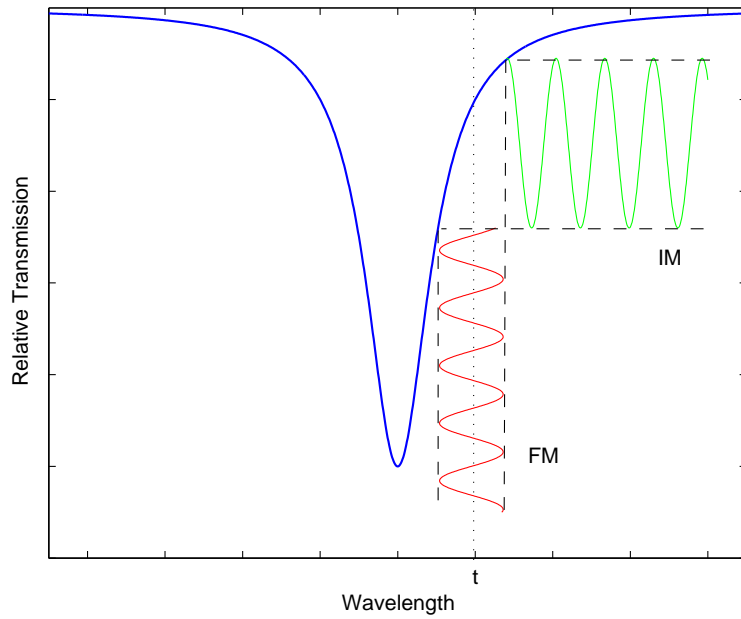


Figure 2.6: A simulated Lorentzian line shape shown with the intensity modulated signals due to the frequency modulation, that result from interaction with laser signal at an instantaneous frequency denoted by the vertical dashed line.

not coincident with the modulation frequency. For recovery of the fundamental frequency the detected signal is multiplied by a reference signal with the same frequency before being low-pass filtered. The resulting DC signal is proportional to the amplitude envelope of the target signal at that frequency. Higher harmonics of the recovered signal can be recovered by using reference signals at integer multiples of the fundamental frequency. Most LIAs will allow simultaneous detection of two orthogonal signal phases of a given harmonic of the modulation frequency. A simulation of the detected AC signal that is used by the lock-in amplifier is shown in Fig. 2.5b. If the lock-in amplifier detection phase coincides with the FM/AM signal produced by the interaction of the frequency modulation and the line shape, the DC output signal recovered is related to the gradient of the absorption line shape. For signals recovered at the fundamental frequency the DC output will be the 1<sup>st</sup> derivative of the original line shape, where the signal is zero in the non-absorbing wings and at line centre, with maxima and minima at the points either side of line centre where the gradient is steepest. The same analysis applies at higher harmonics of order  $n$  which will produce line shapes of the  $n^{\text{th}}$  derivative of the absorption line shape, as shown in Fig. 2.7.

If the intensity modulation is considered in isolation, it can be shown that the non-absorbing regions will exhibit a sinusoidal variation in intensity that is summed with the slowly varying change in intensity due to the DC current ramp. In the presence of gas absorption the background level will fall relative to the ramp background and the peak-to-peak magnitude of the sinusoidal variation will decrease in proportion to the level of absorption. A simulation of the recovered photodiode signal in the purely intensity modulated case is shown in Fig. 2.5c. Demodulation using a lock-in amplifier, with a detection phase that is coincident with the current and therefore intensity modulation, will yield the absorption line shape superimposed onto the background sawtooth ramp signal.

The signals actually recovered by the photodiode are a vector summation of the RAM and FM/AM signals described above. The combination of the signals shown in Figs. 2.5b and 2.5c are shown in Fig. 2.5d, which is a simulation of the actual photodiode signal that is demodulated by the lock-in amplifier. It is the

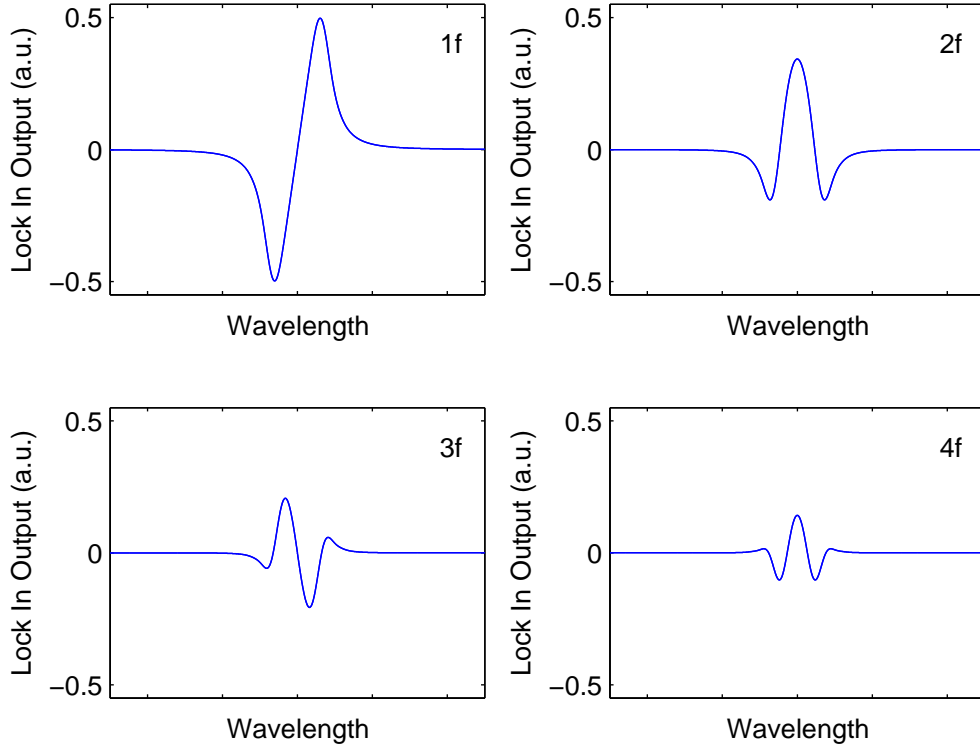


Figure 2.7: Harmonic line shapes at the first four integer multiples of the modulation frequency for purely frequency modulated signals.

amplitude envelope of this modulated output that yields the harmonic line shape in the presence of absorption. In a current modulated WMS system however, the combined effect of the intensity and frequency modulation signals needs to be considered. The relative contributions of the recovered FM/AM and RAM signals at an arbitrary detection phase is strongly dependent on the phase lag,  $\psi$ . If a time index point in the wings of the absorption line shape is considered, the effect of the frequency modulation will be minimal and the output will be dominated by the intensity modulation which is consistent with the earlier analysis of the two separate contributions.

The presence of the intensity modulation has great significance in modulation spectroscopy as it creates backgrounds and asymmetry in the recovered signals. The inability to achieve pure frequency modulation prevents the exact derivatives of the absolute line shapes being recovered due to distortions

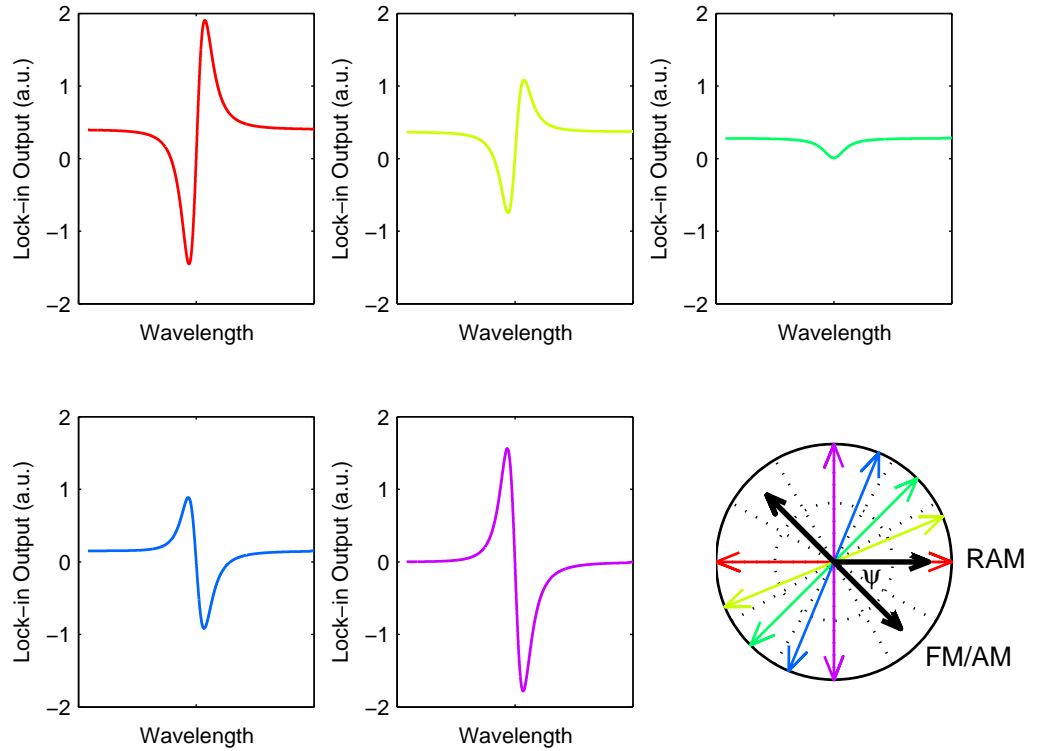


Figure 2.8: Simulated output signals from the lock-in amplifier at 1f. The 5 plots show the output as the detection phase is changed through one quadrant, illustrating the combined effect of the frequency and intensity modulation. The colour of each plot corresponds to a detection phase shown by the relevant coloured vector in the phasor diagram.

from the intensity modulation. The intensity modulation signal due to the frequency modulation is generally the signal of most interest but this is accompanied by a background intensity modulation component, widely known as the RAM. The effect of the linear RAM is important in 1f detection where it creates a non-zero background signal whilst in 2f WMS the background signal for the second harmonic is essentially zero for linear operation, making it desirable for applications requiring high sensitivity.

Fig. 2.8 shows simulated first harmonic lock-in output signals for a range of detection angles. The phasor plot shows the RAM and FM/AM signals separated by an angle of  $\psi = 45^\circ$  and the coloured vectors for detection angle correspond

to the relevant plots. If the LIA detection phase at the fundamental frequency is aligned with RAM signal, for instance, then this signal is fully recovered but the red output also includes a projection of the FM/AM signal, the magnitude of which is dependent upon the phase lag  $\psi$ . The purple output at a detection phase that is orthogonal to the RAM signal will only a projection of the FM/AM signal undistorted by the RAM. The dark green signal shows a projection of the RAM signal, undistorted by the FM/AM signal. The contribution of the background signals is also illustrated in Fig. 2.8 showing a maximum background when the axis of detection coincides with the RAM signal (red) and a zero background when the detection axis is orthogonal to the RAM (purple). An understanding of the relative phases of these signals is important for the work described later in Section 2.4 and Chapter 5.

At the small modulation depths illustrated here, the recovered harmonic signals are dominated by the derivative line shapes but this breaks down as the modulation depth is increased to optimise signal amplitude. The modulation amplitude is defined in terms of the modulation index,  $m = \delta\nu/\gamma$ , which relates the amplitude of the frequency modulation to the absorption HWHM. For low  $m$ , the  $n^{\text{th}}$  harmonic signal sees some distortion from components at the  $(n - 1)^{\text{th}}$  and  $(n + 1)^{\text{th}}$  harmonics, as a result of the linear intensity modulation. At high  $m$ , additional distortions are created by the nonlinear intensity modulation. At  $1f$  this manifests itself as a slight slope on the high background caused by the linear intensity modulation and at  $2f$  a small background signal is evident.

### 2.3.3 Mathematical Descriptions of WMS

Several authors have developed theoretical models of modulation spectroscopy to describe various experimental procedures. Early models took a simplified view and considered only the frequency modulation, neglecting the effects of the intensity modulation [59, 64, 65]. Although the effect of the intensity modulation was known for some time [56], the first attempt to model the simultaneous effects of intensity and frequency modulation was undertaken numerically for the first two harmonics of a Voigt profile by Philippe and Hanson [62]. This was soon

followed by a series of studies by Kluczynski et al. which described an analytical Fourier decomposition of the recovered signals accounting for FM/AM phase shift and both linear and nonlinear contributions to the intensity modulation [66,67]. Schilt and Thevenaz produced an alternative model which extended Arndt's Lorentzian line shape model to account for the linear intensity modulation. Li et al. [30] build upon the work of Kluczynski and Iseki [68] by developing a more practical interpretation of their Fourier analysis, using  $2f/1f$  normalisation and including specific laser parameters and arbitrary lock-in phase settings within the model. Rieker et al. [31] extended this further by accounting for a wide range of operating conditions and generalising the model for use at all optical absorption depths and not just the optically thin sample assumed in the earlier models.

The choice of WMS model is generally determined by the specific operating conditions of the target applications. It is clear that much progress has been made in creating models that can account for an ever greater range of experimental scenarios. The limitations of each model still leave gaps in the field, where there is no appropriate formulation for signal analysis and gas parameter determination. The Rieker model currently provides the most complete framework for calibration-free measurements in terms of capability in determining gas concentration and temperature with high sensitivity in a number of harsh environments yet it still requires knowledge of the local pressure and all laser conditions need to be known and unchanging for accurate operation [31]. The work which this thesis builds upon is based on an alternative model that provides a framework for analysing WMS signals to recover the absolute absorption line shape. This utilises the detection bandwidth advantages of modulation spectroscopy and phase sensitive detection yet allows the gas parameter determination to follow the same simple procedures as in TDLS with direct detection.

### 2.3.4 Taylor Series Approach to Absolute Line shape Recovery

A simpler approach to the analysis of the signals generated in WMS makes use of a Taylor series expansion of the absorption line shape, rather than the more thorough and complex Fourier approach derived by Kluczynski and Axner [32, 69, 70]. Recalling the Beer-Lambert law in (2.1) and assuming for now small absorbance so that  $\alpha(\nu)Cl \ll 1$ , the transmitted intensity becomes  $I_{out} \simeq I_{in}(1 - \alpha(\nu)Cl)$ . The incident laser intensity at instantaneous frequency,  $\nu_1$ , is:

$$I_{in} = I(\nu_1) + \Delta I(\nu_1) \cos(\omega t) \quad (2.3)$$

where  $I(\nu_1)$  is the DC laser output power,  $\Delta I(\nu_1)$  is the amplitude of the intensity modulation and  $\omega$  is the angular frequency of the sinusoidal modulation. Combining equations (2.1) and (2.3) the output intensity becomes:

$$I_{out} = [I(\nu_1) + \Delta I(\nu_1) \cos(\omega t)] (1 - \alpha(\nu_1)Cl) \quad (2.4)$$

For small modulation indices where  $m \ll 1$ , the absorption coefficient,  $\alpha(\nu)$ , can be expanded in a Taylor series to second order to recover explicit terms relating to the line shape derivatives. This formulation provides a useful way of interpreting the various signals recovered at different harmonics and their relation to the absorption profile. The expanded absorption coefficient around instantaneous laser frequency  $\nu_1$  becomes:

$$\alpha(\nu) = \alpha(\nu_1) + \alpha'(\nu_1)[\nu - \nu_1] + \frac{1}{2}\alpha''(\nu_1)[\nu - \nu_1]^2 + \dots \quad (2.5)$$

The frequency at time  $t$  can be related to the laser modulation characteristics through the expression  $[\nu - \nu_1] = \delta\nu \cos(\omega t + \psi)$ , where  $\delta\nu$  is the amplitude of the frequency modulation and  $\psi$  the phase shift between frequency and intensity modulation as before. Making the substitution, the output intensity is now:

$$\begin{aligned}
I_{out} = & [I(\nu_1) + \Delta I(\nu_1) \cos(\omega t)] \\
& \times \left\{ 1 - \alpha(\nu_1)Cl - \alpha'(\nu_1)Cl\delta\nu \cos(\omega t - \psi) \right. \\
& \left. + \frac{1}{2}\alpha''(\nu_1)Cl\delta\nu^2 \cos^2(\omega t - \psi) - \dots \right\} \quad (2.6)
\end{aligned}$$

Collecting the components of the expansion (2.6) at  $1f$ , shows the content of the 1<sup>st</sup> harmonic of the lock-in amplifier signal:

$$\begin{aligned}
I_\omega = & \Delta I(\nu_1) \cos(\omega t) - \Delta I(\nu_1)\alpha(\nu_1)Cl \cos(\omega t) - I(\nu_1)\alpha'(\nu_1)Cl\delta\nu \cos(\omega t - \psi) \\
= & \Delta I(\nu_1)[1 - \alpha(\nu_1)Cl] \cos(\omega t) - I(\nu_1)\alpha'(\nu_1)Cl\delta\nu \cos(\omega t - \psi) \quad (2.7)
\end{aligned}$$

The first term in (2.7) represents the background RAM component which arises from the linear intensity modulation,  $\Delta I(\nu_1)$ , but is independent of any gas absorption. The second term is also proportional to  $\Delta I(\nu_1)$  but contains a term  $\alpha(\nu_1)Cl$  which is the absorption function of the gas. The third term is the signal arising from the interaction of the frequency modulation with the gas absorption line shape, known as the FM/AM signal.

The implications of (2.7) are noteworthy when the phase of the various terms are considered. The FM/AM signal is separated in phase from the RAM signal by the phase shift  $\psi$ , described earlier. With careful selection of the lock-in amplifier measurement axis, it is therefore possible to recover a projection of the RAM-based absorption profile, isolated from the FM/AM signal.

## 2.4 RAM-based Calibration-free TDLS Techniques

### 2.4.1 RAM Method

Recovery of the absolute absorption line shape from the RAM signal was proposed by Duffin et al. who used the Taylor series approach outlined above to interpret

their signals [32]. Fig. 2.9 shows a phasor representation of the 1<sup>st</sup> harmonic terms stated in (2.7). The RAM signal and associated RAM absorption are shown along the x-axis, whilst the FM/AM component is shown at an angle  $\psi'$  from this axis. In this case,  $\psi' = \psi - \pi$  accounts for the intrinsic  $\pi$  phase difference between the FM/AM signal and the RAM. The FM/AM term occupies both the 2<sup>nd</sup> and 4<sup>th</sup> quadrants of the phasor diagram due to the  $\pi$  phase change it undergoes at line centre. Conventional WMS approaches would normally regard the RAM component as a distorting term and choose the lock-in amplifier measurement axis to be perpendicular to the x-axis in order to avoid the RAM contribution, recovering a projection of FM/AM term reduced by a factor of  $\sin \psi'$ .

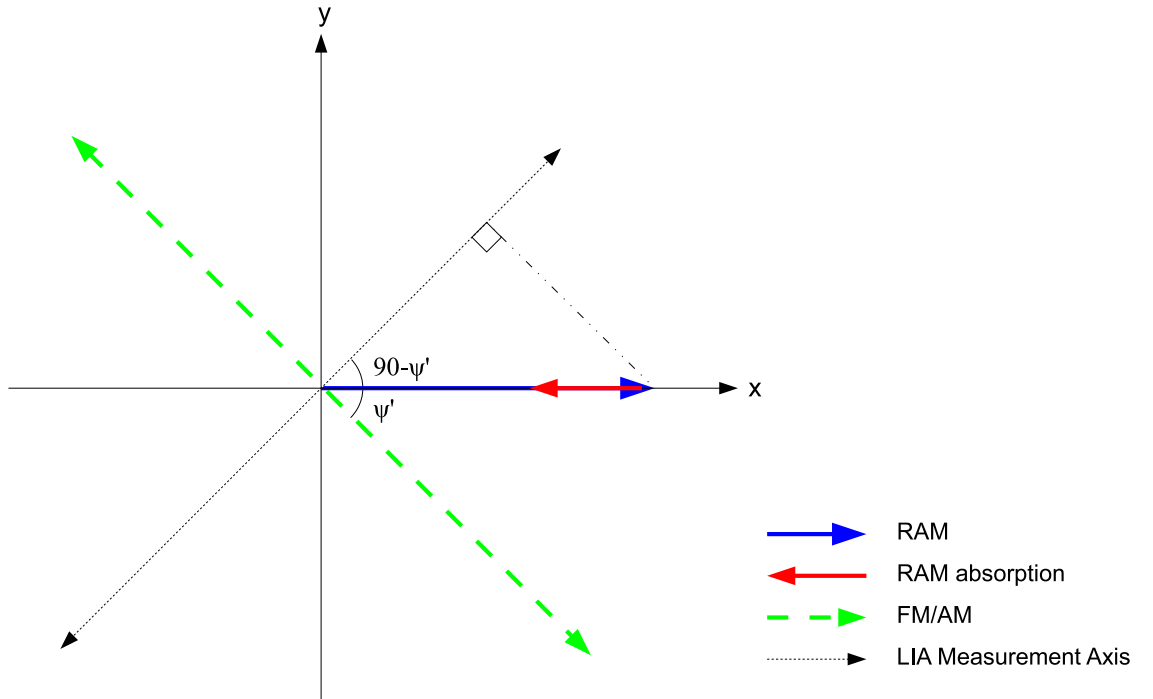


Figure 2.9: Phasor diagram showing the relation between the RAM and FM/AM signals. The lock-in amplifier measurement axis for RAM absorption signals is shown.

Choosing a LIA measurement axis that is perpendicular to the FM/AM signal isolates the RAM signal from any frequency modulation components and allows the first and second terms in (2.7) to be recovered. The output on the measurement channel is now:

$$I_{1f} = \Delta I(\nu_1) [1 - \alpha(\nu_1)Cl] \sin \psi' \quad (2.8)$$

The RAM terms are reduced by a factor  $\sin \psi'$  as only a projection of the total RAM is observed on the measurement channel unless  $\psi' = \frac{\pi}{2}$ . The term  $\Delta I(\nu_1)$  is the background RAM in the absence of absorption. When this can be recovered from a baseline fit or a measurement whilst the cell is purged, it can be used to normalise  $I_{1f}$  and recover the absolute transmission function of the gas absorption. This approach is valid for low modulation indices where  $m < 0.2$  unless, instead of limiting the Taylor series expansion to first order, higher order terms are considered.

The technique has been demonstrated at elevated temperatures and varying pressures, which is the kind of harsh environment in which the method is most advantageous. Measurements at high temperatures are challenging due to the degradation of components, thermal management issues, corrosion in the presence of water and the errors in spectral databases. Environments with varying pressure create measurement issues due to uncertainty in modulation indices and excessive line broadening compromising baseline fits. A rig designed to simulate the conditions in an industrial scale solid oxide fuel cell was used to observe methane and water vapour up to 950 °C [71, 72]. The technique has been demonstrated in the mid-infrared by Armstrong et al. using a difference frequency generation process [73, 74]. A periodically-poled lithium niobate nonlinear crystal was used to generate 3.4  $\mu\text{m}$  (2938  $\text{cm}^{-1}$ ) output that coincided with some strong fundamental rotational-vibrational lines in the methane spectrum.

## 2.4.2 Phasor Decomposition Method

In the RAM method, the target RAM absorption signal is only fully recovered when the angle  $\psi' = \frac{\pi}{2}$  and the whole signal is coincident with the lock-in measurement axis. For a typical DFB the modulation frequency required to achieve this condition is of the order of 1 MHz, at which point high-bandwidth lock-in amplifiers are required. An alternative method was proposed by

McGettrick et al. which recovers the absolute absorption line shape indirectly from the lock-in outputs, regardless of the modulation frequency used [33].

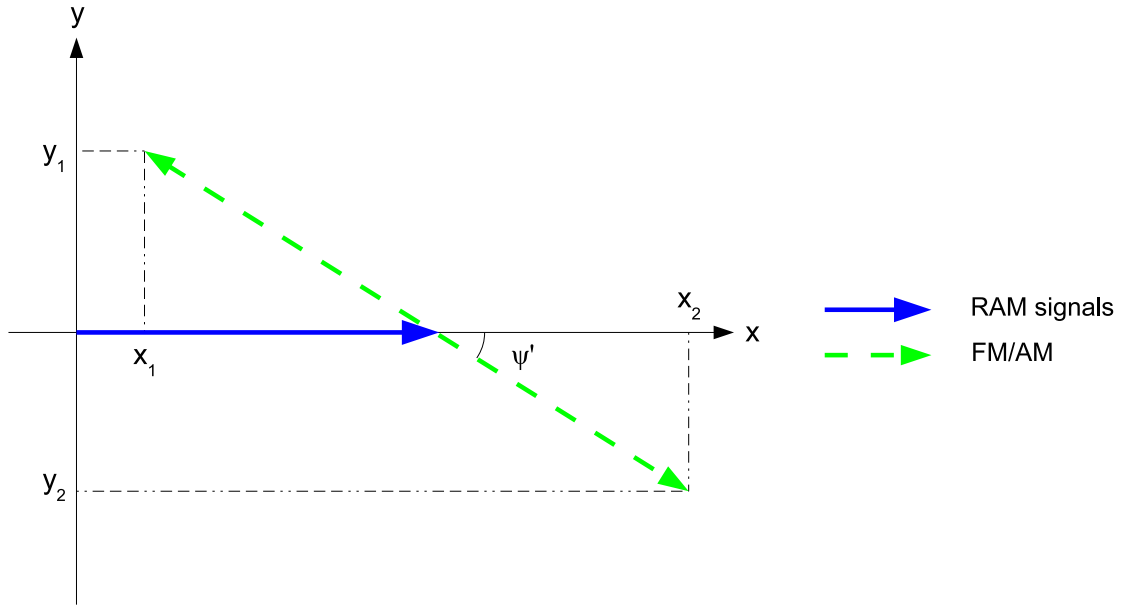


Figure 2.10: Phasor diagram showing the basis for the phasor decomposition method.

The phasor decomposition (PD) method requires the output from both of the orthogonal LIA measurement channels, described here as Channel 1 and Channel 2. To execute this method Channel 1 is aligned with the RAM components as opposed to the alignment with the FM/AM signal in the RAM method. Now the RAM absorption, the background RAM and a projection of the FM/AM signals are recorded on LIA Channel 1 and a projection of the FM/AM is recorded on LIA Channel 2, as shown in the phasor diagram in Fig. 2.10.

$$I_{1f(LIA_1)} = \Delta I(\nu_1) [1 - \alpha(\nu_1)Cl] - I(\nu_1)\alpha'Cl\delta\nu \cos \psi' \quad (2.9)$$

$$I_{1f(LIA_2)} = -I(\nu_1)\alpha'Cl\delta\nu \sin \psi' \quad (2.10)$$

Recording both channels simultaneously enables the two orthogonal lock-in amplifier outputs, represented by equations (2.9) and (2.10), to be used to calculate the full isolated RAM signals:

$$RAM(\nu_1) = LIA_1 + \frac{LIA_2}{\tan \psi'} \quad (2.11)$$

Like the RAM method, the PD method can be used in this simple form for low modulation indices. The signal amplitude increases with the linear intensity modulation,  $\Delta I$ , and also therefore  $m$ , the modulation index. For  $1f$  detection the amplitude of the frequency modulated first harmonic signal will have a maximum value when  $m = 2$  whilst the RAM signal will continue to increase with modulation index. The magnitude of the RAM signal is also determined by the modulation frequency as, for a fixed modulation index, an increase in modulation frequency will increase the magnitude of the RAM signals. This is due to the laser tuning coefficient dropping off at higher frequencies, which will be discussed further in Section 4.7.2. To achieve a given modulation index at higher frequencies will require a greater current dither which will necessarily increase the associated intensity modulation signals. In order to achieve a SNR using RAM-based absorption methods that is comparable to conventional WMS techniques, without pushing the bandwidth limits of detection hardware, it is necessary to operate at higher modulation indices.

### 2.4.3 Operation at High Modulation Indices

In the Taylor series formalism outlined above, the use of higher modulation indices to increase signal amplitude requires consideration of the higher order terms in the expansion rather than limiting the analysis to first order. The inclusion of higher order terms allows the inclusion of a correction function,  $C_f(\nu)$ , that can be applied to the recovered line shape as it becomes distorted at higher  $m$ , to yield the absolute absorption line shape.

$$RAM(\nu_1) = \Delta I(\nu_1) \{1 - \alpha(\nu_1) C_f(\nu_1)\} \quad (2.12)$$

In [32] the second order corrections were included allowing use of modulation indices,  $m < 0.5$ . The odd order terms do not contribute to the recovered first harmonic signal so the third order can be neglected and the fourth order terms

were considered negligible up to this limit. The expansion was extended further in [33] to include second and fourth order corrections which was accurate up to  $m < 0.75$ . At this point the sixth order contribution is approximately 1% and the resultant correction function is restated here for brevity as:

$$C_f(\nu_1) = \left[ 1 + \frac{1}{4}Bm^2 + \frac{1}{8}Dm^4 \right] \quad (2.13)$$

where  $m$  is the modulation index and B and D are given by:

$$B = \frac{3\Delta_\nu^2 - 1}{(1 + \Delta_\nu^2)^2} \quad (2.14)$$

$$D = \frac{5\Delta_\nu^4 - 10\Delta_\nu^2 + 1}{(1 + \Delta_\nu^2)^4} \quad (2.15)$$

and the instantaneous laser frequency,  $\nu_1$ , the line centre frequency,  $\nu_0$ , and the absorption HWHM,  $\gamma$  are substituted above using:

$$\Delta_\nu = \left( \frac{\nu_1 - \nu_0}{\gamma} \right)^2 \quad (2.16)$$

Extending the analysis to even higher orders begins to greatly increase the complexity of the signal recovery whilst providing only a modest increase in allowable modulation index. It is clear that to get optimal signal amplitudes a more efficient way of correcting the distorted signals at high modulation indices is desirable. This was one of the key objectives of this work and in Chapter 5 an alternative correction function is proposed based on a Fourier series expansion of the absorption coefficient, which in principle can correct the distortion at any achievable modulation index.

#### 2.4.4 RAM-nulling

One of the limiting factors of these techniques is the presence of the background RAM signal, which will inevitably impose a limit on sensitivity as the dynamic range of the lock-in amplifier is saturated by the background rather than the signals arising from the absorption. The removal of the non-absorbing background is therefore a key target in improving the overall performance of the technique.



$$\frac{I_t(\nu)}{I_0(\nu)} = 1 + \frac{S_{gas} - S_{baseline}}{\Delta I(\nu) \cos \omega t} \quad (2.17)$$

where  $S_{gas}$  is the photodiode output in the presence of gas,  $S_{baseline}$  is the baseline in the absence of absorption and  $\Delta I(\nu) \cos \omega t$  is the background RAM signal.

By removing the large background signals caused by the RAM, the full dynamic range of the lock-in amplifier and detection electronics can be utilised, increasing overall sensitivity. The suitability of this technique in stand-alone systems is limited due to the strict requirements for balancing the beam power ratios with the VOA and the orthogonal polarization states with the fibre polarization control. An alternative approach to RAM-nulling is investigated in Chapter 6, which uses novel photodiode front ends to achieve RAM nulling electronically.

## 2.5 TDLS in Aero Engine Diagnostics

A number of the major advances in harsh-environment TDLS have occurred in the context of combustion research and other fields closely linked with aero engine diagnostics. The last twenty years in particular have seen a number of significant projects apply TDLS techniques to aero engine processes with particular emphasis on combustion and pollution monitoring and mass flux determination. In this section, a review is given of some important publications that are either directly related, or have important features relevant to, aero engine ground testing. References [5, 37, 39] are useful review articles providing an overview of TDLS capabilities and potential in the field.

### 2.5.1 Monitoring Combustion Products

There is a large body of work dedicated to the observation of combustion gases and flame measurements using TDLS and related techniques. A number of combustion products and pollutants can be monitored at convenient near-IR wavelengths or in the mid-IR, including: O<sub>2</sub>, H<sub>2</sub>O, CO, CO<sub>2</sub>, NO, NO<sub>2</sub>, OH, NH<sub>3</sub> and CH<sub>4</sub>. Naturally, a lot of the studies in this area involve high temperatures,

in some cases up to 1500 K, where the HITRAN database and the associated HITEMP database can exhibit gaps and errors [26, 45]. There are many studies dealing with spectral parameter determination for specific gas absorptions of interest. In order to achieve high sensitivity measurements without the issues associated with in-situ measurements, some researchers use a sampling technique where an exhaust or combustion sample is collected and then tested off-line later at lower temperatures and pressures. Wiesen et al. [79] used off-line TDLS to test for methane and nitrogen dioxide levels in various aero engine ground test conditions. Similarly Mihalcea et al. measured NO, N<sub>2</sub>O, CO, CO<sub>2</sub>, O<sub>2</sub> and H<sub>2</sub>O concentrations by fast extraction of combustion gases from a laboratory burner [80, 81]. This process avoids relying on optics exposed to high temperature flows that often contain soot and other noisy elements. In situ measurements however can provide valuable information that sampled measurements cannot, such as temperature data.

Exhaust plume temperature has been measured in gas turbines, scramjet and other engines using water vapour, carbon dioxide and oxygen. J. Liu et al. used water vapour absorptions between 1.34 and 1.47  $\mu\text{m}$  to recover temperature up to 1500 K in a scramjet combustor [7]. X. Liu et al. demonstrated a water vapour sensor in an industrial gas turbine, recovering temperature at a rate of 3Hz [6]. Rieker et al. demonstrate the signal-to-noise benefits of WMS in a scramjet combustor when measuring temperature using water vapour and carbon dioxide. This work as well as several others consider the limitations of line-of-sight temperature measurements in engine and combustion diagnostics. If a truly uniform temperature distribution is encountered or if the path length is short enough that the distribution approximates to uniformity then path-averaged TDLS measurements are fine. In many cases however, there exists boundary layers and other temperature non-uniformities that need to be accounted for. Multi-line ratio thermometry is able to provide information about non-uniform gas paths given suitable assumptions about the structure of the temperature variation. Zhou et al. attempt to account for temperature non-uniformity by fitting to an assumed temperature distribution [82]. J. Liu et

al. and X. Liu extend this method to use a probabilistic approach to extracting the temperature variation across the absorption path, exploiting the different temperature responses of multiple absorptions [7, 83, 84].

Going beyond the single line-of-sight measurement, chemical species tomography using up to 32 absorbing beam paths has the potential to allow 2D temperature and concentration maps of several species. Wright et al. have demonstrated species selective imaging of the hydrocarbon fuel distribution across the inside of an internal combustion engine cylinder [3, 85, 86]. The high temporal resolution in this case allowed frame rates up to 4000 frames/s, which was greater than the cylinder cycle rate. This type of system could be implemented in an aero engine context, where the spatial resolution of the 2D map is limited by the beam path geometry.

High pressure gases are a particularly difficult environment in which to gather gas information. There are several articles focussing on TDLS signal recovery at high pressures and sometimes also elevated temperature, where pressure broadening leads to blended spectra from which it is difficult to recover gas information. In situ measurements of aero engine combustor gases would rely heavily on these techniques [30, 87–89]. Information on existing commercial developments in this area is limited but Zolo Technologies have marketed a TDLS-based combustor sensor with a range of functionality, called ZoloEFS in addition to a sensor with tomographic mapping capability called ZoloTASS [90].

## 2.5.2 Mass Flux Measurements

One area where TDLS has been applied effectively in aero engine diagnostics is in mass flux measurements. By simultaneously measuring species density and flow velocity, mass flux can be calculated and used to evaluate combustor performance and measure total engine thrust. Standard mass flux measurements use engine-mounted pressure and temperature sensors which often disrupt the gas flow downstream. Alternatives such as laser Doppler velocimetry usually require particle seeding of some kind which is not always convenient. Mass flux sensors based on TDLS are a viable option in aero engine monitoring where the

gas flows are fast enough to observe appreciable Doppler shifts. The majority of sensors demonstrated have used oxygen as the target species due to the convenient absorption features near 760 nm, which have favourable properties for mass flux measurements.

Early use of the mass flux technique was demonstrated in shock tubes by Philippe et al. [62, 91] and Arroyo et al. [92]. The same principle was later applied to aero engine mass flux measurements by Miller and Allen et al. where they were able to demonstrate mass flux measurements in a ground test of a Pratt & Whitney F100 military turbofan engine, achieving 1-2% accuracy for post-processed velocity, density and mass flux data [4, 5, 40]. A more ambitious system is proposed by the same authors that uses optics mounted on the intake duct of a NASA F-18 test jet, that could in principle provide real-time in-flight mass flux data [37]. Lyle later demonstrates real-time intake mass flux measurements on a Pratt & Whitney PW6000 turbofan engine [50]. This system is similar in layout to that adopted by Physical Sciences Inc. previously, a simple schematic of which is shown in Fig. 2.12. Lyle's system uses a unique hybrid modulation technique where the laser is modulated with a double sweep containing a scan with a WMS-type dither and then a direct detection scan consecutively. The WMS signal provides the signal necessary for velocity measurement and the direct detection signal is used to obtain the density measurement. The effect of non-uniform flow fields on the recovered Doppler shift measurements is also considered.

Fig. 2.12 shows a typical mass flux measurement layout, outlining the two beam paths directed upstream and downstream of the gas flow through the engine section. The angle  $2\theta$  is a limiting factor on the Doppler shift of the recovered spectra and in practice the achievable angle is limited by the dimensions of the engine bellmouth or exhaust nozzle. The Doppler shift measured between the counter-propagating spectra,  $\Delta\nu$ , is given by:

$$\Delta\nu = \frac{2V\nu_0 \sin \theta}{c} \quad (2.18)$$

where  $\theta$  is the beam angle from the normal to the flow,  $V$  is the gas velocity,  $c$  is the

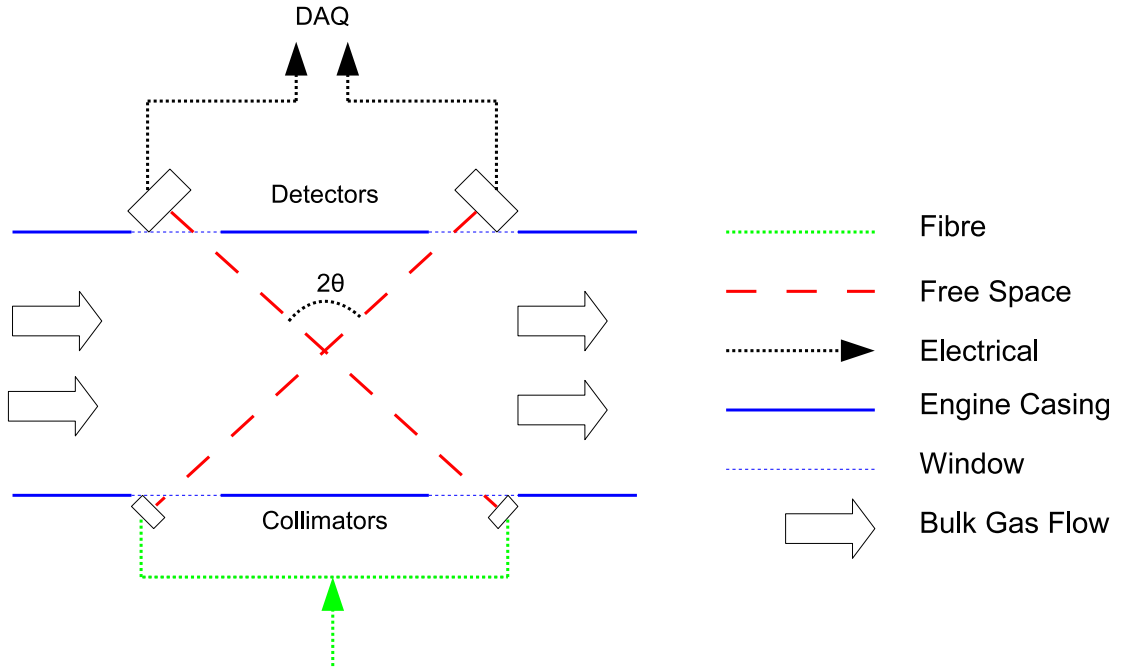


Figure 2.12: Diagram showing the geometry of a typical mass flux measurement system.

speed of light and  $\nu_0$  is the laser operating frequency. The proportionality between achievable  $\Delta\nu$  and  $\nu_0$  will influence the selection of target species and absorption features as lower wavelengths will be more sensitive to velocity, which is one of the reasons why oxygen absorption near 760 nm ( $13150 \text{ cm}^{-1}$ ) is frequently used.

### 2.5.3 TDLS in Misting Environments

An important consideration in this work is the recovery of gas absorption information in the presence of water droplets, which may introduce a scattering effect on the transmitted light. The problem of simultaneous consideration of gas phase and liquid phase was considered by Awtry et al. who were investigating dense mist environments in order to understand fire suppression performance [93–95]. The authors describe a variation of the Beer-Lambert law, similar to (2.1) which accounts for extinction by scattering losses:

$$I_{out} = I_{in} \exp[-\alpha_{droplet} l C_{liquidH_2O}] \quad (2.19)$$

In this case the optical density measurements are a function of  $\alpha_{droplet}$ , the

droplet size-dependent extinction coefficient at a particular wavelength,  $C_{liquidH_2O}$  the liquid water content and  $l$  the path length as before. The losses that this expression accounts for are necessarily distinct from the absorption losses and in this case the non-absorbing peak of the triangle ramp waveform is used to monitor the changes in optical density. This approach could have implications in this project if the geometry of an aero engine intake temperature sensor requires a beam to pass through a misting region.

## 2.6 Summary & Objectives

This chapter has served to give an overview of the field of tunable diode laser spectroscopy with a focus on the techniques that are relevant to this project. The important elements of direct detection and wavelength modulation spectroscopy are covered with reference to the historical progression of the methods used and available hardware. A description has been given of the calibration-free RAM-based line shape recovery techniques. The mathematical background for these techniques is derived and this formalism provides the basis for the key work in Chapters 5 and 6. The current limitations of the Rieker model and the Taylor series model are identified, highlighting the harsh environment scenarios in which the current state-of-the-art fails to provide a suitable TDLS-based solution. The challenges of achieving absolute line shape recovery at high sensitivities using correction at higher modulation indices and background nulling are discussed. The existing and potential applications of TDLS methods in aero engine diagnostics are described, highlighting the work done in combustion monitoring, temperature determination and mass flux measurements. A summary is given of the major aero engine TDLS work that has been previously undertaken and some relevant publications on scattering mist environments, that are applicable to the intake thermometry, are highlighted.

In Chapter 1 the global aims of the project were stated as the following: to further the state of the art techniques in TDLS-based gas parameter determination and to apply TDLS techniques to solving specific problems in

aero engine diagnostics. The specific objectives for the first aim were: Firstly, to extend calibration-free WMS absolute line shape recovery methods to modulation regimes where the signal amplitude is optimised. These techniques are currently limited to relatively low modulation indices with modest signal amplitudes and the algorithms used to recover the signals at the highest sensitivities are not suitable for stand-alone instruments in their current form. The second objective was to investigate recovery methods based on dual detector photoreceivers and evaluate their suitability for deployment in harsh environments, in particular aero engine test platforms. An extension of this work was to demonstrate an electrical analogue of the optical RAM-nulling techniques established previously. A major disadvantage of the RAM-based techniques relative to the well established 2f WMS techniques is the significant RAM background signal that saturates demodulation electronics and greatly reduces overall sensitivity.

The objectives for the second aim were: Firstly to implement a temperature sensor based on TDLS ratio thermometry for measuring intake gas under misting conditions. Existing methods for recovering ambient intake gas temperature become inaccurate when the ambient water vapour content is saturating and a viable TDLS temperature sensor could potentially decrease test bed occupancy time. The second objective was to test experimental setups and optical hardware for use in the harsh environments experienced in aero engine test beds, for future TDLS-based sensing applications. The process of establishing the best techniques for implementing aero engine-based TDLS systems was useful for planning these and future engine tests. There are a number of areas of aero engine diagnostics in which TDLS could provide effective and economical solutions and field testing offers the best platform for evaluating the specific conditions that are likely to be experienced in future work.

# Chapter 3

## Analytical Methods in Tunable Diode Laser Spectroscopy

### 3.1 Introduction to Molecular Spectroscopy

#### 3.1.1 Spectral Absorption Lines

Any molecule that absorbs or emits electromagnetic energy undergoes a change in internal energy. A number of mechanisms exist to change the internal energy by discrete amounts that are governed by Planck's law for the quantisation of radiation,  $\Delta E = h\nu$ . Fig. 3.1 shows an absorption transition between two energy states with the absorbed photon energy corresponding to the energy difference between the two states. Fig. 3.2 shows a generic absorption spectrum that might arise from such a transition.

The mechanisms within the molecule that give rise to these transitions have different characteristic energies associated with them so the absorption and emission properties will correspond to different parts of the electromagnetic spectrum. The highest energy transitions are associated with the gamma ray region (1-100 pm) and are the result of nuclear particle changes. The high energy inner electron transitions have spectra in x-ray region (100 pm-10 nm) whilst lower energy electron transitions can be observed in the UV and visible

spectrum (10 nm-1  $\mu\text{m}$ ). Of interest to this work are the transitions that result from molecular vibrations in the infrared spectrum (1-100  $\mu\text{m}$ ). Transitions with lower energies result from the rotation of molecules which are observed in the microwave region (100  $\mu\text{m}$ -1 cm) whilst at radio wavelengths (1 cm-10 m) spin reversal in electrons and nuclei can be observed with electron spin resonance and nuclear magnetic resonance spectroscopies.

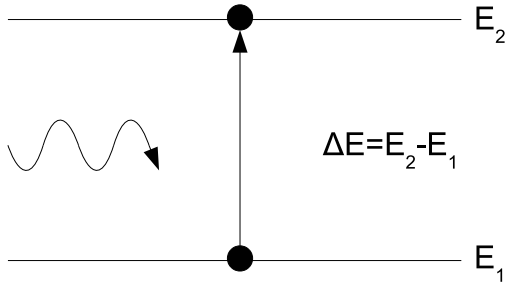


Figure 3.1: Absorption of electromagnetic radiation in a simple two-level system

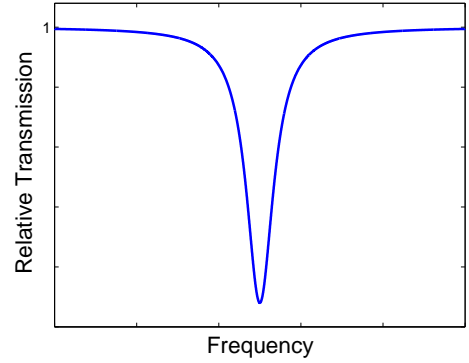


Figure 3.2: Absorption Line at  $\nu = \frac{\Delta E}{h}$

### 3.1.2 Vibrational and Rotational Energy Levels

The absorption transitions of interest to this work are those due to molecular vibrations and rotations. At a given energy the atoms in a molecule will vibrate around some mean position relative to each other whilst the molecule can also undergo rotation. For the allowed transitions of these mechanisms to be observable in the infrared there must be a change in the dipole moment of the molecule. Considering the vibrational spectra first, a useful analysis is obtained by considering the vibrating atom as an anharmonic oscillator. Fig. 3.3 shows the energy function that results from vibration between two atoms in a molecule, which is modelled by the Morse potential function. The solution of the Schrödinger equation using this expression yields quantized energy levels with eigenvalues [96]:

$$E_{vibrational} = \left\{ 1 - \chi_e \left( v + \frac{1}{2} \right) \right\} \left( v + \frac{1}{2} \right) \omega_e \quad (3.1)$$

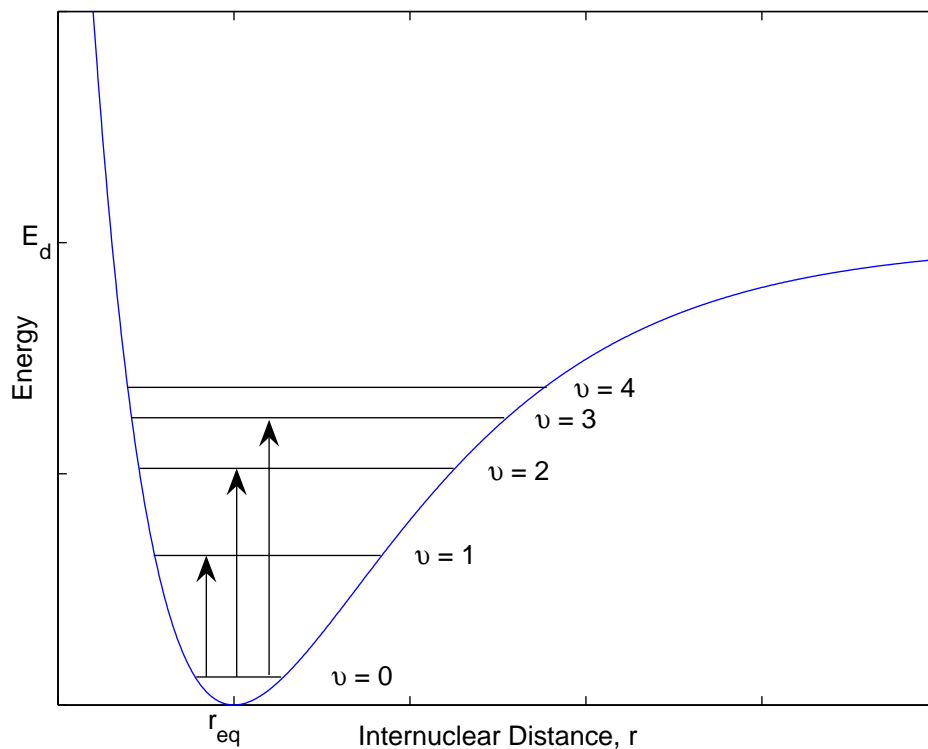


Figure 3.3: Potential energy with internuclear distance for a diatomic molecule, modelled using the Morse function,  $E = E_d(1 - \exp[-a(r - r_{eq})])^2$  where  $E_d$  is the dissociation energy,  $a$  is a molecular constant that relates to the width of the well and  $r_{eq}$  is the equilibrium distance.

where  $\omega_e$  is the oscillation frequency,  $\chi_e$  is the anharmonicity constant and  $v$  is the vibrational quantum number [97]. The selection rules for  $v$  that govern the allowed values of energy are:

$$\Delta v = \pm 1, \pm 2, \pm 3 \dots \quad (3.2)$$

These selection rules dictate the allowable transitions between vibrational energy states. The relative intensity of a given transition is related to the population of the initial state, which is related to the Boltzmann distribution. The fundamental absorption lines are those between  $v = 0 \rightarrow v = 1$  whilst the weaker first overtone absorption,  $v = 0 \rightarrow v = 2$  is important in this work as it is these overtone transitions that occur in the near-infrared region of the spectrum. Transitions

originating from the  $v = 1$  band are typically negligible at lower temperatures but can be observed as ‘hot lines’ when the gas temperature is elevated and the population of the  $v = 1$  state increases according to the Boltzmann distribution.

The vibrational states for diatomic molecules are relatively straightforward to model but for polyatomic molecules the energy structure can become more complex. The number of degrees of vibrational freedom is dictated by the number of atoms and whether the molecule is linear or nonlinear. Linear molecules are those which have atoms arranged along a straight line whilst nonlinear molecules are split into either symmetric top, spherical top and asymmetric top types. A linear molecule with  $N$  atoms will have  $3N - 5$  fundamental vibrations whilst a nonlinear molecule will only have  $3N - 6$ . Water vapour has 3 atoms and therefore 3 fundamental vibrations which are illustrated in Figs. 3.4 to 3.6 [96]. Depending on how the shape of the molecule changes the vibration is described as being a bend or stretch and the symmetric or asymmetric nature of the vibration is also defined. The other molecule that is directly relevant to this work is methane which is also nonlinear but spherical top and has 9 fundamental vibrations. The tetrahedral structure of this molecule leads to some vibrational states having the same energy. This degeneracy yields four vibrational modes, with two states that are triply degenerate and another that is doubly degenerate, shown in 3.7 to 3.10 [98].

A vibrating gas molecule will also be undergoing rotation which will have its own energy structure. The timescale for rotational motion is significantly slower than vibrational motion which allows the Born-Oppenheimer approximation to be used and for vibrations and rotations to be treated separately so that  $E_{total} = E_{vibrational} + E_{rotational}$  and the solution for rotational energy levels is [99]:

$$E_{rotational} = \frac{h^2}{8\pi^2 I} J(J + 1) \quad (3.3)$$

where  $I$  is the moment of inertia and  $J$  is the rotational quantum number. For spherical top molecules such as methane, where the moment of inertia is equal in all three orthogonal axes, the selection rules for transitions between rotational energy states are:

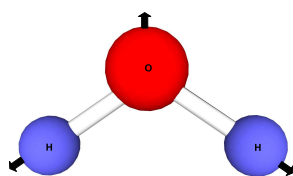


Figure 3.4: H<sub>2</sub>O Symmetric stretch,  $\nu_1$

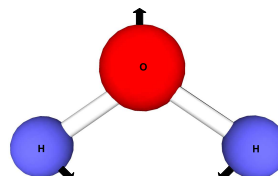


Figure 3.5: H<sub>2</sub>O Bending mode,  $\nu_2$

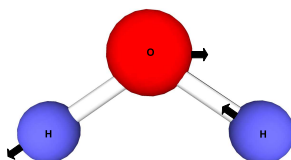


Figure 3.6: H<sub>2</sub>O Asymmetric stretch,  $\nu_3$

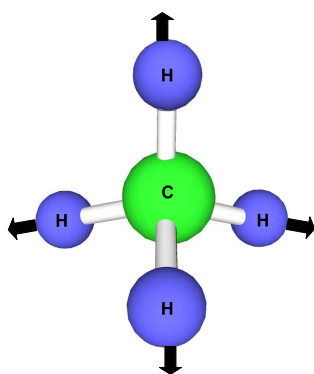


Figure 3.7: CH<sub>4</sub> Symmetric stretch,  $\nu_1$

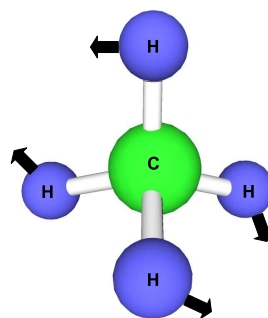


Figure 3.8: CH<sub>4</sub> Symmetric bend,  $\nu_2$

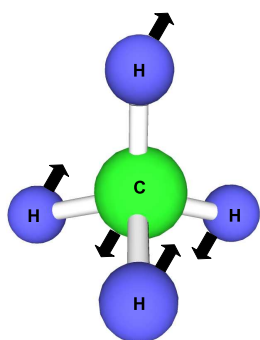


Figure 3.9: CH<sub>4</sub> Asymmetric stretch,  $\nu_3$

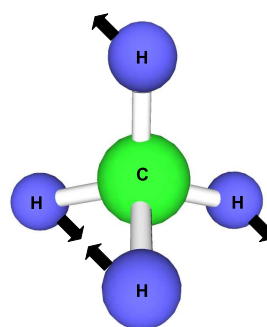


Figure 3.10: CH<sub>4</sub> Asymmetric bend,  $\nu_4$

$$\Delta J = 0, \pm 1 \quad (3.4)$$

The spectroscopic features that arise from these allowed transition bands are generally denoted by the letters  $P$ ,  $Q$  and  $R$  for the  $\Delta J = -1, 0, 1$  states respectively. For asymmetric top molecules such as water vapour, which have different moments of inertia along each axis, no solution exists to the Schrödinger equation and the spectra typically exhibit complex structures.

## 3.2 Absorption Spectra Characteristics

In Chapter 2, the form of the absorption spectra recovered due to the Beer-Lambert law was introduced. Equation (2.2) shows that the total absorbance comprises of a temperature dependent line strength and a line shape function. The line shape function is determined by the broadening mechanisms that dominate the gas being observed. Knowing which function to attribute to a given experimental profile is important for sensor design and also for gas information determination.

### 3.2.1 Spectral Broadening

It is well established that an absorption feature will never exhibit an infinitely narrow spectral profile. Excluding for now the inevitable instrument broadening that will arise when experimental measurements are taken, there are three broadening effects that will affect the recovered line shapes in a typical TDLS system: natural, Doppler and collisional broadening [96, 99]. The effect of power broadening is not considered here due to the modest laser powers used. Natural broadening is the most fundamental broadening mechanism as it represents the absolute limit of resolvable broadening. Any energy state with a finite lifetime will have an associated finite energy spread due to the Heisenberg uncertainty principle, i.e.  $\Delta E \Delta t \geq \hbar$ . The natural broadening mechanism is homogeneous and the line shape function that results is a Lorentzian.

In addition to the natural broadening, the thermal motion of the absorbing molecules will induce Doppler broadening related to the spread of velocities encountered by the radiation. In contrast to the natural broadening, the Doppler broadening is inhomogeneous as the contribution to the overall broadening is specific to the individual molecule and whether its velocity is toward the laser source (blueshifted) or away from the laser source (redshifted). For a uniform temperature distribution the spread of velocities follows a Maxwell distribution and the resulting broadening contribution is modelled using a Gaussian line shape.

The final broadening contribution considered here is the collisional broadening, which affects absorption spectra generated in higher pressure environments. The various molecules in the gas sample will undergo many collisions due to their constant random motion. These collisions will perturb the energy states of the allowed transitions in the absorption spectrum. It is generally assumed that the collisions are binary and the collision duration is much smaller than the mean time between collisions. The amount of broadening is proportional to the collision rate and the line shape is also given by a Lorentzian profile.

Generally the Lorentzian line shape contribution due to natural broadening is small compared to the Doppler and collisional broadening, except possibly in the wings of a strongly Gaussian profile. The Doppler broadening will dominate in low pressure gases whilst for gases around 1 atm and above, the collisional broadening will be dominant. In the pressure regime where neither the Doppler nor the collisional broadening are dominant, the recovered profile will be a convolution of the various contributions. The convolution of a Lorentzian and a Gaussian profile is the Voigt function and is described below.

### **3.2.2 Spectral Line Intensity**

The intensity of a particular spectral line depends on three main contributions: the probability of the given transition absorbing an incident photon, the number of molecules in the transition state from which absorption can occur and the size of the absorbing sample dictated by concentration and path length.

The probability of absorption from a transition is dictated by solutions to

the quantum mechanical wavefunctions related to each state in the transition. Accurate quantitative determination of each transition probability is beyond the scope of this discussion but an understanding of the results of the fundamental spectroscopic theory can identify allowed and forbidden transitions using appropriate selection rules.

The intensity of a spectral line will depend upon the populations of the states in the system. With all else being equal a transition with an initial state that is more populated than an equivalent state with lower population, will exhibit a higher spectral intensity. The relative populations of two states of different energies follow the well established Boltzmann distribution. In this form the relative populations of the two states,  $N_{upper}$  and  $N_{lower}$  are given as a function of the difference in their energies,  $\Delta E = E_{upper} - E_{lower}$ , the Boltzmann constant,  $k$  and the temperature,  $T$ :

$$\frac{N_{upper}}{N_{lower}} = \exp\left(\frac{-\Delta E}{kT}\right) \quad (3.5)$$

The number of molecules contributing to the absorption is a function of both the species concentration and absorbing path length. In either case the intensity of the spectral absorbance will increase the more interactions there are with absorbing molecules. Restating a version of (2.1), the exponential relation between transmitted intensity and the product  $Cl$ , which combines concentration and path length, is shown:

$$\frac{I_{out}}{I_{in}} = \exp(-\alpha(\nu)Cl) \quad (3.6)$$

### 3.3 Modelling Spectral Line Shapes

The most effective way to extract gas parameters from recovered experimental signals is to perform fits of theoretical line shape models to the experimental data. The most straightforward approach is to ensure recovery of the absolute transmission function and then perform a least-squares fit based on an appropriate line shape function. This work focuses on assumptions of either Lorentzian or

Voigt line shapes based on the anticipated applications. In normal circumstances the critical parameters in a fit are concentration, pressure and temperature, some of which may be known with the others to be determined. The fewer unknown parameters there are in the fit, the more accurate and faster it is likely to be. The other key components required for modelling a theoretical fit are the spectroscopic parameters, such as line strength and broadening coefficients which are given, for instance, by the HITRAN database. The spectroscopic parameters provided are usually a good approximation as they are based on a mixture of empirical and theoretical studies. The database is in no way perfect and in some cases these parameters are a source of non-trivial errors and may need to be independently verified.

### 3.3.1 The Lorentzian Profile

The two homogeneous broadening mechanisms, natural and collisional, are modelled using a Lorentzian line shape profile. This line shape profile is given in normalised form such that  $\int_{\nu} \Phi(\nu - \nu_0) d\nu = 1$ , by [100]:

$$\Phi_L = \frac{1}{\pi} \frac{\gamma_L}{(\nu - \nu_0)^2 + \gamma_L^2} \quad (3.7)$$

where, for component species  $j$ , the Lorentzian HWHM is:

$$\gamma_L = P \sum_j (C_j \gamma_j) \quad (3.8)$$

and including the temperature dependence with coefficient  $n$

$$\gamma_j(T) = \gamma_j(T_0) \left( \frac{T_0}{T} \right)^n \quad (3.9)$$

The peak height of the Lorentzian profile can be related to the Lorentzian HWHM using the equation:

$$\Phi_L(\nu_0) = \frac{1}{\gamma_L \pi} \quad (3.10)$$

### 3.3.2 The Gaussian Profile

At lower pressures, below 0.2 atm where the collisional broadening is much smaller than the Doppler contribution, the Gaussian line shape profile can be used:

$$\Phi_G = \frac{4}{\gamma_G} \sqrt{\frac{\ln 2}{\pi}} \exp \left[ -4 \ln(2) \left( \frac{\nu - \nu_0}{\gamma_G} \right)^2 \right] \quad (3.11)$$

The Gaussian HWHM can be represented by:

$$\gamma_G = \frac{\nu_0}{2} \sqrt{\frac{8kT \ln 2}{mc^2}} \quad (3.12)$$

where  $k$  is the Boltzmann constant,  $m$  is the molecular mass and  $c$  is the speed of light in a vacuum. The peak height of the Gaussian profile can be related to the Gaussian HWHM using the equation:

$$\Phi_G(\nu_0) = \frac{4}{\gamma_G} \sqrt{\frac{\ln 2}{\pi}} \quad (3.13)$$

The Gaussian profile has a temperature dependence that is independent of species concentration. As temperature increases the Doppler width will increase as long as the pressure stays low enough for the collisional broadening to have a negligible effect.

### 3.3.3 The Voigt Profile

At intermediate pressures up to around 1 atm it is reasonable to use the Voigt function which will account for both the Gaussian and Lorentzian contributions to the overall line shape. The convolution can be represented by the integral below, using the component line shape contributions  $\phi_G$  and  $\phi_L$ :

$$\Phi_V = \int_{-\infty}^{+\infty} \phi_G(\nu') \phi_L(\nu - \nu') d\nu' \quad (3.14)$$

There is no simple analytical solution to this integral so most implementations of the Voigt function make use of numerical approximations. There are several examples of empirical approximations in the literature [101, 102]

i	$A_i$	$B_i$	$C_i$	$D_i$
1	-1.215	1.2359	-0.3085	0.021
2	-1.3509	0.3786	0.5906	-1.1858
3	-1.215	-1.2359	-0.3-85	-0.021
4	-1.3509	-0.3786	0.5906	1.1858

Table 3.1: Coefficients for McLean’s numerical approximation to the Voigt function [103]

but this work uses the algorithm suggested by McLean et al. to model the Voigt function [103].

$$\Phi_V = \frac{\gamma_L}{\gamma_G} \alpha_L \sqrt{\pi \ln 2} V(X, Y) \quad (3.15)$$

where

$$V(X, Y) = \sum_{i=1}^4 \frac{C_i(Y - A_i) + D_i(X - B_i)}{(Y - A_i)^2 + (X - B_i)^2} \quad (3.16)$$

and

$$X = \frac{2\sqrt{\ln 2}}{\gamma_G} \nu \quad \text{and} \quad Y = \frac{\gamma_L}{\gamma_G} \sqrt{\ln 2} \quad (3.17)$$

The coefficients for  $A_i$ ,  $B_i$ ,  $C_i$  and  $D_i$  are given here in Table 3.1.

### 3.3.4 HITRAN

The HITRAN database provides a range of useful spectral parameters for 39 different molecules and their isotopologues. Table 3.2 lists the parameters provided by the HITRAN and HITEMP databases [25, 26, 45] for each of the listed transitions, of which there are 2,713,968 in the 2008 edition [26]. For basic spectral models, the key parameters are: vacuum wavenumber, intensity (line

Parameter	Description	ASCII Length
M	HITRAN molecule number	1
I	Isotopologue number	1
$\bar{\nu}$	Vacuum wavenumber [ $\text{cm}^{-1}$ ]	12
S	Intensity [ $\text{cm}^{-1}/\text{molecule}\cdot\text{cm}^{-2}$ ] at 296K	10
A	Einstein A coefficient [ $\text{s}^{-1}$ ]	10
$\gamma_{air}$	Air-broadened half-width (HWHM at 296K) [ $\text{cm}^{-1}/\text{atm}$ ]	5
$\gamma_{self}$	Self-broadened half-width (HWHM at 296K) [ $\text{cm}^{-1}/\text{atm}$ ]	5
$E''$	Lower state energy [ $\text{cm}^{-1}$ ]	10
n	Temperature dependence coefficient (for $\gamma_{air}$ )	4
$\delta$	Air pressure shift [ $\text{cm}^{-1}/\text{atm}$ ]	8
$V'$	Upper-state ‘global’ quanta	15
$V''$	Lower-state ‘global’ quanta	15
$Q'$	Upper-state ‘local’ quanta	15
$Q''$	Lower-state ‘local’ quanta	15
$I_{err}$	Uncertainty indices	6
$I_{ref}$	Reference indices	12
(flag)	Flag for line-mixing	1
$g'$	Statistical weight of the upper state	7
$g''$	Statistical weight of the lower state	7

Table 3.2: HITRAN transition parameters [26]

strength), air and self broadened half-widths, lower state energy, temperature dependence coefficient and air pressure shift.

Line shape models based on HITRAN parameters are useful for extracting gas data from experimental signals but also represent a powerful tool for sensor design and preliminary spectral evaluation. Before a laser wavelength is selected it is essential to perform a survey of the relevant spectral regions to ensure the line intensities and temperature dependencies match the experimental requirements. This process also allows the user to judge whether there may be any interference from other species that may be present in any experimental gas mixtures. As mentioned previously the database is not perfect, especially if higher temperatures are involved, but in general the output will give a useful representation of the spectra to be expected.

### 3.4 Extracting Gas Parameters

The primary aim of any gas measurement is to obtain some information about the gas sample being interrogated, whether it is concentration, pressure, temperature or velocity. In most cases every effort will be made to recover some gas data using assumptions about the environment or existing reliable gas detection methods. In some situations, for example, the concentration of a certified gas may be known but the pressure or temperature may be unknown, or alternatively the concentration may be unknown but the pressure and temperature may be monitored using conventional techniques. In this project the focus was on extracting gas information from absolute absorption line shapes, using either direct detection or the RAM-based techniques introduced in Section 2.4. The challenges involved in the recovery of gas data using conventional wavelength modulation spectroscopy are well documented in the literature [7, 31, 62] and in this work only the use of 2f peak height ratio thermometry is discussed in detail, in Chapter 7.

### 3.4.1 Concentration and Pressure

The gas concentration can be related to the integrated absorbance of the absolute line shape profile using (3.18). This process assumes that pressure and temperature can be measured or assumed, that the path length is known and that the absorbance satisfies the linear regime of the Beer-Lambert law. The integrated absorbance is simply the area above the relative transmission curve:

$$C = \frac{A}{PLS(T)} \quad (3.18)$$

where  $S(T)$  is the temperature-dependent absorption line strength, defined later in (3.19). In most practical situations the most convenient and effective method for establishing concentration and pressure from a recovered line shape is to perform a fitting procedure based on a theoretical representation of the recovered signal. If the spectral database data are good enough and the experimental conditions, such as pressure or temperature, that are not parameters in the fit are known with sufficient accuracy, then an optimised least squares error fit will yield the target gas parameters.

A simple fit requires the following line-specific information from the HITRAN database: the line centre frequency, line intensity (line strength), lower state energy, air broadening coefficient, self broadening coefficient, temperature dependence coefficient and the air pressure shift. The other contributions to the model that are experimental parameters, which may or may not be known depending upon the requirements, are: pressure, temperature, concentration and path length. The constants required to create a theoretical absorption spectrum are: HITRAN reference temperature, Boltzmann's constant, molecular mass, speed of light, Planck's constant and the partition function coefficients.

The form of the simulation is taken from the McLean approximation stated in (3.15) and (3.16). This collects together the various contributions from (3.8), (3.12) and (3.17). An important calculation in the simulation process is the temperature dependent line strength  $S(T)$ , given by [6]:

Coefficient	$70 < T(K) < 405$	$400 < T(K) < 1500$	$1500 < T(K) < 3005$
a	$-0.44405 \times 10^1$	$-0.94327 \times 10^2$	$-0.11727 \times 10^4$
b	$0.27678 \times 10^0$	$0.81903 \times 10^0$	$0.29261 \times 10^1$
c	$0.12536 \times 10^{-2}$	$0.74005 \times 10^{-4}$	$-0.13299 \times 10^{-2}$
d	$-0.48938 \times 10^{-6}$	$0.42437 \times 10^{-6}$	$0.74356 \times 10^{-6}$

Table 3.3: Coefficients of the molecular partition function for water vapour [82]

$$\begin{aligned}
S(T) = S(T_0) \frac{Q(T_0)}{Q(T)} \left( \frac{T_0}{T} \right) \exp \left[ -\frac{hcE''}{k} \left( \frac{1}{T} - \frac{1}{T_0} \right) \right] \\
\times \left[ 1 - \exp \left( \frac{-hc\nu_0}{kT} \right) \right] \left[ 1 - \exp \left( \frac{-hc\nu_0}{kT_0} \right) \right]^{-1} \quad (3.19)
\end{aligned}$$

where  $T_0$  refers to the standard reference temperature of 296 K used by HITRAN and  $Q(T)$  is the molecular partition function given in (3.20). The coefficients of  $Q(T)$ , differ according to species and temperature range and the coefficients used for water vapour in this project are those defined by Zhou et al. given in Table 3.3 [82].

$$Q(T) = a + bT + cT^2 + dT^3 \quad (3.20)$$

The values for line intensity in each version of the HITRAN database are given units of  $[\text{cm}^{-1}/(\text{molecule}\cdot\text{cm}^{-2})]$ , as shown in Table 3.2. It is however more convenient for simulation calculations to work in pressure units, such as atmospheres  $[atm]$ . To convert the HITRAN intensity value to one that can be easily implemented in a theoretical simulation, the following conversion can be applied:

$$S[\text{cm}^{-2}/atm] = \frac{S[\text{cm}^{-1}/(\text{molecule} - \text{cm}^{-2})]n_i[\text{molecule} - \text{cm}^{-3}]}{P_i[atm]} \quad (3.21)$$

A further simplification can be made by applying the ideal gas law to (3.21), in order to recover the HITRAN intensity as a function of temperature:

$$S[cm^{-2}/atm] = \frac{7.339 \times 10^{21}[molecule - cm^{-3}K]S[cm^{-1}/(molecule - cm^{-2})]}{T[K]} \quad (3.22)$$

The final transmission function is given by:

$$\frac{I}{I_0} = \exp \left[ -2Pcl\gamma_G S(T) \sqrt{\frac{\ln 2}{\pi}} V(X, Y) \right] \quad (3.23)$$

The result of (3.23) is a Voigt profile for an individual line. In most spectra however, there are contributions from a number of absorption lines in close proximity to one another. It is commonplace therefore to collect HITRAN data for all the absorption features in the region of the target absorption and calculate the transmission profile for all lines that may contribute to the recovered spectra. These spectra are then summed together to recreate the total absorption profile thereby accounting for the absorption from the wings of nearby absorption lines. A version of the MATLAB script used to execute this simulation is provided in Appendix A.

A single simulation will not provide enough information to establish any unknown parameters. To do this a fit must be performed by optimising one or more of the unknown experimental conditions in the simulation. This is performed using an unconstrained nonlinear optimisation technique, based on the sum of the least squares error between the experimental data and successive iterations of the fit. This technique is facilitated in MATLAB by the *fminsearch* function, which allows several parameters to be fitted simultaneously, provided the quantity being optimised has a single minimum value [104]. The computation time will increase with each additional parameter in the fit, as will the risk of introducing local solutions to the fit that do not represent the physical optimisation of each parameter. In these cases where the fit yields unphysical optimised values, constraints can be introduced based on the known or assumed limits of the experimental system.

### 3.4.2 Temperature

Temperature information extraction is of particular interest in aero engine diagnostics for both ambient and combustion measurements. Aside from the low pressure Doppler regime, where temperature information can be inferred directly from an absorption line shape, temperature measurements usually require spectral information from multiple absorption features. We can express (3.18) in an alternate form to show the integration of a line shape over all frequencies to recover the total absorbance, which is a function of the temperature-dependent line strength,  $S(T)$ :

$$A(T) = PCLIS(T) \int_{-\infty}^{+\infty} \Phi(\nu, T) d\nu = PCLIS(T) \quad (3.24)$$

This result shows that for a single transition accurate knowledge of pressure, concentration and path length are required for temperature determination. If two transitions from the target species spectrum are recorded simultaneously, the partial pressure, path length and concentration for both lines will be identical and the only difference will be the temperature dependent line strength. The target transitions can be chosen so that the two line strengths have sufficiently different temperature dependencies that they will behave differently over the temperature range of interest. In this case the ratio of the integrated absorbances is calculated and this is a function of line strength only and has no dependence on pressure or concentration. For two transitions, denoted 1 and 2, the ratio of the integrated absorbances is given by:

$$R_{direct} = \frac{A_1(T)}{A_2(T)} = \frac{S_1(T)}{S_2(T)} = R_{S(T)} \quad (3.25)$$

The ratio of the line strengths can be approximated to the result in (3.26) below, if the values for  $\nu_0$ , the centre frequency, are sufficiently close together. In this case the component of the ratio corresponding to the last two terms in (3.19) will approximate to 1:

$$R_{direct} = R_{S(T)} \approx \frac{S_1(T_0)}{S_2(T_0)} \exp \left[ -\frac{hc\Delta E''}{k} \left( \frac{1}{T} - \frac{1}{T_0} \right) \right] \quad (3.26)$$

The temperature can be recovered analytically from the calculated integrated absorbance ratio,  $R_{direct}$ , using:

$$T = \frac{-\frac{hc}{k}\Delta E''}{\ln R_{direct} + \ln \frac{S_2(T_0)}{S_1(T_0)} - \frac{hc}{k} \frac{\Delta E''}{T_0}} \quad (3.27)$$

The choice of transitions used for a given temperature measurement should reflect the optimum temperature sensitivity that can be achieved given any experimental constraints. The sensitivity of the ratio to temperature depends upon the difference in ground state energies,  $\Delta E''$ , of the two transitions. The peak sensitivity for a pair of transitions will occur at a temperature [105]:

$$T = \frac{hc}{2k} (E_1'' - E_2'') = 0.72\Delta E'' \quad (3.28)$$

The absolute and relative temperature sensitivities are given by equations (3.29) and (3.30) [92, 106]:

$$\frac{\Delta R_{direct}}{\Delta T} \approx \frac{dR_{S(T)}}{dT} = \frac{hc}{k} \frac{\Delta E''}{T^2} R_{S(T)} \quad (3.29)$$

$$\frac{\Delta R_{direct}}{R_{direct}} \bigg/ \frac{\Delta T}{T} \approx \frac{dR_{S(T)}}{dT} \frac{T}{R_{S(T)}} = \frac{hc}{k} \frac{\Delta E''}{T} \quad (3.30)$$

An alternative method for performing ratio thermometry is to use the second harmonic peak height ratio of two transitions. There are a number of advantages to simply recovering the 2f peak height, particularly when absorbance is limited. Firstly, the 2f peak is a very straightforward data point to identify and a measurement can be recovered rapidly. The most significant advantages however are that it does not require a baseline fit to a non-absorbing reference or a wavelength referencing scheme. Similar analysis to the direct detection ratio thermometry is required although the ratio invariably depends on additional factors and not just the line strength. Assuming optically thin transmission, the 2f peak height ratio approximates to:

$$\begin{aligned} R_{2f} &\approx \frac{S_1(T)}{S_2(T)} \frac{a_{2,1}(\nu_{0,1}, m, T) I_{0,1}(\nu_{0,1})}{a_{2,2}(\nu_{0,2}, m, T) I_{0,2}(\nu_{0,2})} \\ &= R_{S(T)} R_{a(m,T)} R_I \end{aligned} \quad (3.31)$$

where  $a_2(\nu_0, m, T)$  is the peak value of the  $2^{nd}$  order Fourier coefficient of the area-normalised line shape function,  $m$  is the modulation index and  $I_0(\nu_0)$  is the laser power at the line centre. The laser power dependence,  $R_I$ , is not a function of temperature and can be normalised out. The  $2^{nd}$  Fourier coefficient peak ratio is more complicated however as this ratio depends on the collisional broadening coefficients,  $\gamma_j(T)$ , introduced in (3.9). If the two transitions are chosen so that the values for  $n$ , the temperature dependence coefficient, are similar then the 2f peak height ratio can be assumed to be only a weak function of  $R_a(m, T)$ .

### 3.5 Summary

This chapter has given an overview of the analytical techniques that form the basis of the studies performed in this thesis. The fundamentals of molecular spectroscopy are introduced to provide the reader with an understanding of the physical mechanism for optical absorption in polyatomic molecules. In particular the vibrational-rotational overtone transitions of water vapour and methane that are used in this study are discussed. The mechanisms that broaden spectral transitions are presented along with descriptions of the mathematical functions used to model the resulting profiles, focussing on the Lorentzian, Gaussian and Voigt line shapes. The use of the HITRAN database to model particular spectra for predictive or fitting purposes has been described. The analytical techniques used to extract gas parameters from fitted absorption spectra are presented, showing how species concentration, pressure and temperature can be recovered in the scenarios pertinent to this work.

# Chapter 4

## Experimental Methodology

### 4.1 Introduction to Experimental Techniques

The experimental data presented in this thesis are a mixture of laboratory-based tests and aero engine test bed field studies. In this chapter a description is given of the two main laboratory experimental configurations and their variants as well as the three aero engine test configurations that were attempted during the course of the project. Details are given about the electro-optical and optomechanical hardware and components used in each setup. A generalised experimental layout of the various experimental systems used in this work is shown in Fig. 4.1. This shows the constituent components of a TDLS system and the optical and electrical connections between them. Each of the experimental systems built to collect the data presented followed this basic structure with slight variations depending on the type of signals being recovered. In addition to a description of the various laboratory and field systems used, the experimental techniques employed to perform TDLS measurements are outlined. These include the methods used for general data acquisition, wavelength referencing, baseline fitting as well as several important laser and system characterisation procedures.

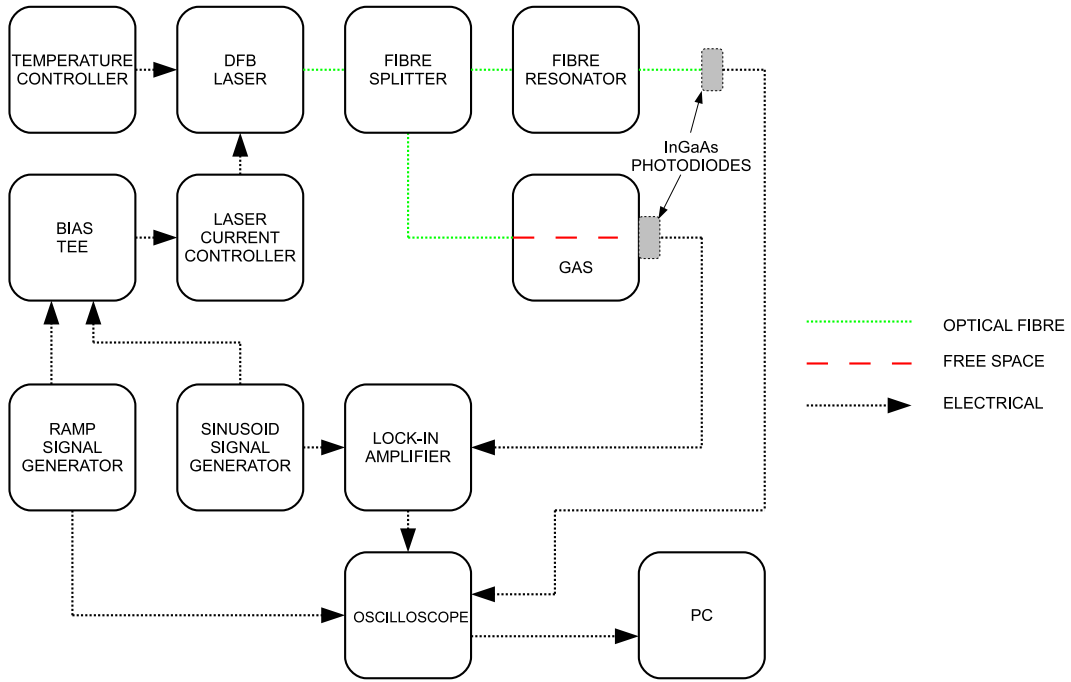


Figure 4.1: A schematic of a typical tunable diode laser spectroscopy system, from which most of the experimental systems used in this work are derived. For direct detection the lock-in amplifier, sinusoidal signal generator and bias tee can be omitted. A balanced detection system requires an additional InGaAs photodiode and fibre connection from the fibre splitter and typically an additional coaxial output to the data acquisition. The Tektronix oscilloscope is sometimes replaced by the National Instruments multifunction DAQ board.

## 4.2 In-Line Gas Cell

A significant body of work undertaken previously by colleagues at the University of Strathclyde had examined the methane R-branch combination line at 1650.956 nm ( $6057.10 \text{ cm}^{-1}$ ). This line had been used in the early investigations into the RAM-based line shape recovery techniques upon which the work in Chapter 5 builds, as well as for the demonstration of optical RAM-nulling [9, 32, 75–78, 107–110]. As the absorption feature and the laser diode were well known and characterised, it was logical to continue using this feature for continuity and to evaluate the effect of the improvements. A 10 mW OKI DFB laser (model OL6109L-10B) with butterfly package and single-mode fibre

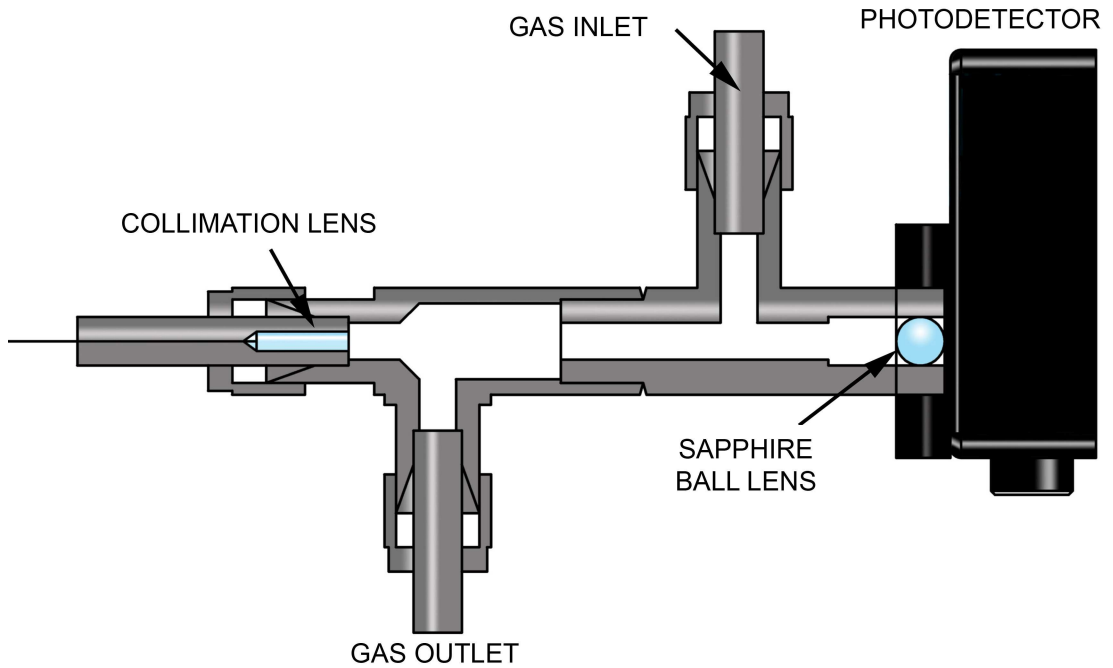


Figure 4.2: Diagram of the in-line gas cell used for the methane experiments.

pigtail was used and the output was transmitted using single-mode fibre patch cords. Angled physical contact FC connectors (FC-APC) were used throughout the setup, for compatibility with various standard fibre components. All the lasers used throughout this work were driven by Thorlabs LDC210 laser diode controllers with Thorlabs TED200C low-noise thermoelectric temperature controllers (TECs).

The work done in Chapter 5 is based on the recovery of methane spectra for use in process control applications. In contrast to the later studies with ambient water vapour, the methane measurements require a sealed gas cell with effective gas extraction to prevent exposure of the potentially explosive methane mixtures to hazardous environments and also to maintain the certified gas mixtures used. The most important requirement was that the detection electronics were isolated from the gas mixtures, which meant that after passing through the gas the beam was either coupled into fibre to a remote detector or transmitted through a sealed window or lens to a local detector. The in-line gas cell shown in Fig. 4.2 was originally designed for monitoring methane levels in the steam reformer of a solid-oxide fuel cell. It was created using Swagelok fittings

so that it could be integrated directly into the fuel cell pipework. A single-mode fibre-coupled focussing graded index (GRIN) lens and a focussing ball lens were sealed into either end of the single pass cell body, which gave an absorbing path length of 6.35 cm. The signals were collected with a Thorlabs PDA10CS InGaAs photodiode.

### 4.3 Free-Space Layout

In contrast to measurements of hazardous methane mixtures, the studies performed on atmospheric water vapour had no need for sealed, low volume gas cells. The laboratory sensors that were constructed needed only to simulate the optical hardware that would be mounted across an aero engine intake bellmouth. This could be achieved using breadboard-mounted free-space optics, where different absorption path lengths could be readily tested up to the limits imposed by the breadboard area. For measurements of ambient water vapour performed with the free space layout, two 20 mW NEL DFB laser diodes were used, namely the NLK1E5GAAA and NLK1B5AAA type diodes at 1430 nm ( $6994\text{ cm}^{-1}$ ) and 1350 nm ( $7402\text{ cm}^{-1}$ ) respectively. The wavelengths for these two lasers were chosen on the basis of the line selection criteria outlined in Chapter 7. The 20 mW version of these diodes were chosen over the 10 mW version to increase the current tuning capability and therefore the potential wavelength coverage and scan range of the laser.

Initial work used an FC-receptacled collimator to couple from single-mode fibre into a collimated free space beam which was eventually incident upon a 1mm large area InGaAs photodiode, with plane mirrors being used to fold the beam if longer path lengths (up to 3.5 m) were required. This layout was satisfactory for basic benchtop measurements, however it proved susceptible to the common vibrations experienced in the laboratory. An even greater problem was the effect of temperature on component alignment when the temperature of the free-space setup was cycled within the environmental chamber, where even small thermal changes could change the beam position and deteriorate the signal. Figs. 4.3

to 4.6 show four possible beam collection schemes. The first shows the original detection method with a collimated beam incident on large area photodiode of approximately the same size. The second collection scheme uses a concave mirror to focus the collimated beam down to a beam waist in the plane of the diode which is smaller than the diode. The third diagram shows a normal collimated beam incident upon a diffuser in front of the diode, which will lead to a large and spatially incoherent beam at the diode. The fourth uses a focussing collimator to create a beam waist and therefore a beam diameter in the plane of the photodiode which is much larger than the diode active area.

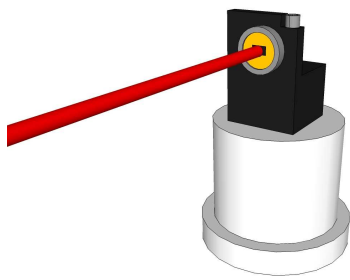


Figure 4.3: beam size  $\approx$  diode size

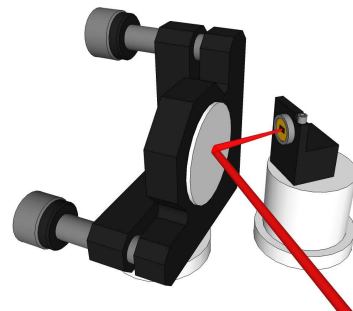


Figure 4.4: beam size  $<$  diode size

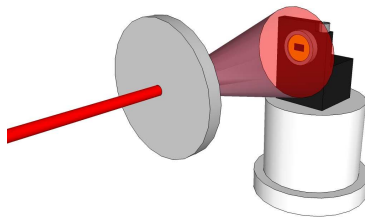


Figure 4.5: beam size  $\gg$  diode size

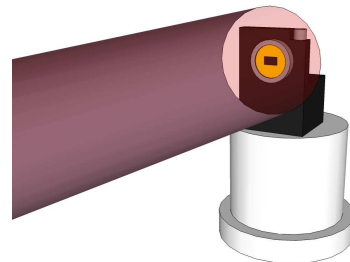


Figure 4.6: beam size  $\gg$  diode size

Preliminary tests indicated that the most flexible and stable collection setup was the one illustrated in Fig. 4.4, where the beam was focussed down to a waist that was significantly smaller than the diode active area. This layout was extremely insensitive to vibrations and most significantly to beam steering caused by thermal changes in the optical hardware. A similar scheme was used for the aero engine exhaust measurement campaign described in Section 8.2. The expanded beam method shown in Fig. 4.6 also performed well in terms

of mechanical stability, as long as the transverse mode structure of the beam approximated to a sufficiently uniform power distribution. This method did suffer from noise due to laser speckle, as the signal recovered by the photodiode would spike when the random intensity jumps from interfering wavefronts happen to coincide with the detector. This phenomenon could be partially mitigated by increasing the signal averaging employed in the data acquisition but the focussed beam method was still preferred as it did not suffer from this and was more flexible in terms of beam path and optical components.

### 4.3.1 Environmental Chamber

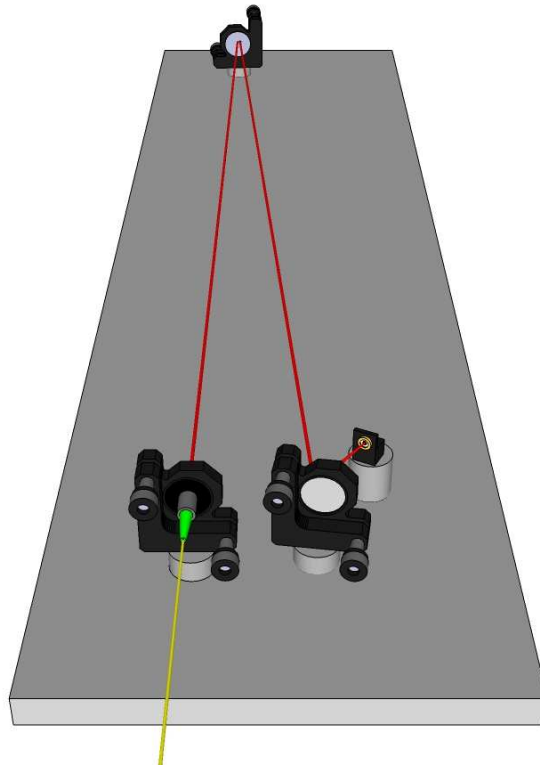


Figure 4.7: Breadboard-mounted free space optical layout.

The study into intake gas temperature determination using ambient water vapour required the path length flexibility of the breadboard mounted free-space optics, illustrated in Fig. 4.7, but also temperature control of the large volume of gas that was to be interrogated and the easiest way to achieve this was to place the breadboard into an environmental chamber. The environmental chamber was a

Thermotron SM32C model with a volume of  $0.9\text{ m}^3$  and temperature and humidity ranges of  $-68$  to  $+177^\circ\text{C}$  and 10 to 98% respectively. The temperature control worked well over the required operation range of 0 to  $40^\circ\text{C}$  but the humidity control was no longer as reliable as the technical specifications indicated. The ambient water concentration is an unknown parameter for the purposes of any fitting procedure and therefore this was not a major problem as long as the concentration was observed to be within acceptable limits, for instance avoiding lock-in amplifier overload. The other consideration when using this type of free space absorption layout was the uniformity of gas temperature over all regions of the beam path. It was necessary to assume that after a given time, typically 1 hour, the gas temperature has had sufficient time to reach a state of uniformity across the whole chamber volume. This was obviously important when gleaning temperature information from spectra from absorption across the whole path and also for comparing to the temperature reference provided by an Omega Pt100 resistance temperature device (RTD) probe positioned in the middle of the breadboard.

## 4.4 Data Acquisition

The data presented in this work was collected using two different data acquisition methods. The first method recorded signal traces directly from a GPIB-interfaced oscilloscope whilst the second used a PCI-interfaced multifunction data acquisition board to perform analogue-to-digital conversion. The oscilloscopes used were Tektronix TDS3014C model with 9 bit resolution and four channel sampling up to  $1.25\text{ GS/s/ch}$ . These oscilloscopes were used in conjunction with Agilent 33250A function generators to provide the required laser drive modulation and signal syncing. The multifunction data acquisition board was a National Instruments PCI6120 DAQ with 16 bit vertical resolution, including two analogue outputs and four analogue inputs with sampling up to  $1\text{ MS/s/ch}$ . For both systems, a LabVIEW virtual instrument was used to control and acquire all the data. The multifunction data acquisition board offered the advantage of

greater flexibility for real-time data monitoring, which was important for the temperature measurements described in Chapter 7. These virtual instruments included MathScript nodes that could perform basic signal processing tasks in real-time for temperature determination or wavelength referencing based on modified MATLAB scripts.

A number of wavelength modulation experiments are presented in this work, particularly in Chapters 5 and 7. The absolute absorption line shape recovery was performed with a Signal Recovery SR7280 high-bandwidth digital lock-in amplifier whilst the temperature measurements and aero engine test data were taken with a Stanford Research Systems SRS830 lock-in amplifier. In these cases the primary analogue-to-digital conversion was performed by the lock-in amplifier before the lock-in outputs were recorded by the relevant DAQ setup.

## 4.5 Wavelength Referencing

The recovery of accurate absorption spectra depends on the ability to record changes in relative transmission as the laser is swept across the absorption feature and also to assign a wavelength scale to the time base of the recovered signals. The principle of using a portion of the laser signal to observe the output of the transmission through an etalon or resonator is widely used in tunable diode laser spectroscopy [62, 107]. In this work, a method of wavelength referencing was used that derived a relative frequency scale from the output of a fibre-ring resonator. The use of a relative frequency scale was in contrast to some recent efforts in high specification spectroscopy experiments where an optical frequency comb has been used to map a high precision absolute frequency scale onto the absorption signal time index [111]. The advantages of using a fibre-based system rather than an etalon or frequency comb in practical applications were the low cost and robust nature of such systems. The relative frequency scale provided by the resonator output was applied to the absorption signal by noting the index position of an absorption peak line centre. The absolute frequency of the line centre position was assumed to correspond to the line centre frequency provided by the HITRAN

database. From this one index point all the other time index values could then be assigned a frequency by mapping the frequency difference from the line centre point.

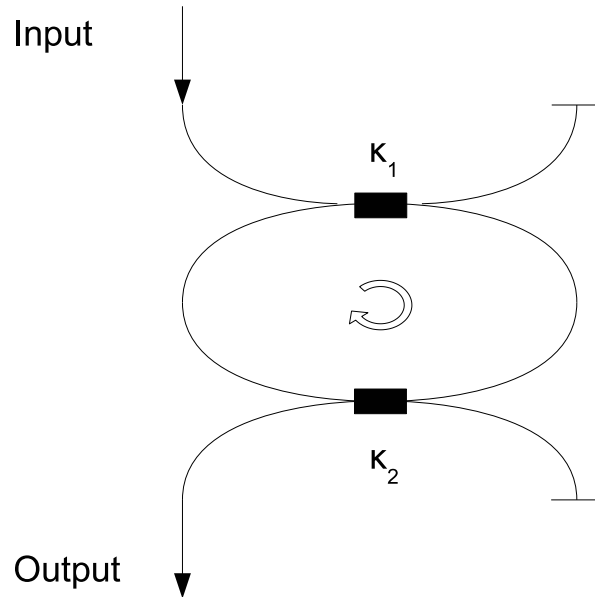


Figure 4.8: Schematic of two-coupler fibre ring resonator layout

The fibre ring resonator used was based on the two-coupler design described by Urquhart [112–114], shown in Fig. 4.8 and built by Duffin and colleagues [34, 35]. The modulated laser signal is fed into coupler 1 which couples a portion of the incident power into the ring and the rest is dumped into the redundant fibre arm. The power circulating in the ring is then transmitted through coupler 2 which has the same coupling coefficient as coupler 1 but this time one output is fed back to coupler 1 and the other is recorded by a photodiode. As the laser signal is ramped in frequency the resonator response periodically satisfies a phase matching condition in which the signal circulating in the ring interferes constructively with the incoming signal and a transmission peak is observed at the output. The two couplers used here were chosen to have coupling coefficients  $\kappa_1$  and  $\kappa_2$ , of 40%, chosen so that the split ratio gave a good compromise between finesse and fringe line width based on the theoretical framework described by Urquhart. The fibre ring created by the two couplers was about 47 cm in length, which ultimately gave a free spectral range of 0.4275 GHz according to initial

tests performed by the makers of the resonator [34].

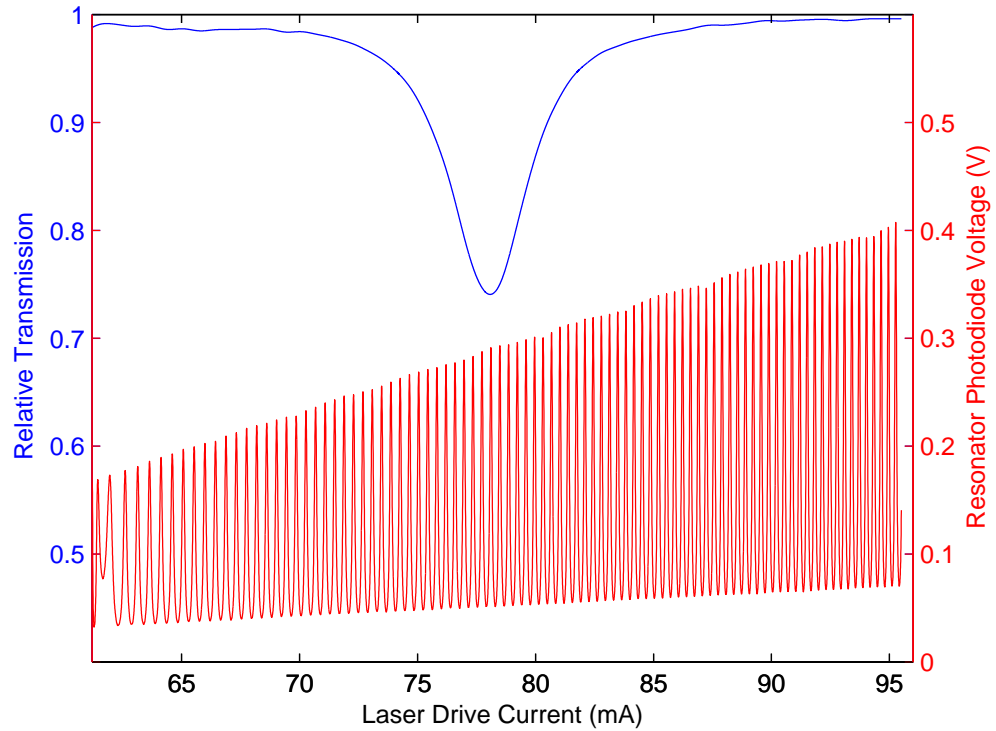


Figure 4.9: Fibre ring resonator output plotted against  $\text{CH}_4$  absorption signal at  $1650 \text{ nm}$  ( $6060 \text{ cm}^{-1}$ )

The peaks were recorded by a reference photodiode, ideally simultaneously to the gas absorption signal acquisition as shown in Fig. 4.9 and the time index position of each peak was identified. It was often necessary to perform some filtering on the recovered signal to remove any noise from the resonator output, as spurious noise peaks often showed up as resonator peaks and distorted the frequency scale. The spacing in frequency terms between successive resonator peaks was determined by the free spectral range (FSR) of the resonator yet the gaps between the time index position of the successive resonator peaks changes across the sweep, which was what could be expected from the nonlinear relation between laser diode current and output frequency that is typical of DFB lasers. The next stage in the wavelength referencing process was to find the peak that was closest in position to the absorption line centre as this was the reference point from which an absolute frequency scale was mapped onto the relative frequency

scale. This relative scale was created by setting the line centre index as a zero and then extrapolating a polynomial fit based on the other peak positions across the whole time index. The line centre was assumed to be known from surveying the HITRAN database and a fully wavelength referenced time base was then extracted. A generalised MATLAB program is provided in Appendix B, which gives an example of how the wavelength referencing procedure was implemented in practice.

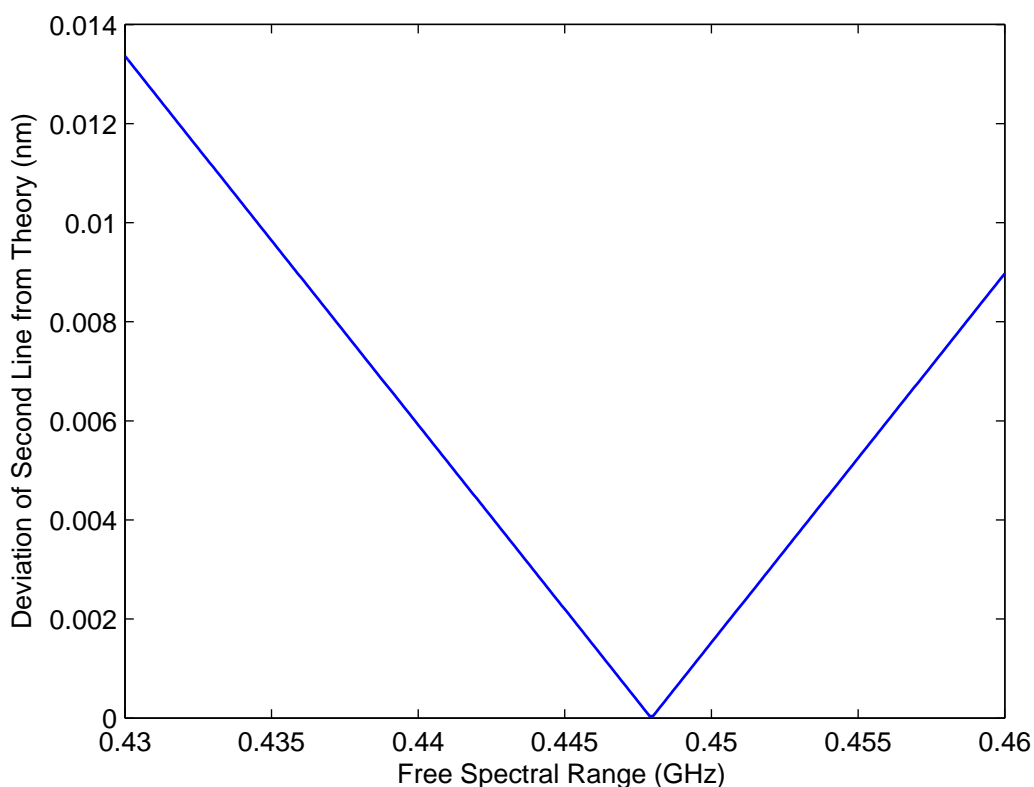


Figure 4.10: Comparing the difference in wavelength of the position of the second absorption peak with FSR

In practice care needed to be taken to ensure the best possible frequency scale was recovered and used for gas analysis, as problems arose for a number of reasons. First of all the FSR of the resonator needed to be known accurately. The original method for determining the FSR described by Duffin and McGettrick used an absorption scan over three methane features near 1665nm ( $6006\text{ cm}^{-1}$ ). The line centre frequencies of two of the peaks were identified using HITRAN

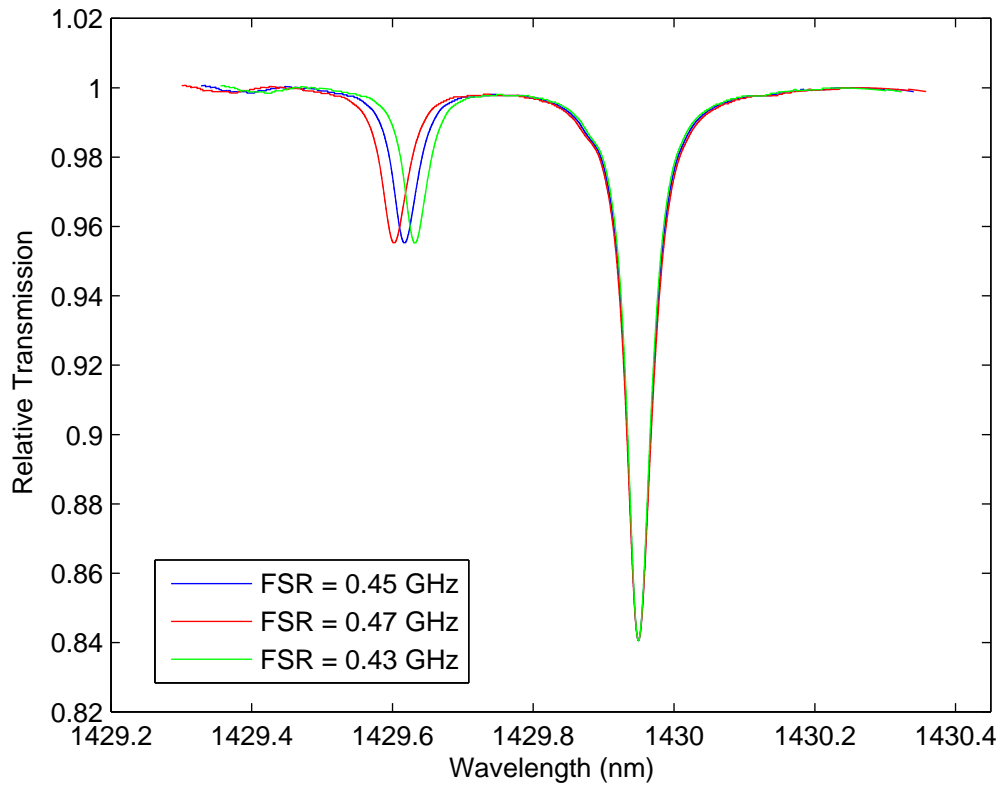


Figure 4.11: The effect of FSR error on the recovered water vapour spectrum. The ideal FSR of 0.448 GHz gives the blue spectrum here and the other two are 0.02 GHz above and below. Note the relatively small effect on the larger peak used as the reference point.

and then the integer number of peaks between these two known frequencies were counted. This characterisation was performed once and then applied to all subsequent data assuming that the FSR was stable, that the effects of temperature were negligible and that the effect of wavelength on the FSR is within the measurement error of the FSR, over the range of 1 - 2  $\mu\text{m}$  ( $5000\text{-}10000\text{ cm}^{-1}$ ). If the target spectrum only recovers one major absorption feature the signal could be wavelength referenced to recover sensible data that shows acceptable agreement with theory yet slight errors due to the referencing procedure would not be immediately obvious. In this study various parts of the water vapour spectrum were recovered which contained two or more major absorption features. If one of these features was selected to be the reference line centre, then the

position of another feature relative to the corresponding point in a theoretical plot was dependent upon the FSR used, if the rest of the wavelength reference procedure was working properly. If the line centre positions from HITRAN were assumed to be correct as before, it was possible to cycle through a range of FSRs to see which value provided the best match between signal and theory, as shown in Fig. 4.10. The errors caused by the FSR could lead to significant mismatch between experimental signals and theoretical models, as illustrated by Fig. 4.11.

In contrast to the one-off FSR determination in the previous work, an extended study of water vapour data recovered at 1430 and 1350 nm (6993 and 7407 cm<sup>-1</sup>) and low pressure methane at 1650 nm (6056 cm<sup>-1</sup>) yielded an FSR value of 0.43 ± 0.02 GHz. This result has implications not only in the accuracy of the wavelength scale applied to the recovered spectra but also to the wavelength characterisation used to calculate modulation indices in wavelength modulation spectroscopy.

The second issue with wavelength referencing occurred when a large wavelength sweep was required and many resonator peaks were recovered. This caused problems when the power variation was significant between the top and bottom of the ramp sweep, as sometimes the filtering of the signal could not be optimised. If the filter parameters were set to remove all the spurious peaks that would lead to false identification of peak positions, then some of the peaks at the top of the sweep would be filtered too strongly. In this situation the filter parameters needed to be changed until the effect was minimised and a variable filter was sometimes needed to provide reliable spectral information. If this problem occurs an alternative solution could be to build a series of resonators with increasing ring lengths to give a decreasing range of free spectral ranges, as in (4.1), which could be used effectively over a range of scan amplitudes. In this equation  $c$  is the speed of light,  $L$  is the fibre ring length and  $n_e$  is the effective index of the single mode fibre ( $\sim 1.45$ ).

$$FSR = \frac{c}{n_e L} \quad (4.1)$$

## 4.6 Baseline Methods

The other key process required to recover absolute absorption line shapes, after wavelength referencing, is normalisation with a baseline signal to give relative transmission. In most cases the baseline signal represents the signal that would be recovered in the absence of the target species. This can be recorded relatively easily in applications that allow gas cells, which can be evacuated or purged in a two-step acquisition process. This method has the advantage of accounting for optical distortions due to etalons and the wavelength dependence of component transmission in the signal path. The signal level will also yield the background level with high accuracy, improving the relative transmission signal and any gas information derived from it. There are however a number of applications that do not allow a ‘no gas’ signal to be taken and baseline data has to be calculated in a different way. Baseline recovery is a major issue in TDLS for aero engine diagnostics because of the free-space paths that are inevitable in these applications. Wiesen was able to use a sampling method to get around this problem at the expense of real-time measurements but in general most researchers adopt baseline fits or use 2f WMS [79]. Baseline fitting identifies non-absorbing regions in the wavelength sweep and uses these to infer a background by fitting a polynomial across the absorbing regions. Identifying isolated absorption features with non-absorbing regions, especially in the complex spectra of water vapour for instance, is a challenge. The contribution of absorbing wings and residual absorption from minor absorption lines is a significant problem that is often the limiting factor in certain TDLS setups.

A good review of automated baseline techniques is given by Schulze et al. identifying potential signal recovery algorithms for different types of spectra [44]. In this work, whenever target species evacuation was not possible, polynomial fitting between non-absorbing regions of a recovered spectrum was used to recover relative transmission. This provided a reasonably robust and repeatable method for assuming the form of a baseline signal. The limitation of the method depends upon the isolation of the recovered spectra. If a spectrum has clean non-absorbing

and interference-free regions either side of the line shape wings then spectral recovery can be acceptable. In heavily interfering or blended high pressure spectra, non-absorbing regions are hard to find, greatly reducing the information from which a fit can be performed.

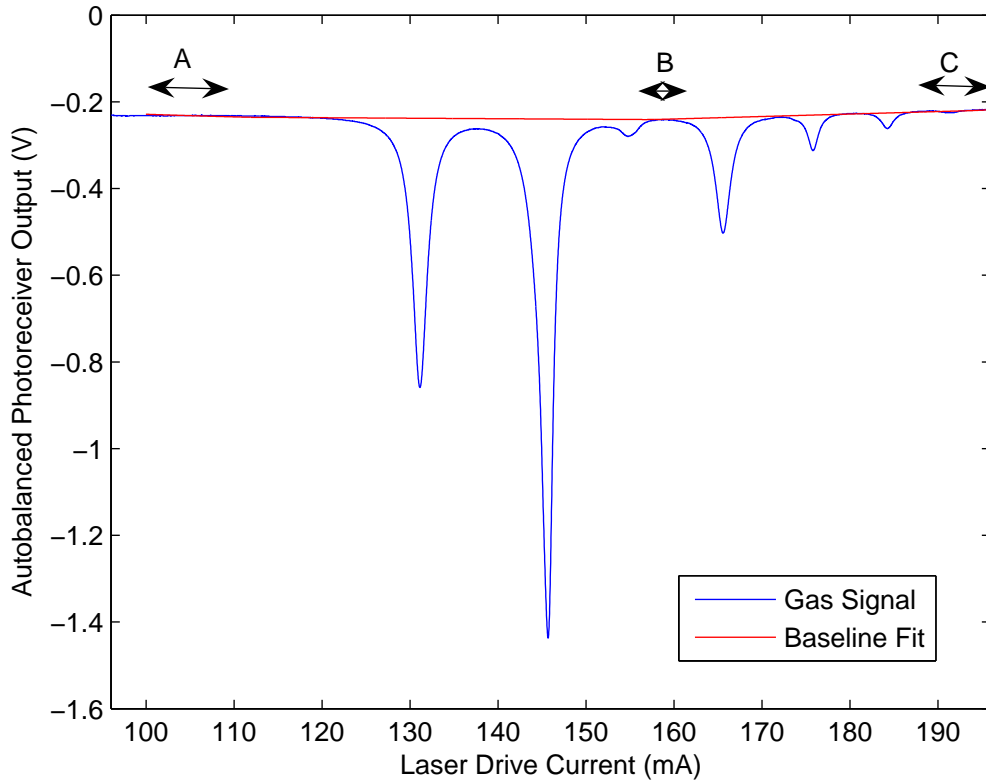


Figure 4.12: An example of a baseline fit recovered from a balanced ratiometric detector. The ‘non-absorbing’ regions marked A, B and C are used to generate a polynomial fit that is extrapolated over the rest of the scan.

Fig. 4.12 shows a polynomial fit over a group of water vapour absorption lines near 1350nm. The ends of the sweep see little absorption but the region in between has a moderately high density of lines. In this case the fit could be performed with just the two regions at the beginning and end of the sweep, A and C. An alternative method might also use the narrow region B in the middle of the sweep, which exhibits a small but significant amount of absorption. In this case the information provided by this region is useful for extracting an accurate polynomial fit but there may be a concentration dependence in this region

that would need to be accounted for. This could be performed by simulating theoretical line shapes over a range of concentrations and estimating from the size of the adjacent peaks, possibly in an iterative process, what concentration range might be expected. For low concentrations, the residual absorbance in region B would be small but for larger concentrations a shift in proportion to the expected concentration may need to be factored in before the final polynomial fit is performed.

## 4.7 Characterisation Techniques

Many tunable diode laser spectroscopy techniques require some knowledge of the the laser operating characteristics and how these relate to the target absorption features. In wavelength modulation spectroscopy in particular it is important to characterise certain parameters prior to any gas measurement to ensure that the correct modulation schemes are used. The laser parameters that are generally of interest are the AM/WM phase shift,  $\psi'$ , the modulation tuning coefficient,  $\frac{\delta\nu}{\delta i}$ , the laser power,  $I_0$  and the linear intensity modulation,  $\Delta I$ . These parameters can vary depending upon laser type, modulation frequency, modulation amplitude and sometimes drive current. Johnstone et al. provide details on several aspects of the system characterisation techniques discussed here and an overview of the relevant methods used in preparation for TDLS measurements is given in the following sections [107].

### 4.7.1 AM/WM Phase Shift

If calibration-free WMS techniques are being used, a key parameter is the phase shift,  $\psi'$ , between the intensity modulation and wavelength modulation. This value will affect how the lock-in amplifier is set up and the total signal size in the RAM method whilst it is a crucial parameter in the phasor decomposition calculation. There are a number of ways to calculate this value. A simple swept current method that makes use of a gas absorption signal compares lock-in amplifier detection phases when the recovered signal exhibits a separated RAM

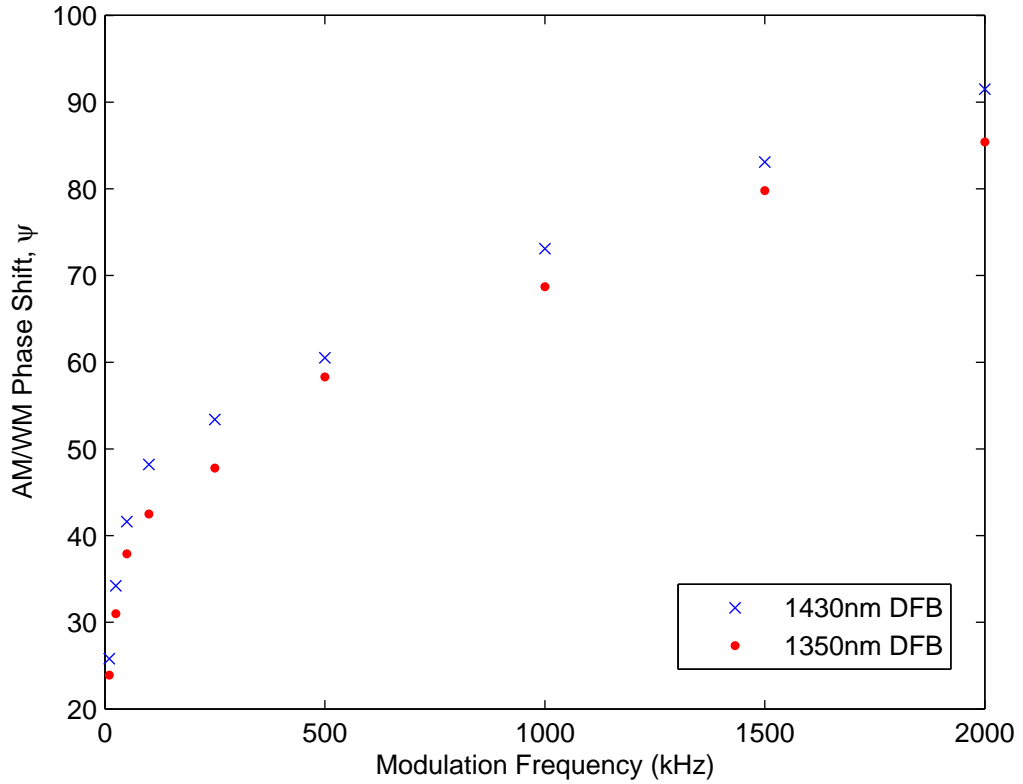


Figure 4.13: The change in AM/WM phase angle with modulation frequency is plotted for the 1350 and 1430 nm DFB lasers.

signal and a separated FM signal. With reference to the simulated signals shown in Chapter 2, this technique would identify the lock in detection phase difference between Figs. 2.8c and 2.8e. The phase angles corresponding to these signals are determined by first of all observing the separated FM signal, which is found by observing the angle at which no RAM background contributes and the non-absorbing wings are sat on a zero background, as in Fig. 2.8e. The next step is to observe the separated RAM point which can be calculated using LabVIEW routine which cycles through a range of detection angles whilst recording the ratio between the peak depth and an offline reference point. The phase angle at which this ratio is minimised corresponds to the separated RAM phase angle, illustrated in Fig. 2.8c. Fig. 4.13 shows the result of this method used to characterise the change in phase shift of two DFB lasers used to detect water vapour, with modulation frequency, up to 2 MHz. This can be relatively easily implemented

although the fixed current ramp will not yield any information about how the phase shift changes with laser drive current. This could cause a problem if the ramp sweep is large and covers numerous absorption lines. In this case it is possible to use a static laser drive current approach with the fibre ring resonator.

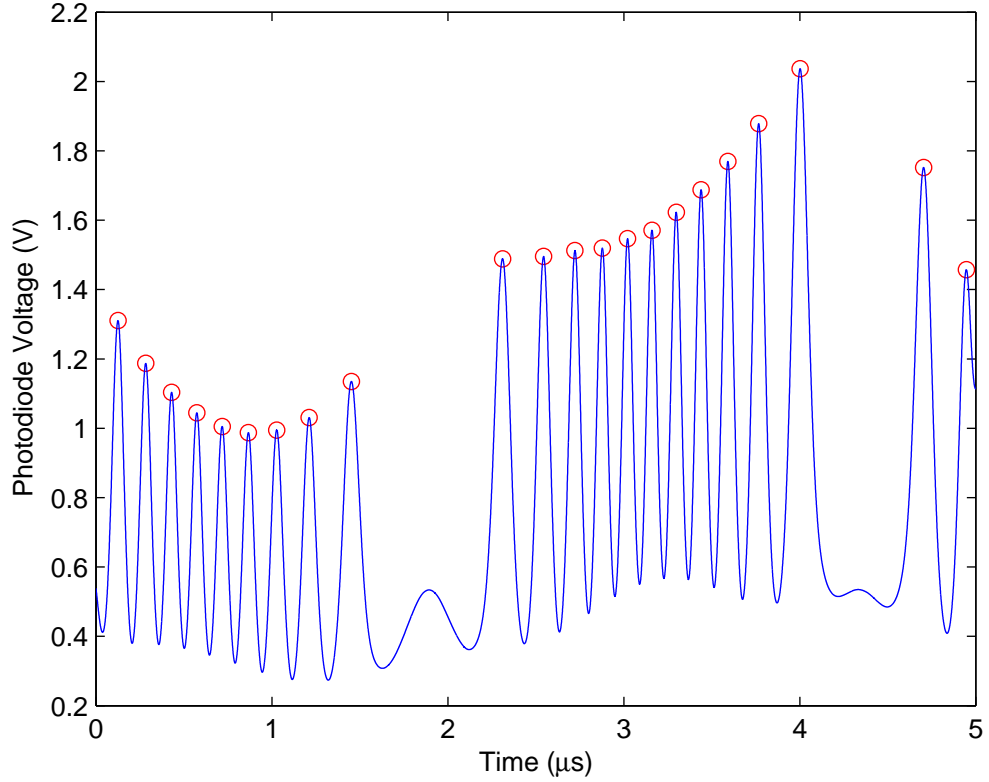


Figure 4.14: The resonator response of the 1430 nm DFB with a modulation frequency of 100kHz and modulation depth of 2000mV. The red circles show the position of the peaks identified for the WM fit.

This technique is based on a method described by Li et al. who examine the response of a resonator when only the sinusoidal modulation dither is applied to the laser [30]. Fig. 4.14 shows the resonator response in this case where the peak positions can be used to infer how fast the frequency is changing across the time index of the modulation cycle. When the frequency change is fitted in the manner shown in Fig. 4.15, the resultant sinusoidal waveform describing the frequency modulation can be compared to the directly observed intensity modulation. The two signals should be slightly offset from one another and the time shift between

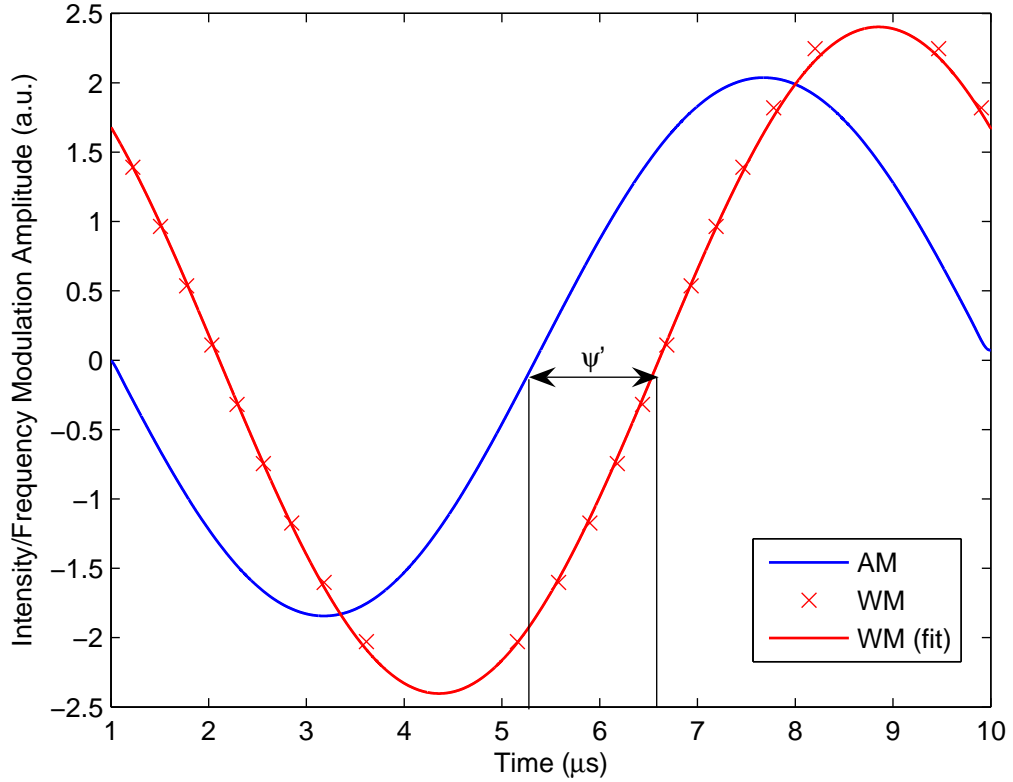


Figure 4.15: The peak positions shown in Fig. 4.14 are used to map out the frequency modulated signal with time and compare with the amplitude modulation signal. The phase difference,  $\psi' = 47.1^\circ$  is shown corresponding to the respective zero crossings.

the two relative to the cycle time gives the AM/WM phase angle under those conditions, which in this example was  $\psi' = 47.1^\circ$ .

A third method for determining the AM/WM phase shift uses the phasor approach of the PD method introduced in Section 2.4.2 [35]. The method identifies the 1f peak positions in a low-m absorption signal and a reinterpretation of Fig. 2.10 is shown in Fig. 4.16, outlining the trigonometric route to the extraction of  $\psi'$  from an absorption signal. The output from LIA Channel 2 is aligned to remove any projection of the RAM signal, by ensuring that a separated FM signal is observed with zero background in the non-absorbing regions. The index values of the peak positions are identified and the peak values at these points are recorded as  $y_1$  and  $y_2$ . The requirement here is that the signal values

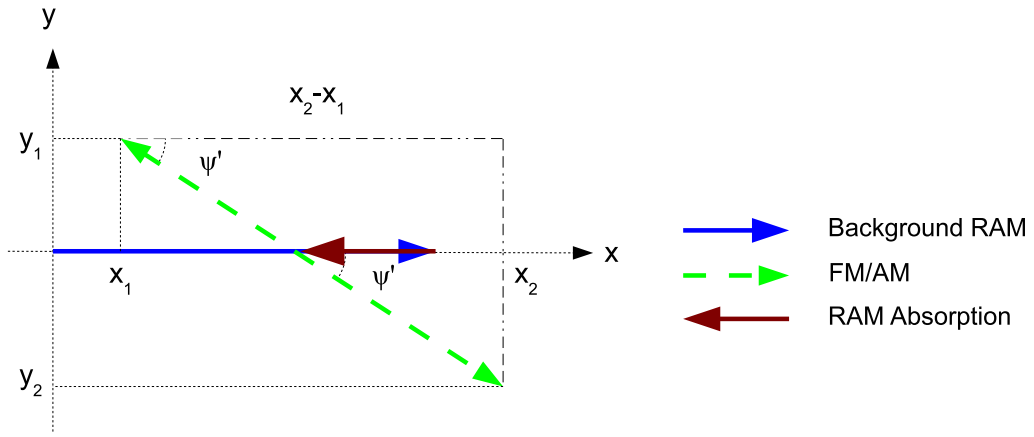


Figure 4.16: A phasor representation illustrating how  $\psi'$  is calculated in quasi-real time in the PD method

are recovered at two index points that are symmetrical about line centre so an alternative method could identify the zero crossing at line centre and then choose two points of equal time index difference either side of this point. The background RAM signal is recovered from the LIA Channel 1 and the signal values at the same index positions as the peaks on the other channel are recorded to give  $x_1$  and  $x_2$ . The value of  $\psi'$  is calculated using (4.2):

$$\psi' = \tan^{-1} \frac{|y_1| + |y_2|}{x_2 - x_1} \quad (4.2)$$

This process is most often used when implementing the PD method as it allows a characterisation of  $\psi'$  in real time based on the experimental conditions. In Chapter 5, a modification of this method is described that will enable it to be used at higher modulation indices.

### 4.7.2 Tuning Coefficient

A well-designed wavelength modulation spectroscopy system should make use of knowledge of the tuning properties of the laser diode. The tuning coefficient,  $\frac{\delta\nu}{\delta i}$  [GHz/mA], gives the amplitude change in laser centre frequency with modulation current and can be used to calculate the operational modulation index for a given or assumed absorption half-width. The modulation index in a practical situation

is given by:

$$m = \frac{\Delta V}{2} \frac{\delta i}{\delta V} \frac{\delta \nu}{\delta i} \frac{1}{\gamma} = \frac{\delta \nu}{\gamma} \quad (4.3)$$

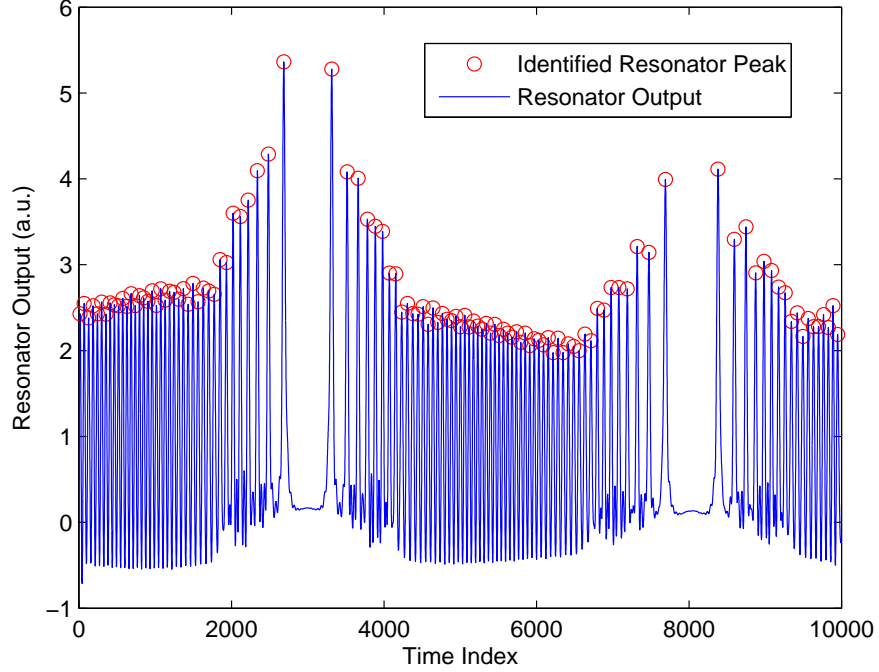


Figure 4.17: The resonator output response as the laser output is swept over one sinusoidal dither cycle. The total peak to peak frequency change is calculated using the total number of peaks between the points of inflexion in the modulation at time indices of 3000 and 8000.

The modulation coefficient of the laser driver  $\frac{\delta i}{\delta V}$ , could be used to convert  $\Delta V$ , the applied peak-to-peak voltage dither to  $\delta i$ , the effective current dither amplitude used in (4.3). If the modulation was applied directly to the Thorlabs LDC210 current controller using the multifunction DAQ board, this modulation coefficient was 100 mA/V (up to the bandwidth limit of 100 kHz). If however the high frequency modulation was created by an external signal generator and added to the ramp with the bias tee circuit, then  $\delta i$  was obtained by dividing  $\Delta V$  by 100.

In order to calculate the  $\frac{\delta \nu}{\delta i}$  term in (4.3) the same resonator-based approach to calculate the AM/WM phase shift was used. The slow ramp was turned off and the resonator response to the dither modulation alone was observed over the

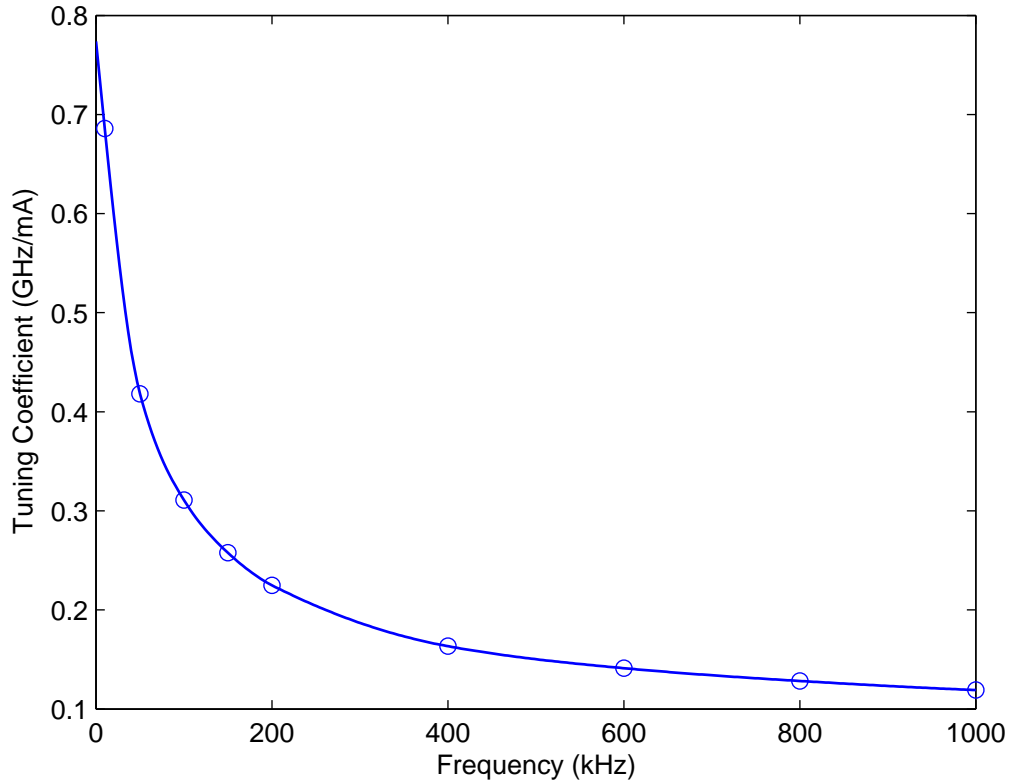


Figure 4.18: The dependence of tuning coefficient on modulation frequency for a typical DFB laser

time period of the sinusoid. In Fig. 4.14 the peak positions were used to map the change in frequency to recover the WM signal, however to calculate the tuning coefficient it was the number of peaks and therefore number of consecutive free spectral ranges that was important. For this reason a large number of peaks, as in Fig. 4.17, was beneficial as there was some error associated with setting the modulation depth so that there was an integer number of peaks between the points of inflexion in the WM, at  $\sim 3000$  and  $\sim 8000$  on the time index of the figure. The 57 peaks in this example showed that the peak to peak frequency sweep due to the sinusoidal dither was 57 times the FSR and the applied peak-to-peak voltage was known so the frequency change relative to current change was easily calculated. The tuning coefficient dropped off with increasing modulation frequency as shown in Fig. 4.18 but showed negligible dependence on modulation depth [30].

## 4.8 TDLS in Harsh Environments

The experimental setups described in the previous sections have all been laboratory based systems, where noise conditions are generally favourable or can be easily mitigated. The aero engine-based environments of interest to this project are some of the harshest environments in which optical systems can be installed. Aero engines are inherently noisy, with extremely large mechanical vibrations arising from several resonances associated with moving parts within the aero engine. Airflow in aero engine test cells was seen to be significant and buffeting also created vibrational resonances on anything mounted near air flows. Prolonged exposure to vibrations of this level often led to mounts and bulk optical elements becoming detached, as grub screws and other mounting mechanisms worked their way loose. Measurements of combustion areas or exhaust flows had to deal with significant amounts of hot gases, which could be  $>1000\text{K}$  and containing soot-based particulates and unburnt hydrocarbons that had a tendency to cover optics positioned near the flow. In the aero engine test campaigns undertaken during this project, a fibre delivery system was used to deliver the laser signal from a central control room to the engine, so that drive electronics and signal sources could be situated remotely. Signal collection was however performed in situ with detection electronics being positioned at or near the aero engine. Whilst the fibres used for delivery were obviously immune to electromagnetic interference from the engine and test cell systems, the coaxial cabling used for signal recovery was inevitably susceptible to interference.

In Chapter 8 detailed descriptions are given of the various experimental setups installed in the field over the course of the project. These included the preliminary test on a small turbojet intake at Ansty, the detuner-mounted tests on high bypass turbofan engines at East Rogerton and the hot exhaust measurements on the Environmentally Friendly Engine (EFE) at Bristol.

# Chapter 5

## Absolute Line Shape Recovery at High Modulation Indices

### 5.1 Introduction

In wavelength modulation spectroscopy an important determinant of overall sensitivity is the modulation depth, which should be set to the optimum value for a given experimental absorption half-width. In conventional WMS systems harmonic detection is most often performed at the modulation index where the frequency modulated signals are at a maximum. For the first four harmonics the modulation indices at which the purely frequency modulated signals are maximal are  $m = 2.00$ ,  $m = 2.20$ ,  $m = 3.59$  and  $m = 4.12$  [67]. The RAM-based techniques introduced in detail in Chapter 2, exhibit no such optimum modulation index as the relative signal size,  $S_{RAM}$ , increases monotonically with modulation index as in Fig. 5.1 based on the last two terms of (5.1):

$$\begin{aligned} S_{RAM} &= \Delta I_0 \frac{A}{\pi} \int_0^\pi \frac{1 - \cos(2\theta)}{1 + m^2 \cos^2(\theta)} d\theta \\ &= A \left[ \frac{\kappa\gamma}{\xi(\omega)} \right] \frac{m}{\pi} \int_0^\pi \frac{1 - \cos(2\theta)}{1 + m^2 \cos^2(\theta)} d\theta \end{aligned} \quad (5.1)$$

where  $A = \alpha_0 Cl$  is the line centre absorbance,  $\xi(\omega)$  is used to represent the

current tuning coefficient,  $\kappa$  is the amplitude modulation coefficient.

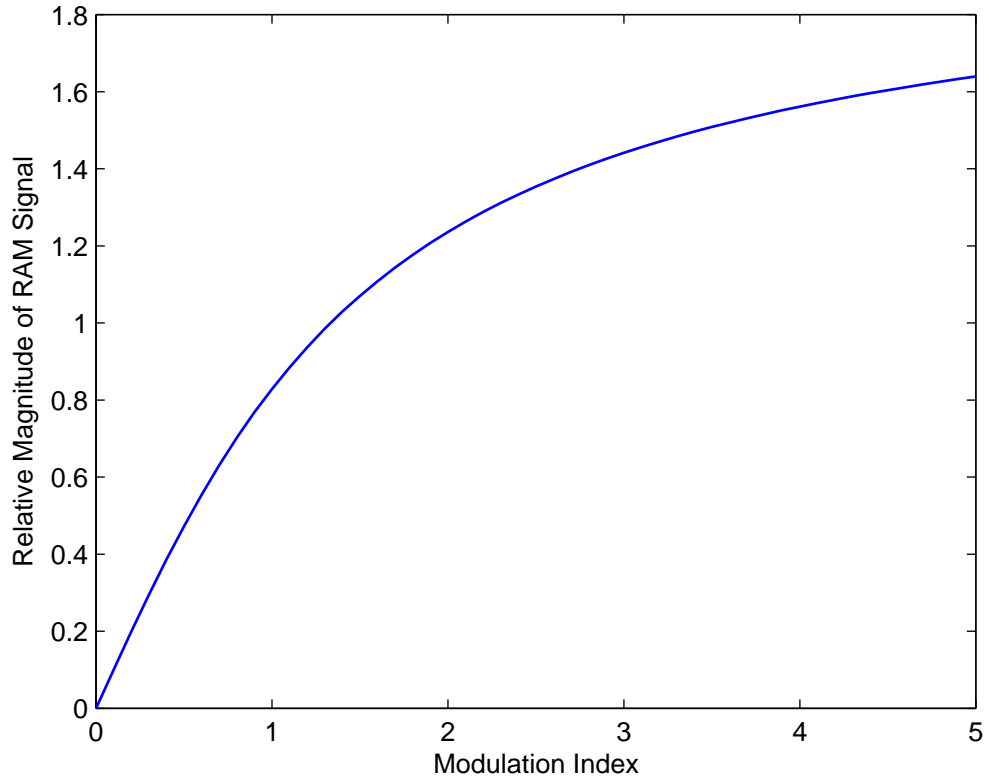


Figure 5.1: The relative magnitude of the RAM signal as a function of modulation index, from (5.1).

There is however a trade off to be made when attempting to maximise the sensitivity of the technique. For a fixed modulation index the magnitude of the RAM signal will increase with modulation frequency, so one option is to use a fast current dither and high-bandwidth demodulation hardware to extract the signals. The use of high-bandwidth lock-in amplifiers or data acquisition hardware, with fast enough sampling to extract effective signals above a megahertz, complicates the laser drive modulation procedure, increases the difficulty of laser characterisation and is more expensive. An alternative method for increasing overall sensitivity is to fix the maximum modulation frequency, in this case to 100 kHz which is the bandwidth limit of the lock-in amplifier and the laser drivers used, and to increase the modulation index.

The process of increasing the modulation index is not a straightforward

one. In the limit of small modulation indices where  $m < 0.1$ , the recovered absolute line shape from the RAM is a good approximation of the actual line shape and therefore can be used directly in a fitting procedure to extract gas information. It is desirable however to operate at a modulation index of  $m = 1$  or higher, where the size of the 1f RAM absorption signal is comparable to other WMS techniques [110, 115]. In Section 2.4.3 the idea of distortions at higher modulation indices was introduced. Previous work had crudely established an approximate modulation index and applied a correction function to the distorted line shape in order to recover the true line shape, up to a maximum modulation index of only  $m = 0.75$  which limited the achievable signal size.

In this chapter an alternative derivation of the correction function is introduced, which in principle will allow absolute absorption line shapes to be recovered at any achievable modulation index. This alternative correction function, formulated by Stewart et al. and described in detail in the following section, is based upon a Fourier series expansion of the absorption coefficient, rather than the Taylor series expansion exploited in (2.5) [116, 117]. The implementation of line shape recovery at elevated modulation indices is discussed including two methods for extracting the experimental modulation index from the recovered signals and an experimental validation of the technique is presented [115, 116].

## 5.2 Mathematical Description of Correction Function

In Chapter 2, the absorption coefficient  $\alpha(\nu)$  was introduced in the context of the Beer-Lambert law for optical transmission. This term can be described as the product of the absorption coefficient at line centre and the line shape function using  $\alpha(\nu) = \alpha_0 f(\nu)$ . In this case the absorption coefficient at line centre,  $\alpha_0$ , is a function of the molecular density at standard temperature and pressure (STP),  $S$ , the line strength in standard units of  $[\text{cm}^2/(\text{molecule}^{-1}\text{-cm}^{-1})]$  and  $\gamma$ , the HWHM:

$$\alpha_0 = \frac{N_0 S}{\pi \gamma} \quad (5.2)$$

Making the assumptions of low absorbance so that  $\alpha(\nu)Cl \ll 1$ , where the linear approximation can be made to the Beer-Lambert law and a Lorentzian line shape for a pressure broadened line, then the  $f(\nu)$  term in the absorption coefficient becomes  $f(\nu) = [1 + \Delta_\nu^2]^{-1}$  where  $\Delta_\nu$  is the same as in (2.16). It is helpful to consider the instantaneous laser frequency resulting from the sinusoidal dither modulation in angular terms so that:

$$\nu = \nu_1 + \delta\nu \cos(\omega t - \psi) = \nu_1 + \delta\nu \cos(\theta) \quad (5.3)$$

The absorption coefficient now becomes  $\alpha(\nu_1) = \alpha_0 f(\theta)$  with the line shape function for a Lorentzian being given by  $f(\theta) = [1 + (\Delta_\nu + m \cos \theta)^2]^{-1}$ .

In Section 2.3.4 the absorption coefficient was expanded using a Taylor series to recover expressions for the harmonics of the output signal. In this analysis a Fourier series expansion of the absorption coefficient at the harmonics of the modulation frequency, give  $f(\theta)$  as:

$$f(\theta) = a_0 + \sum_{n=1}^{\infty} a_n \cos(n\theta) = a_0 + \sum_{n=1}^{\infty} a_n \cos(n\omega t - n\psi) \quad (5.4)$$

where

$$\begin{aligned} a_0 &= \frac{1}{\pi} \int_0^\pi f(\theta) d\theta \\ &= \frac{1}{\pi} \int_0^\pi \frac{1}{1 + (\Delta_\nu + m \cos \theta)^2} d\theta \end{aligned} \quad (5.5)$$

$$\begin{aligned} a_n &= \frac{2}{\pi} \int_0^\pi f(\theta) \cos(n\theta) d\theta \\ &= \frac{2}{\pi} \int_0^\pi \frac{\cos(n\theta)}{1 + (\Delta_\nu + m \cos \theta)^2} d\theta \end{aligned} \quad (5.6)$$

Collecting these terms for  $f(\theta)$  back into the absorption coefficient and substituting into (2.4) gives an output intensity of:

$$I_{out} = [I(\nu_1) + \Delta I(\nu_1) \cos(\omega t)] \left[ 1 - \alpha_0 Cl \left\{ a_0 + \sum_{n=1}^{\infty} a_n \cos(n\omega t - n\psi) \right\} \right] \quad (5.7)$$

This output intensity can be expanded to explicitly state the individual components at each harmonic, which can be subsequently isolated at specific detection harmonics with a lock-in amplifier. The line centre absorbance is denoted here by  $A = \alpha_0 Cl$ .

$$\begin{aligned} I_{out} = & [I(\nu_1) + \Delta I(\nu_1) \cos(\omega t)] \\ & - Aa_0(\nu_1)[I(\nu_1) + \Delta I(\nu_1) \cos(\omega t)] \\ & - Aa_1(\nu_1)[I(\nu_1) + \Delta I(\nu_1) \cos(\omega t)] \cos(\omega t - \psi) \\ & - Aa_2(\nu_1)[I(\nu_1) + \Delta I(\nu_1) \cos(\omega t)] \cos(2\omega t - 2\psi) \\ & - Aa_3(\nu_1)[I(\nu_1) + \Delta I(\nu_1) \cos(\omega t)] \cos(3\omega t - 3\psi) - \dots \end{aligned} \quad (5.8)$$

The signal components of the output in (5.8) can be attributed to the physical signals identified in Section 2.3 in which wavelength modulation was introduced. First of all there exists a series of components at a frequency of  $n\omega$  with a phase of  $-n\psi$  which are proportional to the  $n^{\text{th}}$  Fourier coefficient. These components take the form  $-Aa_n(\nu_1)I(\nu_1) \cos(n\omega t - n\psi)$  and represent the purely frequency modulated components which, as mentioned previously, are equivalent to the line shape derivatives for small values of  $m$ . The simultaneous amplitude modulation, that inevitably accompanies the derivative signals in any current modulated diode laser system, creates additional signal components that must be considered. In a similar analysis to that performed on (2.7), a background RAM signal can be identified which is of the form:  $\Delta I(\nu_1) \cos(\omega t)$ . There is also an absorption-dependent RAM signal which is the target signal in the calibration-free method used here and is proportional to the Fourier coefficient,  $a_0(\nu_1)$ :  $-Aa_0(\nu_1)\Delta I(\nu_1) \cos(\omega t)$ . In addition to this there is also the amplitude modulated component of the derivative signals, which have the form  $-Aa_n(\nu_1)[\Delta I(\nu_1) \cos(\omega t)] \cos(n\omega t - n\psi)$ . Using the trigonometric identity

$\cos(A)\cos(B) = \frac{1}{2}[\cos(A - B) + \cos(A + B)]$ , the resulting substitution yields contributions to the  $n^{\text{th}}$  derivative signal at  $(n \pm 1)\omega$  with phase  $-n\psi$  ultimately giving the series of terms:  $-Aa_n(\nu_1)\Delta I(\nu_1)\frac{1}{2}\{\cos((n+1)\omega t - n\psi) + \cos((n-1)\omega t - n\psi)\}$

The use of phase sensitive detection with a lock-in amplifier allows the contributions to (5.8) at different harmonics of the modulation frequency  $\omega$  to be extracted. The DC output ( $n = 0$ ) is:

$$I_{DC} = I(\nu_1)[1 - Aa_0(\nu_1)] - \frac{A}{2}a_1(\nu_1)\Delta I(\nu_1)\cos\psi \quad (5.9)$$

Whilst the 1<sup>st</sup> harmonic component ( $n = 1$ ) with demodulation at the dither frequency,  $\omega$ , is:

$$I_\omega = \Delta I(\nu_1)\cos(\omega t) - A\left[a_0(\nu_1)\Delta I(\nu_1)\cos(\omega t) + a_1(\nu_1)I(\nu_1)\cos(\omega t - \psi) + \frac{1}{2}a_2(\nu_1)\cos(\omega t - 2\psi)\right] \quad (5.10)$$

The 2<sup>nd</sup> harmonic component ( $n = 2$ ) is:

$$I_{2\omega} = -A\left[\frac{1}{2}a_1(\nu_1)\Delta I(\nu_1)\cos(2\omega t - \psi) + a_2(\nu_1)I(\nu_1)\cos(2\omega t - 2\psi) + \frac{1}{2}a_3(\nu_1)\Delta I(\nu_1)\cos(2\omega t - 3\psi)\right] \quad (5.11)$$

If the first harmonic signals are recovered, the output from the lock-in amplifier will depend upon the detection phase. Following the procedure for the RAM method described in Section 2.4.1 the amplitude modulated signal due to the frequency modulation, or FM/AM signals, are nulled by choosing detection angle,  $\theta_{LIA}$ , so that  $\cos\theta_{LIA} = \sin\psi'$ . This gives an output signal of:

$$I_\omega = \Delta I(\nu_1)\left[1 - A\left\{a_0(\nu_1) - \frac{1}{2}a_2(\nu_1)\right\}\right]\cos\theta_{LIA} \quad (5.12)$$

The same result is achieved using the PD method outlined in Section 2.4.2 where both orthogonal lock-in amplifier channels are simultaneously recorded and the detection phase of one is coincident with the background RAM signal. The

difference here between the PD method and the RAM method is the absence of the  $\cos(\theta_{LIA})$  term, which reduces the total signal amplitude in the RAM method, unless  $\psi' = \frac{\pi}{2}$ .

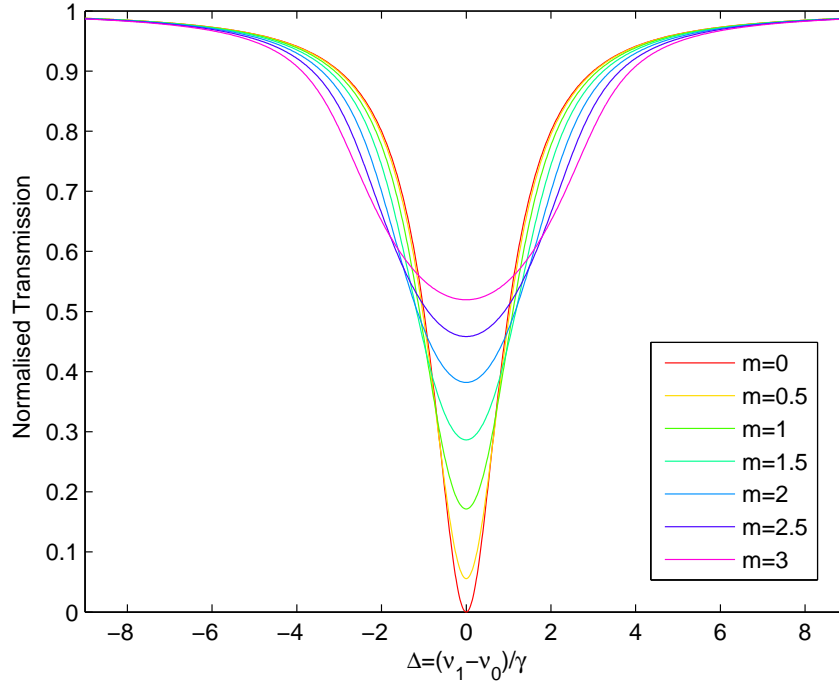


Figure 5.2: The effect of modulation index,  $m$  on the Lorentzian line shape profile for simulated RAM-based 1f signals from  $m = 0$  to  $m = 3$ .

The form of recovered experimental line shape is a function of modulation index as is expected when (5.5) and (5.6) are substituted into (5.12). The change in recovered line shape profile with  $m$  can be seen in Fig. 5.2, which shows the undistorted Lorentzian line shape at  $m = 0$  and progressively higher levels of distortion up to  $m = 3$ . At higher values of  $m$  the extent of the frequency dither,  $\delta\nu$ , is necessarily higher which results in an effective broadening of the laser power spectrum. This is the dominant mechanism for the flattening of the line shape and it can be attributed to the term  $a_0$ , which has been shown to be the convolution of the line shape function and the laser power spectrum, in an analogous way to the effect of performing direct detection with a broad line width laser source [116].

The desired outcome is the extraction of the true absorption line shape,

$f(\nu)$ . To achieve this (5.12) can now be expressed with the following equation where  $C_f(\nu_1)$  is a correction function with the same operation as in (2.12):

$$I_\omega = \Delta I(\nu_1) [1 - Af(\nu_1)C_f(\nu_1)] \cos \theta_{LIA} \quad (5.13)$$

The correction function,  $C_f(\nu_1)$ , is given for an arbitrary absorption line shape by [116]:

$$C_f(\nu_1) = \frac{\{a_0(\nu_1) - \frac{1}{2}a_2(\nu_1)\}}{f(\nu_1)} = \frac{\int_0^\pi [1 - \cos(2\theta)]f(\theta)d\theta}{\pi f(\nu_1)} \quad (5.14)$$

and specifically for a Lorentzian line shape in the pressure broadened regime of interest to this project:

$$C_f(\Delta, m) = \frac{1 + \Delta^2}{\pi} \int_0^\pi \frac{1 - \cos(2\theta)}{[1 + (\Delta + m \cos \theta)^2]} d\theta \quad (5.15)$$

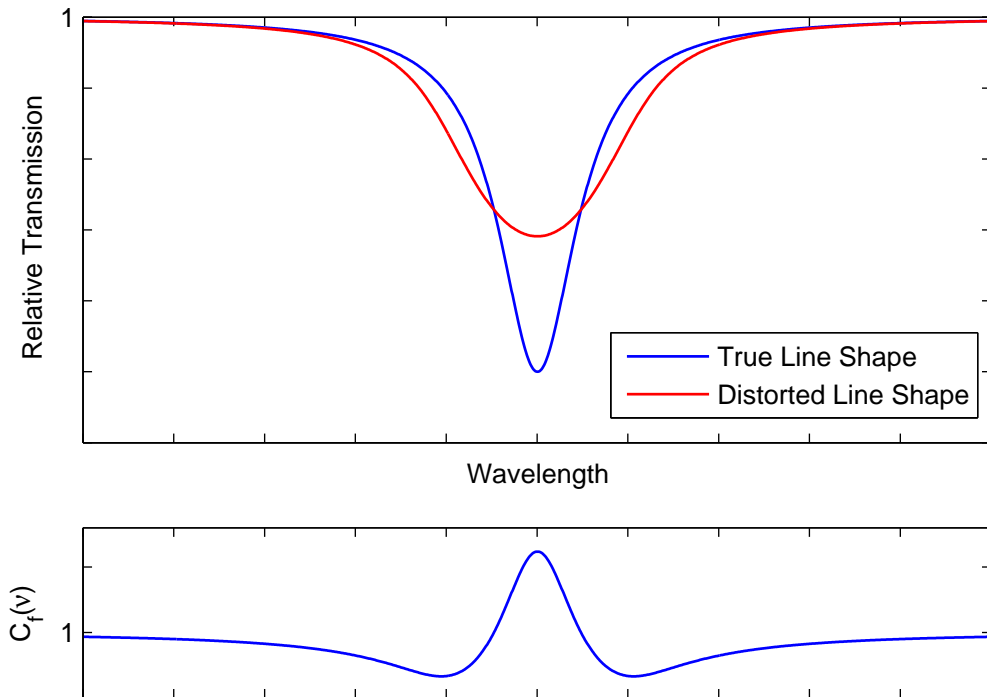


Figure 5.3: A comparison of a true Lorentzian line shape with a distorted line shape at  $m=2$ , with the relevant correction function plotted below.

For small modulation depths, where  $m \ll 1$ , the function  $C_f(\nu_1)$  is effectively unity and the true absorption line shape  $f(\nu)$  can be recovered directly. As the modulation index is increased to maximise the recovered signal size and hence signal-to-noise ratio, the correction function needs to be applied. The original correction function described by Duffin et al. and McGettrick et al. [32, 108], based on the 2<sup>nd</sup> and 4<sup>th</sup> order approximations of the Taylor series expansion of the absorption coefficient, was limited to operation below  $m = 0.75$  which truncated the effective operating regime of this method and compromised the overall sensitivity. The new correction function introduced in this chapter has no such constraints and in theory could be applied at any experimentally achievable modulation index. In reality there are other practical limitations that need to be considered, when assumptions break down at the extremes of operational settings.

The visual form of the correction function relative to the distorted and undistorted line shapes is illustrated in Fig. 5.3. In this figure the line shapes are displayed as transmission spectra to keep with convention. The multiplication process between the distorted line shape and the correction function needs to be applied to a relative absorption, rather than the relative transmission signal shown, before being converted back.

### 5.2.1 Nonlinear Absorption Measurements

The derivation of the previous section was based on the assumption that the absorbance was low and that the linear approximation to the Beer-Lambert law could be applied. When the transmission is higher than  $\sim 90\%$  or when  $\alpha(\nu)Cl \ll 1$ , the exponential form can be neglected.

$$\exp[-\alpha(\nu)Cl] = \exp[-Af(\nu)] \approx 1 - Af(\nu) \quad (5.16)$$

In order to deal with nonlinear absorption at higher concentrations for instance, a function,  $f_{exp}(\nu)$ , is introduced to account for the exact exponential expression:

$$\exp[-Af(\nu)] = 1 - Af_{exp}(\nu) \quad (5.17)$$

which can be rearranged to give a general statement of  $f_{exp}(\nu)$ :

$$f_{exp}(\nu_1) = \frac{1 - \exp[-Af(\nu)]}{A} \quad (5.18)$$

Whilst for the Lorentzian function used in this study the following is used:

$$f_{exp}(\nu_1) = \frac{1 - \exp\left[\frac{-A}{1+(\Delta+m \cos \theta)^2}\right]}{A} \quad (5.19)$$

The correction function can now be given in a form to account for the exponential line shape function:

$$C_f(\nu_1) = \frac{\int_0^\pi (1 - \cos(2\theta))f_{exp}(\theta) d\theta}{\pi f_{exp}(\nu_1)} \quad (5.20)$$

The correction function is applied in the same way as before but now the line centre absorbance,  $A$ , needs to be known or assumed in order to obtain  $f_{exp}$  from (5.18) or (5.19). An estimate for the line centre absorbance could be obtained by performing a preliminary measurement at a low modulation index where the peak height could be easily extracted, allowing  $A$  to be used in a subsequent line shape acquisition.

## 5.2.2 Practical Considerations Related to High Modulation Index Operation

The state of the calibration-free high modulation RAM methods depends upon three important issues. First of all any implementation of the correction function described in (5.15), depends upon accurate knowledge of the operational modulation index,  $m$ , which in turn depends not only on the applied current modulation,  $\delta i$  but also on  $\gamma$ , the HWHM. This parameter could be changing and unknown in conditions of varying pressure or temperature for instance. This being so it is important to find a method of determining the modulation index in real time during the signal acquisition process in order to effectively implement the

correction procedure. In Section 5.3 two methods for determining the modulation index are proposed and investigated.

The second important consideration is the AM/WM phase separation angle which is required to set the lock-in phase angle in the RAM method or to perform the trigonometric decomposition of the signals in the PD method. In Section 4.7.1 three methods for determining the AM/WM phase shift were outlined: The first used the LIA output in a RAM method configuration changing the lock-in detection angle and measuring the phase difference between the separated RAM signal and the separated FM signal. The second method used the fibre ring resonator to characterise the frequency change over one dither cycle relative to the equivalent amplitude change. The third method used the LIA outputs in PD method configuration to identify the peak positions in a low modulation index absorption signal to extract the AM/WM phase angle from (4.2). The latter method is the most powerful when implementing the PD method because it allows real time characterisation of  $\psi'$  directly from the absorption signals, reducing exposure to systematic drift. At higher modulation indices care is needed to ensure that the distorted nature of the recovered signals, as in Fig. 5.2 does not compromise the determination of  $\psi'$  and hence the signal recovery procedure. The steps taken to avoid this will be discussed in Section 5.4.

The final issue affecting the RAM-based methods is the limitation on signal-to-noise ratio imposed by the magnitude of the background RAM signal. The background RAM signal will have the effect of saturating the detection electronics regardless of the size of the recovered absorption signals, in much the same way as in TDLS with direct detection. The ideal scenario would be one on which wavelength modulation could be implemented at the highest sensible modulation frequency and modulation index, whilst the background RAM signals are removed somehow prior to undergoing analogue-to-digital conversion in the lock-in amplifier. In Section 2.4.4 the methods for nulling the RAM background optically using a fibre delay line were described. This work was limited to the regime of either very low modulation indices, i.e. where  $m \ll 1$  or to low modulation indices, where  $m < 0.75$  and the original  $2^{nd}$  and  $4^{th}$  order correction

functions could be used.

### 5.3 Modulation Index Determination

The calculation of the correction function,  $C_f(\nu)$ , depends upon accurate knowledge of the operational modulation index at the time of acquisition. In this analysis the line shape recovery was restricted to a single well isolated line shape rather than spectra involving several major absorptions or heavily interfering nearby lines. As stated previously the modulation index depended upon the applied frequency dither,  $\delta\nu$ , and the absorption half-width,  $\gamma$ . The applied frequency dither was easily calculated using the laser characterisation techniques outlined in Chapter 4 and was independent of the experimental conditions of the gas. The absorption HWHM was obviously dependent upon the experimental conditions and the easiest way to calculate  $\gamma$  was to use an absolute absorption line shape, except recovering this line shape was the reason that  $\gamma$  needs to be calculated. This problem complicated the line shape recovery process and a reliable solution was needed for the method to be useful in practical situations.

Previous studies into absolute line shape recovery at elevated modulation indices did not outline any method for establishing the operational modulation indices [32, 34, 35, 108]. The descriptions of the original 2<sup>nd</sup> and 4<sup>th</sup> order corrections used well defined experimental parameters to acquire knowledge of the modulation index prior to calculation of the correction function. This allowed demonstration of the correction procedure and verification of the effectiveness of the correction itself. For the method to be worthwhile in a practical scenario, the new function would need to hold for all modulation indices using the updated derivation in the previous section, as well as calculate and apply an experimentally determined modulation index. Two methods for recovering modulation indices from experimental signals are described here. The first method established the ratio of  $A_0$  for the high  $m$  signal and a low  $m$  reference which was then used to determine the modulation index analytically. The second method used a fitting procedure to compare the experimental line shape to a series of distorted

Lorentzian line shapes. The relative merits and limitations of these two methods are discussed in the context of practical implementation of sensitive line shape recovery techniques and data processed using each method is presented.

### 5.3.1 Ratio Method

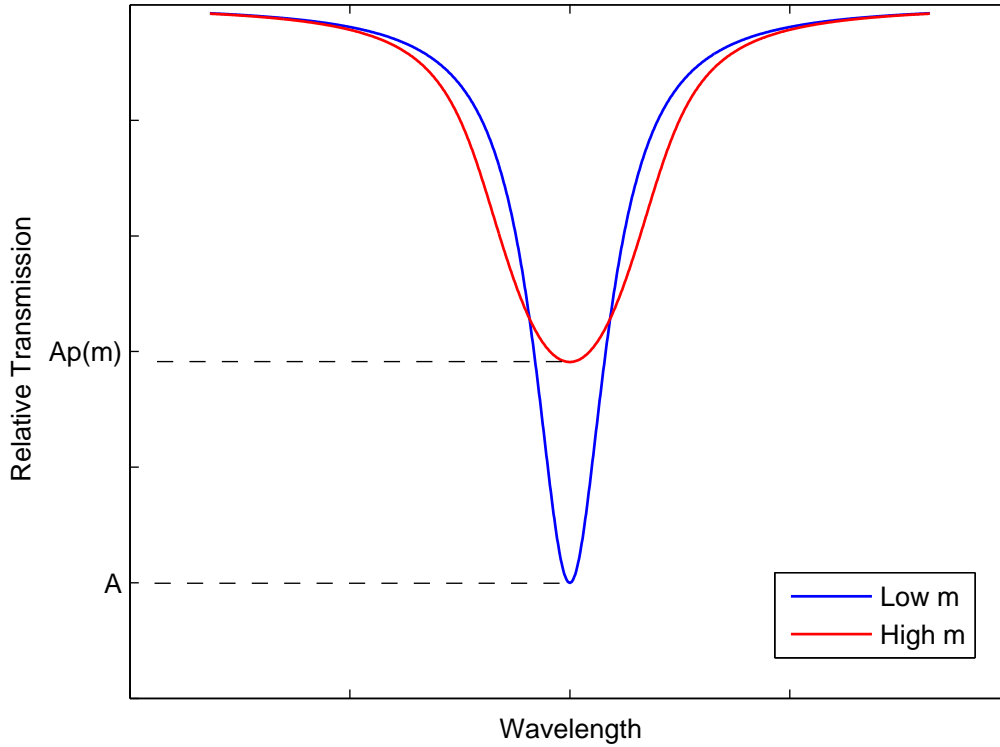


Figure 5.4: The line centre depths of the recovered signal and the low- $m$  reference are simulated. The actual depth  $A$  is shown alongside the distorted depth  $Ap(m)$ .

The first method for establishing the modulation index is referred to here as the ratio method as it aims to establish the ratio of two values of  $A_0$ , which are a function of  $m$  only. The method used a two stage acquisition process where the line shape at some unknown high modulation was recovered before the modulation index was changed so that the modulation index became small, so that  $m \approx 0$  was satisfied. The two resulting line shapes had a form similar to those modelled in Fig. 5.4. The low  $m$  signal had a pure Lorentzian line

shape whilst the high  $m$  signal appeared flattened and broadened in comparison. At line centre the apparent depth of the distorted line shape was less than the undistorted line shape. The following analysis can be used to determine the operational modulation index using only knowledge of the ratio of these two absorption depths. The line shape profile can be written in the form  $1 - A\{a_0(\nu) - \frac{1}{2}a_2(\nu)\}$  using the Fourier coefficients for the absorption,  $\alpha(\nu)$ . For the Lorentzian profile, the absorption exhibits the following  $m$ -dependence:

$$\left\{ a_0(\nu) - \frac{1}{2}a_2(\nu) \right\} = \frac{1}{\pi} \int_0^\pi \frac{1 - \cos(2\theta)}{1 + (\Delta_\nu + m \cos(\theta))^2} d\theta \quad (5.21)$$

At line centre where  $\Delta_\nu = 0$ , a parameter,  $p(m)$ , can be defined.

$$\begin{aligned} p(m) = \left\{ a_0(\nu_0) - \frac{1}{2}a_2(\nu_0) \right\} &= \frac{1}{\pi} \int_0^\pi \frac{1 - \cos(2\theta)}{1 + m^2 \cos^2(\theta)} d\theta \\ &= \frac{2}{\pi} \int_0^\pi \frac{\sin^2(\theta)}{1 + m^2 \cos^2(\theta)} d\theta \end{aligned} \quad (5.22)$$

This expression has the result that when  $m \rightarrow 0$ , then  $p(0) \rightarrow 1$ . This was useful because  $p(m)$  is simply the factor by which the distorted line centre depth differs from the true line centre depth. Therefore, the ratio of the two measured depths was determined by the modulation index only. The relationship between  $m$  and  $p(m)$  given in (5.22) can be calculated beforehand and listed in a look-up table.

The line centre absorbance is a relatively easy parameter to extract experimentally which makes this method particularly useful. A two stage acquisition process is not ideal if experimental conditions are likely to change over the timescale of the signal recovery time. If the absorbance is small, recovering the depth at line centre could be problematic as the increased noise susceptibility might lead to erroneous measurements. The motivation for increasing the modulation depth was to increase the signal to noise ratio, so the dominant source of error here may be the recovered ratio due to uncertainty in the recorded depth of the low  $m$  reference. It is possible to forego the slow ramp sweep and take a static measurement if the laser settings for the line centre can be reliably applied. The static line centre depth would also need to be compared to an off-line reference

point for normalisation, which would increase the number of acquisition steps in determining the ratio.

The preceding analysis was once again confined to the regime of linear absorbance, where the exponential form of the Beer-Lambert law can be neglected. For measurements at higher absorbances (5.22) can be amended to account for the full exponential form, using the absorbance  $A$  which is determined from the low  $m$  signal:

$$p(m, A) = \frac{2}{\pi A} \int_0^\pi \left[ 1 - \exp\left(\frac{-A}{1 + m^2 \cos^2(\theta)}\right) \right] \sin^2 \theta d\theta \quad (5.23)$$

### 5.3.2 Fit Method

An alternative method was proposed for determining the modulation index from experimental line shapes based on the magnitude of the deviation from a true Lorentzian line shape. The underpinning assumption that the target line shape to be recovered was a true Lorentzian allows the actual experimental line shape at high modulation indices to be compared to theoretical models with varying levels of distortion due to changing  $m$  in the model. A least squares error calculation was used, in a similar manner to the gas parameter fit described in Section 3.4, to determine the theoretical line shape that most closely matched the experimental one and hence the actual modulation index.

The fitting method could be performed in a single data acquisition step in contrast to the ratio method which required two or more stages. The process involved matching the distorted experimental signal line shape to theoretically modelled line shapes at various modulation indices. The modulation index was not the only parameter that needed to be considered for line shapes to be compared in this way as the absorbance,  $A$ , also needed to be simultaneously fitted as the theoretical transmission is a function of both. For a given value of  $A_0$ , the peak absorbance, there was a range of solutions where the combination of  $m$  and  $A$  gave a value that matched the apparent depth. For instance if the true peak absorbance had some value  $A_0(1)$  and a modulation index of 1 was used, there might have been another solution where a higher value of peak absorbance,

$A_0(2)$ , yielded the same apparent depth but for a higher but incorrect modulation index. This phenomenon at line centre is tied closely to the process used in the ratio method, described by (5.22). Instead of restricting the analysis to the line centre, a more useful procedure used the information provided by the entire line shape, which generally provided a unique combination of values for  $A$  and  $m$  that matched the recovered experimental line shape.

The following line shape model can be used in an unconstrained nonlinear optimisation fit in order to minimise the least-squares error between the recovered line shape and the theoretical model. An arbitrary line shape can be described using the first two even Fourier coefficients introduced in Section 5.2, using the following:

$$I(A, m) = 1 - A \left\{ a_0(\nu) - \frac{a_2(\nu)}{2} \right\} \quad (5.24)$$

with the two coefficients given in (5.5) and (5.6) restated here,

$$a_0 = \frac{1}{\pi} \int_0^\pi f(\theta) d\theta \quad \text{and} \quad a_n = \frac{2}{\pi} \int_0^\pi f(\theta) \cos(n\theta) d\theta$$

The specific line shape function  $f(\theta)$  is chosen to be a Lorentzian and is substituted into (5.5), (5.6) and (5.24) to give a model with functional dependency on  $A$  and  $m$ . The following Lorentzian form accounts for the full exponential form of the Beer-Lambert law and is therefore valid for all absorption levels:

$$f(\theta) = \frac{1 - \exp \left[ \frac{-A}{1 + (\Delta\nu + m \cos(\theta))^2} \right]}{A} \quad (5.25)$$

## 5.4 Experimental Validation of Correction Function

### 5.4.1 Experimental Procedure and Settings

To test the effectiveness of the correction function procedure a stable, enclosed laboratory system for measuring the methane absorption near 1650 nm

(6060 cm<sup>-1</sup>) was used. The in-line gas cell and detection system are described in detail in Section 4.2 and three CH<sub>4</sub>:N<sub>2</sub> mixtures were flowed through the cell with methane concentrations of 10.13%, 1.02% and 0.1008%. Signals were acquired at these three methane concentration levels using the different gas mixtures and also at different modulation indices between  $m=0.1$  and  $m=2$ , with the upper limit in this case being imposed by the drive current limit of the laser. The performance of the two methods for determining  $m$  in the correction process was examined and the overall line shape recovery evaluated by comparing the recovered line shapes to the low- $m$  reference signals and theoretically modelled line shapes. The MATLAB program shown in Appendix C illustrates the basic form of a practical PD method calculation and examples of the correction procedure are also given.

The experimental components of the operational modulation index are  $\gamma$ , the absorption HWHM and  $\delta\nu$ , the frequency dither amplitude. The HWHM could be estimated from line shape models and examination of the output from the GATS Spectral Calculator showed a significant variation in  $\gamma$  with gas concentration level, shown in Table 5.1 [118, 119]. The apparent minimum in  $\gamma$  as the methane concentration is decreased is due to the absorption level crossing between linear and nonlinear absorption regimes, over the path length defined in the GATS model. The commercially available GATS modelling software provided a convenient method of reliably estimating  $\gamma$  in the nitrogen-broadened experimental signals, as the HITRAN data is defined in terms of air-broadening so any spectral model based on these will need to account for this. Once a modulation frequency had been decided upon, a characterisation of the laser tuning coefficient was required using the resonator technique outlined in Section 4.7.2. Using a modulation frequency of 100 kHz the voltage tuning coefficient for the OKI DFB laser was found to be  $\frac{\delta\nu}{\Delta V}=1.218$  GHz/mV, where the frequency dither is given as an amplitude for equivalence to  $\gamma$ , relative to the applied peak-to-peak voltage signal. The applied dither voltages for the required  $m$  values were then calculated for each concentration level and the voltages used are shown in Table 5.2. The critical settings for the experimental data presented in this chapter are summarised in Table 5.3.

CH <sub>4</sub> Concentration (%)	Theoretical HWHM (GHz)
10	2.35
1	1.96
0.1	2.09

Table 5.1: Theoretical HWHM measured from HITRAN08 output from the GATS Spectral Calculator [118]

m	Dither Voltages (mV)		
	0.1% CH <sub>4</sub>	1% CH <sub>4</sub>	10% CH <sub>4</sub>
0.1	172	160	182
0.5	860	801	912
1	1721	1602	1824
1.5	2580	2403	2736
2	3443	3204	3648

Table 5.2: Peak-to-peak dither voltages required for particular  $m$  values, with a 100kHz dither at each of the certified CH<sub>4</sub> concentrations used.

Experimental Setting	Value
Laser bias current	79.5 mA
Laser TEC thermistor resistance	6.514 k $\Omega$
Sawtooth ramp frequency	5 Hz
Sawtooth ramp drive voltage	350 mV
Sinusoidal dither frequency	100 kHz
Sinusoidal dither amplitude	as per Table 5.2
Lock-in time constant	500 $\mu$ s
Lock-in sensitivity (m=0.1)	5 mV
Lock-in sensitivity (m=1)	20 mV
Lock-in sensitivity (m=2)	50 mV

Table 5.3: Critical settings for the experimental system used in this chapter.

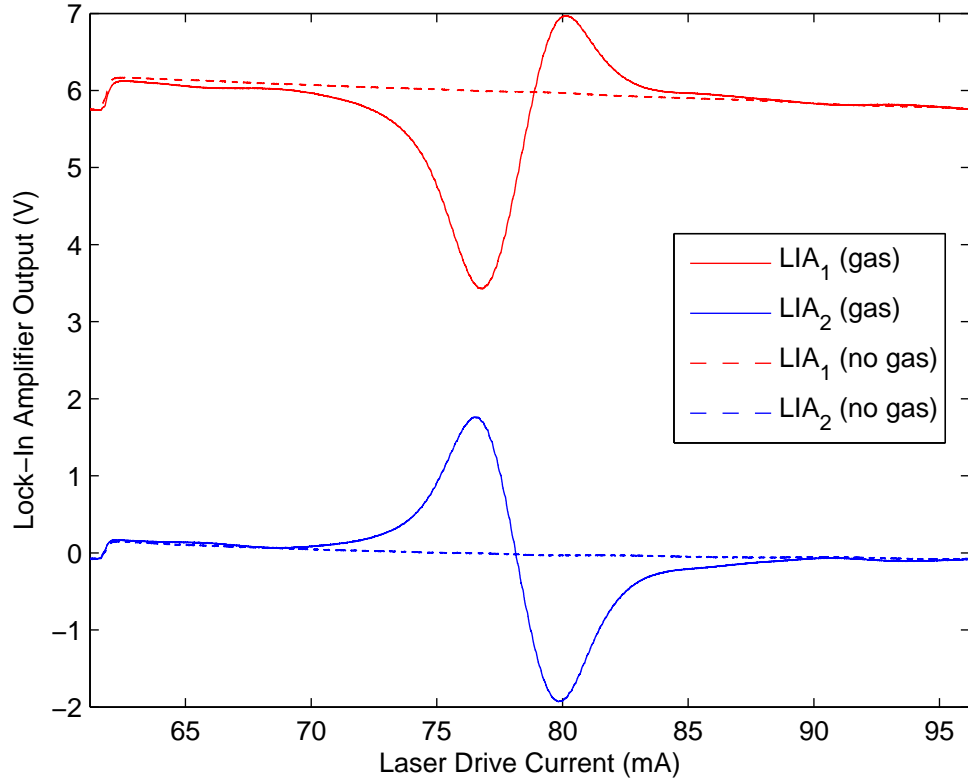


Figure 5.5: Experimental signals recorded from the lock-in amplifier for the phasor decomposition method. The gas signals from the two LIA channels are shown with the corresponding ‘no gas’ signal used for normalisation. The blue signals are the separated FM/AM components whilst the red signals from the orthogonal channel contain projections of both the RAM and FM/AM components.

The photodiode output was demodulated with a lock-in amplifier and the characteristic outputs recovered when using the PD method are shown here in Fig. 5.5 using the procedure described earlier based on (2.11) [35,108]. The basic procedure for performing a PD measurement was to set the lock-in phase so that the LIA<sub>2</sub>-channel contained no contribution from the RAM, by ensuring the non-absorbing regions were zero and the separated FM signal was recovered. Both channels were then recorded and  $\psi'$  was calculated so that the PD calculation from (2.11) could be performed. The only difference between the procedure here and the previous descriptions was in the determination of  $\psi'$ .

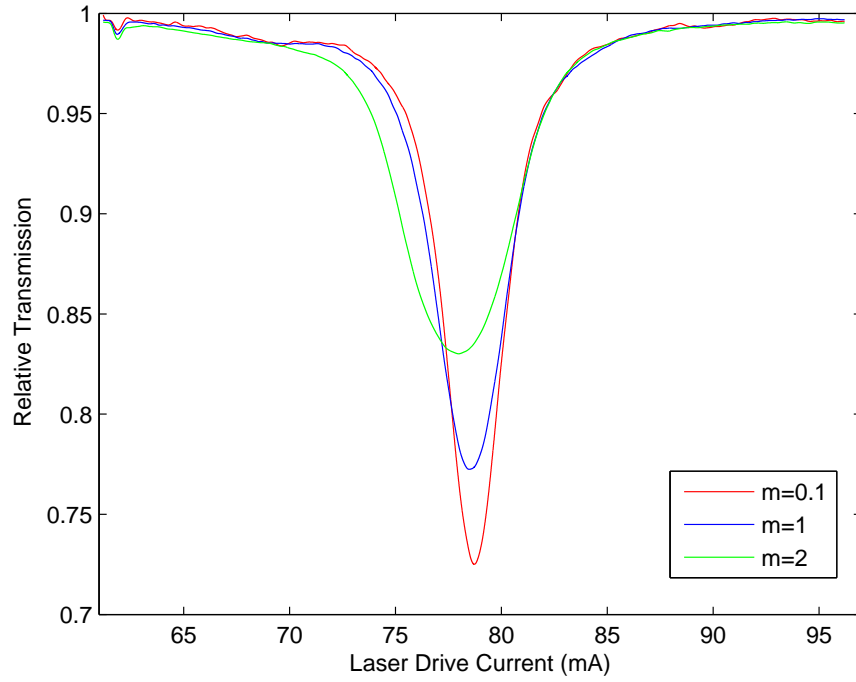


Figure 5.6: Recovered 10% CH<sub>4</sub> line shapes with increasing  $m$  using original  $\psi'$  calculation

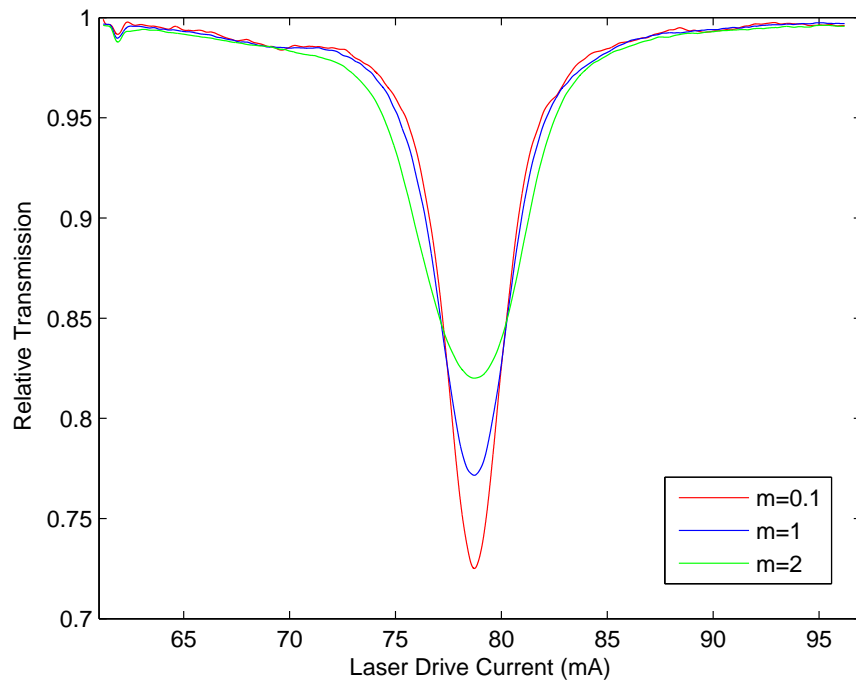


Figure 5.7: Recovered 10% CH<sub>4</sub> line shapes with increasing  $m$  using improved  $\psi'$  calculation

The experimental line shapes shown in Fig. 5.6 were determined from the recovered orthogonal LIA signals using the original method for establishing  $\psi'$  in real time from experimental signals, described in Section 4.7.1. The figure clearly shows that at higher  $m$ -values the line shapes were distorted from the line shapes anticipated from the theoretical model shown in Fig. 5.2 and the apparent line centre position moved down in time index. The reason for this was the determination procedure for the position indices,  $x_1$  and  $x_2$ , in the calculation of  $\psi'$  illustrated earlier in Fig. 4.16. At low modulation indices the maximum and minimum peak positions of the separated FM signal from the LIA<sub>2</sub> channel were identified and used as the index points. If the low modulation index condition was satisfied then these positions were symmetric about the line centre position providing a good calculation of  $\psi'$ . An increase in the modulation index increased the relative contribution of the projection of the amplitude modulated  $2^{nd}$  derivative component, the  $\frac{1}{2}a_2(\nu_1) \cos(\omega t - 2\psi')$  term in (5.10). The combination of the symmetric ( $a_0$ ) and asymmetric ( $a_2$ ) functions lead to an uneven change in the position of the peaks either side of line centre and the apparent line centre became shifted. The best solution for this was to establish the line centre position through a characterisation procedure or a low  $m$  reading and then to use two index positions at equal index shifts from this known line centre position. These new index positions for  $x_1$  and  $x_2$  could now be used in the same way as before and the line shapes were now be free of the characteristic skew, which can be seen in Fig. 5.7.

### 5.4.2 Modulation Index Determination

The crux of the correction function implementation process was the establishment of the instantaneous modulation index required in the calculation of the function. In Tables 5.4 and 5.5 the results are presented of repeated experimental measurements of modulation index using both the methods outlined in Section 5.3. Experimental signals were acquired at modulation indices of  $m=0.1$ ,  $m=1$  and  $m=2$  at the three certified methane concentration levels and repeated 10 times for each. The mean percentage error and standard deviation of each measurement

set are also given with the percentage error defined relative to the modulation index derived from the assumed and calculated values for  $\gamma$  and  $\delta\nu/\Delta V$ .

		Measurement # (Fit Method)										% Error	$\sigma$
		#1	#2	#3	#4	#5	#6	#7	#8	#9	#10		
10%	m=1	1.03	1.03	1.02	1.02	1.00	1.03	1.02	1.01	1.01	0.98	1.5	0.015
	m=2	2.08	2.09	2.03	2.16	2.02	2.06	2.08	2.01	2.01	2.01	2.75	0.049
1%	m=1	1.03	0.99	1.04	1.01	0.98	1.01	1.01	1.03	1.00	1.00	1	0.019
	m=2	1.96	2.02	1.86	1.91	1.91	1.87	1.96	2.00	1.99	1.92	-3	0.055
0.1%	m=1	1.09	1.15	0.97	1.18	1.18	1.08	0.95	1.00	0.78	0.98	3.6	0.125
	m=2	2.17	2.08	1.73	1.39	2.76	2.13	2.00	1.68	1.78	2.08	-1	0.364

Table 5.4: Repeated gas measurements to examine  $m$  determination by the fit method at different gas concentrations and modulation indices.

		Measurement # (Ratio Method)										% Error	$\sigma$
		#1	#2	#3	#4	#5	#6	#7	#8	#9	#10		
10%	m=1	1.04	1.04	1.03	1.04	1.04	1.04	1.05	1.03	1.04	1.04	3.9	0.005
	m=2	1.92	1.91	1.92	1.91	1.93	1.92	1.91	1.93	1.95	1.96	-3.7	0.017
1%	m=1	0.99	1.05	1.07	1.05	1.06	1.04	1.09	1.11	1.09	1.13	6.8	0.040
	m=2	2.05	2.12	2.14	2.10	2.13	2.16	2.15	2.22	2.15	2.18	7	0.046
0.1%	m=1	0.92	0.83	0.74	1.02	1.16	0.78	0.94	1.08	1.04	1.09	-4	0.142
	m=2	1.92	2.23	2.17	1.98	2.08	1.64	1.97	2.08	1.56	1.95	-2.1	0.214

Table 5.5: Repeated gas measurements to examine  $m$  determination by the ratio method at different gas concentrations and modulation indices.

The error in the applied modulation index is stated with a confidence level within  $\pm 10\%$ . The contributions to this stated error arise from the uncertainty in the assumed HWHM  $\gamma$  from both the model used and the uncertainty in the atmospheric pressure, as well as the tuning coefficient error which arises from the resonator free spectral range and the determination error of the frequency dither relative to the applied voltage dither. This error represents the accumulation of uncertainties in the characterisation of the experimental conditions. This level of uncertainty in the operational settings should not have a particularly detrimental effect on the overall error in the recovered gas information. Once the modulation amplitude has been set at an appropriate level, the tuning coefficient will remain stable and the experimentally determined modulation indices should represent the actual conditions to a level of uncertainty that is acceptable for the intended

applications, most notably for process control in solid oxide fuel cells [35].

In general the fit method appears to provide a robust and reasonably repeatable method for determining modulation indices in each scenario. As expected the standard deviation of the measurements increases noticeably for measurements at the 0.1% CH<sub>4</sub> level at which the signal to noise ratio is considerably lower due to an absorption level of only  $4 \times 10^{-4}$ . The ratio method also returns modulation index values that fall within the limit of possible error but with slightly lower performance. The particularly high values for percentage error at the 1% CH<sub>4</sub> are due to the structure of the noise on the  $m=0.1$  signal that was used as a reference for  $A_0$  when executing the ratio method calculation, which can be seen in Fig. 5.8. The noise apparent at the line centre is noticeable in the line shape and the residual, when compared to the signal recovered and corrected at a high modulation index. The recovered peak depth used in the ratio method will clearly not be correct in this case and the resulting error therefore propagates through into the determination of  $m$  and the correction function calculated from it. This example highlights the main limitation of the ratio method as a two-step method for determining the modulation index.

### 5.4.3 Absolute Line Shape Recovery

The aim of the process under investigation was to recover the absolute absorption line shape. To judge the efficacy of the proposed techniques the corrected line shapes were compared to undistorted signals at low  $m$  values if these signals were strong enough, or by performing a theoretical fit and comparing the calculated gas parameters to known values for concentration and pressure.

In Figs. 5.8 and 5.9 the before and after results of two corrections can be seen relative to the equivalent  $m=0.1$  signal. The first signal shows absorption due to 1% CH<sub>4</sub> at a modulation index of  $m=1$ , where even this relatively modest increase in  $m$  exhibits a significant improvement in SNR. The second signal showing 10% CH<sub>4</sub> at a modulation index of  $m=2$  shows a less pronounced increase in SNR. Figs. 5.10 and 5.11 show absorption signals due to 1% and 10% CH<sub>4</sub> but this time they are compared to theoretical fits based on the HITRAN08 database

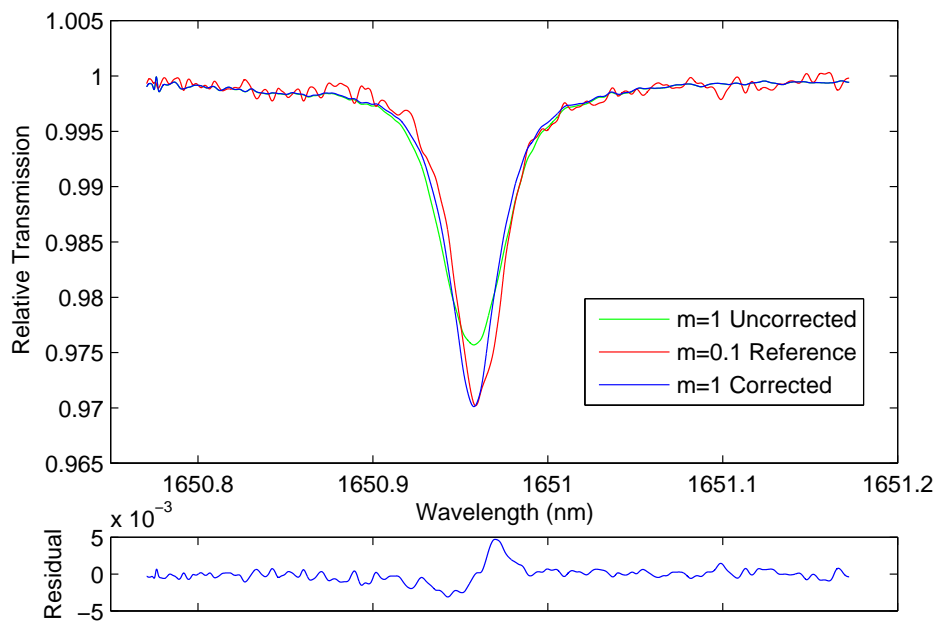


Figure 5.8: Uncorrected and corrected 1% CH<sub>4</sub>:N<sub>2</sub> signals at m=1 with m=0.1 reference signal.

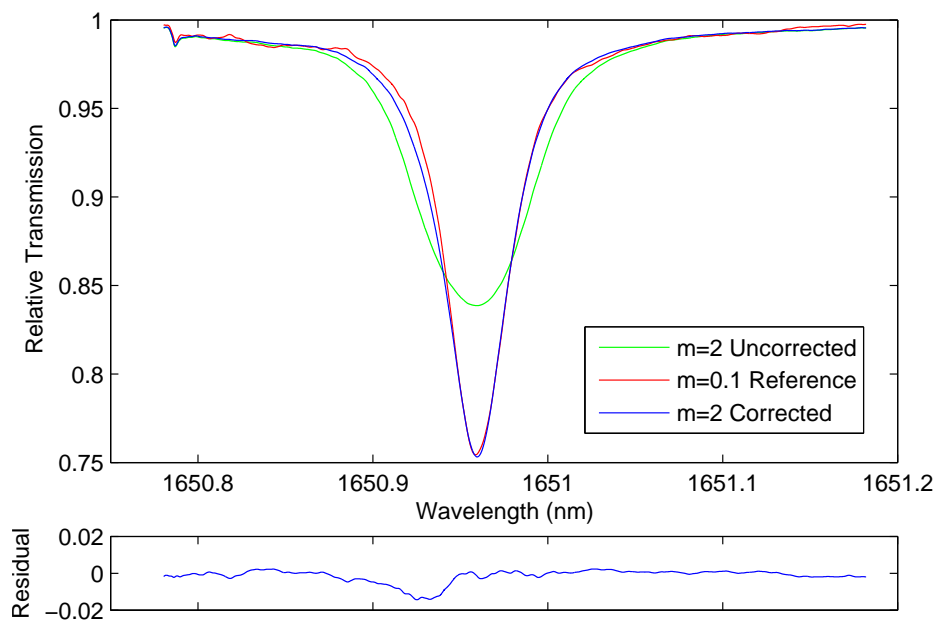


Figure 5.9: Uncorrected and corrected 10% CH<sub>4</sub>:N<sub>2</sub> signals at m=2 with m=0.1 reference signal.

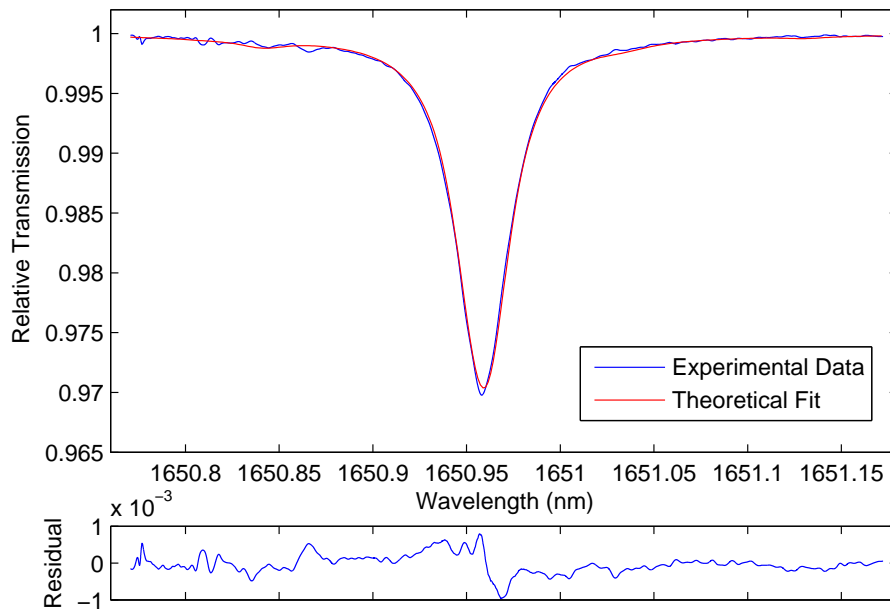


Figure 5.10: Corrected 1% CH<sub>4</sub>:N<sub>2</sub> signals at m=2 with the resulting theoretical Voigt fit.

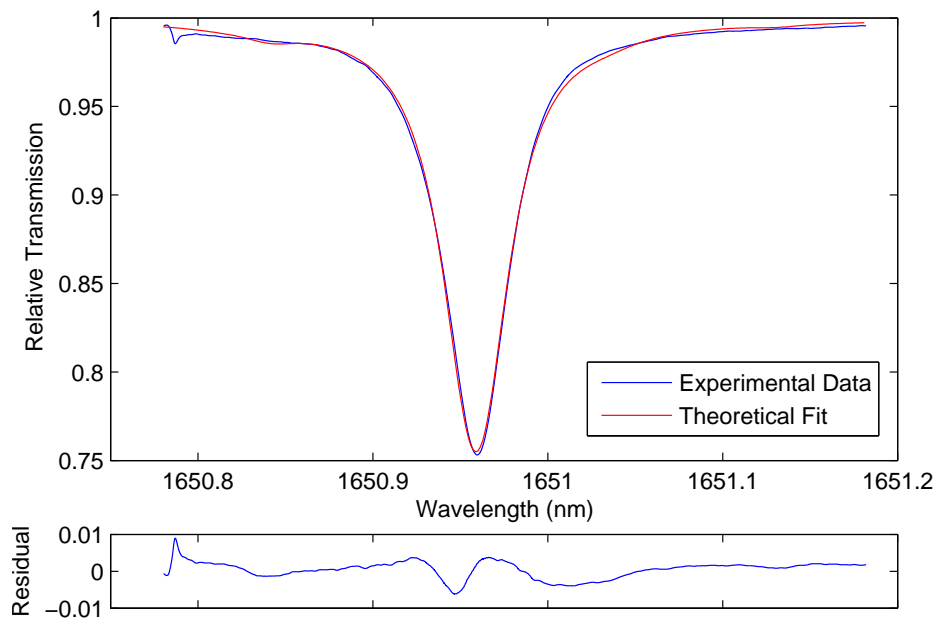


Figure 5.11: Corrected 10% CH<sub>4</sub>:N<sub>2</sub> signals at m=2 with the resulting theoretical Voigt fit.

			Measurement #						
			#1	#2	#3	#4	#5	% Error	$\sigma$
10%	m=1	C(%)	9.14	9.15	9.16	9.14	9.14	-9.4	0.01
		P(bar)	1.04	1.04	1.09	1.09	1.09	4.9	0.03
	m=2	C(%)	9.68	9.71	9.68	9.7	9.64	-4.1	0.03
		P(bar)	1.05	1.05	1.06	1.06	1.06	3.5	0.01
1%	m=1	C(%)	0.95	0.93	0.92	0.93	0.93	-6.8	0.01
		P(bar)	0.96	0.96	0.96	0.98	0.97	-5.2	0.01
	m=2	C(%)	0.91	0.87	0.96	0.92	0.92	-8.4	0.03
		P(bar)	0.97	0.99	0.95	0.96	0.95	-5.5	0.02
0.1%	m=1	C(%)	0.09	0.09	0.09	0.09	0.09	-10.0	0.00
		P(bar)	1.05	1.12	1.24	1.29	1.20	15.7	0.10
	m=2	C(%)	0.09	0.09	0.09	0.09	0.12	-4	0.01
		P(bar)	1.06	1.10	1.26	1.55	0.76	12.4	0.29

Table 5.6: Repeated gas measurements to examine concentration and pressure determination from the corrected line shapes at different gas concentrations and modulation indices.

using the Voigt line shape model described in Section 3.3.3. The residuals to these fits exhibit some structure that was due to noise and also to the limiting assumption in this case, that the experimental line shapes were purely Lorentzian. The theoretical fits are based on Voigt profiles yet the corrected signals were made up of strongly-Lorentzian Voigt signals corrected by the Lorentzian-derived correction function.

The theoretical fits for each signal set yielded recovered values for concentration and pressure that could be compared to the known experimental conditions to indicate the relative error of the experimental signals. Table 5.6 shows the concentrations and pressures determined from line shapes at 0.1 %, 1 % and 10 % CH<sub>4</sub> at  $m$ -values of 1 and 2 with pressure at  $P = 1.02$  bar. The recovered concentrations were within 10 % mean relative error of the expected concentration from the gas certification, which itself had a  $\pm 5$  % filling tolerance. The recovered pressures had similar relative errors above the 0.1 % CH<sub>4</sub>, below which the errors started to increase due to the small signal size. It is clear that for both low and high modulation indices the recovered RAM absorption signals can provide a similar level of line shape recovery to direct detection, extending the scope of initial studies into RAM-based line shape recovery [32–35, 120]. The

intended applications for these techniques are in harsh environments where the SNR benefits of LIA detection can provide significant improvement in recovered signal outputs, compared to direct measurements. A practical illustration of the contrast in line shape recovery potential between direct and RAM-based detection is evident during testing of the aero engine intake sensor described in Section 8.1.

## 5.5 Summary

In this chapter a new correction formalism, that allowed RAM-based line shape recovery methods to be used at high modulation depths, was proposed and experimentally validated. The SNR of these measurements could be improved significantly by increasing the modulation index, although the line shape recovery process became more complex due to distortions that needed to be corrected. A Fourier expansion of the absorption coefficient was used to describe the recovered signals at the first harmonic and a correction function,  $C_f(\nu)$ , was derived for a Lorentzian line shape that yielded the true transmission function from a distorted experimental signal measured at a high modulation index. The calculation of the correction function required accurate knowledge of the modulation index that depended upon the frequency dither amplitude and the experimental HWHM. Two new methods were described that allowed the modulation index to be calculated using experimental signals, without definite knowledge of the gas properties. A comparison was made between the two methods, one of which took the ratio of absorbances at high and low modulation indices whilst the other used a fitting procedure based on simulated line shapes. The fit method was shown to recover the modulation index more effectively than the ratio method whilst also using a more practical single acquisition recovery process.

The experimentally determined modulation index could then be used to calculate the correction function needed to recover the true absorption line shape from the recovered signal. To examine the effectiveness of this technique, signals were acquired at a range of methane concentrations and modulation indices. The corrected line shapes were compared to line shapes recovered at low modulation

indices where there is no distortion and theoretical fits were also performed to see the effect of the process on gas parameter recovery. The process was shown to work effectively over a wide range of absorption levels and up to the achievable modulation limits of the DFB laser. The strength of the technique lies in its applicability to harsh environments where direct detection using DC modulation cannot feasibly be used. The use of high sensitivity wavelength modulation methods that use narrow band detection at RF frequencies, whilst maintaining calibration-free gas determination, was previously impossible.

# Chapter 6

## Autobalanced Photoreceivers for Direct Detection and Electronic RAM-nulling

### 6.1 Introduction to Autobalanced Photoreceivers

In Chapter 2 a brief introduction was given into balanced ratiometric detection, a subset of direct detection which uses an autobalanced dual-beam photoreceiver as the front end optical-to-electrical signal converter. The technique and the analogue circuit required were first described by Hobbs and co-workers as a low-cost method of obtaining shot-noise limited dual-beam measurements [47–49, 121]. The concept of using a reference beam in addition to a signal and recording both to obtain comparative measurements to cancel common-mode laser noise through subtraction or division, has been widely used for a number of different spectroscopic applications encompassing direct detection, WMS and FMS [52, 58, 122–126]. The autobalanced noise cancelling detectors of interest in this project have also been used by a number of groups either in the Hobbs form [4, 5, 50, 51, 127, 128], in other forms such as with digital autobalancing [129, 130]

or with alternative feedback mechanisms for different applications [131].

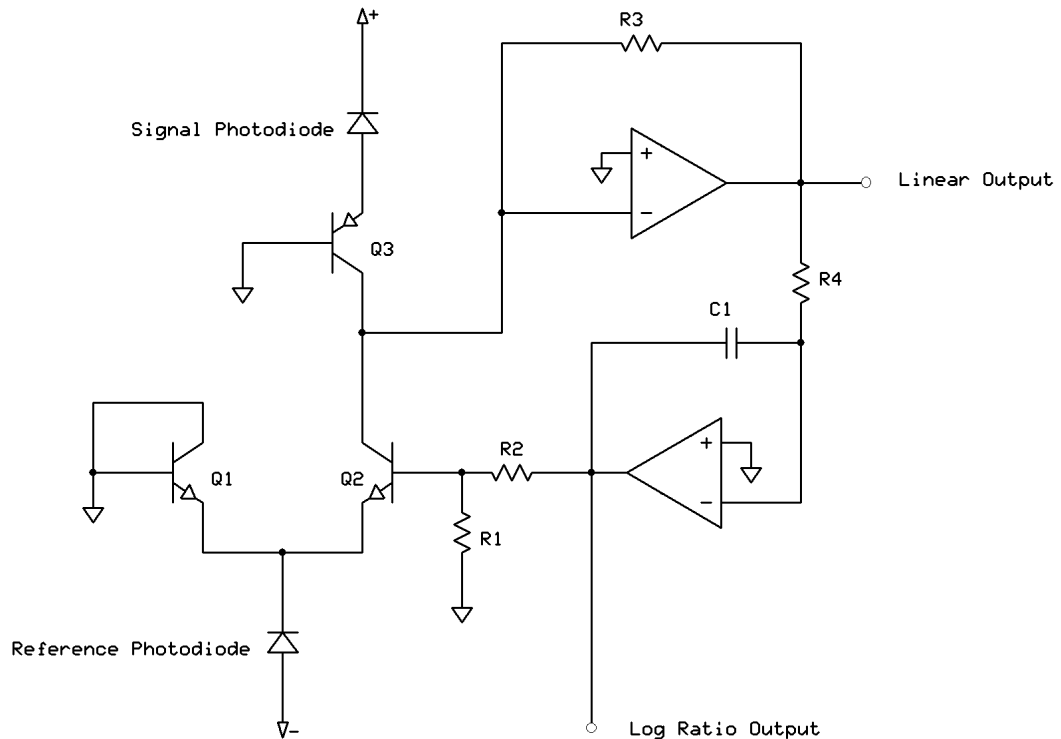


Figure 6.1: Electronic circuit diagram of Hobbs' autobalanced laser noise canceller

In a generic autobalanced dual-beam detector system the laser output is split into two paths, one of which will encounter an absorption path before reaching a detector whilst the other will be directly incident on a different detector. Once the beam is split the excess noise in each path will be made up of the shot noise which is uncorrelated and any optical noise affecting the beam. The Hobbs-type circuit, shown in Fig. 6.1, operates when the photocurrent created by the reference beam is greater than the photocurrent due to the signal beam. At this point the reference photocurrent is split by  $Q_1$  and  $Q_2$ , a pair of bipolar junction transistors (BJTs) which have the function of a highly linear voltage-controlled current splitter. The split ratio is dictated by the base voltage ratio, which in this circuit is dictated by the servo feedback from the nulled transimpedance output that occurs when the photocurrents are matched at the summing junction between  $Q_2$  and  $Q_3$ . This base voltage of  $Q_2$  is essentially the

lowpass filtered output of the feedback element, which is a ratiometric output of the difference between the two photocurrents. This is generally known as the ‘log ratio’ output and it yields the gas absorption minus any common-mode noise over a noise cancellation bandwidth limited only by the gain-bandwidth product of the BJTs. The bandwidth of the feedback element dictates the lowpass cut-off frequency and therefore the response time of the circuit providing a manageable limit on the allowed ramp frequencies.

Component	Part Type or Value
Q1,Q2	BC550
Q3	BC560
Op-amps	OP27G
R1	25 $\Omega$
R2	1 k $\Omega$
R3	10 k $\Omega$
R4	10 k $\Omega$
C1	8 pF

Table 6.1: Component types and values for the Hobbs circuits constructed

The components used for the circuit constructed based on Fig. 6.1 are listed in Table 6.1. Variants were built with a number of different component values for R4 and C1, to change the bandwidth properties of the integrator circuitry. With the component values listed in the table the 3 dB corner frequency in an idealised circuit would be 2 MHz. The 3 dB frequency was not necessarily the practical limit for circuit operation which was in fact seen to be around 3-8 kHz, depending on the circuit iteration. At this point the absorption line shape was clearly not being faithfully recovered as the log ratio feedback signal exhibited skew and distortion.

## 6.2 Derivation of Normalisation Technique for Autobalanced Detectors

The physical interpretation of the log ratio output signal is more complicated than for a simple transimpedance output which is easily normalised. The starting point for this analysis is the result of the Ebers-Moll equation governing the behaviour of the bipolar junction transistors [47, 117]. The ratio of the collector currents of the transistor pair  $Q_1$  and  $Q_2$  in Fig. 6.1 can be related to the difference in their base-emitter voltages:

$$\frac{I_{C_1}}{I_{C_2}} = \exp \left[ \frac{q\Delta V_{BE}}{kT} \right] \quad (6.1)$$

where  $q$  is the electron charge,  $k$  is Boltzmann's constant,  $T$  is the operating temperature and  $\Delta V_{BE}$  is given by:

$$\Delta V_{BE} = V_{BE_2} - V_{BE_1} = (V_{B_2} - V_{E_2}) - (V_{B_1} - V_{E_1}) \quad (6.2)$$

In the circuit the collector and base of  $Q_1$  are grounded so  $V_{B_1} = 0$  and the two emitters are connected so that  $V_{E_1} = V_{E_2}$ , meaning  $\Delta V_{BE} = V_{B_2}$ , which can be substituted into (6.1)

$$\frac{I_{C_1}}{I_{C_2}} = \exp \left[ \frac{qV_{B_2}}{kT} \right] \quad (6.3)$$

The circuit has an operating condition that is satisfied when  $i_{signal} < i_{reference}$ . In this case the collector current in  $Q_1$  will match the signal photocurrent,  $I_{C_1} = i_{signal}$  and the reference photocurrent will be the sum of both collector currents,  $I_{C_1} + I_{C_2} = i_{reference}$ . These equations can be rearranged and substituted into (6.3) to state the collector current ratio dependence in terms of the two photocurrents.

$$\frac{i_{signal}}{i_{reference} - i_{signal}} = \exp \left[ \frac{qV_{B_2}}{kT} \right] \quad (6.4)$$

Hence, after rearranging for  $V_{B_2}$ :

$$V_{B_2} = \frac{-kT}{q} \ln \left[ \frac{i_{reference}}{i_{signal}} - 1 \right] \quad (6.5)$$

The term  $V_{B_2}$  can be stated in terms of the output of the feedback amplifier  $V_0$ , the ‘log ratio’ output:

$$V_{B_2} = \left( \frac{R_1}{R_1 + R_2} \right) V_0 \quad (6.6)$$

So the log ratio output,  $V_0$ , becomes:

$$V_0 = \frac{-kT}{q} \left( \frac{R_1}{R_1 + R_2} \right) \ln \left[ \frac{i_{reference}}{i_{signal}} - 1 \right] \quad (6.7)$$

The photodiodes will have a known responsivity,  $\mathfrak{R}$  which can be used to relate the photocurrent to the incident light intensity by:  $i_{photodiode} = \mathfrak{R}I$ . If the two photodiodes are well matched and the assumption can be made that  $\mathfrak{R}_1 = \mathfrak{R}_2$ , then the log ratio output in (6.7) can be rewritten:

$$V_0 = \frac{-kT}{q} \left( \frac{R_1}{R_1 + R_2} \right) \ln \left[ \frac{I_{reference}}{I_{signal}} - 1 \right] \quad (6.8)$$

$$\begin{aligned} \frac{I_{reference}}{I_{signal}} - 1 &= \exp \left[ \frac{-kT}{q} \left( \frac{R_1}{R_1 + R_2} \right) V_0 \right] \\ I_{signal} &= \frac{I_{reference}}{1 + \exp \left[ \frac{-kT}{q} \left( \frac{R_1}{R_1 + R_2} \right) V_0 \right]} \end{aligned} \quad (6.9)$$

The nature of the direct-type absorption signal requires that a baseline fit or ‘no gas’ signal be used for normalisation purposes. This means that two signals will be generated: the first one will measure just the background signals and noise generated in the signal arm,  $V_{0_1}$ , proportional to the incident optical intensity  $I_1$ . The second contains the full gas absorption,  $V_{0_2}$ , which is proportional to the incident optical intensity in the presence of absorption  $I_2$ . The relative transmission is therefore given by:

$$\frac{I_2}{I_1} = \frac{1 + \exp \left[ \frac{-q}{kT} \left( \frac{R_1}{R_1 + R_2} \right) V_{0_1} \right]}{1 + \exp \left[ \frac{-q}{kT} \left( \frac{R_1}{R_1 + R_2} \right) V_{0_2} \right]} \quad (6.10)$$

## 6.3 Experimental Validation of Normalisation Technique

In order to use the normalisation procedure derived above which culminates in (6.10), the behaviour of the photoreceiver circuit built in the lab was tested to see if its output matched theoretically predicted spectra. To do this the in-line gas cell was used with a Fermionics InGaAs diode used to replace the Thorlabs PDA10CS photoreceiver shown in Fig. 4.2. Certified concentrations of methane in nitrogen were flowed through cell and the absorption was recovered using an autobalanced photoreceiver circuit once the power levels in the signal and reference beams had been optimised using a variable optical attenuator (VOA) in the reference path.

Spectra were acquired at methane concentrations of 10.13 % and 0.1008 %, certified by the supplier with a  $\pm 5$  % filling tolerance and the atmospheric pressure was recorded as 1.02 bar. Figs. 6.2 and 6.3 show the normalised spectra with theoretical Voigt fits which were calculated using the process described in Section 3.4. The residuals between experimental and theoretical spectra exhibited no obvious structure other than the random noise and despite having a SNR  $\sim 60$  times smaller the 0.1 % CH<sub>4</sub> signal still provided a usable line shape. The gas parameters calculated from the theoretical fits suggested a concentration of the 9.91 % and pressure of 1.03 bar for the higher concentration and 0.13 % and 1.06 bar for the lower concentration. Given the small absorption from the 0.1 % CH<sub>4</sub> signal the slight drop in overall accuracy compared to the much stronger signal was to be expected. It is clear that where SNR is not an issue the normalisation technique is able to recover spectra to a high level of accuracy yielding gas parameters that are within the margin of error of the certified gas concentrations.

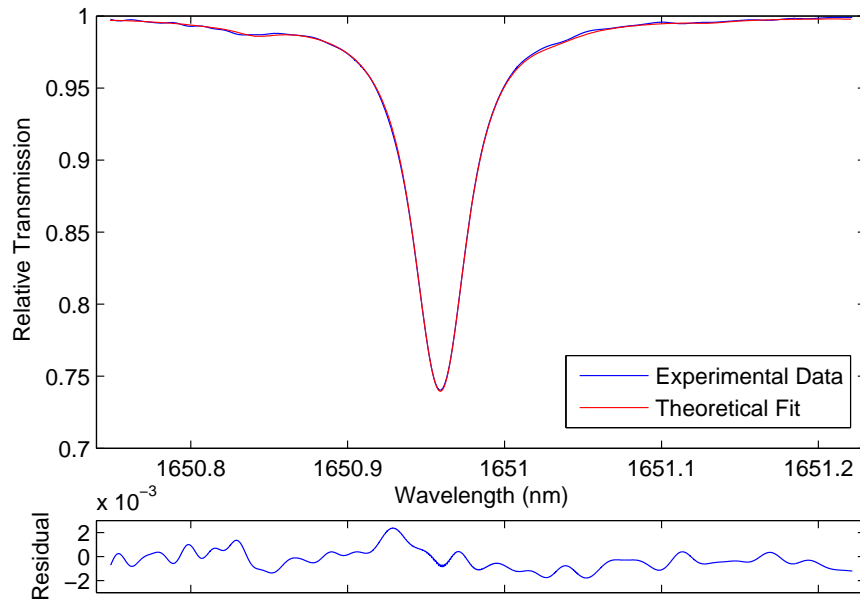


Figure 6.2: Experimental 10%  $CH_4$  absorption at 1650 nm ( $6060\text{ cm}^{-1}$ ) recovered using Hobbs circuit and normalised using (6.9), with accompanying Voigt fit.

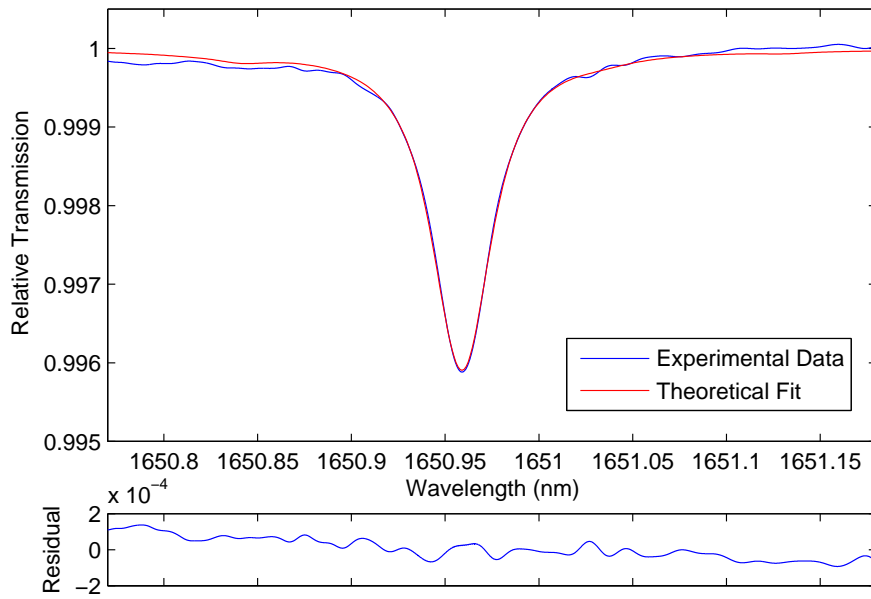


Figure 6.3: Experimental 0.1%  $CH_4$  absorption at 1650 nm ( $6060\text{ cm}^{-1}$ ) recovered using Hobbs circuit and normalised using (6.9), with accompanying Voigt fit.

## 6.4 Autobalanced Photoreceivers for Electronic RAM-nulling

Looking back to the analysis of WMS signals in Chapter 2 the form of the total intensity given in (2.3) can now be extended to second order:

$$I_{in} = I(\nu_1) + \Delta I_1(\nu_1) \cos(\omega t) + \Delta I_2(\nu_1) \cos(2\omega t + \psi'') \quad (6.11)$$

Where  $\Delta I_1(\nu_1)$  is the linear intensity modulation,  $\Delta I_2(\nu_1)$  is the nonlinear intensity modulation and  $\psi''$  is the phase angle between the linear and nonlinear intensity modulation. Following the same Taylor series expansion procedure as in (2.6) to give the output intensity that results from the interaction of the input signal with the absorption:

$$\begin{aligned} I_{out} = & [I(\nu_1) + \Delta I_1(\nu_1) \cos(\omega t) + \Delta I_2(\nu_1) \cos(2\omega t + \psi'')] \\ & \times \left\{ 1 - \alpha(\nu_1)Cl - \alpha'(\nu_1)Cl(\delta\nu) \cos(\omega t - \psi) \right. \\ & + \frac{1}{2}\alpha''(\nu_1)Cl(\delta\nu)^2 \cos^2(\omega t - \psi) \\ & \left. + \frac{1}{6}\alpha'''(\nu_1)Cl(\delta\nu)^3 \cos^3(\omega t - \psi) - \dots \right\} \quad (6.12) \end{aligned}$$

The expansion of this result will give the total intensity at all frequencies. This desired outcome of this analysis was to establish the terms that will contribute to the LIA output in conventional 2f WMS where the ratio of the line centre peak heights can be measured to gain temperature information from appropriate spectra. To do this the terms at  $2\omega$  in (6.12) can be collected to give the following expression which describes the various terms in the 2f output [109]:

$$\begin{aligned}
I_{2\omega} = & -\frac{1}{4}I(\nu_1)\alpha''(\nu_1)Cl(\delta\nu)^2 \cos(2\omega t - 2\psi) \\
& -\frac{1}{2}\Delta I_1(\nu_1)\alpha'(\nu_1)Cl(\delta\nu) \cos(2\omega t - \psi) \\
& -\frac{1}{16}\Delta I_1(\nu_1)\alpha'''(\nu_1)Cl(\delta\nu)^3 \cos(2\omega t - \psi) \\
& -\frac{1}{48}\Delta I_1(\nu_1)\alpha'''(\nu_1)Cl(\delta\nu)^3 \cos(2\omega t - 3\psi) \\
& +\Delta I_2(\nu_1)[1 - \alpha(\nu_1)Cl] \cos(2\omega t + \psi'') \\
& -\frac{1}{4}\Delta I_2(\nu_1)\alpha''(\nu_1)Cl(\delta\nu)^2 \cos(2\omega t + \psi'')
\end{aligned} \tag{6.13}$$

The output from the autobalanced photoreceiver will remove the 2f RAM term,  $\Delta I_2(\nu_1)[1 - \alpha(\nu_1)Cl] \cos(2\omega t + \psi'')$ , which scales with the DC signal and therefore is removed by the noise canceller operation. For measurements based on 2f peak heights the only part of the line shape that is relevant is the line centre, which for the odd-ordered derivatives is zero. This means that the 2<sup>nd</sup>, 3<sup>rd</sup> and 4<sup>th</sup> terms in (6.13) are also irrelevant leaving only the first and last terms which result from the second derivative. The last term is proportional to the nonlinear intensity,  $\Delta I_2(\nu_1)$ , which even at high modulation indices is small compared to the main second derivative proportional to the laser power,  $I$ . The effect of removing the background 2f RAM signal can be observed in Figs. 6.4 and 6.5 which show 2f outputs at a range of modulation amplitudes recovered from both a normal transimpedance photoreceiver and a Hobbs-type autobalanced photoreceiver. The effect of the background RAM was clearly increasing as the modulation amplitude was increased using the transimpedance amplifier but with the autobalanced photoreceiver the background signal remained small even above the 2f signal maximum which for these signals was near to 30 mA applied dither current.

This background removal effect could also be seen by observing the output voltage with an Agilent E4404B electrical spectrum analyser. To do this both signal and reference photodiodes were used to record two beams without any gas absorption present but in the same configuration as for a gas measurement. This means that only the background signals were evident as can be seen in Fig.

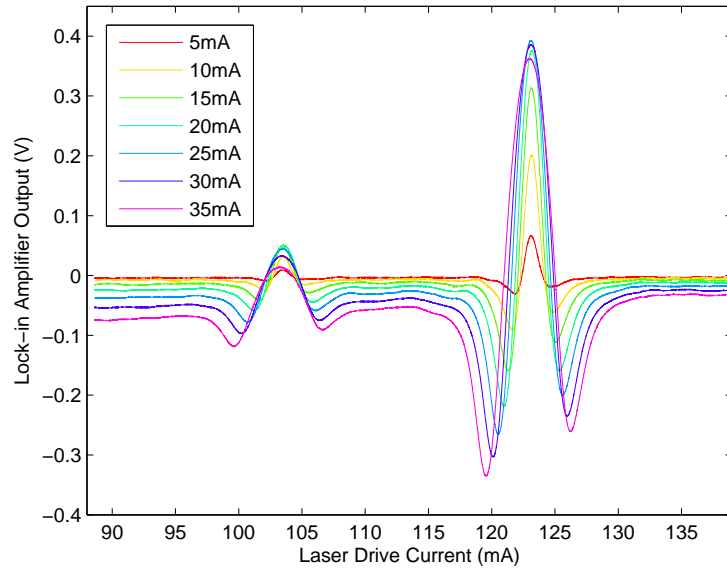


Figure 6.4: Water vapour at 1430 nm ( $6993\text{ cm}^{-1}$ ) recovered using normal transimpedance amplifier with  $2f$  detection. The modulation index is varied to highlight the increasing  $2f$  RAM component at higher modulation depths, with the legend stating the applied dither voltages.

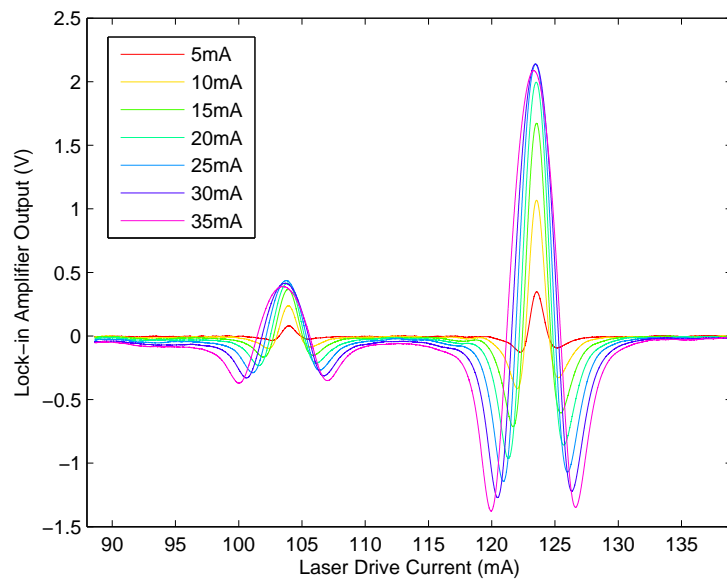


Figure 6.5: Water vapour at 1430 nm ( $6993\text{ cm}^{-1}$ ) recovered using Hobbs-type autobalanced noise canceller. The linear output is recorded using  $2f$  detection and this time the  $2f$  RAM is effectively nulled at higher modulation depths.

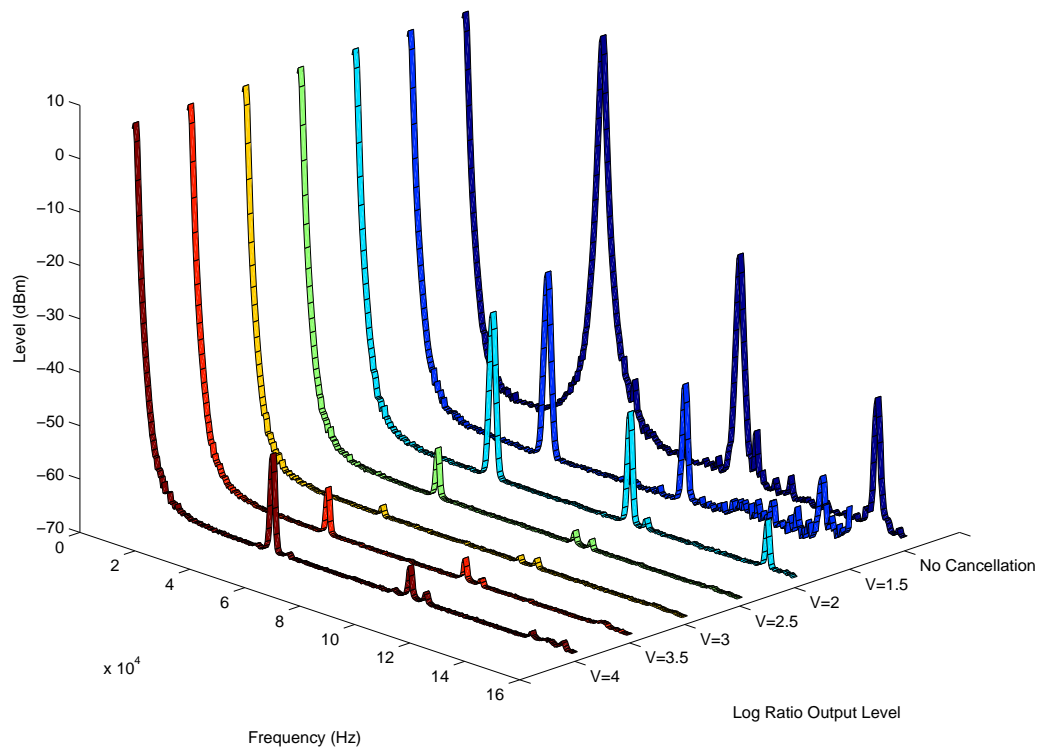


Figure 6.6: Spectral power density output of background signals (no absorption) from the electrical spectrum analyser showing the spectrum from DC up to the first three harmonics at 50 kHz, 100 kHz and 150 kHz whilst varying the beam power ratio in the photoreceiver.

6.6. This figure shows the spectral power density of the output between DC and 160kHz with the input signals modulated at 50kHz, allowing the  $1f$ ,  $2f$  and  $3f$  signals to be observed to illustrate the extent of the background cancellation and the ideal operating point of the receiver. The signal labelled ‘No Cancellation’ illustrates the output spectrum when the noise canceller operation was turned off and the circuit was effectively operating in transimpedance mode. The circuit operates when the reference photocurrent exceeds the signal photocurrent but there is an optimum beam power ratio at which the noise cancellation performance is maximised. Previous work has suggested that the optimum beam power ratio is  $\sim 2$  [48, 127]. The other signals in Fig. 6.6 show the change in background

signals as the relative beam powers were varied through the optimum beam power ratio for noise cancellation performance, which for this circuit was when the mean log ratio output level was at 3 V. At this optimum beam power ratio setting the background signals were reduced by 58 dBm at the point of the first harmonic and 43 dBm for the second harmonic, compared with the non-cancelled case. In some applications the user might be willing to sacrifice some noise cancellation performance to increase the dynamic range over which detector will perform good noise cancellation, if for instance the power in the signal arm was likely to be fluctuating and the reference beam power could not always be corrected using the variable optical attenuator. This could be achieved by varying the feedback resistor and capacitor values (R4 and C1 in Fig. 6.1), which changes the feedback loop bandwidth and flattens the drop-off in noise cancellation performance observed in Fig. 6.6.

There are two alternative methods for removing the unwanted 2f RAM signal. The first is described by Chakraborty et al. who use a fibre delay line to null the RAM contribution in addition to an application of the phasor decomposition method modified for the second harmonic [77, 109]. This is an effective solution but does not lend itself to the practical real-time recovery required in this case. The second alternative is to modify the output waveform of a multifunction DAQ board, like the National Instruments NI6120 described in Chapter 4 [30, 88, 132]. Normally a LabVIEW program is used to create an analogue output consisting of a summed sawtooth or triangle wave ramp signal and a high frequency sinusoidal dither. It is relatively easy to include a third component which is another sinusoid at 2f with a specific amplitude and phase that will have the effect of removing the 2f background RAM signal. This condition is satisfied only if the amplitude and phase of the additional component are chosen so that the modulation offsets the effect of the laser current-power nonlinearity. This solution is more appropriate for real-time data acquisition than the optical RAM-nulling method although it does require characterisation to set the phase and amplitude. For this work the autobalanced method was favoured as it provided a passive RAM-nulling system with the additional benefit

of common-mode noise cancellation.

## 6.5 Electronic Background Nulling for RAM-based Signals

### 6.5.1 Principles of Electronic RAM Nulling

The calibration-free RAM-based methods using wavelength modulation have been introduced and discussed in detail in Chapters 2 and 5. One of the key limitations of these methods is the high background RAM signal which saturates detection electronics and reduces the overall sensitivity of the system relative to alternative methods, such as 2f WMS. An optical approach to removing the non-absorbing RAM background was described in Section 2.4.4. This technique made use of an optical fibre delay line to introduce a phase delay into a reference modulation signal which when recombined with the recovered optical absorption signal, produced a RAM-nulled output signal that was detected with a fibre-coupled photodiode. Successful destructive interference and therefore RAM-nulling required that the phase shift in the modulation induced in the fibre delay line be  $\pi$ , whilst also maintaining equal optical power and orthogonal polarisation states between the two fibre arms. The fibre length required for a  $\pi$  phase change is given by:

$$L_{fibre} = \frac{c}{2n_e f_m} \quad (6.14)$$

Where  $c$  is the speed of light,  $n_e$  is the effective index of the fibre and  $f_m$  is the sinusoidal modulation frequency. The dependence of the delay length on the applied modulation frequency is a disadvantage as the allowed modulation frequencies in a given system are effectively fixed by the length of delay fibre used. It has been mentioned previously that the overall sensitivity can be improved for a given modulation index if the modulation frequency is increased, as the RAM absorption and RAM background signals increase with  $f_m$ . Using a shorter fibre length for higher frequencies is feasible until the length of the delay fibre

approaches the coherence length of the laser, at which point interference and noise become a major problem. In the studies performed by Chakraborty and colleagues the coherence length of the OKI DFB laser was calculated to be  $\sim 43$  m whilst they used a modulation frequency of 100 kHz and a delay length of 1 km to satisfy the condition,  $L_{coherence} \ll L_{fibre}$  [75–78, 109]. The potential of optical RAM-nulling for use in stand-alone systems is limited by the strict requirements for adjusting the intensity and polarisation of the two beam paths for operation. A VOA is used in the reference arm to adjust the relative beam intensities to the levels required for effective nulling. Polarisation control paddles are also used on both arms to ensure that the polarisation states of the two arms are orthogonal to reduce optical interference noise.

In this chapter the Hobbs-type autobalanced photoreceiver circuit was modified so that it was able to null the background RAM signal whilst still observing the RAM absorption signal. In a normal transimpedance amplifier both the RAM absorption and RAM background appear and saturate the detection and demodulation electronics, reducing the overall sensitivity. If a typical Hobbs-type photoreceiver were to be used instead, the modulated high frequency signals will be observable through the linear output as the feedback element acts as a high pass filter in this case. The LIA signal from the linear output will exhibit a RAM-nulled output as the background RAM is removed due to the common mode noise cancellation from the feedback. The RAM absorption, which clearly is not common to both paths, is unfortunately also cancelled because it scales exactly with the DC absorption and is therefore removed due to the correction by the feedback loop. This would be fine if the target signals were the purely frequency modulated signals that are left, however, it is the amplitude modulated signals that can yield the absolute absorption line shapes that are of interest in this work.

In Section 6.4 the effect of changing the feedback loop bandwidth on noise cancellation performance was introduced. In many circumstances it is desirable to have a high loop bandwidth that will allow laser ramp frequencies to be extended up into the kilohertz range. The achievable levels of common-mode noise

cancellation, especially unwanted background RAM signals, are also improved in this way. If the loop bandwidth is made smaller so that the ramp frequencies used are outside the loop bandwidth of the feedback element then it will not be able to respond fast enough to changes in the signal beam and the log ratio output is no longer representative of the difference between signal and reference beams. This operating scenario has some useful properties that can be exploited to significantly reduce the background RAM signals and increase the achievable lock-in sensitivities by as much an order of magnitude.

To operate in this mode the ramp frequency needed to be sufficiently higher than the feedback response bandwidth and the sinusoidal modulation needed to be significantly higher than the ramp as in any typical WMS system. The ramp frequency could not be increased indefinitely as the time constant of the LIA (typically  $30\mu\text{s}$  for the SRS830) dictated the upper limit at which useful data could be recovered. The other parameter that could be modified was the loop bandwidth of the circuit which could be reduced by increasing the values of the resistor, R4, and capacitor, C1, in Fig. 6.1. To achieve this the values of R4 and C1 were changed from  $10\text{ k}\Omega$  and  $8\text{ pF}$  to  $105\text{ k}\Omega$  and  $10\text{ }\mu\text{F}$  used with a sawtooth ramp frequency of  $10\text{ Hz}$  and a  $50\text{ kHz}$  dither modulation. There was another trade-off to be made when modifying the properties of the feedback amplifier and that was to do with the noise cancellation performance. In Fig. 6.6 the noise cancellation properties change significantly over the range of beam power ratios observed, which in this case was shown for six discrete ratio levels. If the system was stable and the beam power ratio could be set and no changes or drift affected the signal beam power then this situation was ideal for normal DC measurements. If the relative beam powers were likely to change and the reference diode could not be changed to return the receiver to its optimum operating point then the noise cancellation performance would vary. With a low feedback bandwidth, as proposed in this section, the noise cancellation performance was not as high as for the optimised design described earlier but was highly insensitive to signal beam power fluctuations, which is likely to be very beneficial in harsh environments.

The slow response of this circuit to changes in the signal beam did not

allow the target gas signal to be observed in the log ratio output as before. The log ratio output in this case still provided a useful feedback signal but now it yielded a stable output based on the mean signal level. The absorption signal was evident at the linear output on a nominally 0 V background. This output could be demodulated using a LIA to recover the RAM absorption signal. The reduced effectiveness of the noise cancellation typically lead to a small RAM background signal remaining on the LIA output but the aim in this case was to increase detection sensitivity by preventing the LIA from input overloading.

The validity of this proposed technique depended upon the reliability of the normalisation technique that enabled the LIA output signal to be converted into a relative transmission signal. In practice the magnitude of the RAM absorption signal depended upon the magnitude of the RAM background which was necessarily removed from the target signals. To establish the absorption relative to the background for normalisation, the nulling mechanism needed to be turned off in order to measure the magnitude of the RAM background in the absence of absorption. This process required a two stage acquisition process that could easily be automated into an operational system with an electronic switch to connect and disconnect the feedback signal that controls the base voltage on transistor Q2 in Fig. 6.1.

The same normalisation procedure used to recover transmission signals in optical RAM-nulling was applied in this case:

$$\frac{I_t(\nu)}{I_0(\nu)} = 1 + \frac{S_{gas} - S_{baseline}}{\Delta I(\nu) \cos \omega t} \quad (6.15)$$

The gas absorption signal,  $S_{gas}$ , was recorded and the near-zero background,  $S_{baseline}$ , recovered using a baseline fit or by removing the absorbing species, was subtracted. The term  $\Delta I(\nu) \cos \omega t$  was the background RAM signal which was measured with the nulling switched off either in the absence of the absorbing gas or by a baseline fit. For low modulation indices the resultant line shape represent the absolute absorption line shape. An improvement in the normalisation process was noted with the addition of a 7 pF feedback capacitor in parallel with the feedback resistor, R3. The effectiveness of the technique is illustrated by the

preliminary testing of this detector configuration in Fig. 6.7 which shows an absorption profile recovered at  $m=0.1$  for 10%  $\text{CH}_4$ . The theoretical fit exhibited excellent agreement with the equivalent direct detection fits and the resultant gas concentration was within 1.5% and pressures within 5% of their nominal values.

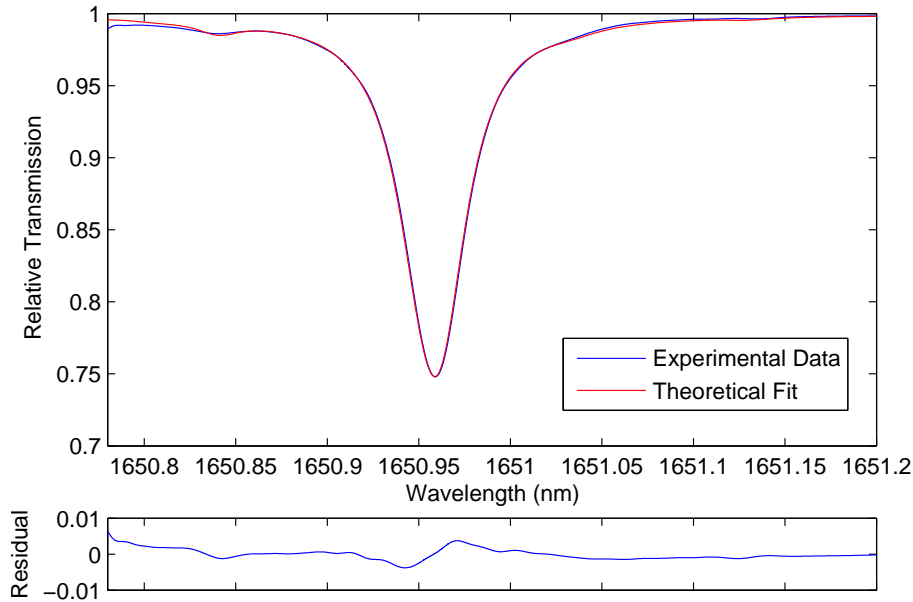


Figure 6.7: Experimental 10%  $\text{CH}_4:\text{N}_2$  line shape recovered at  $m = 0.1$  using electronically RAM-nulled output with theoretical fit.

This method of nulling the background RAM and isolating the RAM-dependent absorption has four main advantages over the optical RAM-nulling described above. Firstly the sinusoidal modulation frequency is not fixed by any constraint such as fibre delay length. There is no requirement to recouple into single mode fibre which will increase the range of potential applications as it provides more flexibility with detection options. Associated with this is that there is no longer any need for polarisation changing optics in the fibre setup. The electronic system in this form is essentially passive as the optical balance between the signal and reference photocurrents will be corrected automatically and exhibit consistent noise-cancelling performance within the operating limits of the receiver.

## 6.5.2 Preliminary Investigations into External Pure Amplitude Modulation with RAM-Nulling

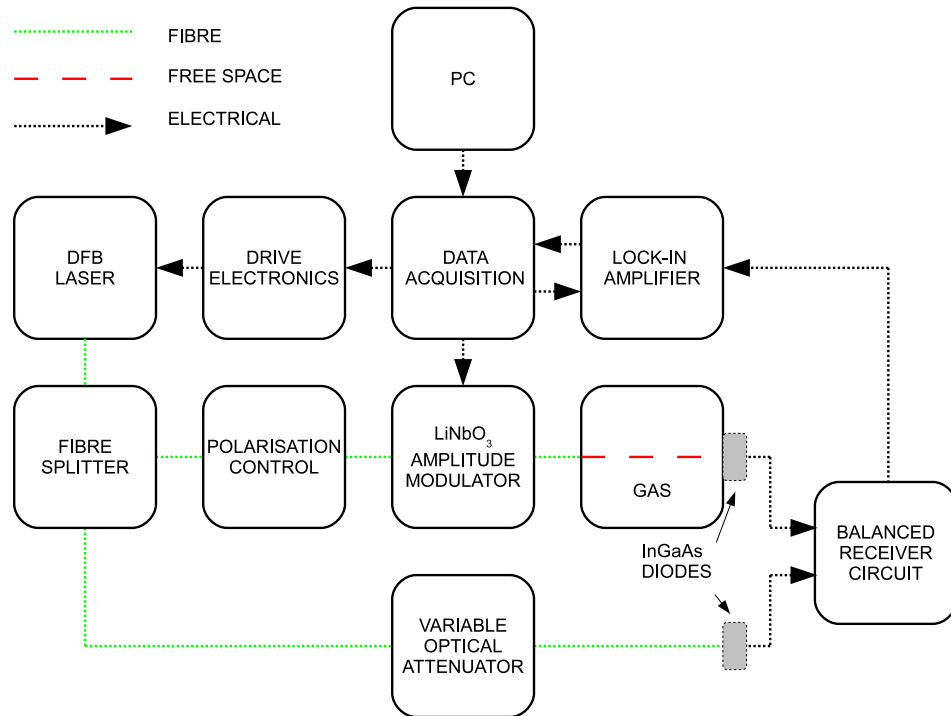


Figure 6.8: A typical experimental layout for an external amplitude modulation system with background-nulling.

Removal of background RAM-signals in TDLS with wavelength modulation will improve the overall sensitivity of the detection of absolute absorption line shapes from the RAM techniques. The application of this process to direct laser current modulated signals will always be complicated by the effects of the frequency modulation, which will create FM/AM signals that need to be accounted for and which will distort the RAM signals at high modulation indices. An alternative method of generating RAM signals was to maintain a sawtooth current ramp and to modulate the laser output externally using a lithium niobate amplitude modulator. The laser output in this case could be varied at high frequencies between full transmission and close to full extinction in a similar manner to the optical chopper systems employed in early TDLS studies [65, 133]. The primary advantages of such a detection scheme were that large intensity modulation signals were recovered by the lock-in amplifier, with no distortion due

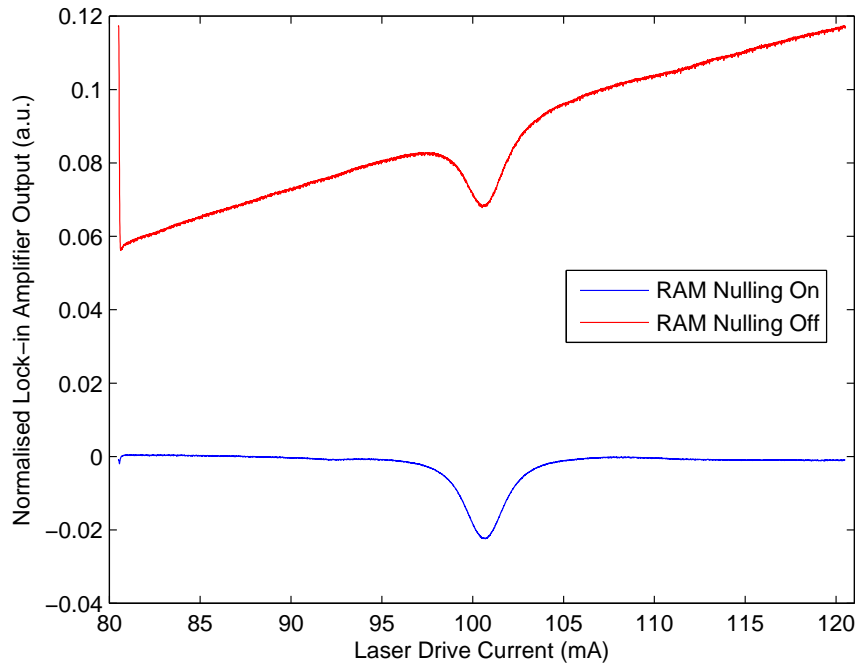


Figure 6.9: Experimental 10 % CH<sub>4</sub>:N<sub>2</sub> line shape recovered using external amplitude modulation signals with and without RAM-nulling.

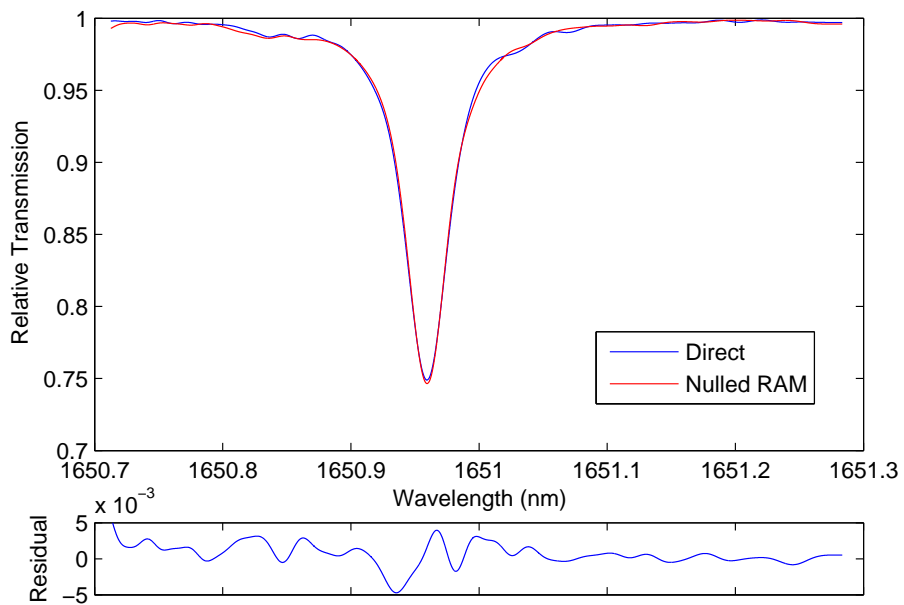


Figure 6.10: Experimental 10 % CH<sub>4</sub>:N<sub>2</sub> line shape recovered using background-nulled external amplitude modulation with equivalent direct detection signal.

to simultaneous frequency modulation. The normalisation and signal processing were reduced to the basic procedure used in direct detection, which was simple and could be implemented with minimal computational burden. A major benefit of pure amplitude modulation detection relative to direct detection was that the detection frequency can be set in the RF range well above the noise spectrum of vibrational resonances and other noise sources that severely compromise direct detection schemes in harsh environments. The main disadvantages of this method were the high signal background due to the current-power characteristic of the ramp sweep and the cost of the lithium niobate modulators.

The strength of this technique was improved further by utilising the RAM-nulling process outlined in the previous section. A schematic illustrating the experimental layout for this system is shown in Fig. 6.8. The laser output is split into two paths with one propagating through a fibre polarisation controller before reaching the amplitude modulator and then a gas path before detection and the other split passing through a VOA before being recorded by the reference detector. Removing the background through balanced detection prevented the lock-in amplifier from saturating as a result of the background RAM rather than the target signal. Each lock-in amplifier has a maximum input voltage which determines the overall sensitivity of the signal recovery. The improvement enabled by this technique can be seen in Fig. 6.9 which shows the LIA signals that are recovered with the RAM-nulling on and off. The bandwidth requirements of this circuit prevented the background RAM from being entirely removed but the requirement of preventing the saturation of the LIA input was satisfied. In the absence of any additional distortions the signal magnitudes can be optimised with ease and the recovered signals in preliminary investigations appear to agree well with the equivalent direct detection signals, as can be seen in Fig. 6.10.

## 6.6 Summary

The use of autobalanced laser noise cancelling photoreceivers has been investigated in the context of application in harsh environments. For direct

detection measurements the dual detector autobalancing circuit proposed by Hobbs was used with an appropriate normalisation procedure to recover absolute absorption line shapes from the DC feedback response of the circuit. As in all direct detection methods the normalisation process required a gas signal and an equivalent signal with no absorption present, from either evacuating the gas cell or by performing a baseline fit. An estimate of the photodiode temperature was also required to perform the normalisation calculation needed to establish the absorption spectrum. The recovery process was validated by recovering absorption spectra from calibrated gas mixtures and evaluating theoretical fits based on the experimental signals.

Autobalanced detectors are one of several methods that can be used for removing unwanted background signals in conventional 2f WMS. This RAM-nulling technique was advantageous due to its inherently passive nature and its lack of requirement for system characterisation or fixed modulation frequencies. For practical applications this method was shown to compare favourably to optical RAM-nulling and output modulation correction methods. One limiting factor was the trade-off between achievable nulling performance and the dynamic range of suitable operational signal and reference beam ratios. The suitability of the RAM-nulling circuit for 2f peak height measurements in WMS-based ratio thermometry measurements was established for use in the work described in Chapter 7 and for proposed future testing.

In the recovery methods based on the 1f RAM techniques introduced in Chapters 2 and 5, the standard autobalancing circuit configuration was not able to remove the unwanted RAM background without also removing the target RAM absorption signal, in contrast with the optical RAM-nulling method. This was due to the RAM absorption scaling exactly with the DC absorption signal removed by the feedback. A solution to this problem was proposed which involves a laser current ramp at a frequency outside the loop bandwidth of the feedback circuitry which did not allow the circuit to respond quickly enough to changes in transmission during the ramp. Preliminary results using absorption spectra recovered from certified methane mixtures showed that the absolute absorption

line shapes could be recovered reliably from the RAM signal with lock-in amplifier sensitivities over an order of magnitude higher than in the non-nulled case. The ability to recover absolute line shapes whilst utilising the noise benefits of dual beam detection, minimal background signals and LIA demodulation at high sensitivities, with suitably low sensitivity to changing signal power levels, is ideal for TDLS systems in harsh environments.

The use of high frequency external amplitude modulation rather than conventional sinusoidal current modulation was introduced. The advantages of this signal recovery method were described and its suitability for effective sensor deployment in harsh environments were discussed. The primary disadvantage of using externally amplitude modulated signals was the large background signals that saturate detection electronics and reduce overall sensitivity. The application of the electronic RAM-nulling detector to remove these background signals was demonstrated. Preliminary laboratory investigations suggest that this technique was able to recover absorption line shapes faithfully with high sensitivity, comparing favourably to, if not exceeding, the performance of the conventional WMS and direct detection methods with which it shares useful attributes. This method clearly has the potential to be a robust, sensitive, simple and repeatable technique for recovering absolute absorption line shapes, and therefore gas information, in a range of challenging applications.

# Chapter 7

## Aero Engine Intake Temperature Sensor Development

### 7.1 Introduction

In Chapter 1 several areas of aero engine diagnostics were identified for which TDLS could potentially provide measurement solutions. Ground testing of aero engines is an important function that is carried out during the development, test and refurbishment phases of an engine's lifetime. A large amount of collected data is necessary to fully evaluate the performance and status of a particular engine. One important measurement is the temperature of the intake gas flow, which has implications for the fuel mixing and combustion process. Accurate knowledge of the intake temperature is essential for any engine evaluation and inaccuracy in this measurement will require that the engine be shut down, at significant cost to the engine operators. The primary reason for failure to determine the intake gas flow temperature accurately, is misting at high humidities in the bellmouth where the thermocouples are positioned. If misting occurs the accuracy of the thermocouples will degrade sufficiently and compromise the ability of the operator to establish reliable engine performance data. In this chapter, an investigation is presented into the feasibility of using a TDLS-based ambient temperature sensor

based on the near-infrared water vapour spectrum. Each stage of the sensor design and evaluation process is discussed from the spectral database survey for selection of suitable absorption spectra to environmental chamber testing of the achievable temperature accuracy and precision. The initial sensor design requirements are summarised in Table 7.1.

Design Criterion	Requirement
Temperature range	273-313 K
Temperature accuracy	0.1 K
Data refresh rate	~ Seconds
Spatial constraints	Non-invasive bellmouth-mountable optics
Max. cabling distance	~ 70 m
Test cell power supply	240 V, 110 V, battery

Table 7.1: Sensor design specifications for ambient engine intake temperature sensor.

## 7.2 Selection of Absorption Lines for Ratio Thermometry

The first task in the development of a ratio thermometry sensor is to define the gas analysis problem and identify the experimental system constraints within which the final sensor will be expected to operate. These constraints include: constituent gas species, absorption path length, temperature range, anticipated gas concentrations and diode laser availability. With this information it is then possible to begin the process of identifying regions of the target species spectrum that would provide the optimum spectra from which to recover the required temperature information. In this work, the absorption line selection framework suggested by Zhou and co-workers was followed as this provided a comprehensive yet flexible method for filtering out unsuitable absorption features across a wide region of the HITRAN database [2, 82, 100]. The aim of this analysis was to

identify the most suitable absorption features for the target application, which may be entirely different from previous reports on TDLS ratio thermometry. This study in particular had an unusual target temperature range as very few researchers require TDLS-based measurements of ambient temperature due to the vast majority of applications using thermocouples and RTDs which outperform all other sensors. The high-value nature of the application suggested here and unusual circumstances that prevent traditional temperature sensors from being used made TDLS a viable alternative and a new survey of the spectral databases was required. The Zhou framework provided a list of selection rules that could be amended or omitted depending upon the individual requirements of the application.

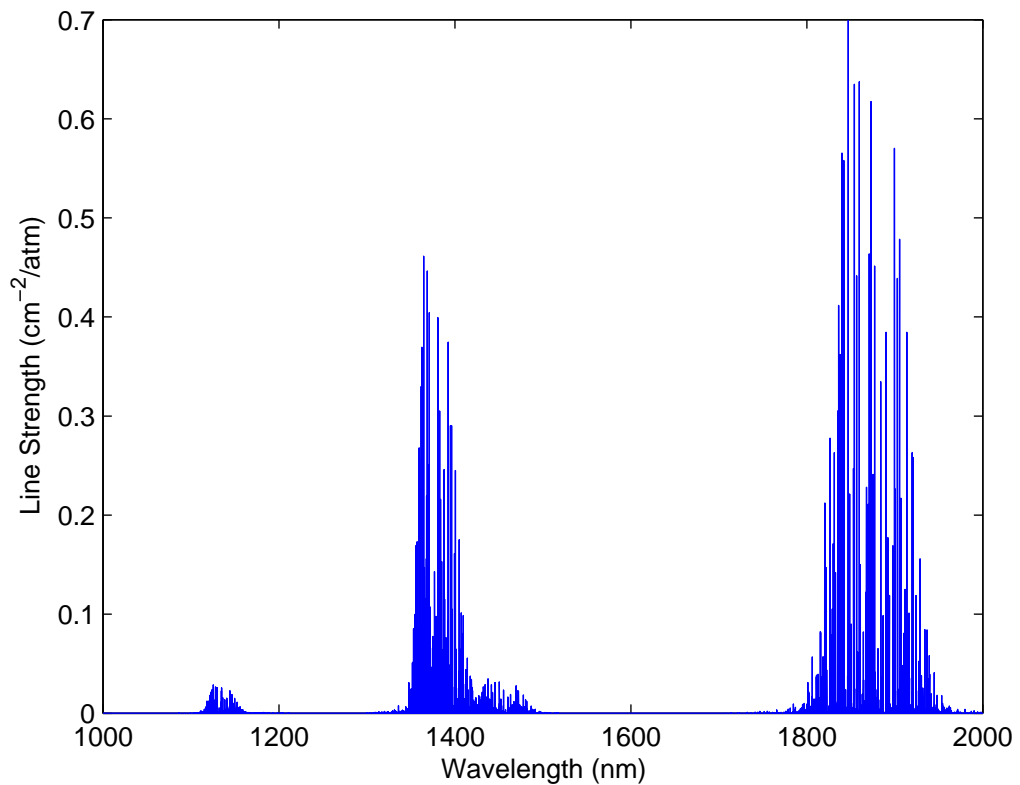


Figure 7.1: HITRAN 2008 data for water vapour line strengths at 296 K between 1-2  $\mu\text{m}$  ( $5000\text{-}10000\text{ cm}^{-1}$ )

The starting point for absorption line selection was the HITRAN 08 database for water vapour between 1000-2000 nm ( $5000\text{-}10000\text{ cm}^{-1}$ ), which

comprises 40672 individual lines. Water vapour was identified as the gas species most likely to provide absorption lines with suitable absorption and temperature characteristics at convenient detection wavelengths. The line strengths of those lines between 1000-2000 nm ( $5000\text{-}10000\text{ cm}^{-1}$ ) are shown in Fig. 7.1, which clearly shows three major overtone absorption bands. The smallest band centred on 1140 nm ( $8771\text{ cm}^{-1}$ ) is made up of the  $2\nu_1 + \nu_2$ ,  $\nu_1 + \nu_2 + \nu_3$  and  $\nu_2 + 2\nu_3$  vibrational assignments. The first larger band centred at 1400 nm ( $7140\text{ cm}^{-1}$ ) comprises the  $2\nu_1$ ,  $\nu_1 + \nu_3$  and  $2\nu_3$  vibration states. This band is of particular interest as it coincides with a region of extensive laser availability due to the mature telecommunications sources and peripherals available across this whole band. The other large band around 1890 nm ( $5290\text{ cm}^{-1}$ ) is from the  $\nu_1 + \nu_2$  and  $\nu_2 + \nu_3$  states. The entire spectrum in this region can be modelled given the appropriate experimental input parameters. The filtering and line selection process made use of the following selection rules, some of which were particular to the specific absorption and some related to a pair of lines that could potentially be used together for temperature determination.

1. **The total absorbance of each line needs to be appropriate for signal recovery.** The total absorption level for each line can be calculated to make sure that over a given path and with a certain concentration the absorption is sufficiently greater than the noise level to achieve an acceptable signal to noise ratio. For stronger absorbances it is also recommended that optically thick measurements ( $A > 0.8$ ) be avoided. The minimum absorption level in the filtering program was specified to be  $10^{-2}$  which was designed to give a generous SNR without being prohibitive due to the anticipated path lengths of 1 m and above.
2. **The absorption line should exhibit good spectral isolation.** The water vapour spectrum has several densely packed absorption bands, where many lines arising from different rotational-vibrational modes overlap and interfere with one another, even at atmospheric pressures. There are some lines that exhibit good isolation and these are preferred for obtaining gas

information as their line shapes do not contain significant contributions from the wings of nearby lines. If there are regions in the vicinity of the absorption line that exhibit minimal absorption, then these can be used for baseline fitting if direct detection or 1f RAM methods are used. This type of baseline fitting would not work if there was significant absorption across the entire laser scan range. A check should also be done to ensure that no other species that are likely to be present in significant quantities have any absorption features that might also interfere.

3. **The line pair would ideally be accessible within a single laser current sweep.** For a ratio thermometry system it is sensible to minimise the number of possible sources of error that might affect the recovered ratio and therefore output temperature. If two well separated absorption lines are used then two time- or wavelength- multiplexed lasers are needed to record the absorbances of both. The maximum ramp scan range of a typical DFB laser is between 1-2 nm so it is possible to recover multiple absorption lines with a single laser. If multiplexing is to be avoided to ensure the same conditions for both absorption lines, then the two lines should be close enough together spectrally that they can be recovered with a single laser.
4. **The line pair should have strong sensitivity to temperature changes.** The sensitivity of a line pair to changes in temperature is primarily a function of the lower state energy difference,  $\Delta E''$ , as shown earlier in equations (3.28) to (3.30). The line pair data should be checked to ensure that the lower state energy difference is capable of meeting the target sensitivity.
5. **The two lines should have similar SNR** Ideally the two lines should have similar absorbances so that the noise properties are equivalent for both. In reference [82] arbitrary limits on the allowed range of R, the line strength ratio, of  $0.2 < R < 5$  are imposed but there is some flexibility in this limit if necessary.

6. **The line strength ratio should be unambiguous over the target temperature range.** If the line strength ratio was to reach some maximum within the temperature range of interest, then there will be some ambiguous ratio values either side of the maximum which represent two distinct temperature values. The relatively small range of temperatures (273-313 K) that the sensor is designed to recover means that this requirement is unlikely to be a problem yet should still be checked.
  
7. **The two lines should have similar line shapes** This requirement is less important if direct detection is used exclusively but for WMS 2f peak height measurements, differences in the broadening coefficients and temperature dependence coefficient can have an effect on the recovered ratio. To avoid any dependencies that might arise from this, lines should be selected with similar values of  $\gamma_{air}$ ,  $\gamma_{self}$  and  $n$  [100, 106].

A MATLAB program was created to filter through HITRAN database for the water molecule, using the criteria outlined above. With so many absorption features contained within the 1-2  $\mu m$  (5000-10000  $cm^{-1}$ ) range it was difficult to optimise the line selection process without significant automation. The importance of each selection rule could be changed by altering the values of the constraints, allowing a manageable number of potential absorption lines to be output. The program made use of the Voigt profile simulation described in Section 3.3.3, allowing a visualisation for qualitative evaluation of each potential spectral region.

Two spectral regions were identified that provided favourable absorption features that satisfied the various selection criteria. The first line pair was at 1430 nm (6993  $cm^{-1}$ ) which exhibited good spectral isolation but was slightly less sensitive to temperature than a trio of lines near 1350 nm (7407  $cm^{-1}$ ), which were less well isolated. The spectral data for the lines of interest are shown here in Tables 7.2 and 7.3. A further advantage of these wavelength regions is the availability of high quality yet low-cost telecommunications lasers. The International Telecommunications Union (ITU) T-Grid standards for Coarse

Line	$\lambda$	$\bar{\nu}$	$S(T_0)$	$E''$	n	$\gamma_{air}$	$\gamma_{self}$	Band
1430A	1429.61	6994.904	$1.38 \times 10^{-22}$	885.6	0.53	0.0722	0.39	$2\nu_1$
1430B	1429.95	6993.263	$6.78 \times 10^{-22}$	212.2	0.73	0.084	0.454	$2\nu_2 + \nu_3$

Table 7.2: Spectral data for the line pair near 1430 nm ( $6993\text{cm}^{-1}$ ) with units as per Table 3.2 [26, 134]

Line	$\lambda$	$\bar{\nu}$	$S(T_0)$	$E''$	n	$\gamma_{air}$	$\gamma_{self}$	Band
1350A	1350.69	7403.615	$5.61 \times 10^{-22}$	931.2	0.65	0.0777	0.42	$\nu_1 + \nu_3$
1350B	1350.85	7402.744	$1.15 \times 10^{-22}$	1258.2	0.23	0.0583	0.35	$\nu_1 + \nu_3$
1350C	1350.99	7401.977	$9.08 \times 10^{-23}$	382.5	0.56	0.0753	0.395	$2\nu_1$

Table 7.3: Spectral data for the line pair near 1350 nm ( $7407\text{cm}^{-1}$ ) with units as per Table 3.2 [26, 134]

Wavelength-Division Multiplexing (CWDM) identify a range of wavelengths between 1271-1611 nm ( $6207\text{-}7867\text{ cm}^{-1}$ ) at spacings of 20 nm which coincide well with the wavelength regions identified by the line selection program [135].

## 7.3 Temperature Determination with Direct Detection

To examine the feasibility of a ratio thermometry temperature sensor based on ambient water vapour absorption a free space path was set up on a breadboard in the environmental chamber described in Section 4.3.1. A schematic of the experimental system is shown in Fig. 7.2 highlighting the positioning of the photodiodes and photoreceiver within the environmental chamber along with the free space optics. Initial experiments to test the sensitivity of the targeted water vapour absorption lines to temperature used a basic InGaAs transimpedance amplifier to recover spectra by cycling the chamber over the temperature range of interest. It soon became clear that to recover spectra with sufficient accuracy required a more sensitive detection method and preferably one where a baseline fit is more straightforward and repeatable or not required at all. For applications

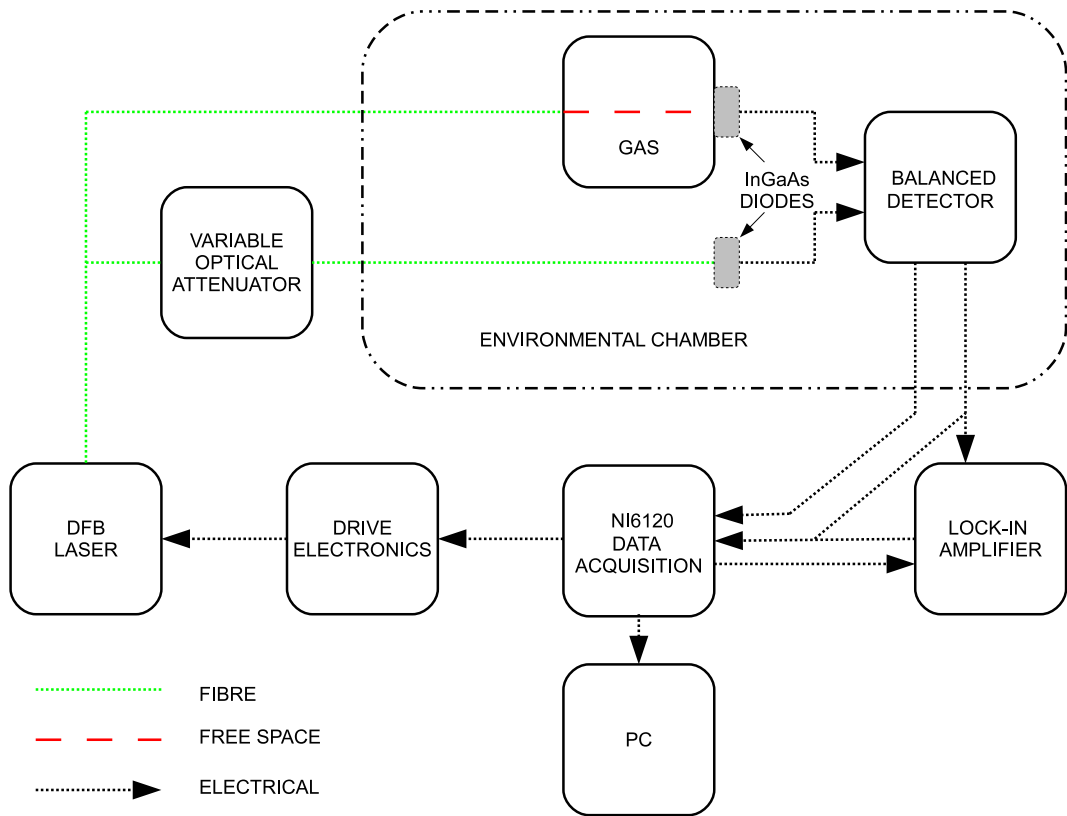


Figure 7.2: Schematic of experimental system used for measurements in the environmental chamber. The free space path is within the chamber and Hobbs-type autobalanced detectors were used to collect the signals. For direct detection the log ratio output was recorded directly by the data acquisition hardware and for WMS measurements a lock-in amplifier demodulated the linear output signal.

where the absorption is strong it was desirable to attempt to recover true absorption spectra in order to recover an absolute temperature reading rather than one which relied upon a calibration.

To test the ratio thermometry recovery methods, using the experimental layout shown in Fig. 7.2, the chamber temperature was cycled over the operating range of the potential application, between 273 and 313 K. The changes in recovered direct detection spectra over this temperature range using the two targeted spectral regions at 1430 nm ( $6993\text{cm}^{-1}$ ) and 1350 nm ( $7407\text{cm}^{-1}$ ) are shown in Figs. 7.3 and 7.4. These spectra show that as the temperature was changed the most noticeable difference in the spectra was due to the changes

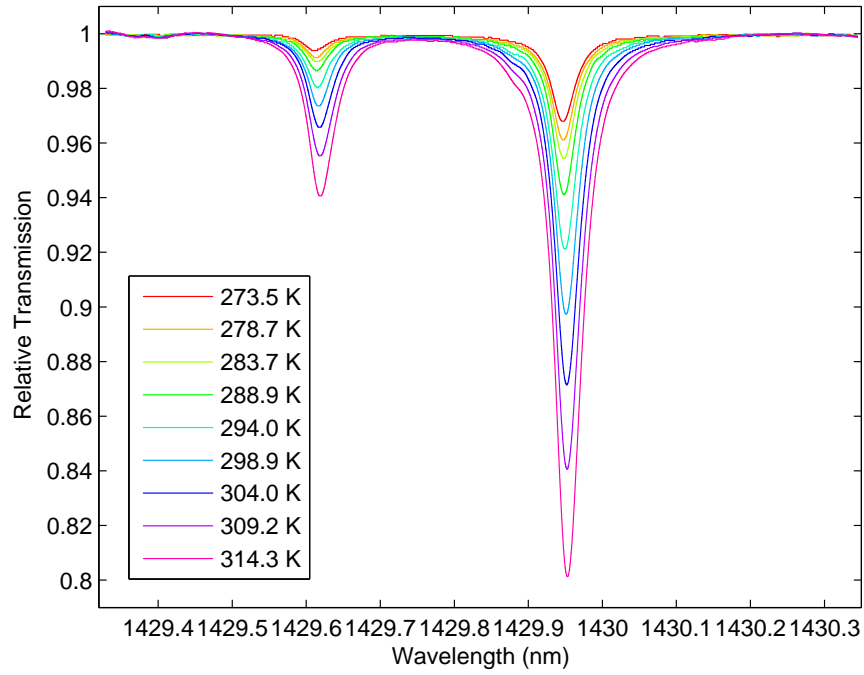


Figure 7.3: Direct detection output near 1430 nm ( $6993\text{ cm}^{-1}$ ) between 273-313 K at  $\sim 5\text{ K}$  increments.

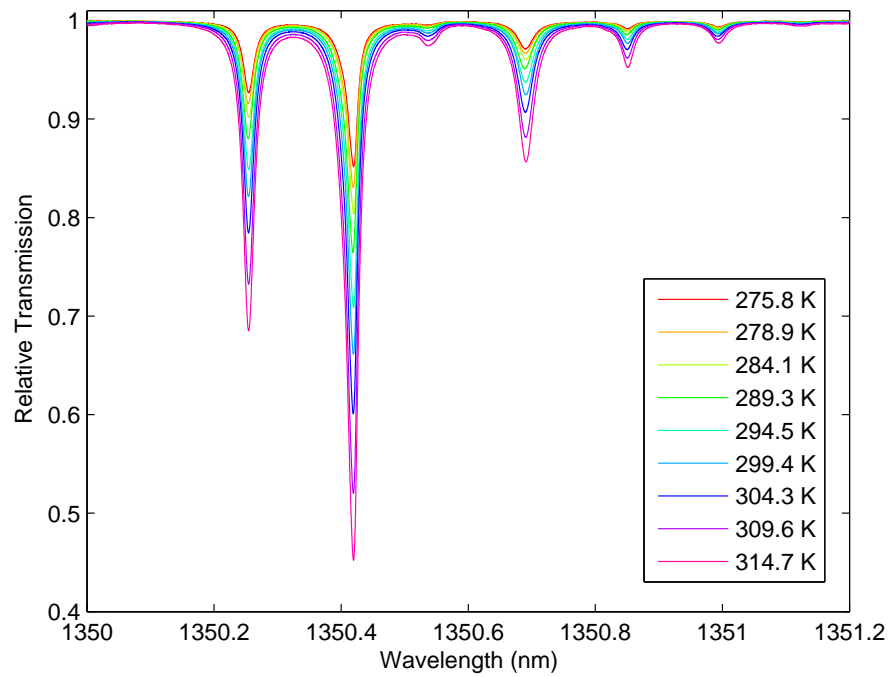


Figure 7.4: Direct detection output near 1350 nm ( $7407\text{ cm}^{-1}$ ) between 273-313 K at  $\sim 5\text{ K}$  increments.

in concentration. The humidity control function of the environmental chamber was coarse at best making it impossible to change temperature and maintain a constant water vapour concentration. As a result the concentration became an additional variable to consider in the fitting procedure.

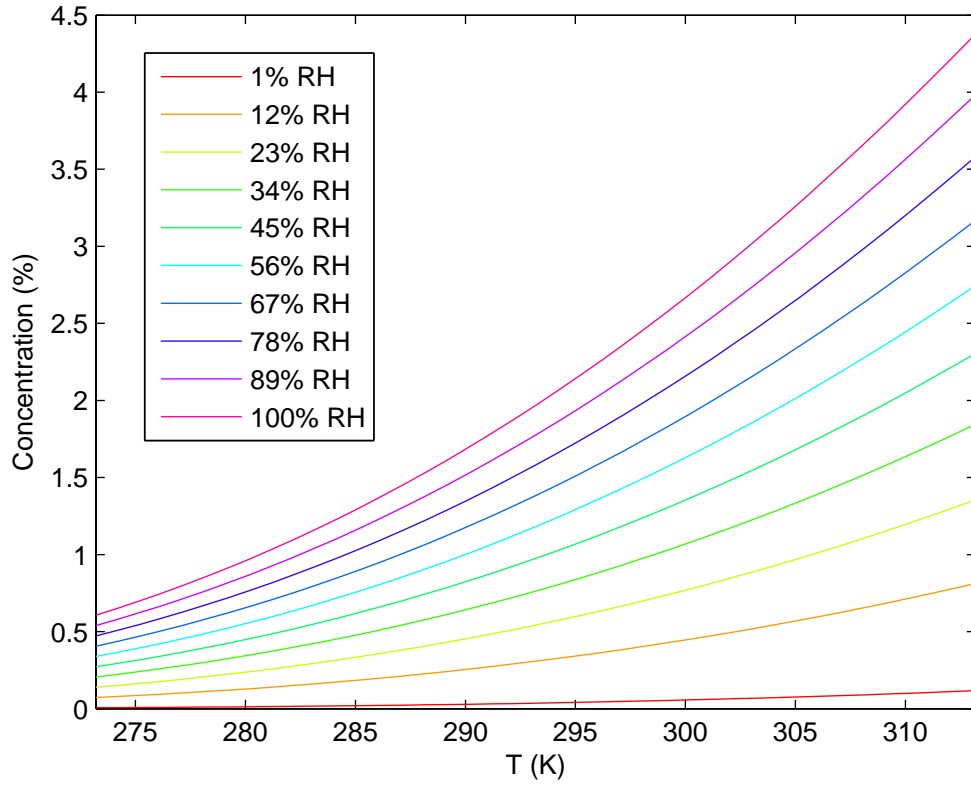


Figure 7.5: The results of an empirical model to calculate the change in water vapour concentration with temperature at various levels of relative humidity (RH).

A model was used to estimate the expected water vapour concentration at different levels of temperature and humidity experienced in the chamber environment. The dew point, or the temperature at which a cooling body of air at constant pressure and water content becomes saturated, can be calculated using the following equation from Puig et al. [136]:

$$\text{Dew Point (DP)} = \left( \frac{\ln\left(\frac{RH}{100}\right) + \frac{17.502T}{240.9+T}}{17.502 - \ln\left(\frac{RH}{100}\right) + \frac{17.502T}{240.9+T}} \right) 240.9 \quad (7.1)$$

where  $RH$  is the relative humidity in % and  $T$  is the temperature in °C. This was

then used to calculate a vapour pressure, in this case using an empirical model based on [137]:

$$\text{Vapour Pressure (VP)} = a_1 + a_2\text{DP} + a_3\text{DP}^2 + a_4\text{DP}^3 + a_5\text{DP}^4 + a_6\text{DP}^5 + a_7\text{DP}^6 \quad (7.2)$$

where the coefficients of the polynomial are given in Table 7.4. The water vapour concentration (in %) was then given by:

$$\text{Concentration} = \frac{(1 \times 10^6)\text{VP}}{10000(P - \text{VP})} \quad (7.3)$$

where  $P$  is the pressure [mbar]. Fig. 7.5 shows the result of this concentration calculation at a range of humidities and temperatures.

Coefficient	Value
$a_1$	6.11176750
$a_2$	0.443986062
$a_3$	$0.143053301 \times 10^{-1}$
$a_4$	$0.265027242 \times 10^{-3}$
$a_5$	$0.302246994 \times 10^{-5}$
$a_6$	$0.203886313 \times 10^{-7}$
$a_7$	$0.638780966 \times 10^{-10}$

Table 7.4: Polynomial coefficients for vapour pressure from Flatau et al. [137]

To test the effectiveness of the temperature recovery process a theoretical fit, with both gas concentration and temperature as variables, was performed on the absorption signal. The fit can be broken down into individual line contributions that could be integrated separately to establish the absorbance ratio or the temperature could be output as a result of the fitting process. These two methods lead to very similar output temperatures and a typical fit is shown in Fig. 7.6. This spectrum was recovered with a chamber temperature of 275.8 K and normalised using the same baseline fitting procedure outlined in Section 4.6.

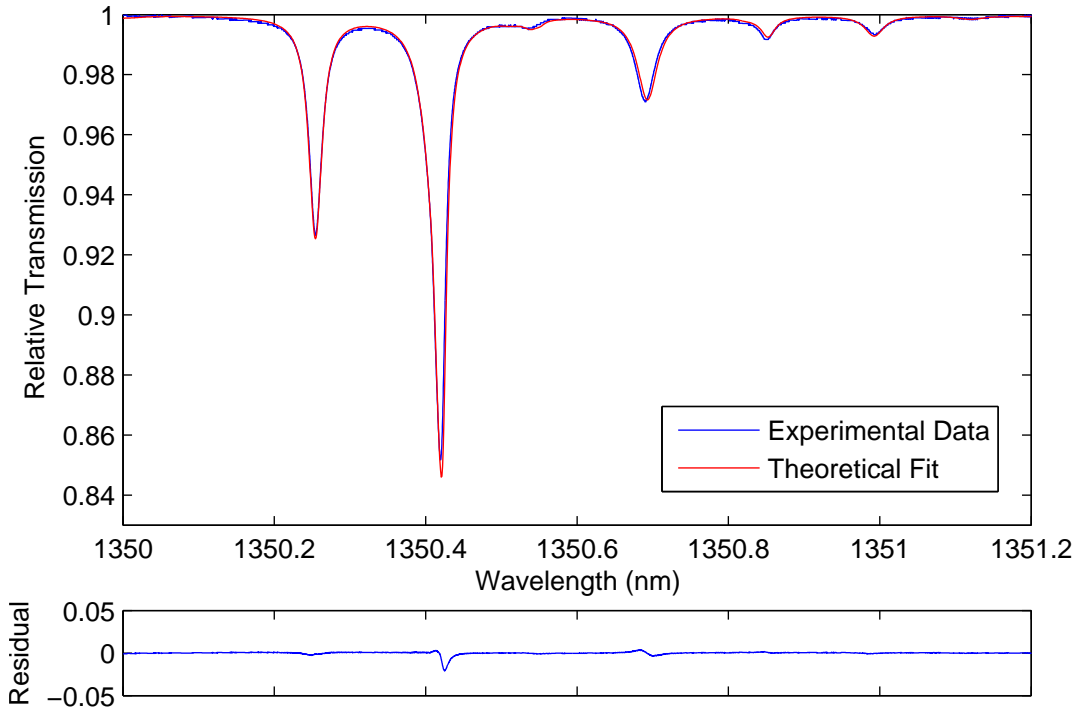


Figure 7.6: An example fit of the direct detection signal near 1350 nm ( $7407\text{ cm}^{-1}$ ) shown with the HITRAN08 theoretical fit.

The temperature fit concentrates on the three lines at the right hand side of the figure that exhibit the strongest sensitivity to temperature.

An indication of the accuracy of this process is given by Fig. 7.7 which compares the temperature readings from the fits with the temperature reference values from the Pt100 probe inside the environmental chamber. At each chamber temperature the signals were recovered at least five times and the standard deviation of the fit results are shown by the error bars. The figure shows that the recovered temperature was typically a significant underestimation of the actual gas temperature. The reason for the large errors and low repeatability of the measurements was the difficulty of baseline fitting with high accuracy. The error in wavelength referencing may also have contributed to the overall error in this procedure. This method was clearly not capable of giving temperature measurements with accuracy and precision close to that required for the aero

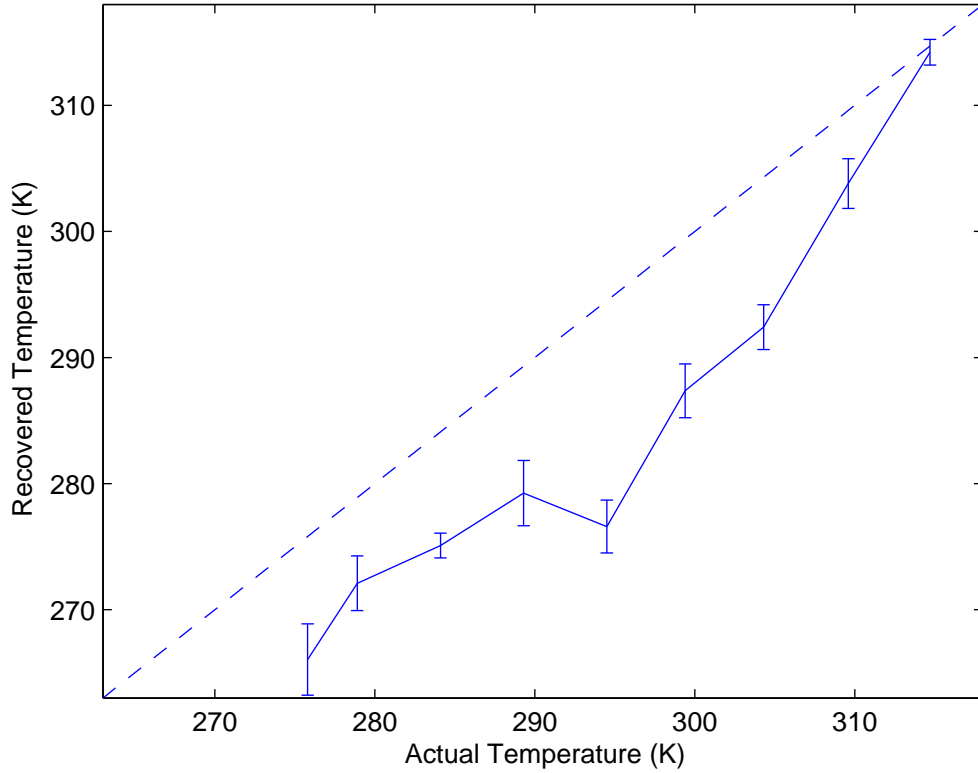


Figure 7.7: Repeated results of temperature fits across the temperature range of interest compared with the Pt100 reference temperatures. The error bars show the standard deviations of the repeated measurements at each chamber temperature.

engine intake application intended.

## 7.4 Temperature Determination with 2f WMS

The primary disadvantages of ratio thermometry with direct detection was the reliance on baseline fit and wavelength reference procedures that often have poor repeatability. To move away from temperature recovery based on absolute line shapes would have required the introduction of a calibration procedure to relate the recovered ratios to temperature. This is not an ideal situation because for a field deployable sensor maintaining constant experimental settings would be difficult and frequent calibrations would have been neither straightforward nor

desirable. With this in mind an attempt was made to compare the effectiveness and stability of a ratio thermometry system based on 2f peak height. This method had no requirement for a baseline fit or a wavelength reference scale which simplified the recovery procedure and also made the overall temperature acquisition time significantly faster.

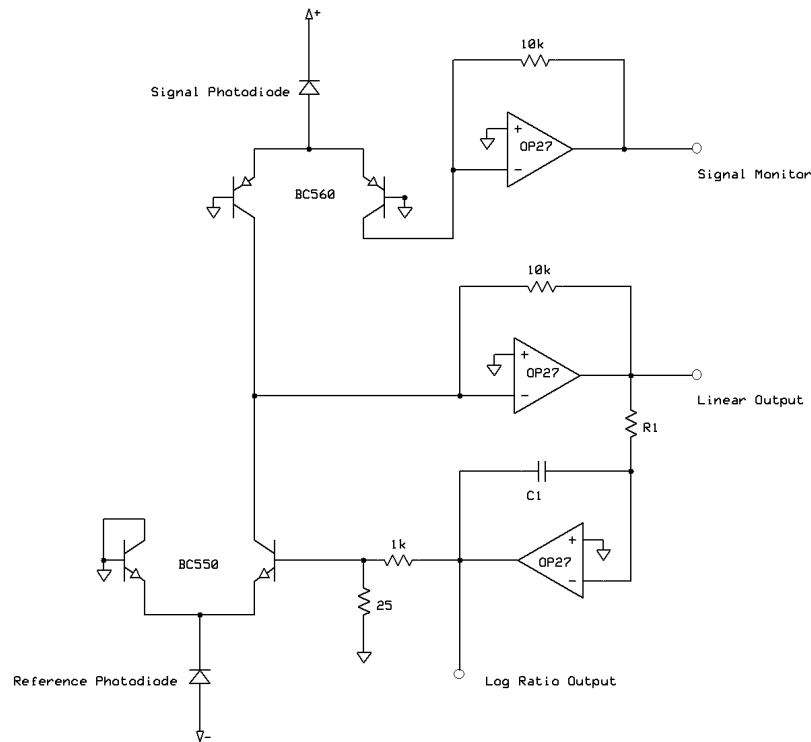


Figure 7.8: A modified version of the Hobbs autobalanced photoreceiver. The signal photocurrent is split 50:50 so that a voltage signal proportional to the signal power can be monitored.

A decision was made to use a variant of the Hobbs autobalanced photoreceiver, shown in Fig. 7.8, to cancel out the common mode laser noise and background RAM signals from the 2f signal as described in Chapter 6. Using the photoreceiver in this configuration required that the linear output be demodulated by the LIA rather than the log ratio output which was recovered in normal operation. This output was ostensibly 0 V if the feedback circuit was operating correctly, however, with the addition of the high frequency current modulation the RAM signals that were proportional to the DC signals were cancelled. This

left only the frequency modulated signals if the modulation frequency was well outside the bandwidth of the feedback.

The circuit shown in Fig. 7.8 was different from the similar layout shown earlier in Fig. 6.1 because in this case the signal photocurrent was split 50:50 between the feedback circuit and an additional transimpedance amplifier. The purpose of this was to recover a voltage signal that was exactly in proportion with the signal beam power that could be used to account for the beam power when establishing the 2f peak height ratio.

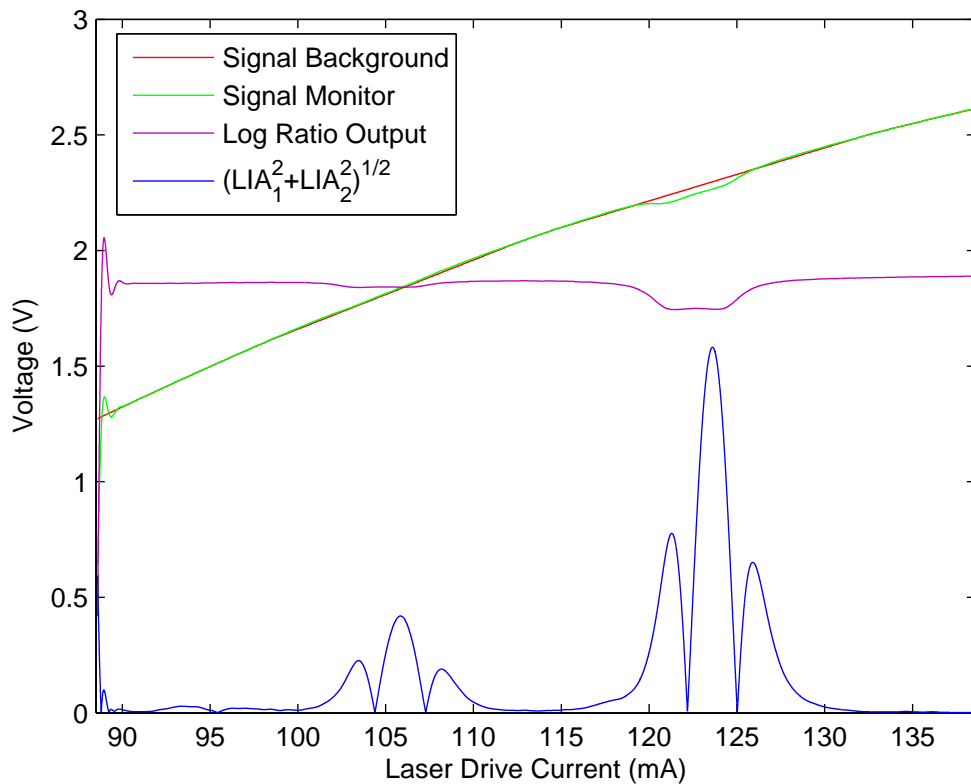


Figure 7.9: The signals recovered by the LabVIEW program include: the absolute magnitude of the two orthogonal LIA channels, a filtered signal photodiode monitor and a filtered log ratio output.

The NI6120 multifunction DAQ board was used in conjunction with a LabVIEW program to simultaneously output, record and process the signals required to make a temperature measurement. One of the two analogue outputs from the DAQ board was used to modulate the laser current driver with a

combined slow triangle wave and sinusoidal dither whilst the other provided a square wave reference signal for the external lock-in amplifier. It is possible in principle to create a software lock-in amplifier that would require only the DAQ hardware and remove the need for a stand alone lock-in amplifier entirely but to create a program with as much flexibility and functionality as the hardware option is a significant undertaking and was not necessary for this investigation. The four analogue inputs consisted of the two orthogonal LIA output channels, the photoreceiver log ratio output and the signal monitor. In addition to nulling the background RAM on the  $2f$  signal, a phase insensitive recovery method was used to remove any error in the  $2f$  peak height due to LIA initial settings or drift. This was achieved by taking the absolute magnitude of the two orthogonal LIA channels, which can be seen in Fig. 7.9 as the blue signal. The magenta signal shows the log ratio output level which could be monitored to indicate changes in the beam power ratio and to ensure the autobalancing was operating at the optimum power levels. The green signal is the signal monitor which was a voltage signal that was directly proportional to the signal photocurrent. The main term of interest in (6.13) is the term  $-\frac{1}{4}I(\nu_1)\alpha''(\nu_1)Cl\delta\nu^2 \cos(2\omega t - 2\psi)$  which is proportional to the laser power. To use this for a peak height ratio measurement the absolute magnitude of the LIA outputs was divided by a power reference. The signal photocurrent and therefore signal monitor will clearly exhibit attenuation due to absorption at the line centre points, with the added effect of the modulation. A baseline fit to this filtered signal did however provide a good approximation to the background power level which could then be used for the normalisation, shown in red in the figure. Within the LabVIEW acquisition program MathScript nodes allowed text-based mathematical programming, consistent with the MATLAB programs used throughout the project, to be used in real time during operation. By using MathScript nodes it was straightforward to implement filters, polynomial fits and peak identification routines that could then yield an output ratio value.

The first experiments with this recovery system used the absorption lines near 1430 nm ( $6993 \text{ cm}^{-1}$ ). A temperature calibration was required before ratio

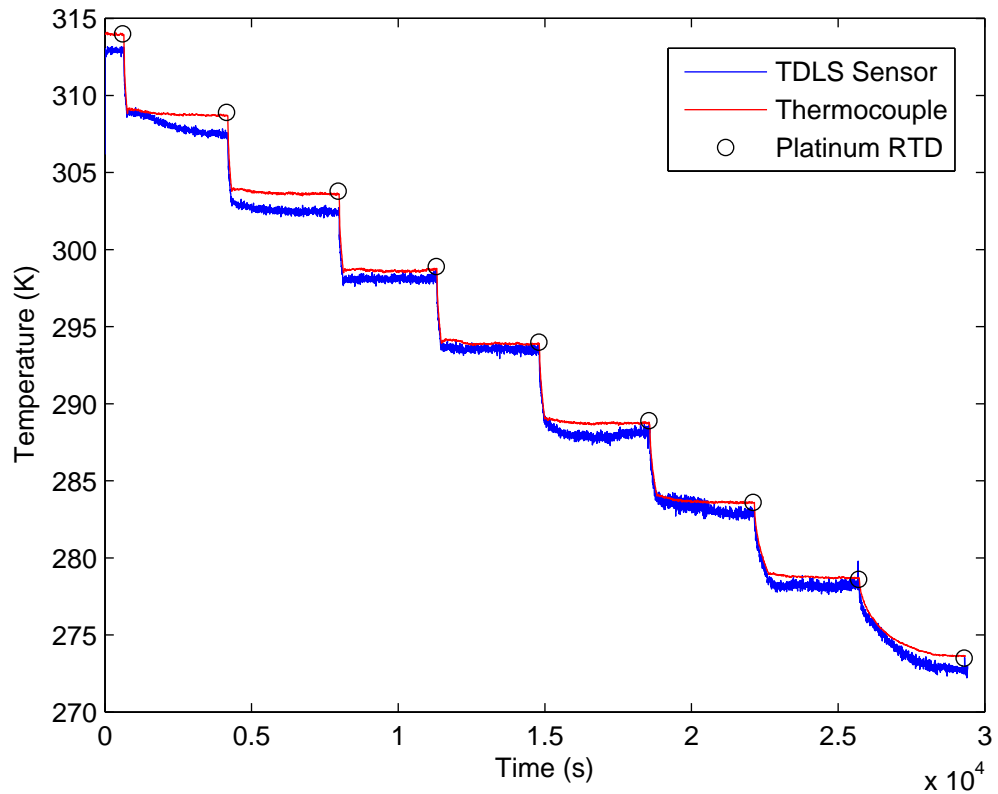


Figure 7.10: A single temperature cycle in the environmental chamber showing a comparison of TDLS temperature output with logged K-type thermocouple and single-point Pt100 measurements, using the 1430 nm ( $6993 \text{ cm}^{-1}$ ) absorption lines.

values could be used to output temperature values directly. The calibration run acquired ratio measurements continually over the course of a day-long chamber temperature cycle between 273 K and 313 K at 5 K increments. The Pt100 sensor was used to note the temperature after the chamber had been allowed to settle at each temperature, making a note of the time to compare with the time-stamped ratio data later. Once the full range of ratio and temperature data has been recovered a polynomial fit can be performed and the polynomial coefficients of this fit can then be used within the updated acquisition program to directly relate an experimentally recorded ratio to an output temperature. The calibrated program was able to output and record temperature values at a rate of 1 Hz, which was considerably faster rate than could be achieved if integrated

wavelength referencing and temperature fitting was required for direct detection temperature measurements. Fig. 7.10 shows a day-long chamber temperature cycle comparing the TDLS temperature output with the Pt100 reference and a logged thermocouple output. The Pt100 reference shows excellent agreement with the K-type thermocouple but the temperature output recovered using TDLS was as much as 1 K out from the reference, suggesting poor temperature accuracy. The precision of the measurements was significantly better than for any measurements obtained using direct detection which was largely the result of removing the main sources of error in those measurements; the baseline fit and the wavelength reference. Fig. 7.10 exhibits a noisy section at around 20000 seconds which produced a noticeable deterioration in precision. This was most likely the result of electromagnetic interference from a nearby monitor power supply, which was switched on during this period.

Efforts were made to identify the cause of the drift between calibration and test ratio values. The process was also adapted to utilise the most sensitive line pair near 1350 nm ( $7407\text{cm}^{-1}$ ) which would offer even higher precision without the need to increase the averaging time therefore reducing the temperature output rate. Fig. 7.11 shows recorded temperature data over a week long period. The first day was used for calibration and the resultant temperature values for the next four days are shown in the figure. Fig. 7.12 shows the change in ratio with recorded reference temperature over the course of the same week, which amounted to a mean deviation of 1.2%. This slight change in the polynomial coefficients each day lead to the presence of the residuals shown in Fig. 7.11. The accuracy of the TDLS measurements relative to the Pt100 reference was  $\pm 0.9\text{ K}$ , which was well above the overall target accuracy of 0.1 K. The technique does however offer relatively good temperature resolution due to the high precision of the measurements. In the second of the two examples shown the standard deviation of the recovered temperature, at those times during the week at which the chamber temperature was assumed to be settled and uniform, was  $\pm 0.4\text{ K}$ . If the integrating time could be increased at the expense of repetition rate then there is no reason why this could not be improved further.

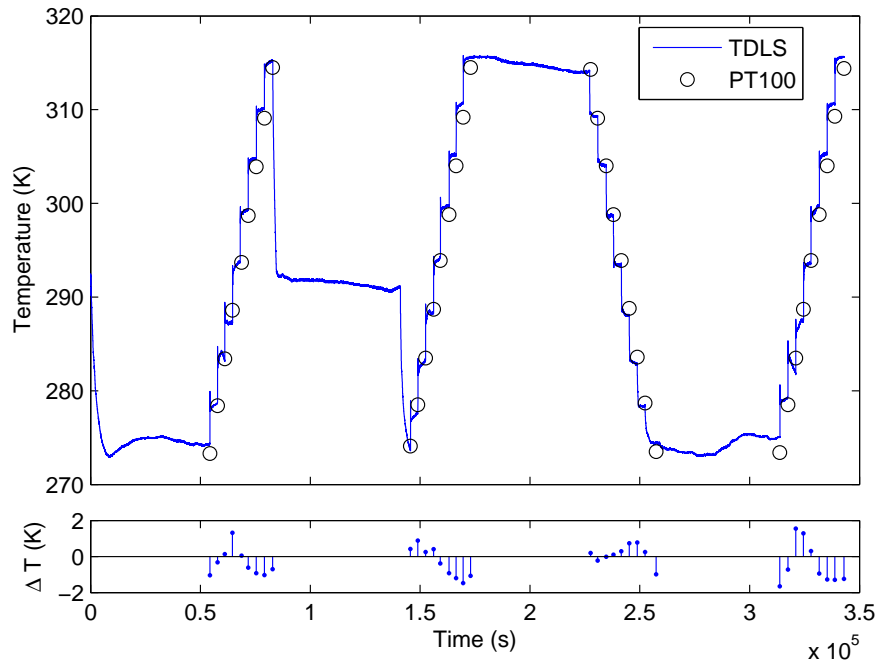


Figure 7.11: Calibrated temperature readings of the chamber temperature over the course of a week with an acquisition rate of  $\sim 1$  Hz. Single point reference temperature readings were taken periodically with a Pt100 RTD.

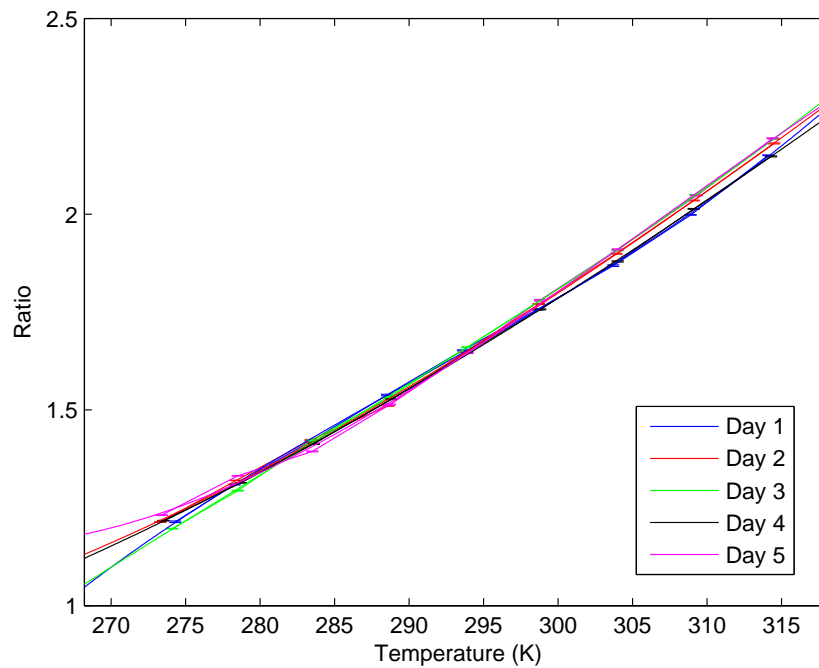


Figure 7.12: A comparison of the recorded ratios with temperature over the course of the week shown in Fig. 7.11.

An extensive literature search has not found any TDLS measurements that outperform this level of precision and associated temperature resolution, although most applications in this temperature regime would use traditional sensing methods which are more accurate and do not require calibration. There are several pertinent examples of TDLS-based temperature measurement that have been documented, most often related to combustion processes at elevated temperatures. Arroyo et al. observe direct absorption of water vapour in a heated shock tube achieving accuracies of  $\pm 2$  K at 295 K and  $\pm 18$  K at 598 K [92]. Allen et al. simulate turbine exhaust conditions in a laboratory hydrogen-air burner achieving a  $\pm 15$  K precision and 50 K maximum temperature error over the range 1200-2100 K [37]. J.T.C. Liu et al. demonstrate high speed temperature measurements at 1300 K using both direct detection and 2f WMS, achieving repetition rates of 4 kHz and 2 kHz with precisions of  $\pm 40$  K and  $\pm 21$  K respectively [7]. X. Liu et al. made laboratory temperature measurements over the range 350-1000 K with an average error of 2 K and achieved a precision of  $\pm 11$  K in an industrial gas turbine [6]. It can be seen that the general improvement in sensitivity and therefore temperature recovery precision and accuracy exhibited in this work, when changing from direct absorption to wavelength modulation spectroscopy, is reflected in the work of the wider TDLS community.

## 7.5 Summary

In this chapter the feasibility of creating an ambient temperature sensor based on TDLS ratio thermometry is described. There exists a need in aero engine ground testing to be able to recover accurate temperature readings of intake gases particularly when the air is saturated enough to cause misting which prevents standard temperature sensors from working properly. An absorption line selection procedure was undertaken using the HITRAN database to identify absorption lines in the water vapour spectrum that are sensitive to temperature. Using specific selection criteria relating to the potential application and using assumptions as to how best to approach the problem, two regions of the water

vapour spectrum were identified that contained multiple absorption features within a single DFB laser scan range and that provided good temperature sensitivity.

Using an autobalanced photoreceiver placed in an environmental chamber with a breadboard-mounted free space absorption path, absorption spectra were acquired at a range of temperatures. Theoretical Voigt fits for concentration and temperature, the two unknowns in this case, showed that the temperatures recovered in this way had low repeatability and accuracy due to the difficulty of recovering spectra with sufficient accuracy. A calibration-based method was developed that used the  $2f$  peak height of the absorption lines, which did not depend upon the same baseline fit normalisation procedure or require a wavelength reference. This method was shown to have a very high precision compared to other TDLS temperature studies yet the accuracy was still not high enough for the target application and also appeared to be prone to drift over extended periods. As a practical solution to the problem at hand, the need for calibration and systematic drift prevented this method from being a viable alternative to existing methods in this case.

# Chapter 8

## Aero Engine Ground Testing

### 8.1 Ansty Tests

The first engine test campaign undertaken during the project was intended to be a preliminary test investigating intake absorption signals for temperature measurement. Permission was given to install a basic system upstream of a small turbojet engine bellmouth at Rolls-Royce Ansty. The aims of the test, which occurred in the initial stages of the project, were to get experience of installing TDLS systems in engine test cells whilst gathering valuable information about system performance during engine operation. A comparison of how different TDLS techniques perform would provide valuable information for future tests.

#### 8.1.1 Experimental Setup

The Ansty tests were performed on a Rolls-Royce Viper turbojet engine owned and operated by SciTek Ltd. The drive and signal electronics were housed in the test bed control room adjacent to the test cell. Single mode fibre patch cables were used to deliver the laser signal to the vicinity of the engine and coaxial cable fed the photodiode signal back to the data acquisition hardware. The absorption signal was recorded using a movable mounting frame that was positioned upstream of the engine bellmouth, as modifications to the bellmouth

itself were not allowed in this case. The mount used to hold the collimator and photodiode was a proprietary frame with a motorised base built by SciTek Ltd. The absorption path was created vertically perpendicular to the engine axis by mounting the fibre collimator facing upwards with a Thorlabs PDA10CS InGaAs photodiode facing downwards at a distance of 110 cm from the collimator, as shown in Fig. 8.1.

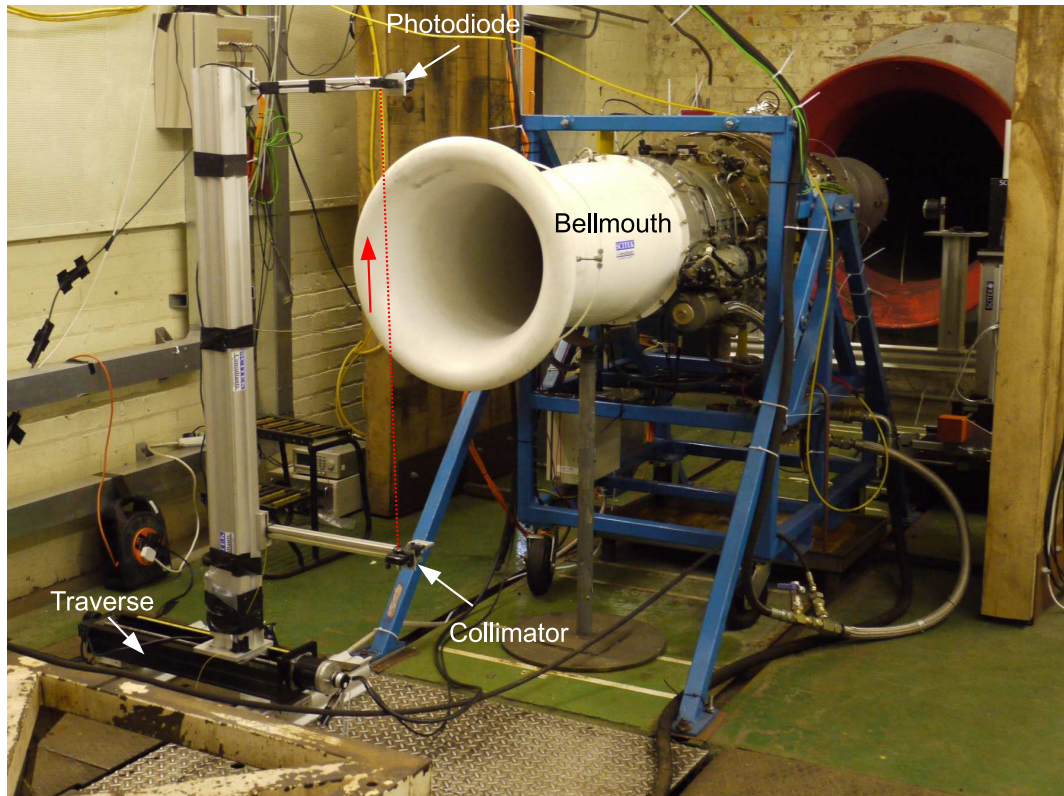


Figure 8.1: Rolls-Royce Ansty: Viper engine test cell. Experimental layout for intake absorption measurements. The laser beam path is shown with a red line.

The motorised mount was able to traverse the position of the beam from the engine axis to a position outside of the main flow into the bellmouth entry. A water mist sprayer was installed upstream of the beam path which could be turned on from the control room. This was designed to create fine water droplets intended to simulate the misting conditions that would be encountered in the target application.

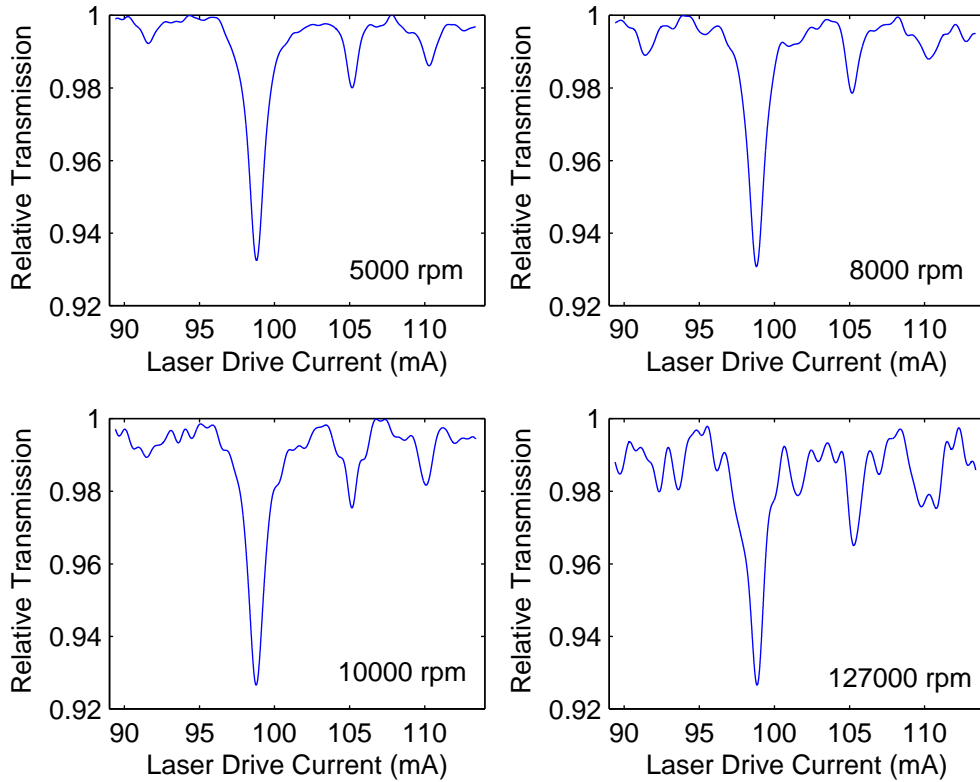


Figure 8.2: Direct detection signals taken at 5 Hz with 128 averages at four different engine speeds between idle (5000 rpm) and full throttle (12700 rpm)

### 8.1.2 Direct Detection

Direct detection signals were recovered at a range of engine speeds from switch off to full throttle. The current was modulated with a sawtooth ramp at an amplitude of 80 mA and at a rate of 5 Hz. A reference signal from a similar fibre-coupled photodiode was used to normalise the recovered absorption signals.

The change in recovered signals with engine speed is illustrated in Fig. 8.2. As soon as the engine was switched on and accelerated to idle, noise became apparent on the collected signals. As the engine speed approached its maximum at 12700 rpm, the effect of the noise became increasingly significant and the SNR deteriorated noticeably. The spectra in the figure were averaged over 128 cycles (25.6s), which improved the SNR relative to sampling mode when no integration is employed. As the engine accelerated between the static engine speeds occasional spikes in noise were observed that were assumed to coincide

with various resonances in the system. The noise in this case was primarily due to the effect of the arms on the mount setup which were prone to moving relative to each other and therefore displacing the positions and orientations of the collimator and detector. In this setup the size of the laser beam was comparable to the detector active area so any displacement of the beam's position relative to the diode would be seen as a change in voltage on the photodiode output. The changing noise spectrum of this vibrating system when the engine is running is unknown but when this effect became apparent it was hoped that using higher frequency wavelength modulation might reduce the effect of the noise.

### 8.1.3 Wavelength Modulation Spectroscopy

In order to perform a comparison between potential TDLS methods the direct detection signals were compared with RAM-based signals and basic 2f WMS. The advantage of using wavelength modulation was to increase the detection frequency to a point that was ideally above the upper limit of the vibrational noise frequency spectrum. Reducing the detection bandwidth will help but if there are still resonances as high as the detection frequency then this noise would still be evident on the DC signal after demodulation.

The RAM method signals used a modulation frequency of 100 kHz and a modulation index of  $\sim 1$ . This value was chosen to avoid an artefact of the lock-in amplifier output visible at low signal levels, without introducing too much of the distortion evident at high  $m$  values. The second harmonic signals were maximised with a modulation index of  $\sim 2.2$  at the same modulation frequency. The unnormalised signals obtained from using the RAM method at different engine speeds are shown in Fig. 8.3. At low engine speeds the RAM signals exhibited minimal vibrational noise yet at higher engine speeds the SNR deteriorated significantly, suggesting that the frequency spectrum of the vibrational noise contained significant contributions up to 100 kHz. The recorded 2f WMS signals shown here in Fig. 8.4 contained no noticeable noise, even at full throttle and without any signal averaging. This could have been because 200 kHz was higher in frequency than any of the frequency components or possibly that no significant

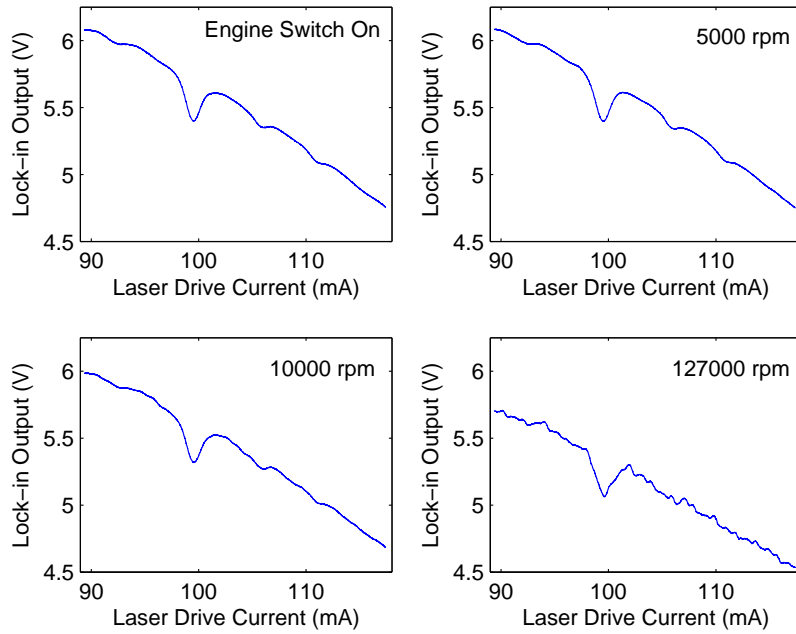


Figure 8.3: Raw RAM signals ( $m \sim 1$ ,  $f = 100 \text{ kHz}$ ) with 64 averages at four different engine speeds between engine start and full throttle (12700 rpm)

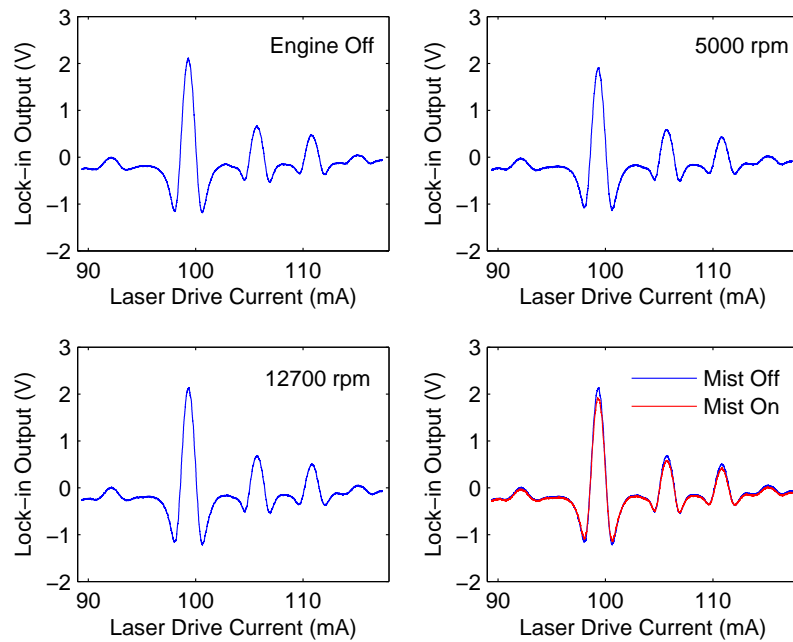


Figure 8.4: Raw  $2^{\text{nd}}$  harmonic signals ( $m \sim 2.2$ ,  $f = 100 \text{ kHz}$ ) taken at three different engine speeds between idle (5000 rpm) and full throttle (12700 rpm) and a comparison of the full throttle signal with the water mist turned on and off.

resonances occurred at this frequency, which could account for the noise observed on the 1f RAM at 100 kHz. Due to their favourable SNR, the 2f WMS signals were used to examine the effect of the fine water mist spray. Signal attenuation of around 10-15% was observed in the magnitude of the 2f signal due to droplet scattering in the water vapour mist suggesting that signals could potentially be recovered in all but the densest intake misting conditions.

## 8.2 East Rogerton Tests

The second engine test campaign was undertaken over several weeks at Rolls-Royce East Rogerton on a test bed for refurbished Tay engines. The tests were to look at the feasibility of using a detuner-mounted TDLS system to observe the exhaust plume of the high-bypass turbofan Tay engine. Detuners are test cell exhaust systems used to route exhaust gases from the engine to the exterior open air, an example of which can be seen in Fig. 8.5. The motivation for attempting a detuner-mounted system was to assess whether such a system could be used in a tomographic mapping application where many absorption paths would be created across the exhaust plume. Using the information provided by the previous tests at Rolls-Royce Ansty a folded path arrangement was used across the detuner lip with an improved optical layout intended to reduce sensitivity to beam steering and an autobalanced detection method was tested.

### 8.2.1 Experimental Setup

The experimental system used for this campaign was split between the test bed control room and the in situ components at the detuner. The drive electronics, laser source and data acquisition hardware were all situated remotely with two single-mode fibre patch cables and two coaxial cables covering 30 m to the send/receive hardware mounted on the detuner lip. A photograph of the test cell detuner with the mounts and cabling in place is shown in Fig. 8.5, with red lines drawn in to illustrate the folded beam path across the detuner. The free-space beam was launched using an FC-APC connectorised collimator before

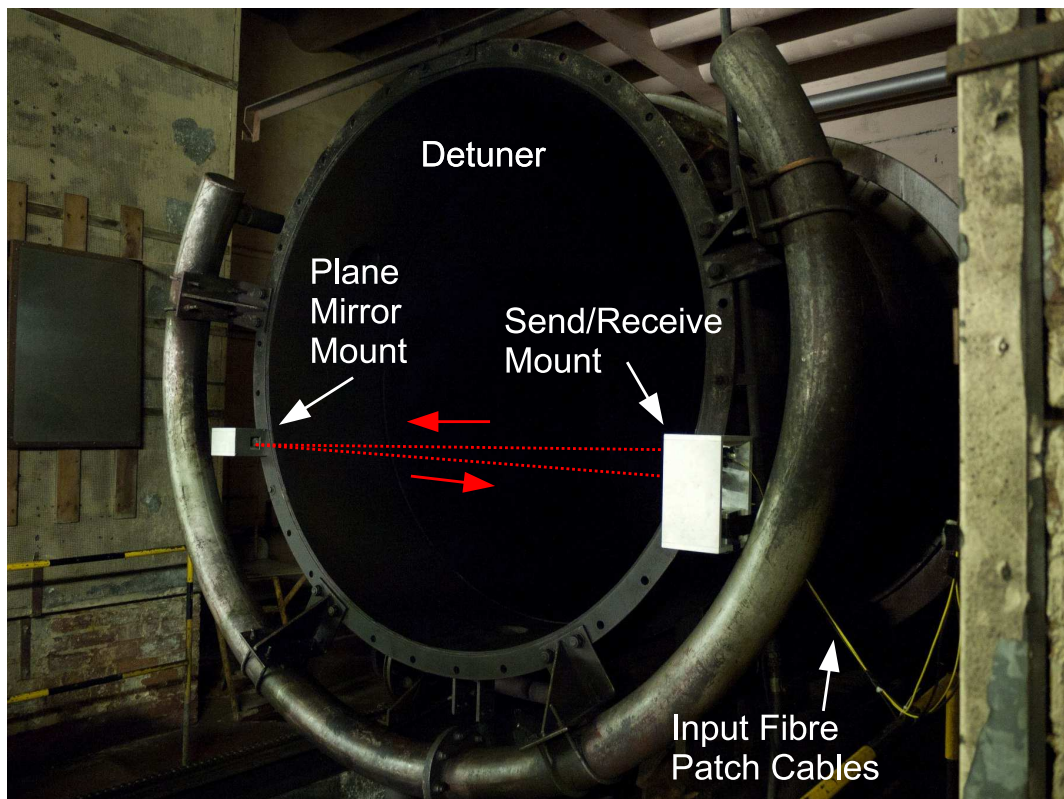


Figure 8.5: Rolls-Royce East Rogerton: Tay engine test cell. Experimental layout for detuner-mounted exhaust plume absorption measurements. The laser beam path is shown with a red line.

traversing the detuner, reflecting at a plane mirror on the opposite side of the detuner and returning to a concave mirror adjacent to the collimator, as shown in Fig. 8.6. The concave mirror focussed the beam to a 1.5 mm photodiode at a distance equal to the focal length of the mirror. A small die cast box containing a Hobbs-type autobalanced photoreceiver was situated next to the photodiode mount and a FC-APC connectorised InGaAs diode in the box was used to connect the reference fibre path to the autobalanced receiver. The proximity of the photodiode front-end circuitry to the photodiode itself was important in order to minimise the noise pick-up in the shielded dual-core coaxial cable used to carry the signal photocurrent from the diode to the amplifier. The photoreceiver circuit was also required to run on battery power as no 240 V power supplies were allowed in that region of the test cell for safety reasons. As a result the operational amplifier power and photodiode bias voltages were supplied by two

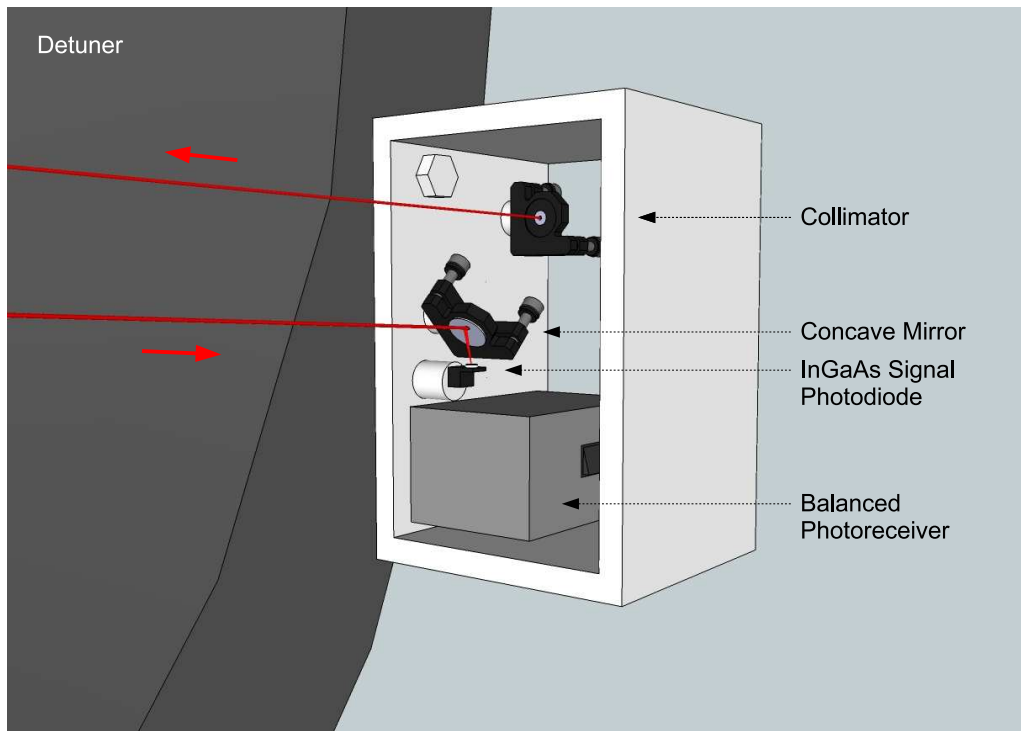


Figure 8.6: A schematic of the send/receive optics mounted on the detuner showing the position of the collimation and detection optics.

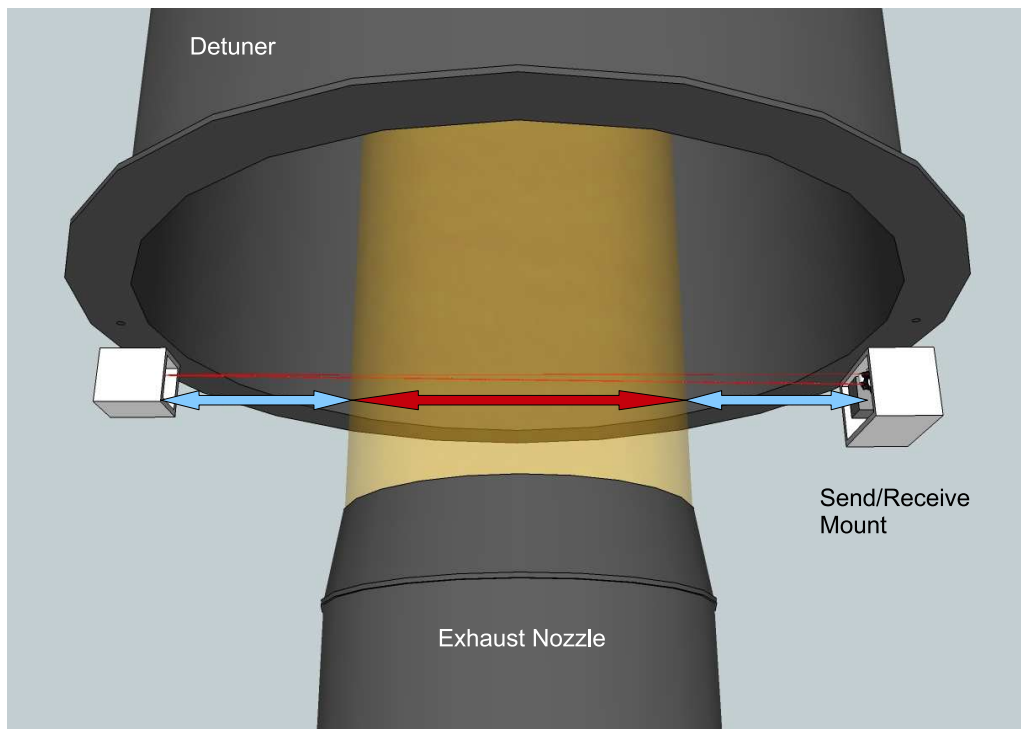


Figure 8.7: Schematic of detuner-mounted system showing the hot and cold regions traversed by the beam in the folded path arrangement.

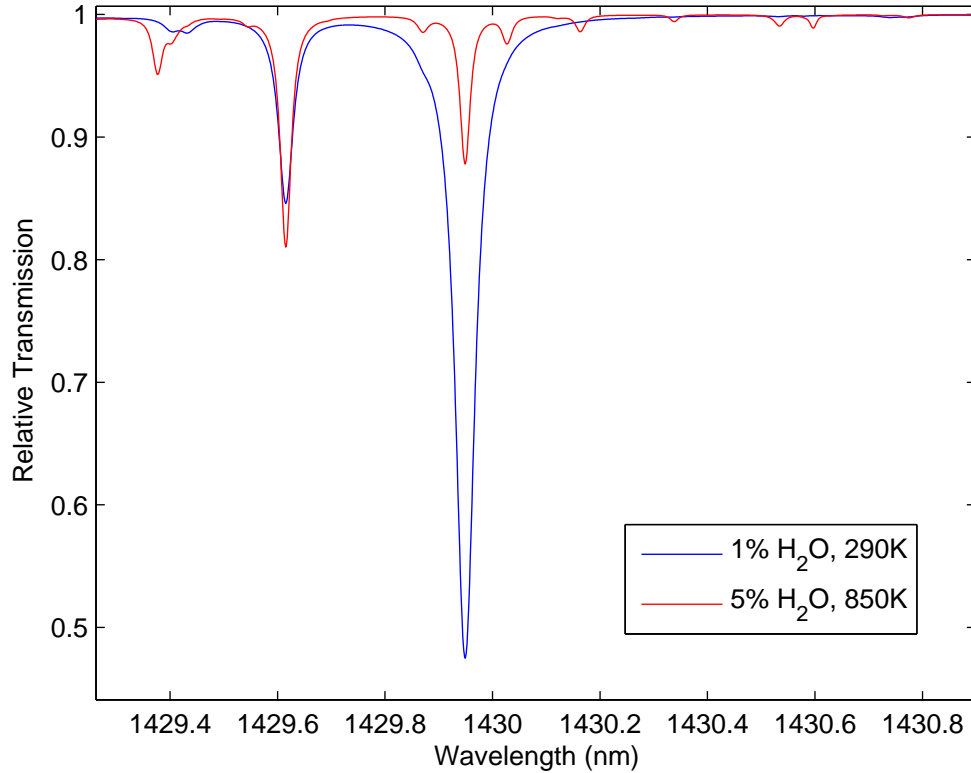


Figure 8.8: Simulated spectra based on HITRAN08 database showing two contributions to the path averaged signal. The blue signal is the ambient (1%, 290 K)  $\text{H}_2\text{O}$  absorption outside the plume whilst the red signal shows the contribution from the hot exhaust  $\text{H}_2\text{O}$  vapour (5%, 850 K).

9 V PP3 batteries.

The laser source used was the 20 mW 1430 nm ( $6993 \text{ cm}^{-1}$ ) DFB chosen to recover the water vapour absorption in the exhaust plume. Due to the absorption path arrangement dictated by the detuner diameter, the path-averaged absorption was a mixture of the ambient water vapour either side of the plume and of the hot water vapour in the plume created during the combustion process, as illustrated in Fig. 8.7. The water vapour spectrum accessible with this particular DFB laser was advantageous because the ambient absorption spectrum had a large region with minimal absorption which coincides with the position of some weakly absorbing hot lines that could be observed if the path length, temperature and concentration of the hot water vapour were favourable relative to the ambient

background absorption. These two main absorption lines, shown at ambient and hot temperatures in Fig. 8.8, were originally chosen for their sensitivity to changes in ambient temperature but the same behaviour applies to the much larger temperature differences observed here although these absorption lines were used for this test because they had the most interesting spectra that could be accessed with our existing DFB laser inventory.

### 8.2.2 Signal Recovery

The autobalanced photoreceiver was used to recover direct detection signals at a range of ramp frequencies from 8 Hz to 1 kHz, the latter limit being the highest sensible frequency allowed by the feedback components used. The effect of signal averaging on the recovered spectra was observed, shown in Figs 8.9 and 8.10, where increasing the number of averages was seen to significantly improve the achievable SNR although the gains began to diminish at higher integrating times where noise still remained. In this case the presence of hot lines could not be confirmed due to insufficient SNR. The constraints on the detuner mounting position prevented the beam from passing through the engine centre line which reduced the path length of the hot gas region, making observation of any hot lines even more difficult. There was a modest benefit, in terms of SNR, of increasing the ramp modulation frequency up to the noise cancelling bandwidth limit of 1 kHz. The signals at the higher ramp frequency were observed to follow more closely, the law of ideal averaging where the SNR increases in proportion to the square root of the number of averages. Increasing the frequency will also reduce the total acquisition time for equivalent numbers of averages which is often desirable when the engine state is changing on short time scales.

The spectra in Fig. 8.11 are unnormalised log ratio output signals recovered at three different engine states: engine off, idle speed and full throttle. With the engine switched off the signals exhibited excellent signal to noise properties as expected. At idle speed the signal to noise level deteriorated significantly although the largest absorption peak was still identifiable whilst at full throttle the noise dominated and no signal was apparent. The downward shift of the

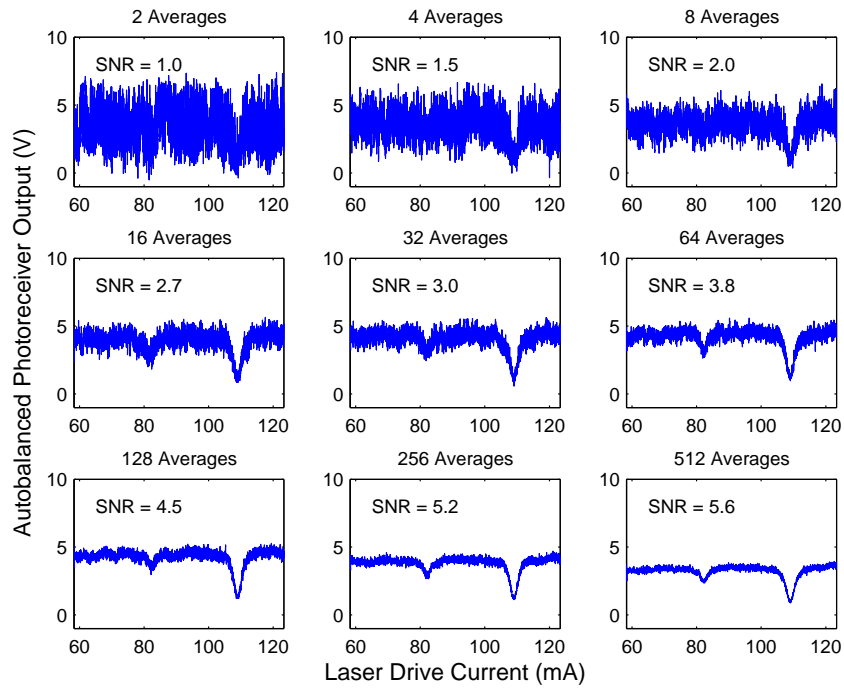


Figure 8.9: Direct detection signals from the autobalanced photoreceiver with increasing integration times at a ramp rate of 8 Hz.

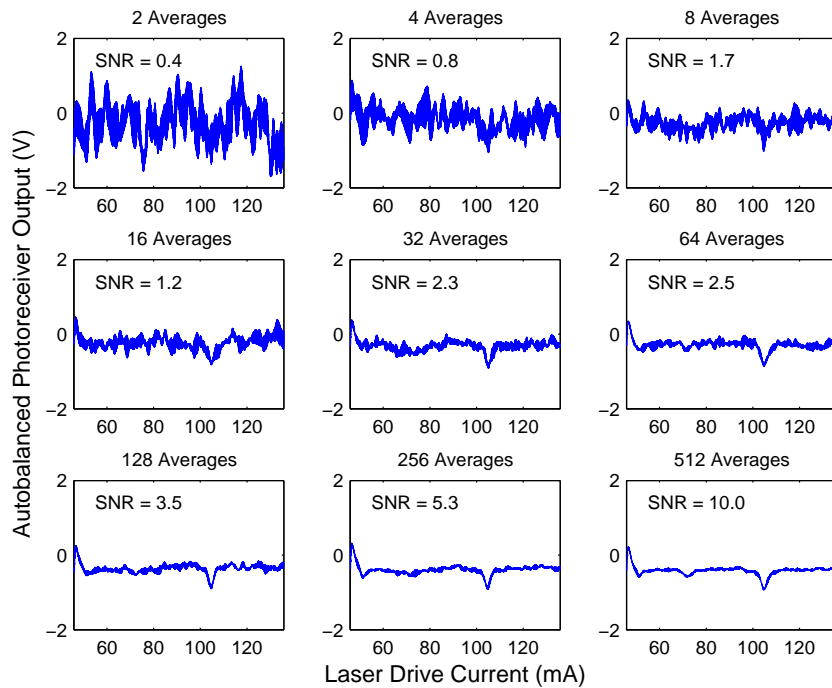


Figure 8.10: Direct detection signals from the autobalanced photoreceiver with increasing integration times at a ramp rate of 1 kHz.

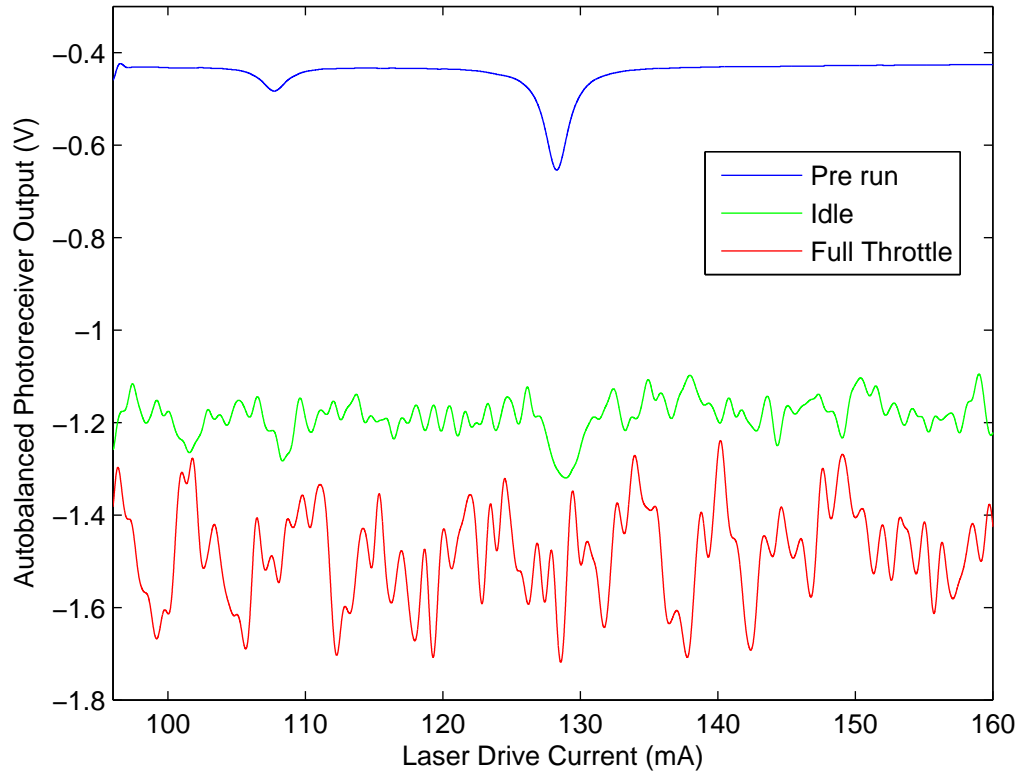


Figure 8.11: Unnormalised direct detection signals from the autobalanced photoreceiver with engine off, at idle speed and at full throttle. Signals taken with a ramp frequency of 100 Hz and no signal averaging

signal was significant in this figure as changes in the non-absorbing background level of the log ratio output were indicative of changes in the power ratio of the signal and reference beams. The shift downwards with increasing engine speed suggested that the recovered optical power and therefore signal photocurrent were decreasing due to beam steering and scattering. Investigations were performed to assess the impact of electromagnetic interference and fibre vibrations on the recovered signals. These effects were not apparent whilst the engine was off but were potentially problematic when the engine was running. By isolating the signals in turn during engine operation it was clear that these effects were in fact negligible and the noise observed was primarily in the signal beam path despite efforts made in the free space design to minimise these effects.

### 8.2.3 Beam Steering in Turbulent Exhaust Gases

One of the most significant challenges for recovering absorption spectra from turbulent media such as aero engine exhaust plumes is coping with beam steering [50, 138]. A turbulent medium will cause a propagating beam to wander in terms of lateral position ( $x$ ) and angular deviation ( $\theta$ ) from the path the beam would have followed in the absence of turbulence. It is the local, time-varying changes in pressure, temperature and therefore refractive index that cause the changes in the beam path [139–141]. This beam wander effect depends on a number of variables and the most important are the specific properties of the turbulent flow which are unknown or ill-defined in most cases. In particular the magnitude of the refractive index gradients, the size of any structures in the flow relative to the beam size and the temporal characteristics of the distortions all have an effect on the properties of the beam as it leaves the turbulent section.

There are a number of collection methods that can increase the allowable extent of the beam steering and each application may require its own tailored solution. A simple and effective scheme uses a short focal length lens or concave mirror in combination with a large area diode to maximise the tolerance to changes in the beam. Assuming that the beam deviation is well within the paraxial limit, a concave mirror can be modelled using the equivalent lens model to avoid etalons. The axial location of the beam at a detector plane can be described as  $x_2 = f\theta_1$  meaning that only the input angle will affect the location of the beam.

An alternative method is to use a retroreflector or retroreflector array to return the beam along the same path in a double-pass arrangement. In principle the distortion acquired on the first pass is undone on the return pass provided that the beam follows the same path and therefore sees the same turbulence [142]. A bulk retroreflector is likely to introduce a significant lateral shift in the position of the beam and if the magnitude of the shift is greater than the scale of any turbulent structures then the benefit will be small. An alternative to bulk retroreflectors are arrays of micro corner cubes or glass beads which can return a beam along the same path with very small lateral displacement.

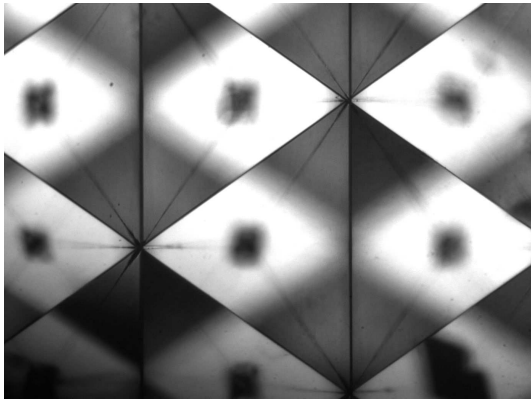


Figure 8.12: 3M retroreflective tape based on a micro corner cube structure. Horizontal extent of image  $\sim 900\mu m$ .

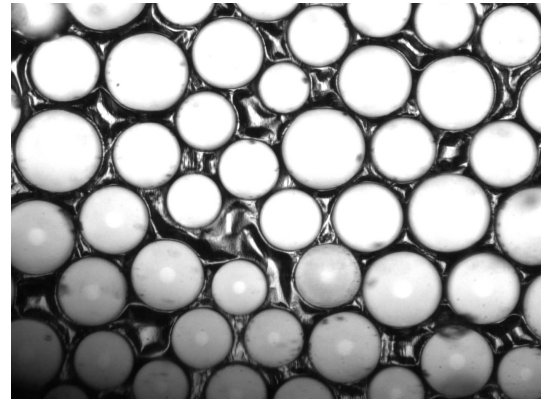


Figure 8.13: Retroreflective tape based on glass bead structure. Horizontal extent of image  $\sim 500\mu m$ .

The use of retroreflector arrays for in-situ, single-ended measurements in aero engine diagnostics has been investigated before by Black and co-workers [143,144]. Preliminary investigations using retroreflective sheets designed for road signs, shown in Figs. 8.12 and 8.13, showed that it was possible to recover signals for TDLS in some applications. The limitations of this method were due to the reflection efficiency and the diffractive properties of the reflected beams. A retroreflective system will also usually require a beam splitter with the collimator and detector orthogonal to one another, which wastes up to 75% of the output power. This can have implications for an optical power budget and over long path lengths the spreading return beam may only provide a weak signal which may not be optimal for signal recovery. Another option is to use an integrating sphere with a large aperture which can significantly reduce sensitivity to beam steering but with a low collection efficiency and a tendency to low-pass filter modulated signals [138].

### 8.3 Bristol Tests

The third test campaign was undertaken at Rolls-Royce Bristol on the Environmentally Friendly Engine (EFE) test bed. The engine test was a single

short term test used to run the prototype engine up to 90% NH (i.e. 90% of the maximum high pressure spool speed) and monitor the operating temperature using thermal paint. The unusual exhaust nozzle layout of this engine was of significant interest for future tomographic mapping experiments that are planned on the same test bed. The exhaust also provided higher temperature water vapour over a longer and more accessible path than for the Tay engine exhaust plume.

### 8.3.1 Experimental Setup

The primary challenge in taking water vapour measurements across the exhaust plume during the run cycle of the EFE engine was designing a simple, reliable system that would only require minimal test bed technician time whilst still providing useful information. Developing a system off-site that could then be installed rapidly was an important requirement and the experimental layout had to minimise the risk of component failure during the test due to the single-shot test schedule. For this reason the standard Thorlabs PDA10CS InGaAs photodiodes were used in place of the autobalanced detectors used in the previous test campaign at East Rogerton, which suffered occasional failures during testing. There was no restriction on having a 240 V power supply downstream of the engine on this bed which meant that the standard Thorlabs photodiode power supply could be used. A heavy duty steel box was used to house the fibre collimation optics and detection optics and hardware. The beam was directed out of a 50 mm wedged quartz window and traversed a 7 m path across the engine exhaust centre line before being returned by a large bulk retroreflector. The return beam was parallel to the outgoing beam but displaced laterally by an amount less than the diameter of the wedged window. The return beam was then reflected with a plane mirror through a ground glass diffuser (220 grit) before being incident upon the photodiode. The diffuser was used to expand the beam in order to reduce the sensitivity of the recovered signal to vibrations and beam steering as in Fig. 4.5.

The steel box containing the send/receive hardware and the retroreflector were installed on the side of steel walkways on opposite sides of the test cell.

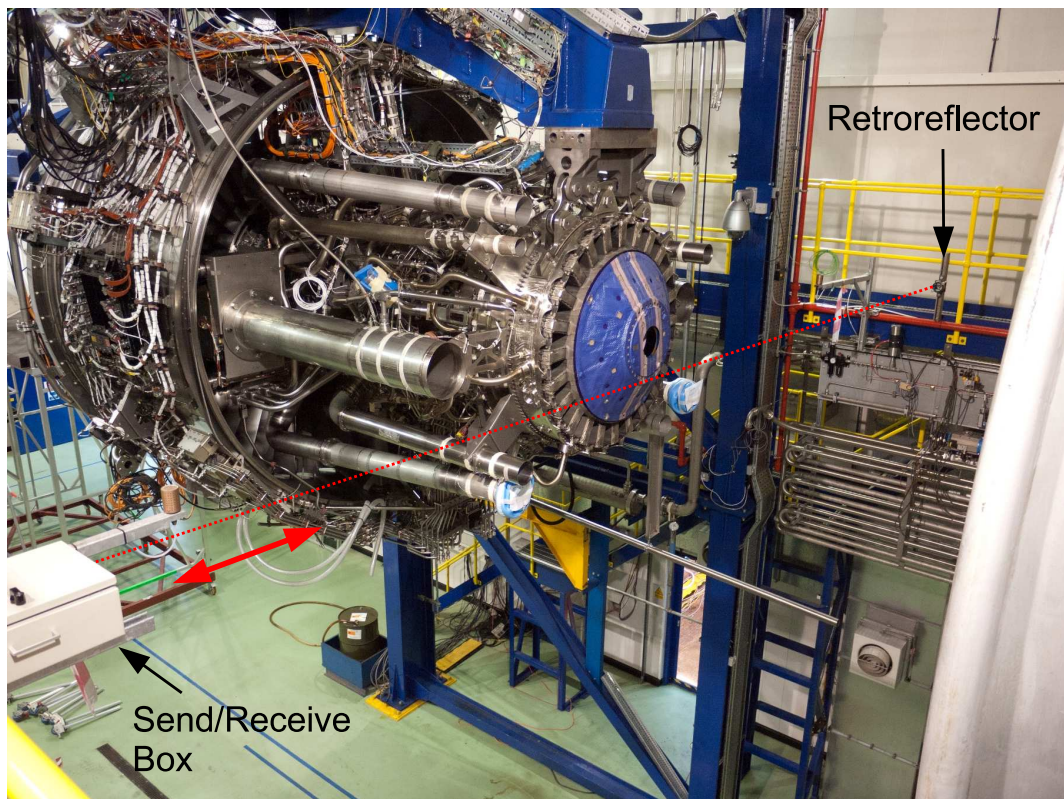


Figure 8.14: Rolls-Royce Bristol: EFE engine test cell. Experimental layout for exhaust plume absorption measurements. The laser beam path is shown with a red line.

The walkway sections were close in height to the engine centre line and mounts were made to allow the beam to travel across the centre of the exhaust plume. The walkways were considered a relatively solid base for mounting the box and retroreflector but the installed components on either side were also connected to the walkway handrail for support. This was unfortunate as the handrail was much less stable than the walkway and was therefore particularly prone to vibrations and buffeting from airflow. Fig. 8.14 is a photograph of the back section of the EFE engine showing the steel box in the bottom left of the photo, the detuner at the far right hand side and a red line illustrating the path of the beam across the exhaust to the retroreflector mounted on the opposite walkway. The 24 exhaust nozzles can be seen surrounding the blue heat shield at the rear of the engine. The drive electronics, data acquisition hardware and PC were situated in a van outside the test bed building. A single-mode fibre patch cable and a coaxial cable,

both 60 m in length, were used to connect the laser source to the fibre collimator and the photodiode to the data acquisition respectively.

The absorption signal that was recorded had contributions from the hot exhaust gas and the ambient air either side of the plume in a similar fashion to the East Rogerton exhaust measurements shown in Fig. 8.7. The exhaust gas was assumed to have a path length approximately equal to the horizontal extent of the nozzles including the separation distance between the nozzles which would contain recirculated hot gas, which amounted to 112 cm per pass. The relatively cold gas on either side of the plume was assumed to have ambient temperature and water vapour concentration. Once again using the water vapour spectrum near 1430 nm ( $6993\text{ cm}^{-1}$ ), the two contributions to the overall absorption are shown in Fig. 8.8 which exhibits the strong high temperature absorption of the smaller of the two main peaks along with the small hot lines that appear in the spectral regions with low ambient absorption. Future tests would presumably benefit from a fresh survey of the HITRAN database to find the optimum target spectral features.

### 8.3.2 Experimental Data

The main thermal paint run of the EFE engine consisted of a switch-on phase and a gradual acceleration from idle speed (62% NH, where NH refers to the high pressure spool speed) up to the purge point (73% NH) at which the engine would sit for 15 mins. There was another gradual acceleration to the performance calibration point (80% NH) which was held for another 15 mins. The final acceleration was up to the top condition for the test (90% NH) which took two attempts to reach and which was held for 2 mins. A range of signals was acquired during the run using both direct detection and first and second harmonic wavelength modulation spectroscopy. A sawtooth ramp frequency of 5 Hz was used for all measurements so that the extent of the frequency sweep could be maximised for the maximum achievable laser diode drive current sweep. At higher ramp frequencies the decreasing modulation coefficient reduces the spectral range covered by the sweep. One of the aims of the test was to try and observe the

small hot lines away from the two main lines shown in Fig. 8.8, which required driving the laser at the limits of its current range. The disadvantage of using a relatively slow ramp frequency was the signal acquisition time. The characteristic noise of the operating engine and the resonances associated with the mounting components, were significant at this detection rate. Signal averaging was used extensively during the signal recovery with the number of averages changed to suit the window of opportunity for acquisition, dictated by the run schedule. When the engine was stable for an extended period 512 averages could be used despite the 102 s acquisition time. The improvements in signal-to-noise ratios that comes with increasing averages was shown clearly during the East Rogerton tests and the same was apparent during this test campaign. In an ideal situation the frequency sweep would not need to be so large and faster ramp rates could be used up to several kilohertz.

Figs. 8.15 and 8.16 show two direct detection signals taken at the engine idle and performance calculation points (62 % NH and 80 % NH). Despite extensive averaging the SNR was still quite poor but the two main absorption peaks were clearly visible. The smaller hot lines may be present but are lost in the noise. Information can still be gleaned from these signals due to the differing temperature behaviour of the two lines. A simple gas distribution model was assumed to provide a temperature and concentration structure for creating an absorption profile based on both ambient and hot water vapour. A top hat model was used where the surrounding air had typical ambient temperature and concentration values at the ends of the path and the exhaust gas region in the middle was hotter and higher in concentration. The step function between the hot and cold regions in this model may not provide a perfect picture of the actual temperature and concentration distributions but it does allow a simple model to be used to extract some quantitative data about the exhaust gas, in the absence of any solid information about the plume structure. Theoretical line shapes based upon this two phase absorption model were fitted to the experimental line shapes, shown by the red traces in Figs. 8.15 and 8.16. The fit data suggested that the output temperature at engine idle was around 700 K with a water

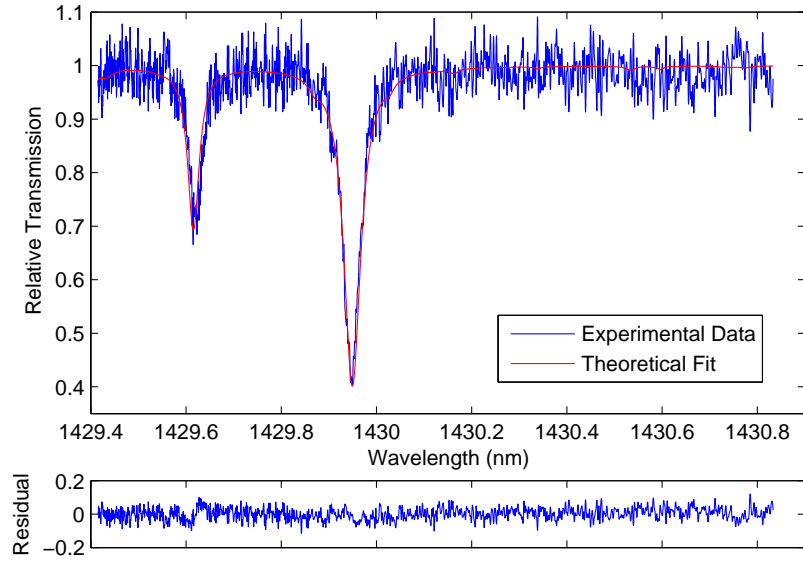


Figure 8.15: Direct detection signal and theoretical fit over 64 averages with the engine at idle speed (62% of the maximum high pressure spool speed). Using an assumed hot gas distribution the fit indicates H<sub>2</sub>O output content at 3.5% and 700K.

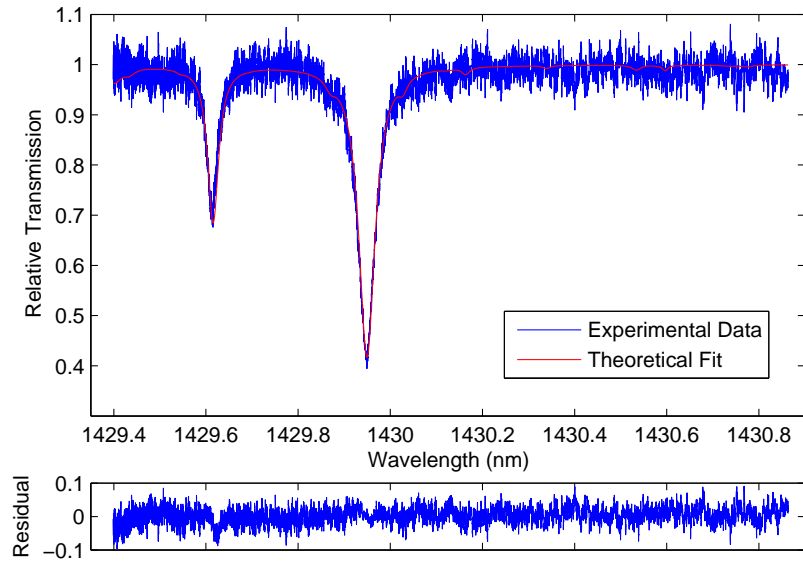


Figure 8.16: Direct detection signal and theoretical fit over 512 averages with the engine at 80% of the maximum high pressure spool speed. Here the theoretical fit indicates H<sub>2</sub>O output content at 4% and 850K.

vapour concentration of 3.5 %, compared to 1.05 % ambient concentration. As the engine speed was increased to the performance calibration point (80 % NH) the fit temperature was now 850 K and the concentration was 4 %. The gas data extracted in this way was only as good as the temperature distribution model but the values are in line with the test engineer’s expected values. The temperature in the combustor was expected to be over 1000 K so with the mixed gas in the output a temperature of 850 K would appear reasonable.

In addition to the direct detection signals some second harmonic wavelength modulation spectroscopy signals were acquired at various stages of the engine run. The process of changing detection methods or modulation setting once the run has started was difficult and so a limited range of target signals needed to be decided upon and prepared beforehand. In this case a series of low modulation index ( $m \sim 0.2$ ) second harmonic line shapes were recovered with the intention of observing any hot lines that appear and comparing normalised line shapes to theoretical derivative signals. Fig. 8.17 shows the second harmonic signals at four engine states from engine off to the final acceleration to the top condition. When the engine was off (top left diagram) the etalon effect of the window is visible at the right hand (higher power) end of the signal. The signals at the idle (62 % NH), performance calibration (80 % NH) and top condition (90 % NH) speeds show increasingly large amounts of noise at higher speeds but also the clear presence of water vapour hot lines. Fig. 8.18 shows the second harmonic signal at engine idle (top right diagram in Fig. 8.17) plotted alongside the individual HITRAN 08 line strengths of all the contributing absorption lines. The blue points show the line strengths at the HITRAN reference temperature of 296 K whilst the red points show the line strengths at 850 K. This gives an indication of where hot lines might be expected if there is a noticeable increase in line strength between the two temperatures. Several hot lines are visible that appear to match wavelengths that show noticeable increases in line strength at higher temperature, identified with downward pointing arrows in the figure. The line strength threshold for observable absorption in this case lies at approximately  $10^{-23} \text{ cm}^{-1}/\text{molecule}\cdot\text{cm}^{-2}$ . There also appears to be two absorption features

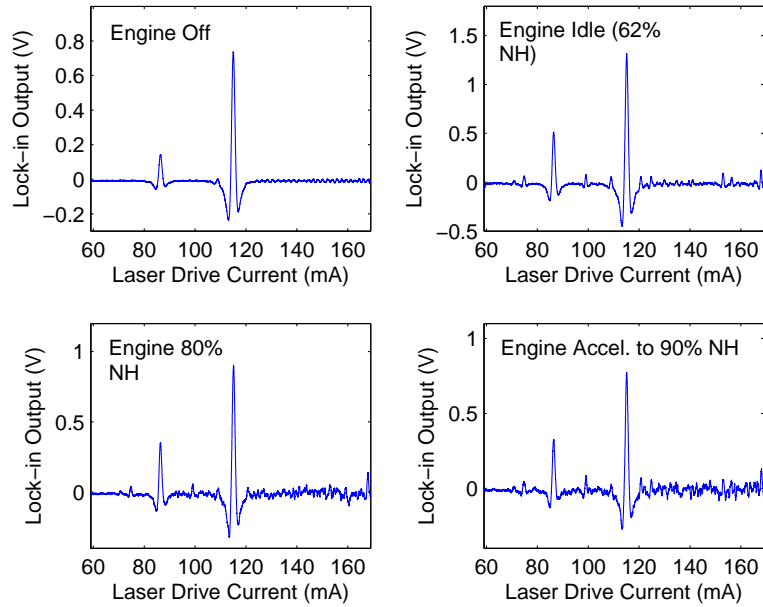


Figure 8.17: Second harmonic line shapes recovered at different engine speeds showing the presence of H<sub>2</sub>O hot lines ( $m \sim 0.2$ ,  $f_m = 50$  kHz).

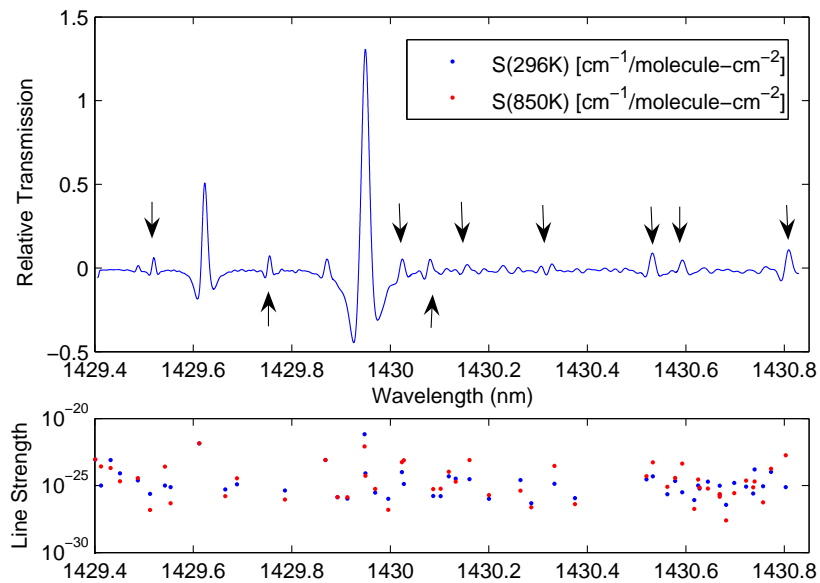


Figure 8.18: Experimental 2f line shape at engine idle speed showing appearance of H<sub>2</sub>O hot lines plotted with ambient and hot line strength values from HITRAN 2008. For a given line at a particular wavelength a red marker at a higher line strength than a blue marker, indicates one which will be somewhat stronger at 850 K than 296 K.

that do not correspond to anticipated hot lines, identified with upward pointing arrows in the figure, the most obvious of which was the feature midway between the two large peaks at around 1429.75 nm. It could be that these were due to interfering species such as nitric oxide which does absorb extremely weakly in this region but the most likely explanation was that there is an omission in the high temperature spectrum of water vapour in HITRAN database.

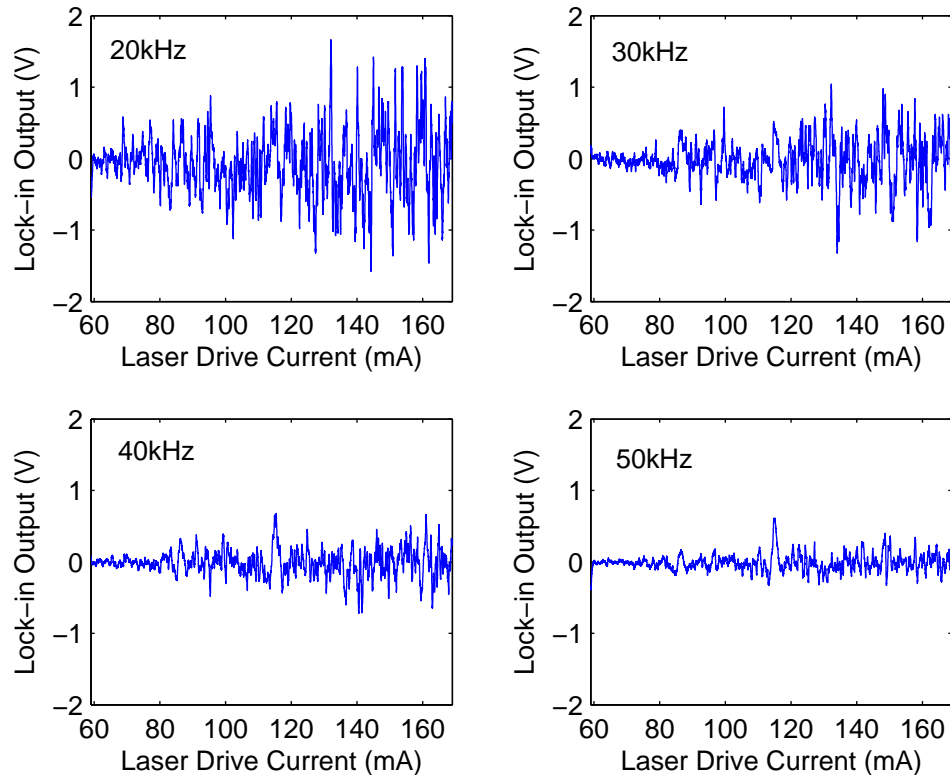


Figure 8.19: Comparison of  $2f$  signals at engine purge speed (73% NH) with modulation frequencies from 20 kHz up to 50 kHz and with no signal averaging employed.

The WMS signals in Fig. 8.17 were acquired using a 50 kHz current dither at a low modulation index. The presence of significant noise at the higher engine speeds indicate that the vibrational noise spectrum that affects the recorded signals reaches up to the modulation frequency of 50 kHz. Fig. 8.19 shows the effect of increasing the modulation frequency on the sampled spectra. The highest modulation frequency used was 50 kHz due to the 100 kHz bandwidth of

the lock-in amplifier available. The modulation frequency limit in this system was dictated by the available lock-in amplifier but even with higher bandwidth demodulation hardware the performance could still be limited, only this time by the bandwidth of the detector front end. The Thorlabs PDA10CS InGaAs photodiode had a range of gain settings with different associated detection bandwidths. The optical power budget was a major factor in determining the optimum photodiode gain setting, which in this setup was 30 dB giving a bandwidth of 775 kHz. At the highest gain setting the bandwidth drops to 12 kHz which would clearly make optical layouts with low overall transmission impractical. Due to the position of the photodiode in the test cell, the gain setting could not be changed once the engine was running so a compromise was necessary for the different measurements that were required. It would have been feasible to acquire different photoreceivers with higher bandwidths although these are typically based on small diodes in contrast to the large active area diodes that are advantageous in typical aero engine applications.

## 8.4 Summary

Three engine test campaigns are described each with their own distinct desired outcomes, constraints and timescales. The first test at Rolls-Royce Ansty was a preliminary test, intended to provide experience of test bed environments and highlight experimental considerations for an intake mounted temperature sensor. No modifiable bellmouth was available so a traversable structure upstream of the engine was provided by colleagues at SciTek Ltd. on which a fibre collimator and photodiode were mounted. A comparison of different TDLS signal types showed the SNR problems associated with direct detection in such a highly vibrating environment. Wavelength modulation was seen to greatly improve sensitivity at the expense of signal processing simplicity, with 2f signals showing minimal sensitivity to the vibrational noise caused by airflow around the mount structure. A fine water mist spray was sprayed across the beam path to simulate the misting environments in which traditional temperature sensors fail to operate, indicating

only a small amount of scattering and overall attenuation.

The second test campaign at Rolls-Royce East Rogerton was based in a test facility for repaired and overhauled engines which allowed a longer preparation time and for modifications to be made to the setup between engine tests. The aim of the test was to demonstrate a detuner-mounted detection system as a precursor to a tomographic mapping project based on absorption spectroscopy. An improved optical design was used with the hope of reducing the signal sensitivity to beam steering in the hot exhaust plume. A battery powered autobalanced photoreceiver was also used in an attempt to recover a direct detection signal with sufficient SNR to observe weakly absorbing hot water vapour lines near the stronger ambient absorption lines near 1430 nm ( $6993\text{ cm}^{-1}$ ). The effect of the beam steering was stronger than anticipated and even with a larger 3 mm diameter photodiode in place the modest absorption from the hot water vapour in the exhaust plume was not apparent. The effects of signal averaging and ramp frequency choice were examined. The primary benefit from increasing the current ramp frequency, up to the operating limit of the autobalanced photoreceiver, was reducing the integration time for a given number of signal averages. Signal averaging was the most effective tool in this situation for improving SNR when the timescales for changes in engine state allow extended integration times as the observable noise was largely uncorrelated with the target signal.

The third test campaign at Rolls-Royce Bristol was another exhaust plume water vapour measurement. The large experimental Environmentally Friendly Engine was expected to have a hotter exhaust plume than the Tay engines at East Rogerton. Various time and technical constraints dictated that a detuner-mounted setup could not be used for this test but a double pass setup was created attached to access walkways just downstream of the exhaust nozzle array at the level of the engine centre line. This maximised the beam exposure to hot exhaust gas and the resulting hot lines were clearly visible on the second harmonic spectra recovered during the test. Direct detection signals were also acquired although at a significantly lower SNR than the WMS measurements. Despite the absence of the small hot lines in these spectra, the major absorption

peaks near 1430 nm ( $6993\text{ cm}^{-1}$ ) proved useful in combination with an assumed top hat model for water vapour concentration and temperature across the hot and cold regions of the absorbing path. The model attempted to deconvolve the spectra that resulted from the ambient water vapour content of the test cell air either side of the exhaust plume and the hot water vapour that resulted from combustion. The results of this analysis were in line with the test engineers anticipated values for exhaust gas temperature. A useful outcome of the test was the information on the effect of modulation frequency and detection bandwidths. It was clear that increasing the modulation frequency benefited SNR considerably up to the limits imposed by the bandwidths of the detector and lock-in amplifier used.

# Chapter 9

## Conclusions and Further Work

### 9.1 Discussion and Conclusions

#### 9.1.1 Introduction: Aims & Objectives

The aims of this project were to further the state of the art of TDLS techniques for gas parameter determination and to use these and existing methods for the purpose of solving specific problems related to aero engine ground testing. The specific objectives outlined in the introduction were as follows:

- To extend the calibration-free RAM methods to higher modulation index operation for improved sensitivity.
- To evaluate dual-detection methods and their suitability for practical sensor systems.
- To demonstrate an electronic analogue of the optical RAM-nulling technique.
- To develop a ratio thermometry- based temperature sensor for ambient temperature recovery in misting environments.
- To test a variety of harsh environment recovery methods and evaluate the best approaches for gas information recovery in aero engine test beds.

### 9.1.2 Extending RAM-based Line Shape Recovery Techniques to High Modulation Indices

One challenge of particular interest was to enhance the sensitivity of the recently described technique of recovering absolute absorption line shapes using RAM-based calibration-free methods employing wavelength modulation. Phase sensitive detection at RF modulation frequencies is a widely used method that usually recovers harmonic line shapes with a narrow detection bandwidth at frequencies that can reduce the contribution of  $1/f$  noise. Whilst highly sensitive these methods typically require a calibration for useful quantitative gas information to be recovered. Calibration-based sensors are often compromised by calibration drift and changing system characteristics, such as laser tuning coefficient, making them unsuitable for long-term field deployment in many applications. The use of calibration-free wavelength modulation techniques to isolate the absorption line shape that can be recovered from the RAM signal represents a significant step forward for field-deployable TDLs sensors. The sensitivities achievable with this technique were limited by distortion effects that occurred when the signal magnitude is increased with the applied current dither amplitude. Initial attempts to correct this distortion worked well up to a relatively low modulation index of  $m = 0.75$ . In this work an updated correction procedure was presented based on a Fourier series expansion of the absorption coefficient that can in principle be applied at any achievable modulation index. The procedure applies a correction function that can be calculated with prior knowledge of the modulation index, which is a function of the applied frequency dither and the HWHM of the gas absorption line. This presents a problem since determination of the gas properties that affect the HWHM are the aim of the line shape recovery process. To solve this, two different techniques were proposed that used experimentally acquired signals to determine the operational modulation index, which was then used to calculate the correction function and recover the true absorption line shape. The recovery of gas information was then straightforward using the same least-squares fitting that is used on direct

detection signals.

In Chapter 5 this process was described in detail and methane absorption signals were recovered in a small in-line gas cell at concentrations of 0.1 %, 1 % and 10 % and at modulation indices from  $m=0.1$  to  $m=2$ . The two methods for modulation index determination, based on peak ratios and ideal Lorentzian fits, were tested and shown to recover experimental values of  $m$  well within the range expected from the system characterisation. The signals were corrected and the recovered spectra were compared to both undistorted low- $m$  line shapes and theoretical Voigt line shapes based on information from the HITRAN database, which also allowed the accuracy of gas parameter determination to be examined. Increasing the modulation depth (and therefore  $m$ ) significantly improved the signal size and therefore SNR in these measurements compared to the original system performance, indicating that performance in harsh environments would be similarly improved.

A novel correction function and implementation procedure for high modulation index operation were experimentally investigated and validated. To achieve this two online methods for establishing operational modulation indices were proposed and validated for use in the application of the correction function. The use of higher modulation indices allowed spectra to be recovered at higher sensitivities, thereby improving the achievable signal-to-noise ratios in the calibration-free RAM-based line shape recovery methods.

### **9.1.3 Autobalanced Photoreceivers for Noise Cancellation and RAM-nulling**

In Chapter 6 the use of autobalanced photoreceivers was investigated for potential use in aero engine applications. The ability to achieve significant common-mode noise rejection provides excellent DC absorption spectra with reasonably straightforward normalisation procedures. Spectra from the Hobbs-type receivers are still susceptible to noise in the signal beam path due to the DC nature of the recovered signals. In addition to normal direct detection measurements

the extremely large bandwidth of common-mode noise cancellation from the autobalancing proved effective at nulling background RAM signals in conventional 2f WMS. The use of these detectors for RAM-nulling of the harmonic output signals was examined and the potential for accurate 2f peak height measurements was demonstrated and used later in Section 7.4 for studies into ambient temperature information recovery.

The use of the normal configuration of autobalanced dual photoreceivers for background RAM-nulling with the RAM-based calibration free methods is not possible. The high background signal on these measurements prevent the highest possible sensitivities from being achieved and despite the optical RAM-nulling approach described in Section 2.4.4 providing an elegant solution to this problem, a more passive electronic system could potentially be more practical for industrial applications. A modified version of Hobbs' autobalanced detector is proposed that is capable of nulling the background RAM signal whilst maintaining the target absorption. This method uses the same normalisation process used in previous efforts to null the background RAM, based on an optical fibre delay line, with some additional benefits such as: modulation frequency flexibility, no requirement for polarisation and intensity control and minimal sensitivity to changing signal levels. Initial experiments to test the performance of the detector were presented to show the potential of this system as a way of achieving the highest possible sensitivities with RAM-based absolute line shape recovery techniques.

The extension of this technique to null RAM signals from a pure external amplitude modulator is demonstrated in the laboratory. This simple, sensitive and robust detection method shows significant potential for recovering calibration-free gas information in harsh environments.

#### **9.1.4 Sensor Design for Ambient Aero Engine Intake Water Vapour Temperature**

The autobalanced detectors were used in Chapter 7 for direct detection line shape recovery and for 2f WMS ratio thermometry experiments. Rolls-Royce

had identified the need for an ambient temperature sensor that could be used on aero engine intake structures in conditions of water vapour saturation. When misting occurs in aero engine intakes the highly accurate thermocouples, that are normally used to provide intake gas information, become inaccurate. In this work the feasibility of using a TDLS system based on ambient intake water vapour absorption was investigated. This involved undertaking a major survey of the HITRAN database to identify water vapour lines that coincided with spectral regions with good laser availability. Two regions were identified that fortuitously coincided with the ITU T-grid for CWDM in telecommunications at 1350 nm ( $7407\text{ cm}^{-1}$ ) and 1430 nm ( $6993\text{ cm}^{-1}$ ), where low-cost DFB lasers were readily available. A breadboard-mounted free-space layout, simulating an aero engine bellmouth cross-section, was set up in an environmental chamber with suitable temperature control. A series of investigations were undertaken to evaluate the suitability of TDLS ratio thermometry for use in a field-deployable temperature recovery system. Initial efforts to use a simple autobalanced direct detection method with line shape fits for concentration and temperature, were clearly not capable of recovering temperature with sufficient accuracy or precision. The main limitations were from the baseline fitting process required in the signal normalisation and the wavelength referencing procedure. An alternative method was attempted based on recovering the 2f peak height ratio. This relied upon a calibration process but allowed peak height ratios to be recovered in a repeatable manner without the need of a wavelength reference or baseline fit. The performance of this system was a significant improvement on the direct detection-based system achieving an overall precision of  $\pm 0.4\text{ K}$  at a rate of 1 Hz. The mean accuracy over the course of a week showed greater variation at  $\pm 0.9\text{ K}$ , which is roughly an order of magnitude short of the target accuracy. Extended temperature cycling in the environmental chamber showed that the system was prone to drifts in the calibration curve for the polynomial fit used to establish the output temperature. Even if the accuracy could be improved the requirement for a regular in situ calibration would prevent this method from becoming an effective solution to the problem at hand.

In the early stages of the temperature sensor investigations, an aero engine test campaign was undertaken at Rolls-Royce Ansty on a small turbojet engine. The test was designed to recover water vapour absorption signals from the intake flow, evaluating the viability of an intake temperature sensor. The test provided a useful platform for evaluating the strengths and weaknesses of various signal recovery methods in harsh environments that could not be simulated in the laboratory. The experience gained in planning and operating TDLS systems in an engine test bed was invaluable for future tests due to acquired awareness of previously unknown issues. The most significant finding was the scale of the mechanical vibrations and resonances, due to moving parts and fast moving airflow in the vicinity of the engine, which was significantly larger than first anticipated. It was clear from the recovered signals that direct detection was very susceptible to vibrational noise due to the broadband DC detection. WMS signals could provide isolation from a significant proportion of the noise spectrum but was not totally immune as shown by the poor SNR seen in the 1f RAM signals at full throttle. At low engine speeds the 1f RAM signal had looked quite favourable in terms of SNR but as the engine speed increased the vibrational resonances of the test setup began to coincide with the detection bandwidth. In addition the ability to recover TDLS signals through a fine water mist was verified, with a small amount of signal attenuation observed due to droplet scattering.

### **9.1.5 Aero Engine Exhaust Plume Measurement Systems**

The subsequent test campaigns at Rolls-Royce East Rogerton and Rolls-Royce Bristol were intended to recover high-temperature water vapour absorption across the exhaust plume. The purpose of the tests was to establish the most effective techniques for recovering absorption signals across engine exhaust plumes in preparation for a major project using absorption spectroscopy for tomographic mapping. Water vapour was used as a target species due to the availability of sources at short notice and a region of the spectrum near 1430 nm ( $6993\text{ cm}^{-1}$ ) that overlapped with the region used for ratio thermometry was identified that provided useful spectral properties for this series of tests. The long-term goal was

to establish a detuner-mounted absorption path array so any hot gas absorption signals would be acquired alongside ambient absorption signals from either side of the plume. The spectral region chosen had some small hot lines that coincided with a region of very low ambient absorption alongside some much stronger absorption lines that would also change significantly with temperature. The tests at East Kilbride primarily dealt with testing detuner-mounted optics which were shown to be fairly robust despite the incredibly harsh conditions experienced. Battery-powered autobalanced photoreceivers were used in situ and provided a useful means of acquiring direct detection signals. The beam steering experienced across the plume in the dual-pass optical layout proved a major issue, despite attempts to mitigate the problem with a focussing mirror. A larger area photodiode did improve the SNR when used along with high signal averaging although within the 1 kHz bandwidth of the autobalancing there was no apparent noise benefit in maximising the ramp frequency. For the Rolls-Royce Bristol test an alternative approach was used with a divergent beam and a diffuser so that any beam steering in the plume would only cause a minimal change in the power received by the photodiode. The effectiveness of this optical layout remains unclear due to the unfavourable mounting hardware but useful direct detection signals were acquired even at the highest engine speeds. To view the weakly absorbing hot lines in the water vapour spectrum required the use of 2f WMS, which had sufficient SNR to observe a number of the anticipated hot lines and some additional unidentified absorption features. A spectral analysis of 2f signals at different modulation frequencies highlighted the clear SNR benefits of higher frequency modulation. The bandwidth limits imposed by the detection hardware prevented an upper limit on the optimum modulation frequency from being determined.

### **9.1.6 Summary**

With reference to the aims and objectives that were outlined in the introduction and restated in Section 9.1.1, the achievements of this work can be summarised by the following:

- A new correction function was derived for the calibration-free RAM methods that could account for line shape distortions at any achievable modulation index.
- Two online methods for determining operational modulation indices were developed to facilitate the application of the correction function.
- A normalisation procedure for autobalanced dual beam detectors was derived and validated.
- The use of autobalanced detectors for nulling 2f-RAM signals in conventional 2f WMS peak height ratio thermometry was investigated.
- An electronic approach to 1f RAM-nulling for calibration-free line shape recovery methods, based on autobalanced dual beam detectors, was demonstrated.
- The use of external amplitude modulation, as an alternative to high frequency current modulation for phase sensitive detection, was demonstrated and shown to have many desirable attributes for sensor systems based in harsh environments.
- The electronic RAM-nulling approach was applied to externally amplitude modulated signals to achieve the highest possible sensitivities through background signal removal.
- An ambient temperature sensor based on atmospheric water vapour was developed, capable of precise temperature information recovery at high refresh rates.
- A series of aero engine test bed field trials were undertaken in order to evaluate a range of detection methods in noisy engine environments.
- High temperature water vapour measurements were taken on the Rolls-Royce Environmentally Friendly Engine demonstrator, using direct detection with an assumed exhaust plume distribution.

## 9.2 Further Work

### 9.2.1 High Sensitivity Absolute Line Shape Recovery

In Chapter 5 a function was derived that corrected distorted line shapes at high modulation indices to recover absolute transmission functions. The technique was shown to work reasonably well for a methane absorption line shape that was dominated by collisional broadening and was therefore strongly Lorentzian. To perform a similar analysis at very low pressures where the line shape is strongly Gaussian should be possible if an application makes this worthwhile. A more accurate process could take into account the Gaussian component that leads to an overall Voigt profile at these and lower pressures. There is, however, no analytical solution to the Voigt function that dominates at intermediate pressures, making it difficult to correct the distortion in a convolved line shape. Any empirical solution to this would presumably need an estimation of the contribution of each function which would change with pressure, often the target variable.

A useful extension of this process would be to implement a compound correction function that is able to account for multiple absorption lines that may interfere slightly with one another, especially at high pressures where line broadening becomes an issue. As it stands the process is based on a single non-interfering line shape, yet many species exhibit complex spectra that do not exhibit convenient clean absorption features. Establishing a modulation index for each of the contributing absorption lines would be the most significant challenge in such a process.

### 9.2.2 RAM-Nulling and Pure Amplitude Modulation

The idea of using RAM-based line shape recovery techniques in conjunction with nulling of the background RAM signal was introduced in Chapter 6, where an electronic analogue of the existing optical RAM-nulling method was demonstrated. The advantage of this is to increase the sensitivity achievable with the lock-in amplifier by as much as an order of magnitude. Refining this

technique further would offer significant benefits to the overall usefulness of the wavelength modulation-based absolute line shape recovery techniques. An obvious and achievable goal would be to combine the RAM nulling technique with the correction function used for high modulation index operation to achieve the highest possible sensitivities offered by the RAM-based methods.

The logical extension of these techniques is to move away from using a current dither to establish a RF modulation and to use an intensity modulating lithium niobate crystal or fibre-based Mach-Zehnder interferometer. This technique is introduced in Chapter 6 and systems of this type maintain the DC current ramp required to sweep the laser output wavelength but now the output is modulated at a high frequency by the intensity modulator. The pure amplitude modulation creates the same RAM components that were exploited by the techniques used in this work, yet there is no associated frequency modulation. The intensity modulation,  $\Delta I(\nu)$ , is still determined by the current-power characteristics of the laser scan, with the result that there still exists a background RAM and an absorption-dependent RAM signal. Initial laboratory demonstrations of this technique showed significant potential in solving the major problems of harsh environment gas information recovery. Further study of this technique and demonstration of its effectiveness in, for example, an aero engine test bed would be very useful. A quantification of the achievable SNR of this method, relative to conventional WMS methods would allow competing techniques to be evaluated effectively.

### 9.2.3 Ambient Ratio Thermometry Measurements

It was clear from the results shown in Chapter 7 that the absolute temperature determination methods fell well short of the target accuracy and precision in their current form. The two main contributing factors to the errors that compromised the temperature determination were the baseline fitting and the wavelength referencing. There is a trend in certain high-value spectroscopic applications towards using broadband frequency combs to establish absolute wavelength scales at a very high level of accuracy. Any line shape recovery method could benefit

from such a robust procedure for establishing a wavelength scale yet it remains to be seen whether any practical low-cost system could make use of this technology in the future.

The more significant of the two problems remains the error in line shape recovery due to baseline fitting. The outcome of any spectroscopic fitting process is highly sensitive to changes and errors in the baseline fitting process. Each baseline fitting algorithm must be designed to reflect the total range of anticipated spectra. The more the spectra and detector outputs are likely to vary the more difficult it becomes to automate a fitting program that can recover spectra with sufficient accuracy. One suggested baseline fitting algorithm mentioned by Schulze et al. makes use of artificial neural networks (ANNs) [44]. This method would use existing spectra within a certain window of expectation to train the ANN, which is then able to recover the true baseline from unknown experimental data. The potential performance of this method compares extremely favourably with other methods in the review mentioned although the difficulty of implementation may require some collaboration.

#### **9.2.4 Future Aero Engine Test Bed Systems**

There remains several potential avenues of development for TDLS-based aero engine sensors related to the work done in this project. The emphasis and direction in the latter stages of this project, particularly during the Rolls-Royce Bristol tests, had the impending EPSRC-backed Fibre Laser Imaging of gas Turbine Exhaust Species (FLITES) project in mind. This project will build upon some of the single line-of-sight water vapour absorption sensors demonstrated in this project. These will be extended to large scale multipath tunable diode laser and tunable fibre laser sensors for near and mid-infrared carbon dioxide and nitric oxide accessible wavelengths. The use of detuner-mounted optics has been established as a viable platform for exhaust plume sensing during the Rolls-Royce East Rogerton tests. The EFE engine in Bristol had been identified as a suitable engine for the development of a tomographic mapping system due to its unusual annular exhaust plume. The practical and logistical lessons learnt during the

Rolls-Royce Bristol test campaign will provide useful information for the planning and execution of engine tests during the FLITES programme.

In addition to the FLITES project there are four other areas that would be suitable for further study. The first is to continue the study into the minimisation of beam steering and vibrational noise. After taking into account the beam steering noise evident at Rolls-Royce East Rogerton, an alternative optical setup was used. Unfortunately this was compromised by the mounting mechanism that was used to install the send/receive box, which was inadvertently connected to a strongly vibrating handrail. Further work would be beneficial to see by how much this problem can be reduced and whether the SNR can be reduced enough to make direct detection competitive. It was clear from the data collected at Rolls-Royce Bristol that methods involving wavelength modulation benefit from increasing the frequency of modulation above the noise bandwidth. Further study to establish the ideal modulation and detection setup would allow the detection bandwidth to be optimised relative to the most appropriate photodetectors and demodulation hardware. Alternatively high frequency amplitude modulation may provide the most practical solution for recovering calibration-free spectra without interference from the problematic noise, if the highly promising initial observations in Section 6.5.2 can be replicated in a field application.

A second area of potential study is to simultaneously monitor intake and exhaust mass flux in order to calculate an indirect core mass flux. This would involve using density and Doppler shift measurements of a convenient species, probably oxygen near 760 nm ( $13150\text{ cm}^{-1}$ ) or water vapour near 1130 nm ( $8850\text{ cm}^{-1}$ ) which contains ambient and hot lines within the same laser sweep range.

A third avenue of possible study could be to examine the use of single-ended sensors that use backscatter or water droplet seeding of an exhaust plume to generate a return signal. This type of optical layout provides a different challenge to the previous experiments but could utilise DFB-seeded erbium doped fibre amplifiers (EDFAs) that deliver high power output through Raman amplification. These techniques have been demonstrated for remote backscatter sensing of

methane leaks with up to 2 W of near infrared output power [145].

The final area of further investigation would combine the techniques used for the temperature recovery investigation in Chapter 7 and the exhaust plume measurements from the Rolls-Royce Bristol tests to monitor shock wave structure in reheated engines. This would involve measuring temperature gradients at the shock wave boundaries that arise in reheated engine plumes, by traversing an absorption path down the plume axis, information can be obtained about the combustion and health of the engine under observation. As well as building upon the high temperature exhaust plume analysis performed on the EFE test the fast temperature recovery systems, developed to evaluate the feasibility of the ambient temperature sensor in Chapter 7, could be applied effectively in this proposed test bed system.

# References

- [1] J. Hodgkinson, J. Saffell, J. Luff, J. Shaw, J. Ramsden, C. Huggins, R. Bogue, and R. Carline, “MNT Gas Sensor Roadmap,” December 2006. URL: <http://goo.gl/Kpg8J>.
- [2] X. Zhou, X. Liu, J. B. Jeffries, and R. K. Hanson, “Selection of NIR H<sub>2</sub>O absorption transitions for in-cylinder measurement of temperature in IC engines,” *Measurement Science and Technology*, vol. 16, pp. 2437–2445, 2005.
- [3] P. Wright, C. Garcia-Stewart, S. Carey, F. Hindle, S. Pegrum, S. Colbourne, P. Turner, W. Hurr, T. Litt, S. Murray, S. Crossley, K. Ozanyan, and H. McCann, “Toward in-cylinder absorption tomography in a production engine,” *Applied Optics*, vol. 44, no. 31, pp. 6578–6592, 2005.
- [4] M. Miller, W. Kessler, and M. Allen, “Diode laser-based air mass flux sensor for subsonic aeropropulsion inlets,” *Applied Optics*, vol. 35, no. 24, pp. 4905–4912, 1996.
- [5] M. G. Allen, “Diode laser absorption sensors for gas-dynamic and combustion flows,” *Measurement Science and Technology*, vol. 9, pp. 545–562, 1998.
- [6] X. Liu, J. B. Jeffries, R. K. Hanson, K. M. Hinckley, and M. A. Woodmansee, “Development of a tunable diode laser sensor for measurements of gas turbine exhaust,” *Applied Physics B*, vol. 82, pp. 469–478, 2006.

- [7] J. Liu, G. Rieker, J. Jeffries, M. Gruber, C. Carter, T. Mathur, and R. Hanson, "Near-infrared diode laser absorption diagnostic for temperature and water vapor in a scramjet combustor," *Applied Optics*, vol. 44, no. 31, pp. 6701–6711, 2005.
- [8] C. Massie, G. Stewart, G. McGregor, and J. Gilchrist, "Design of a portable optical sensor for methane gas detection," *Sensors and Actuators B-Chemical*, vol. 113, no. 2, pp. 830–836, 2006.
- [9] K. Duffin, W. Johnstone, A. McGettrick, D. Moodie, G. Stewart, G. Thursby, and B. Culshaw, "Chemical Sensor Networks for Gas Detection and Environmental Monitoring," *Current Analytical Chemistry*, vol. 4, no. 4, pp. 391–402, 2008.
- [10] I. Linnerud, P. Kaspersen, and T. Jaeger, "Gas monitoring in the process industry using diode laser spectroscopy," *Applied Physics B: Lasers and Optics*, vol. 67, no. 3, pp. 297–305, 1998.
- [11] M. Lengden, R. Cunningham, and W. Johnstone, "Tuneable diode laser gas analyser for methane measurements on a large scale solid oxide fuel cell," *Journal of Power Sources*, vol. 196, pp. 8406–8408, OCT 15 2011.
- [12] P. Werle, R. Mucke, F. D'Amato, and T. Lancia, "Near-infrared trace-gas sensors based on room-temperature diode lasers," *Applied Physics B-Lasers And Optics*, vol. 67, no. 3, pp. 307–315, 1998.
- [13] R. Clement, P. Yang, and C. Koester, "Environmental analysis," *Analytical Chemistry*, vol. 69, no. 12, pp. R251–R287, 1997.
- [14] P. Martin, "Near-infrared diode laser spectroscopy in chemical process and environmental air monitoring," *Chemical Society Reviews*, vol. 31, no. 4, pp. 201–210, 2002.
- [15] D.-D. Lee and D.-S. Lee, "Environmental gas sensors," *Sensors Journal, IEEE*, vol. 1, pp. 214 –224, Oct 2001.

- [16] W. Cao and Y. Duan, “Breath analysis: Potential for clinical diagnosis and exposure assessment,” *Clinical Chemistry*, vol. 52, no. 5, pp. 800–811, 2006.
- [17] E. Comini, *Solid State Gas Sensing*. Springer, 2009.
- [18] P. R. Griffiths, D. A. Heaps, and P. R. Brejna, “The Gas Chromatography/Infrared Interface: Past, Present, and Future,” *Applied Spectroscopy*, vol. 62, pp. 259A–270A, OCT 2008.
- [19] B. C. Smith, *Fundamentals of Fourier Transform Infrared Spectroscopy*. CRC Press, 2011.
- [20] E. D. Hinkley, “High-resolution infrared spectroscopy with a tunable diode laser,” *Applied Physics Letters*, vol. 16, no. 9, pp. 351–354, 1970.
- [21] J. Reid, B. K. Garside, J. Shewchun, M. El-Sherbiny, and E. A. Ballik, “High sensitivity point monitoring of atmospheric gases employing tunable diode lasers,” *Applied Optics*, vol. 17, no. 11, pp. 1806–1810, 1978.
- [22] J. Reid, J. Shewchun, B. K. Garside, and E. A. Ballik, “High sensitivity pollution detection employing tunable diode lasers,” *Applied Optics*, vol. 17, no. 2, pp. 300–307, 1978.
- [23] P. Werle, “A review of recent advances in semiconductor laser based gas monitors,” *Spectrochimica Acta Part A: Molecular and Biomolecular Spectroscopy*, vol. 54, no. 2, pp. 197–236, 1998.
- [24] P. Werle, F. Slemr, K. Maurer, R. Kormann, R. Mücke, and B. Jänker, “Near- and mid-infrared laser-optical sensors for gas analysis,” *Optics and Lasers in Engineering*, vol. 37, no. 2-3, pp. 101 – 114, 2002.
- [25] L. S. Rothman, D. Jacquemart, A. Barbe, D. Chris Benner, M. Birk, L. R. Brown, M. R. Carleer, J. C. Chackerian, K. Chance, L. H. Coudert, V. Dana, V. M. Devi, J. M. Flaud, R. R. Gamache, A. Goldman, J. M. Hartmann, K. W. Jucks, A. G. Maki, J. Y. Mandin, S. T. Massie, J. Orphal, A. Perrin, C. P. Rinsland, M. A. H. Smith, J. Tennyson, R. N. Tolchenov,

- R. A. Toth, J. Vander Auwera, P. Varanasi, and G. Wagner, “The HITRAN 2004 molecular spectroscopic database,” *Journal of Quantitative Spectroscopy and Radiative Transfer*, vol. 96, no. 2, pp. 139–204, 2005.
- [26] L. S. Rothman, I. E. Gordon, A. Barbe, D. C. Benner, P. E. Bernath, M. Birk, V. Boudon, L. R. Brown, A. Campargue, J. P. Champion, K. Chance, L. H. Coudert, V. Dana, V. M. Devi, S. Fally, J. M. Flaud, R. R. Gamache, A. Goldman, D. Jacquemart, I. Kleiner, N. Lacome, W. J. Lafferty, J. Y. Mandin, S. T. Massie, S. N. Mikhailenko, C. E. Miller, N. Moazzen-Ahmadi, O. V. Naumenko, A. V. Nikitin, J. Orphal, V. I. Perevalov, A. Perrin, A. Predoi-Cross, C. P. Rinsland, M. Rotger, M. Simeckova, M. A. H. Smith, K. Sung, S. A. Tashkun, J. Tennyson, R. A. Toth, A. C. Vandaele, and J. Vander Auwera, “The HITRAN 2008 molecular spectroscopic database,” *Journal of Quantitative Spectroscopy & Radiative Transfer*, vol. 110, no. 9-10, Sp. Iss. SI, pp. 533–572, 2009.
- [27] D. T. Cassidy and J. Reid, “Atmospheric pressure monitoring of trace gases using tunable diode lasers,” *Applied Optics*, vol. 21, no. 7, pp. 1185–1190, 1982.
- [28] D. S. Bomse, A. C. Stanton, and J. A. Silver, “Frequency modulation and wavelength modulation spectroscopies: comparison of experimental methods using a lead–salt diode laser,” *Applied Optics*, vol. 31, no. 6, pp. 718–731, 1992.
- [29] F. S. Pavone and M. Inguscio, “Frequency– and wavelength–modulation spectroscopies: Comparison of experimental methods using an AlGaAs diode laser,” *Applied Physics B: Lasers and Optics*, vol. 56, no. 2, pp. 118–122, 1993.
- [30] H. Li, G. Rieker, X. Liu, J. Jeffries, and R. Hanson, “Extension of wavelength-modulation spectroscopy to large modulation depth for diode laser absorption measurements in high-pressure gases,” *Applied Optics*, vol. 45, no. 5, pp. 1052–1061, 2006.

- [31] G. B. Rieker, J. B. Jeffries, and R. K. Hanson, “Calibration-free wavelength-modulation spectroscopy for measurements of gas temperature and concentration in harsh environments,” *Applied Optics*, vol. 48, no. 29, pp. 5546–5560, 2009.
- [32] K. Duffin, A. J. McGettrick, W. Johnstone, G. Stewart, and D. G. Moodie, “Tunable diode-laser spectroscopy with wavelength modulation: A calibration-free approach to the recovery of absolute gas absorption line shapes,” *Journal of Lightwave Technology*, vol. 25, no. 10, pp. 3114–3125, 2007.
- [33] A. J. McGettrick, K. Duffin, W. Johnstone, G. Stewart, and D. G. Moodie, “Tunable Diode Laser Spectroscopy With Wavelength Modulation : A Phasor Decomposition Method for Calibration-Free Measurements of Gas Concentration and Pressure,” *Journal of Lightwave Technology*, vol. 26, no. 4, pp. 432–440, 2008.
- [34] K. Duffin, *Wavelength Modulation Spectroscopy with Tunable Diode Lasers: a Calibration-Free Approach to the Recovery of Absolute Gas Absorption Line-Shapes*. PhD thesis, University of Strathclyde, 2007.
- [35] A. McGettrick, *Novel Techniques for Tunable Diode Laser Spectroscopy and their Application in Solid Oxide Fuel Cell Diagnostics*. PhD thesis, University of Strathclyde, 2007.
- [36] R. Parker and M. Lathoud, “Green aero-engines: technology to mitigate aviation impact on environment,” *Proceedings of The Institution of Mechanical Engineers Part C-Journal of Mechanical Engineering Science*, vol. 224, no. C3, pp. 529–538, 2010.
- [37] M. G. Allen, B. L. Upschulte, D. M. Sonnenfroh, W. J. Kessler, P. A. Mulhall, and J. Denver, “Overview of Diode Laser Measurements in Large-Scale Test Facilities,” *21st AIAA Aerodynamic Measurement Technology and Ground Testing Conference*, no. June, 2000.

- [38] R. K. Hanson, J. B. Jeffries, and M. G. Allen, “Tunable diode laser absorption sensor applications to aeropropulsion testing,” in *Applied Vehicle Technology Panel Specialists’ Meeting on Recent Developments in Non-Intrusive Measurement Technology (Budapest, Hungary) NATO RSM-017*, American Institute of Aeronautics and Astronautics, 2005.
- [39] R. K. Hanson and J. B. Jeffries, “Diode laser sensors for ground testing,” in *25<sup>th</sup> AIAA Aerodynamic Measurement Technology and Ground Testing Conference*, American Institute of Aeronautics and Astronautics, 2006.
- [40] M. Miller, W. Kessler, and M. Allen, “Diode laser-based air mass flux sensor for subsonic aeropropulsion inlets,” *Applied Optics*, vol. 35, no. 24, pp. 4905–4912, 1996.
- [41] K. Huenecke, *Jet engines: fundamentals of theory, design, and operation*. Motorbooks International Publishers & Wholesalers, 1997.
- [42] Private Communication - Dr. John D. Black, Rolls-Royce plc.
- [43] D. T. Cassidy and L. J. Bonnell, “Trace gas detection with short-external-cavity InGaAsP diode laser transmitter modules operating at  $1.58\mu\text{m}$ ,” *Applied Optics*, vol. 27, no. 13, pp. 2688–2693, 1988.
- [44] G. Schulze, A. Jirasek, M. M. L. Yu, A. Lim, F. B. Turner, and M. W. Blades, “Investigation of Selected Baseline Removal Techniques as Candidates for Automated Implementation,” *Applied Spectroscopy*, vol. 59, no. 5, pp. 545–574, 2005.
- [45] L. Rothman, I. Gordon, R. Barber, H. Dothe, R. Gamache, A. Goldman, V. Perevalov, S. Tashkun, and J. Tennyson, “HITEMP, the high-temperature molecular spectroscopic database,” *Journal of Quantitative Spectroscopy and Radiative Transfer*, vol. 111, no. 15, pp. 2139–2150, 2010.
- [46] N. Jacquinet-Husson, N. Scott, A. Chedin, K. Garceran, R. Armante, A. Chursin, A. Barbe, M. Birk, L. Brown, C. Camy-Peyret, C. Claveau,

- C. Clerbaux, P. Coheur, V. Dana, L. Daumont, M. Debacker-Barilly, J. Flaud, A. Goldman, A. Hamdouni, M. Hess, D. Jacquemart, P. Kopke, J. Mandin, S. Massie, S. Mikhailenko, V. Nemtchinov, A. Nikitin, D. Newnham, A. Perrin, V. Perevalov, L. Regalia-Jarlot, A. Rublev, F. Schreier, I. Schult, K. Smith, S. Tashkun, J. Teffo, R. Toth, V. Tyuterev, J. Auwera, P. Varanasi, and G. Wagner, “The 2003 edition of the GEISA/IASI spectroscopic database,” *Journal of Quantitative Spectroscopy & Radiative Transfer*, vol. 95, no. 4, pp. 429–467, 2005.
- [47] K. Haller and P. Hobbs, “Double Beam Laser-Absorption Spectroscopy - Shot Noise-Limited Performance at Baseband with a Novel Electronic Noise Canceller,” in *Optical Methods for Ultrasensitive Detection and Analysis : Techniques and Applications* (Fearey, BL, ed.), vol. 1435 of *Proceedings of the Society of Photo-Optical Instrumentation Engineers (SPIE)*, pp. 293–309, Society of Photo-Optical Instrumentation Engineers, 1991. Conf. on Optical Methods for Ultrasensitive Detection and Analysis : Techniques and Applications, Los Angeles, CA, Jan 21-23, 1991.
- [48] P. C. D. Hobbs, “Shot noise limited optical measurements at baseband with noisy lasers (proceedings only),” in *Laser Noise*, vol. 1376, (Boston, MA, USA), pp. 216–221, SPIE, 1991.
- [49] P. C. Hobbs, “Ultrasensitive laser measurements without tears,” *Applied Optics*, vol. 36, no. 4, pp. 903–920, 1997.
- [50] K. Lyle, *Development of a Real-Time Diode Laser Mass Flux Sensor for Simultaneous Measurement of Density and Velocity of Oxygen*. PhD thesis, Stanford University, 2005.
- [51] D. Sonnenfroh, W. Rawlins, M. Allen, C. Gmachl, F. Capasso, A. Hutchinson, D. Sivco, J. Baillargeon, and A. Cho, “Application of balanced detection to absorption measurements of trace gases with room-temperature, quasi-CW quantum-cascade lasers,” *Applied Optics*, vol. 40, no. 6, pp. 812–820, 2001.

- [52] P. Vogel and V. Ebert, “Near shot noise detection of oxygen in the A-band with vertical-cavity surface-emitting lasers,” *Applied Physics B*, vol. 72, pp. 127–135, 2001.
- [53] New Focus Nirvana - URL: <http://goo.gl/HOFN9>.
- [54] W. Lenth, C. Ortiz, and G. C. Bjorklund, “Pulsed frequency-modulation spectroscopy as a means for fast absorption measurements,” *Optics Letters*, vol. 6, pp. 351–353, Jul 1981.
- [55] G. C. Bjorklund, “Frequency-modulation spectroscopy: a new method for measuring weak absorptions and dispersions,” *Optics Letters*, vol. 5, pp. 15–17, Jan 1980.
- [56] W. Lenth, “Optical heterodyne spectroscopy with frequency- and amplitude-modulated semiconductor lasers,” *Optics Letters*, vol. 8, no. 11, pp. 575–577, 1983.
- [57] M. Gehrtz, E. A. Whittaker, and G. C. Bjorklund, “Quantum-limited laser frequency-modulation spectroscopy,” *Journal of the Optical Society of America*, vol. 2, no. 9, pp. 1510–1526, 1985.
- [58] C. B. Carlisle and D. E. Cooper, “Tunable diode laser frequency modulation spectroscopy through an optical fiber: High-sensitivity detection of water vapor,” *Applied Physics Letters*, vol. 56, no. 9, pp. 805–807, 1990.
- [59] J. Supplee, E. Whittaker, and W. Lenth, “Theoretical Description of Frequency-Modulation and Wavelength Modulation Spectroscopy,” *Applied Optics*, vol. 33, no. 27, pp. 6294–6302, 1994.
- [60] X. Zhu and D. T. Cassidy, “Modulation Spectroscopy With A Semiconductor Diode Laser By Injection-current Modulation,” *Journal of the Optical Society of America B*, vol. 14, no. 8, pp. 1945–1950, 1997.
- [61] E. D. Hinkley and P. L. Kelley, “Detection of Air Pollutants With Tunable Diode Lasers,” *Science*, vol. 171, no. 3972, pp. 635–639, 1971.

- [62] L. C. Philippe and R. K. Hanson, "Laser diode wavelength-modulation spectroscopy for simultaneous measurement of temperature, pressure and velocity in shock-heated oxygen flows," *Applied Optics*, vol. 32, no. 30, pp. 6090–6103, 1993.
- [63] G. Jacobsen, H. Olesen, F. Birkedahl, and B. Tromborg, "Current/frequency-modulation characteristics for directly optical frequency-modulated injection lasers at 830nm and 1.3 $\mu$ m," *Electronics Letters*, vol. 18, no. 20, pp. 874–876, 1982.
- [64] R. Arndt, "Analytical line shapes for Lorentzian signals broadened by modulation," *Journal of Applied Physics*, vol. 36, no. 8, pp. 2522–2524, 1965.
- [65] J. Reid and D. Labrie, "2nd-Harmonic Detection With Tunable Diode-Lasers - Comparison of Experiment and Theory," *Applied Physics B-Photophysics and Laser Chemistry*, vol. 26, no. 3, pp. 203–210, 1981.
- [66] P. Kluczynski and O. Axner, "Theoretical description based on Fourier analysis of wavelength-modulation spectrometry in terms of analytical and background signals," *Applied Optics*, vol. 38, no. 27, pp. 5803–5815, 1999.
- [67] P. Kluczynski, J. Gustafsson, A. M. Lindberg, and O. Axner, "Wavelength modulation absorption spectrometry – an extensive scrutiny of the generation of signals," *Spectrochimica Acta Part B: Atomic Spectroscopy*, vol. 56, no. 8, pp. 1277 – 1354, 2001.
- [68] T. Iseki, "Calculation of the ratio between the second and first harmonic signals in wavelength-modulation spectroscopy for absorption measurement," *Optical Review*, vol. 10, no. 1, pp. 24–30, 2003.
- [69] O. E. Myers and E. J. Putzer, "Measurement broadening in magnetic resonance," *Journal of Applied Physics*, vol. 30, no. 12, pp. 1987–1991, 1959.

- [70] A. M. Russell and D. A. Torchia, "Harmonic analysis in systems using phase sensitive detectors," *Review of Scientific Instruments*, vol. 33, no. 4, pp. 442–444, 1962.
- [71] A. McGettrick, W. Johnstone, R. Cunningham, and J. Black, "Tunable Diode Laser Spectroscopy With Wavelength Modulation: Calibration-Free Measurement of Gas Compositions at Elevated Temperatures and Varying Pressure," *Journal of Lightwave Technology*, vol. 27, pp. 3150–3161, Aug. 2009.
- [72] M. Lengden, J. R. P. Bain, I. Armstrong, and W. Johnstone, "Two gas spectrometers for the investigation of gas absorption parameters at elevated temperatures and pressures," in *International Conference on Field Laser Applications in Industry and Research, Grainau, Germany*, September 2009.
- [73] I. Armstrong, A. L. Chakraborty, K. Ruxton, and W. Johnstone, "An investigation of TDLS modulation schemes as applied to the mid-IR spectral region by difference frequency generation in PPLN," in *7th International Conference on Tunable Diode Laser Spectroscopy (TDLS), Zermatt, Switzerland*, July 2009.
- [74] I. Armstrong, W. Johnstone, K. Duffin, M. Lengden, A. L. Chakraborty, and K. Ruxton, "Detection of CH<sub>4</sub> in the Mid-IR Using Difference Frequency Generation With Tunable Diode Laser Spectroscopy," *Journal of Lightwave Technology*, vol. 28, no. 10, pp. 1435–1442, 2010.
- [75] A. L. Chakraborty, K. Ruxton, W. Johnstone, M. Lengden, and K. Duffin, "Elimination of residual amplitude modulation in tunable diode laser wavelength modulation spectroscopy using an optical fiber delay line," *Optics Express*, vol. 17, no. 12, pp. 9602–9607, 2009.
- [76] A. L. Chakraborty, K. Ruxton, and W. Johnstone, "Influence of the wavelength-dependence of fiber couplers on the background signal in

- wavelength modulation spectroscopy with RAM-nulling,” *Optics Express*, vol. 18, no. 1, pp. 267–280, 2010.
- [77] A. L. Chakraborty, K. Ruxton, and W. Johnstone, “Suppression of intensity modulation contributions to signals in second harmonic wavelength modulation spectroscopy,” *Optics letters*, vol. 35, pp. 2400–2, July 2010.
- [78] K. Ruxton, A. Chakraborty, W. Johnstone, M. Lengden, G. Stewart, and K. Duffin, “Tunable diode laser spectroscopy with wavelength modulation: Elimination of residual amplitude modulation in a phasor decomposition approach,” *Sensors and Actuators B: Chemical*, vol. 150, pp. 367–375, Sept. 2010.
- [79] P. Wiesen, J. Kleffmann, R. Kurtenbach, and K. H. Becker, “Emission of nitrous oxide and methane from aero engines: monitoring by tunable diode laser spectroscopy,” *Infrared Physics & Technology*, vol. 37, no. 1, pp. 75 – 81, 1996. Proceedings of the 4th International Symposium on Monitoring of Gaseous Pollutants by Tunable Diode Lasers.
- [80] R. M. Mihalcea, D. S. Baer, and R. K. Hanson, “Diode laser sensor for measurements of CO, CO<sub>2</sub>, and CH<sub>4</sub> in combustion flows,” *Applied Optics*, vol. 36, pp. 8745–8752, Nov 1997.
- [81] R. Mihalcea, D. Baer, and R. Hanson, “A diode-laser absorption sensor system for combustion emission measurements,” *Measurement Science & Technology*, vol. 9, no. 3, pp. 327–338, 1998.
- [82] X. Zhou, X. Liu, J. Jeffries, and R. Hanson, “Development of a sensor for temperature and water concentration in combustion gases using a single tunable diode laser,” *Measurement Science & Technology*, vol. 14, no. 8, pp. 1459–1468, 2003.
- [83] S. T. Sanders, J. Wang, J. B. Jeffries, and R. K. Hanson, “Diode-laser absorption sensor for line-of-sight gas temperature distributions,” *Applied Optics*, vol. 40, pp. 4404–4415, Aug 2001.

- [84] X. Liu, *Line-of-Sight Absorption of H<sub>2</sub>O Vapor: Gas Temperature Sensing in Uniform and Nonuniform Flows*. PhD thesis, Stanford University, 2006.
- [85] N. Terzija, J. L. Davidson, C. A. Garcia-Stewart, P. Wright, K. B. Ozanyan, S. Pegrum, T. J. Litt, and H. McCann, “Image optimization for chemical species tomography with an irregular and sparse beam array,” *Measurement Science & Technology*, vol. 19, no. 9, 2008.
- [86] P. Wright, N. Terzija, J. L. Davidson, S. Garcia-Castillo, C. Garcia-Stewart, S. Pegrum, S. Colbourne, P. Turner, S. D. Crossley, T. Litt, S. Murray, K. B. Ozanyan, and H. McCann, “High-speed chemical species tomography in a multi-cylinder automotive engine,” *Chemical Engineering Journal*, vol. 158, no. 1, Sp. Iss. SI, pp. 2–10, 2010.
- [87] V. Nagali and R. K. Hanson, “Design of a diode-laser sensor to monitor water vapor in high-pressure combustion gases,” *Applied Optics*, vol. 36, pp. 9518–9527, Dec 1997.
- [88] J. T. C. Liu, J. B. Jeffries, and R. K. Hanson, “Large-modulation-depth 2f spectroscopy with diode lasers for rapid temperature and species measurements in gases with blended and broadened spectra,” *Applied Optics*, vol. 43, no. 35, pp. 6500–6509, 2004.
- [89] X. Liu, J. B. Jeffries, R. K. Hanson, and X. Liu, “Measurements of spectral parameters of water-vapour transitions near 1388 and 1345 nm for accurate simulation of high-pressure absorption spectra,” *Measurement Science and Technology*, vol. 18, pp. 1185–1194, 2007.
- [90] Zolo Technologies - URL: <http://www.zolotech.com/sub/aerospace/>.
- [91] L. C. Philippe and R. K. Hanson, “Laser-Absorption Mass Flux Sensor for High-Speed Air-Flows,” *Optics Letters*, vol. 16, no. 24, pp. 2002–2004, 1991.
- [92] M. Arroyo, S. Langlois, and R. Hanson, “Diode-Laser Absorption Technique for Simultaneous Measurements of Multiple Gasdynamic Parameters in

- High-Speed Flows Containing Water-Vapor,” *Applied Optics*, vol. 33, no. 15, pp. 3296–3307, 1994.
- [93] A. R. Awtry and J. W. Fleming, “Simultaneous diode-laser-based in situ measurement of liquid water content and oxygen mole fraction in dense water mist environments,” *Optics Letters*, vol. 31, no. 7, pp. 900–902, 2006.
- [94] A. R. Awtry, B. T. Fisher, R. A. Moffatt, V. Ebert, and J. W. Fleming, “Simultaneous diode laser based in situ quantification of oxygen , carbon monoxide , water vapor , and liquid water in a dense water mist environment,” *Proceedings of the Combustion Institute*, vol. 31, pp. 799–806, 2007.
- [95] B. T. Fisher, A. R. Awtry, R. S. Sheinson, and J. W. Fleming, “Flow behavior impact on the suppression effectiveness of sub-10- $\mu$  m water drops in propane/air co-flow non-premixed flames,” *Proceedings of the Combustion Institute*, vol. 31, no. Part 2, pp. 2731–2739, 2007.
- [96] C. N. Banwell and E. M. McCash, *Fundamentals of Molecular Spectroscopy: Fourth Edition*. McGraw-Hill, 1994.
- [97] J. M. Brown, *Molecular Spectroscopy*. Oxford University Press, 1998.
- [98] B. P. Straughan and S. Walker, *Spectroscopy Volume Two: Molecular, Microwave, Infrared, Far-infrared and Raman Spectroscopy, Force Constants, Group Theory, and Thermodynamic Functions*. Chapman and Hall Ltd., 1976.
- [99] J. M. Hollas, *Modern Spectroscopy*. Wiley, 2004.
- [100] X. Zhou, *Diode-Laser Absorption Sensors for Combustion Control*. PhD thesis, Stanford University, 2005.
- [101] E. Whiting, “An Empirical Approximation To Voigt Profile,” *Journal Of Quantitative Spectroscopy & Radiative Transfer*, vol. 8, no. 6, pp. 1379–&, 1968.

- [102] J. Olivero and R. Longbothum, “Empirical fits to the Voigt line width: A brief review,” *Journal of Quantitative Spectroscopy and Radiative Transfer*, vol. 17, no. 2, pp. 233 – 236, 1977.
- [103] A. McLean, C. Mitchell, and D. Swanston, “Implementation of an efficient analytical approximation to the Voigt function for photoemission lineshape analysis,” *Journal of Electron Spectroscopy and Related Phenomena*, vol. 69, no. 2, pp. 125–132, 1994.
- [104] “Matlab online help - *fminsearch*,” 2011. URL: <http://goo.gl/GPxgw>.
- [105] M. Arroyo and R. Hanson, “Absorption-Measurements of Water-Vapor Concentration, Temperature, and Line-Shape Parameters Using a Tunable InGaAsP Diode-Laser,” *Applied Optics*, vol. 32, no. 30, pp. 6104–6116, 1993.
- [106] J. Shao, L. Lathdavong, S. Lundqvist, P. Kluczynski, and O. Axner, “Methodology for temperature measurements in water vapor using wavelength-modulation tunable diode laser absorption spectrometry in the telecom C-band,” *Applied Physics B*, vol. 97, pp. 727–748, 2009.
- [107] W. Johnstone, A. J. McGettrick, K. Duffin, A. Cheung, and G. Stewart, “Tunable Diode Laser Spectroscopy for Industrial Process Applications : System Characterization in Conventional and New Approaches,” *IEEE Sensors*, vol. 8, no. 7, pp. 1079–1088, 2008.
- [108] A. J. McGettrick, K. Duffin, W. Johnstone, G. Stewart, and D. G. Moodie, “Tunable Diode Laser Spectroscopy With Wavelength Modulation : A Phasor Decomposition Method for Calibration-Free Measurements of Gas Concentration and Pressure,” *Journal of Lightwave Technology*, vol. 26, no. 4, pp. 432–440, 2008.
- [109] A. L. Chakraborty, *Calibration-free Wavelength Modulation Spectroscopy with Elimination of Residual Amplitude Modulation*. PhD thesis, University of Strathclyde, 2010.

- [110] K. Ruxton, *Advances in Tunable Diode Laser Spectroscopy using Residual Amplitude Modulation Techniques*. PhD thesis, 2010.
- [111] P. Cancio, S. Bartalini, S. Borri, I. Galli, G. Gagliardi, G. Giusfredi, P. Maddaloni, P. Malara, D. Mazzotti, and P. De Natale, “Frequency-comb-referenced mid-IR sources for next-generation environmental sensors,” *Applied Physics B-Lasers and Optics*, vol. 102, pp. 255–269, FEB 2011.
- [112] P. Urquhart, “Transversely coupled fiber Fabry-Perot resonator: theory,” *Applied Optics*, vol. 26, no. 3, pp. 456–463, 1987.
- [113] P. Urquhart, “Compound optical-fiber-based resonators,” *Journal of the Optical Society of America A*, vol. 5, no. 6, pp. 803–812, 1988.
- [114] L. F. Stokes, M. Chodorow, and H. J. Shaw, “All-single-mode fiber resonator,” *Optics Letters*, vol. 7, no. 6, pp. 288–290, 1982.
- [115] J. R. P. Bain, W. Johnstone, K. Ruxton, G. Stewart, M. Lengden, and K. Duffin, “Recovery of Absolute Gas Absorption Line Shapes Using Tunable Diode Laser Spectroscopy With Wavelength Modulation-Part 2: Experimental Investigation,” *Journal of Lightwave Technology*, vol. 29, no. 7, pp. 987–996, 2011.
- [116] G. Stewart, W. Johnstone, J. R. P. Bain, K. Ruxton, and K. Duffin, “Recovery of Absolute Gas Absorption Line Shapes Using Tunable Diode Laser Spectroscopy With Wavelength Modulation-Part I: Theoretical Analysis,” *Journal of Lightwave Technology*, vol. 29, no. 6, pp. 811–821, 2011.
- [117] Private Communication - Prof. George Stewart, University of Strathclyde.
- [118] GATS Spectral Calculator - URL: <http://www.spectralcalc.com>.
- [119] L. Gordley, B. Marshall, and D. Chu, “LINEPAK - Algorithms for Modeling Spectral Transmittance and Radiance,” *Journal of Quantitative Spectroscopy & Radiative Transfer*, vol. 52, pp. 563–580, NOV 1994.

- [120] A. McGettrick, W. Johnstone, R. Cunningham, and J. Black, “Tunable Diode Laser Spectroscopy With Wavelength Modulation: Calibration-Free Measurement of Gas Compositions at Elevated Temperatures and Varying Pressure,” *Journal of Lightwave Technology*, vol. 27, pp. 3150–3161, Aug. 2009.
- [121] P. C. D. Hobbs, *Building Electro-Optical Systems: Making It All Work*. Wiley, 2000.
- [122] A. Bandyopadhyay, A. Ray, B. Ray, and P. Ghosh, “Lineshape study of argon broadened water vapour overtone transitions in the 818-834nm wavelength region,” *Journal of Molecular Spectroscopy*, vol. 234, pp. 93–98, Nov. 2005.
- [123] R. Engelbrecht, “A compact NIR fiber-optic diode laser spectrometer for CO and CO(2): analysis of observed 2f wavelength modulation spectroscopy line shapes,” *Spectrochimica Acta Part A-Molecular and Biomolecular Spectroscopy*, vol. 60, no. 14, pp. 3291–3298, 2004.
- [124] G. Houser and E. Garmire, “Balanced Detection Technique to Measure Small Changes in Transmission,” *Applied Optics*, vol. 33, no. 6, pp. 1059–1062, 1994.
- [125] T. Kraetschmer and S. T. Sanders, “Background-free absorption spectroscopy using delayed balanced detection,” *Applied Physics B-Lasers and Optics*, vol. 98, no. 2-3, pp. 249–252, 2010.
- [126] P. Weibring, D. Richter, A. Fried, J. G. Walega, and D. C, “Ultra-high-precision mid-IR spectrometer II : system description and spectroscopic performance,” *Applied Physics B*, vol. 85, pp. 207–218, 2006.
- [127] M. Allen, K. Carleton, S. Davis, W. Kessler, C. Otis, D. Palombo, and D. Sonnenfroh, “Ultrasensitive Dual-Beam Absorption and Gain Spectroscopy - Applications for Near-Infrared and Visible Diode-Laser Sensors,” *Applied Optics*, vol. 34, no. 18, pp. 3240–3249, 1995.

- [128] L. Persson, F. Andersson, M. Andersson, and S. Svanberg, "Approach to optical interference fringes reduction in diode laser absorption spectroscopy," *Applied Physics B-Lasers and Optics*, vol. 87, no. 3, pp. 523–530, 2007.
- [129] R. Hafiz and K. B. Ozanyan, "Digitally balanced detection for optical tomography," *Review of Scientific Instruments*, vol. 78, no. 10, 2007.
- [130] S. Pal, *Sensitive Detection Techniques and Systems for Minor Species Tomography*. PhD thesis, University of Manchester, 2009.
- [131] X. Zhu and D. T. Cassidy, "Electronic subtracter for trace-gas detection with InGaAsP diode lasers," *Applied Optics*, vol. 34, no. 36, pp. 8303–8308, 1995.
- [132] J. T. C. Liu, *Near-Infrared Diode Laser Absorption Diagnostics for Temperature and Species in Engines*. PhD thesis, Stanford University, 2004.
- [133] R. T. Ku, E. D. Hinkley, and J. O. Sample, "Long-path monitoring of atmospheric carbon monoxide with a tunable diode laser system," *Applied Optics*, vol. 14, pp. 854–861, Apr 1975.
- [134] R. Toth, "Extensive Measurements of (H<sub>2</sub>O)-O-16 Line Frequencies and Strengths - 5750 TO 7965 CM(-1)," *Applied Optics*, vol. 33, no. 21, pp. 4851–&, 1994.
- [135] International Telecommunications Union - URL: <http://goo.gl/wnjEv>.
- [136] O. Puig, C. Martinot, and P. Roustan, "Moisture ingress and absorption in a CCD package characterisation, modelisation and measurement," in *Proceedings of POLY98 Mechanical Reliability of Polymeric Materials & Plastic Packages of IC Devices, Hotel Concorde Saint-Lazare, Paris, France / November 29 - December 3, 1998*, DEC 1998.
- [137] P. Flatau, R. Walko, and W. Cotton, "Polynomial Fits To Saturation Vapor-Pressure," *Journal of Applied Meteorology*, vol. 31, pp. 1507–1513, DEC 1992.

- [138] S. Sanders, *Diode-Laser Sensors for Harsh Environments with Application to Pulse Detonation Engines*. PhD thesis, Stanford University, 2005.
- [139] T. Chiba, “Spot Dancing of Laser Beam Propagated Through Turbulent Atmosphere,” *Applied Optics*, vol. 10, no. 11, pp. 2456–&, 1971.
- [140] J. Churnside and R. Lataitis, “Wander of an Optical Beam in the Turbulent Atmosphere,” *Applied Optics*, vol. 29, no. 7, pp. 926–930, 1990.
- [141] R. Cook, “Beam Wander in a Turbulent Medium - Application of Ehrenfest’s Theorem,” *Journal of the Optical Society of America*, vol. 65, no. 8, pp. 942–948, 1975.
- [142] R. A. Chipman, J. Shamir, H. J. Caulfield, and Q.-B. Zhou, “Wavefront correcting properties of corner-cube arrays,” *Applied Optics*, vol. 27, pp. 3203–3209, Aug 1988.
- [143] “Investigation into the Optical Properties of Retro-reflective Sheets” - C. M. Wallis, J. D. Black, Rolls-Royce Internal Report.
- [144] J. D. Black and R. J. Parker, “Use of retroreflective material for pseudo single-ended CARS,” *Optics Communications*, vol. 8, no. 1, pp. 85–88, 1991.
- [145] D. Mitchell, *A Long Range Spectroscopic Methane Leak Sensor Using a High Power Raman Amplifier*. PhD thesis, University of Strathclyde, 2010.

# Publications

## Journal Publications

### Accepted

G. Stewart, W. Johnstone, J. R. P. Bain, K. Ruxton and K. Duffin, “Recovery of Absolute Gas Absorption Line Shapes Using Tuneable Diode Laser Spectroscopy with Wavelength Modulation Part I: Theoretical Analysis”, *Journal of Lightwave Technology*, vol. 29, no. 6, pp. 811-821, 2011.

J. R. P. Bain, W. Johnstone, K. Ruxton, G. Stewart, M. Lengden and K. Duffin, “Recovery of Absolute Gas Absorption Line Shapes Using Tuneable Diode Laser Spectroscopy with Wavelength Modulation Part 2: Experimental Investigation”, *Journal of Lightwave Technology*, vol. 29, no. 7, pp. 987-996, 2011.

### In Preparation

J. R. P. Bain, M. Lengden, G. Stewart and W. Johnstone, “Elimination of Residual Amplitude Modulation in Tunable Diode Laser Wavelength Modulation Spectroscopy with Current and External Modulation using Balanced Photoreceivers”, In preparation.

M. Lengden, J. R. P. Bain, I. Armstrong, G. Stewart and W. Johnstone, “Tunable Diode Laser Spectroscopy with Wavelength Modulation: Characterisation of FM/IM Phase Shift”, In preparation.

## Conference Publications

M. Lengden, W. Johnstone, J.R.P. Bain, G. Stewart and I. Armstrong, “Preliminary gas composition investigations at elevated temperatures and pressures using calibration-free TDLS with the residual amplitude modulation

technique”, 7th International Conference on Tunable Diode Laser Spectroscopy (TDLS), Zermatt, Switzerland, 13-17 July 2009.

J.R.P. Bain, G. Stewart, K. Duffin, M. Lengden, K. Ruxton and W. Johnstone, “Recovery of absolute gas absorption lineshapes using TDLS at arbitrary modulation indices”, International Conference on Field Laser Applications in Industry and Research, Grainau, Germany, 6-11 September 2009.

M. Lengden, J.R.P. Bain, I. Armstrong and W. Johnstone, “Two gas spectrometers for the investigation of gas absorption parameters at elevated temperatures and pressures”, International Conference on Field Laser Applications in Industry and Research, Grainau, Germany, 6-11 September 2009.

J.R.P. Bain, M. Lengden, J. Black and W. Johnstone, “Development of a TDLS-based Ambient Water Vapour Sensor for Aeroengine Intake Temperature Determination”, 8th International Conference on Tunable Diode Laser Spectroscopy (TDLS), Zermatt, Switzerland, 11-15 July 2011.

J.R.P. Bain, M. Lengden, J. Black and W. Johnstone, “Measurement of Aeroengine Intake Gas Temperature Using TDLS of Atmospheric Water Vapour”, International Conference on Field Laser Applications in Industry and Research, Murnau, Germany, 13-17 September 2011.

J.R.P. Bain, J.D. Black, W. Johnstone, “Development of Tunable Diode Laser Spectroscopy Sensor Systems for Line-of-sight Measurement of Water Vapour in Aero Engine Exhaust Plumes”, Photon 12, Durham, UK, 3-6 September 2012

## List of Abbreviations and Symbols

$A$	Integrated absorbance
$a_n$	Fourier coefficient
AC	Alternating Current
AM	Amplitude modulation
ANN	Artificial neural network
BJT	Bipolar junction transistor
$C$	Concentration
$c$	Speed of light
$C_f(\nu)$	Correction function
CWDM	Coarse wavelength division multiplexing
DAQ	Data acquisition
DC	Direct current
DFB	Distributed feedback
DP	Dew point
$E$	Energy
$E''$	Lower state energy
ECDL	External cavity diode laser
EDFA	Erbium-doped fibre amplifier
EFE	Environmentally friendly engine
EPSRC	Engineering and Physical Sciences Research Council
$f, f_m$	Sinusoidal modulation frequency
FC-APC	Ferrule connector with angled physical contact
FFT	Fast Fourier transform
FLITES	Fibre Laser Imaging of Gas Turbine Exhaust Species
FM	Frequency modulation
FMS	Frequency modulation spectroscopy
FSR	Free spectral range
FTIR	Fourier transform infrared
GEISA	Gestion et etude des informations spectroscopiques atmosphériques

GPIB	General purpose interface bus
GRIN	Graded index
$h$	Planck's constant
HWHM	Half width at half maximum
HITEMP	High temperature molecular spectroscopic database
HITRAN	High resolution transmission molecular absorption database
$I$	Optical power
IM	Intensity modulation
InGaAs	Indium gallium arsenide
InGaAsP	Indium gallium arsenide phosphide
InSb	Indium antimonide
IR	Infrared
ITU	International Telecommunications Union
$J$	Rotational quantum number
$k$	Boltzmann's constant
$L$	Path length
LIA	Lock-in amplifier
$m$	Modulation index
NH	High pressure spool speed
NDIR	Nondispersive infrared
$P$	Pressure
$P(m)$	Line centre absorbance ratio
PCI	Peripheral component interconnect
PD	Phasor decomposition
$Q(T)$	Partition function
QCL	Quantum cascade laser
RAM	Residual amplitude modulation
RF	Radio frequency
RH	Relative humidity
rpm	Revolutions per minute
RTD	Resistance temperature detector

$S(T)$	Line strength
Si	Silicon
SNR	Signal-to-noise ratio
STP	Standard temperature and pressure
$T$	Temperature
$T_0$	HITRAN reference temperature
TDLS	Tunable diode laser spectroscopy
TEC	Thermoelectric cooler
UV	Ultra violet
$V_B$	Transistor base voltage
$V_E$	Transistor emitter voltage
$V_{BE}$	Transistor base-emitter voltage
VCSEL	Vertical cavity surface emitting laser
VOA	Variable optical attenuator
VOC	Volatile organic compound
VP	Vapour pressure
WM	Wavelength modulation
WMS	Wavelength modulation spectroscopy
$\alpha$	Absorption coefficient
$\alpha_0$	Line centre absorption coefficient
$\beta$	Frequency modulation index
$\gamma$	Line width half width at half maxima
$\gamma_L$	Lorentzian line width
$\gamma_G$	Gaussian line width
$\Delta\nu$	$\frac{\nu-\nu_0}{\gamma}$
$\Delta I, \Delta I_1$	Linear intensity modulation
$\Delta I_2$	Nonlinear intensity modulation
$\delta\nu$	Frequency dither amplitude
$\delta i$	Current dither amplitude
$\kappa$	Modulation coefficient
$\lambda$	Wavelength

$\nu$	Laser frequency
$\nu_0$	Line centre frequency
$\nu_1$	Instantaneous laser frequency
$\xi$	Current tuning coefficient
$\nu$	Vibrational quantum number
$\Phi_G$	Gaussian line shape function
$\Phi_L$	Lorentzian line shape function
$\Phi_V$	Voigt line shape function
$\psi$	Phase shift between FM and linear IM
$\psi'$	Phase shift between WM and linear IM
$\psi''$	Phase shift between linear and nonlinear IM
$\omega$	Angular frequency
$\mathfrak{R}$	Photodiode responsivity

# Appendix A

## MATLAB Voigt Simulation Code

```
%=====
% H2O VOIGT SIMULATION =====
%=====
% MICHAEL LENGDEN, JAMES BAIN =====
%=====

clc

close all

clear

format long

% =====
% DEFINING EXPERIMENTAL PARAMETERS FOR VOIGT PROFILE (MCLEAN)
% =====

% Defining all constants
% Boltzmann's constant
k = 1.3806503e-23;
% Methane molecular mass
M = 18;
% Speed of light (cm^-1)
c = 299792458e2;
```

```

% Planck's constant
h = 6.626e-34;
% Path length of cell (cm)
L = 134.5;
% Defining HITRAN reference temperature
T_0 = 296;
% Defining gas temperature (input Celsius output Kelvin)
T_K = 273.15;
T = 2.5;
T = T+T_K;
% Define concentration and pressure
conc = 0.005;
pressure = 1;

% Input spreadsheet with HITRAN08 Data
h2olines = xlsread('_insert HITRAN file path_');

z = length(h2olines);
% Defining frequency scale with arbitrary number of steps
vsteps = 2000;
v = linspace(7400,7410,vsteps);
% Convert to wavelength (nm)
wavelength = 1./v.*1e7;

% =====
% PARTITION FUNCTION 1 - ORIGINAL
% =====
% Polynomial coefficients for partition function 70<T<405K
a1 = -4.4405;
b1 = 0.27678;
c1 = 0.12536-2;

```

```

d1 = -0.48938e-6;
% % Polynomial coefficients for partition function 405<T<1500K
% a1 = -0.94327e2;
% b1 = 0.81903;
% c1 = 0.74005e-4;
% d1 = 0.42437e-6;
% Calculation of partition function at HITRAN reference and gas
% temperatures
Q_T0 = a1+b1*T_0+c1*(T_0^2)+d1*(T_0^3);
Q_T = a1+b1*T+c1*(T^2)+d1*(T^3);

% =====
% PARTITION FUNCTION 2 - VIDLER & TENNYSON, J CHEM PHYS, 2000
% =====
% % Alternative calculation for partition function
% % Polynomial coefficients for partition function 70<T<405K
% a0 = -14.0874691574179;
% a1 = 37.9243248539882;
% a2 = -42.6817978731789;
% a3 = 25.3302448517916;
% a4 = -8.10851262935532;
% a5 = 1.33106871720535;
% a6 = -20.087298105109575;
%
% Q_T2 = exp(a0*(log(T)^0)+a1*(log(T)^1)+a2*(log(T)^2)+...
a3*(log(T)^3)+a4*(log(T)^4)+a5*(log(T)^5)+a6*(log(T)^6));
% Q_T02 = exp(a0*(log(T_0)^0)+a1*(log(T_0)^1)+a2*(log(T_0)^2)+a3*...
(log(T_0)^3)+a4*(log(T_0)^4)+a5*(log(T_0)^5)+a6*(log(T_0)^6));

% Calculate individual linestrengths
S1 = 1-exp(-(h*c.*h2olines(:,3))/(k*T));

```

```

S2 = 1-exp(-(h*c.*h2olines(:,3))/(k*T_0));
S3 = S1./S2;
S4 = Q_T0./Q_T;
S5 = T_0/T;
S6 = exp((-h*c*h2olines(:,8)/k)*((1/T)-(1/T_0)));
S7 = S3.*S4.*S5.*S6;
S_T = S7.*h2olines(:,4);

% Air broadening parameter
air_broadening_parameter = h2olines(:,6).*(T_0/T).^h2olines(:,9);
% Self broadening parameter
self_broadening_parameter = h2olines(:,7).*(T_0/T).^h2olines(:,9);

% Gaussian Broadening
gammaG = 7.1625e-7.*h2olines(:,3).*(T/M)^0.5;
gammaG = gammaG';

% Lorentzian broadening
gammaL = (2*pressure).*((conc.*self_broadening_parameter)+...
(1-conc).*air_broadening_parameter));
gammaL=gammaL';

% Calculate X for Mclean calculation
for j = 1:z
X(:,j) = 2*sqrt(log(2))*(v-h2olines(j,3)-h2olines(j,10))./gammaG(j);
end

% McLean function coefficients
A = [-1.2150 -1.3509 -1.2150 -1.3509];
B = [1.2359 0.3786 -1.2359 -0.3786];
C = [-0.3085 0.5906 -0.3085 0.5906];

```

```

D = [0.0210 -1.1858 -0.0210 1.1858];

% Calculate Y for Mclean calculation
Y = (gammaL./gammaG)*sqrt(log(2));

for j = 1:z
    for i = 1:4
        V_top(i,:) = (C(i)*(Y(j)-A(i)))+(D(i)*(X(:,j)-B(i)));
        V_bottom(i,:) = (Y(j)-A(i))^2+(X(:,j)-B(i)).^2;
    end
    V = V_top./V_bottom;
    Vfinal(:,j) = (2/gammaG(j))*(log(2)/pi)^0.5*conc*(7.339e21/T_0)*...
        S_T(j)*sum(V);
end

% Sum contributions from all absorption lines in the range
voigt = pressure*sum(Vfinal');
% Calculate final Voigt profile
relative_transmission = exp(-voigt.*L);

```

# Appendix B

## MATLAB Wavelength Reference Code

```
%=====
% WAVELENGTH REFERENCE PROGRAM =====
%=====
% ARUP LAL CHAKRABORTY, JAMES BAIN =====
%=====

clc

close all

clear

format long

% =====
% READ IN EXPERIMENTAL SIGNALS AND THEORY FILES
% =====

signal = dlmread('_insert signal file path_');
theory = dlmread('_insert theory file path_');
% Extract absorption spectra and resonator trace from signal file
transmission = signal(:,1);
res = signal(:,2);
```

```

% Extract wavelength and amplitude from theoretical simulation file
waves = theory(:,1);
amps = theory(:,2);

% =====
% PEAK IDENTIFICATION
% =====

diff_res      = diff(res);
peak          = [];
for n = 1:length(diff_res)-1
    if ( ne(sign(diff_res(n)),sign(diff_res(n+1)))...
        && (diff_res(n) > diff_res(n+1)) )
        peak = [peak n+1];
    end
end

% Check that no spurious resonator peaks are included
figure; hold on
plot(peak, res(peak), 'o')
plot(res)

% =====
% PERFORM REFERENCING PROCEDURE
% =====

% Find the line centre wavelength of the theory plot
% Arbitrary constant for relative wavelength/frequency scale
line_cent_wave = 150000;
% Read off index point of line centre point
line_cent_index = find(transmission == min(transmission));
% Res peak closest to Line_Cent_Index
[error1, closest_peak] = min(abs(peak - line_cent_index));

```

```

% FSR of fiber ring resonator (GHz)
FSR = 0.43;
% Convert zero-crossing indices to frequencies
res_peak_wave = [];
res_peak_wave(closest_peak)= 150000;
leftside = line_cent_wave + ((closest_peak) - [1:closest_peak])*FSR;
rightside = line_cent_wave - (((closest_peak+1):length(peak)) - ...
closest_peak)*FSR;
res_peak_wave = [leftside rightside];
res_peak_wave = res_peak_wave(:);
% Make 2nd order poly fit to interpolate between resonator frequencies
P = polyfit(peak(:),res_peak_wave(:),2);
x = (1:length(transmission));
% Extract values of polynomial fit at each increment x
YYY = polyval(P(:),x(:));
% Shift polynomial to match experimental file at line centre & outwards
theory_cent_freq = 3e8./waves(find(amps == min(amps)));
shift = theory_cent_freq - YYY(line_cent_index);
YYY = YYY + shift;
% Final wavelength vector
wavelength = 3e8./YYY;

```

# Appendix C

## MATLAB Phasor Decomposition Method and Correction Function Code

```
%=====
% PHASOR DECOMPOSITION METHOD AND CORRECTION FUNCTION PROGRAM =====
%=====
% JAMES BAIN, KEVIN DUFFIN, ANDREW MCGETTRICK =====
%=====

clc
close all
clear
format long

% =====
% READ IN EXPERIMENTAL SIGNALS AND THEORY FILES
% =====

signals = dlmread('_insert signal file path_');
% Extract absorption spectra from signal file
AM_FM      = signal(:,1);
```

```

AM_FM_no_gas = signal(:,2);
sep_FM       = signal(:,3);
sep_FM_no_gas = signal(:,4);
% Determine wavelength scale from calculation or previously saved file
wavelength   = signal(:,5);

% =====
% CALCULATION OF PHI - AM/WM PHASE SHIFT
% =====
% Locate +ive & -ive peaks of sep_FM signal
y1 = min(sep_FM);
y1_index = find(sep_FM == y1);
y2 = max(sep_FM);
y2_index = find(sep_FM == y2);

% Calculate x1, x2 corresponding to indices for y2 and y2
min_AM_FM = AM_FM(y2_index);
max_AM_FM = AM_FM(y1_index);

% Calculate corresponding values on RAM- to be subtracted from x1 and x2
% RAM corresp to sep_FM -ive peak
RAM_negative_peak = RAM_amps(y1_index);
% RAM corresp to sep_FM +ive peak
RAM_positive_peak = RAM_amps(y2_index);

% Therefore, actual values of x1 and x2...
x1 = (max_AM_FM(1) - RAM_negative_peak(1));
x2 = (min_AM_FM(1) - RAM_positive_peak(1));
% FINALLY...Calculate phi = AM_WM_phase_shift in degrees
phi = (180/pi)*atan((abs(y2)+abs(y1))/abs((x1-x2)));

```

```

% =====
% PERFORM PDM CALCULATION FOR ABSOLUTE TRANSMISSION FUNCTION
% =====
% Calculate direct signal using phasor decomposition method
AM_whole      = AM_FM + ( sep_FM./tan((phi)*pi/180) );
AM_base       = RAM_amps + ( sep_FM_no_gas./tan((phi)* pi/180) );
transmission  = AM_whole(:)./AM_base(:);

% =====
% M DETERMINATION - FIT METHOD
% =====
% Fminsearch function will optimise 'm' and 'A'
% Calls function 'm_determination1' with initial values...
% Returns vector ZZ
[ZZ, fval, exitflag] = fminsearch(@m_determination1, [2 0.1]);

% Fit results for 'm' and 'A'
m_ref = ZZ(1);
A_2 = ZZ(2);

% Alternatively...

% =====
% 'M' DETERMINATION - RATIO METHOD
% =====
% Require low 'm' reference signal
transmission2 = signal(:,6);

% Read off the peak depths
distorted_min = min(transmission);
low_m_min = min(transmission2);

```

```

% Calculate 'A' factor; A=alphaCl
A0 = -log(low_m_min);

% Calculate ratio
ratio = (1-distorted_min)/A0;

% Create multipliers for creating matrices from vectors
multiplier1      = linspace(1,1,10000);
multiplier2      = linspace(1,1,360);

% Define 'theta' for integration
theta            = linspace(0,pi,360);
% Keep 'theta' as a vector for later, but use 'multiplier1' for
% 'theta_1' to create matrix compatible with 'delta_1' in integral
theta_1          = theta';
theta_1          = theta_1*multiplier1;

% Define number of reference points in look-up table
n_increments =1000;

% Open loop to calculate P(m) at a range of m values
for n = 1:n_increments
    bbb = 2.5/n_increments;
    m(:,n) = 0+(bbb*n);

    y = (sin(theta).^2).*(1-exp(-A0./(1+(m(:,n))^2)...
    .*(cos(theta).^2)));
    zz = trapz(theta,y);
    P_m(:,n) = (2/(pi*A0))*zz;
end

```

```

% Use the look up table and compare to the experimental P(m) ratio
look_up_table = [m' P_m'];
look_up_table = look_up_table';
[zero look_up_index] = min(abs(ratio-look_up_table(2,:)));
m_ref = look_up_table(1,look_up_index);

% =====
% CORRECTION FUNCTION CALCULATION
% =====
% Ask user for current dither size
voltage_dither = input('\n Input voltage dither applied in mV?');
% Read in delta_nu/delta_V value,obtained previously from laser
% characterisation procedure
del_nu = 1.2171e-3;
del_nu = 1e9*del_nu*voltage_dither;
del_nu_cm = del_nu/3e10;

% Define HWHM for delta, based on new m
HWHM = del_nu/m_ref;

% Calculating Correction Factors, start with delta values
delta = (abs(frequencies)-line_cent_freq)./HWHM;
% Keep 'delta' as a vector and use 'delta_i' as a matrix.
delta_i = delta*multiplier2;
delta_i = delta_i';

% y is the integrand of the correction factor
y = (1-cos(2*theta_1))./(1+(delta_i+(m_ref*cos(theta_1))).^2);
zz = trapz(theta,y);

% Obtain correction factor

```

```

correction_function = ((1+delta.^2)./pi).*zz';
correction_function = 1./correction_function;

% =====
% APPLY CORRECTION FUNCTION TO RECOVER ABSOLUTE ABSORPTION LINESHAPE
% =====
% Apply each new correction factor to original data
amps_corrected = (1-transmission).*correction_function;
amps_corrected = 1-amps_corrected;
relative_transmission = amps_corrected;

```